UNIVERSITÀ
DEGLI STUDI
DI PADOVA

Head Office: Università degli Studi di Padova

Department of Chemical Sciences

Ph.D. COURSE IN MOLECULAR SCIENCES

CURRICULUM CHEMICAL SCIENCES

XXIV CYCLE

HETEROGENEOUS CATALYSIS FOR ENVIRONMENTAL APPLICATIONS

Thesis written with the financial contribution of University of Padova

Coordinator: Prof. Leonard J. Prins

Supervisor: Prof. Antonella Glisenti

Co-Supervisor: Prof. Mauro Sambi

Ph.D. candidate : Elena Brusamarello

ABSTRACT

In this thesis various metal oxides have been employed to tackle the issue of atmospheric pollution with the final perspective of climate change mitigation. Efforts have been devoted to the abatement of both CO, NO and other pollutants deriving from automotive engine sources and carbon dioxide. In this latter case the final aim is the valorization of carbon dioxide into an easily applicable fuel, methane, with high selectivity and yield. In this way the advantages are several: firstly this enables the decrease of its concentration in the atmosphere and on the other side it allows the production of a valuable fuel, with already established applications, closing the carbon cycle that led to carbon dioxide emission in the atmosphere itself. Extensive characterization of the materials developed allowed to correlate such results with the catalytic activity performances, shedding light on the mechanisms involved and contributing to the enhancement of the catalytic performances as well.

Together with some conventional approaches to heterogeneous catalysis techniques, an innovative procedure was developed to incorporate nickel (the active catalyst) into an unusual support, a molecular sieve carbon membrane. This particular support was chosen in order to optimize the carbon dioxide methanization process, since this technology is already used for water separation from gaseous mixture and this reaction carries with it the by-production of water.

Therefore both material design and process optimization have been addressed in the present work in order to maximize the catalytic performances and decrease as much as possible Platinum Group Metals that nowadays represent critical raw materials, both in terms of supply and recycling potentialities.

Summary

1. Introduction

The scope of the present work is to apply heterogeneous catalysis methods to environmental remediation for atmospheric pollution.

The scientific community, as well as the general population, are nowadays aware of the effects and the causes of the emergency of climate change resulting from human-induced emission of greenhouse gases. Weather patterns are changing in a large scale and at this point global warming has already been found to be a critical issue: temperature rise on land is about twice the global average increase, and it is also amplified in the Arctic region, where it has contributed to melting permafrost, glacial retreat and sea ice loss.[1]

Warmer temperatures are also the cause of more intense storms and weather extremes due to the higher evaporation rates, giving a profound impact on ecosystems and therefore relocation or extinction of many animal and plant species. Climate change threatens people with food insecurity, water scarcity, flooding, infectious diseases, extreme heat, economic losses and displacement.[2] Due to these concerning consequences the World Health Organization declared climate change the greatest threat to global health in the twenty-first century.[3] As aforementioned, greenhouse gases are responsible for dramatic effects and they prevalently consist of water vapor, carbon dioxide, methane and ozone. In this group CO_2 and CH_4 are the ones endowed with the greatest greenhouse effect; moreover the increment of their concentration in the atmosphere enhances their harmful effect towards the balance of earth's carbon cycle.[4]

The Intergovernmental Panel on Climate Change (IPCC) is the United Nation body for assessing the science related to climate change and it is in charge of producing periodic scientific reports on the risks and trends of human-induced climate change, its natural, political, and economic impacts, and on possible response options. Based on their most recent models, the prediction is that global warming

will grow with a 0.2°C per decade and they report that most populations in the world have already experienced warming in at least one season.

Therefore, global warming is an urgent issue and significant technologic and scientific efforts should be directed to its solution or, at least, control. For this reason, heterogenous catalysis to promote environmentally sustainable reactions can be a viable opportunity to relieve the urgency of this significative task.

The PhD project herein presented focuses on two classes of environmentally purposeful processes: Three- Way Catalysis (from now on abbreviated as TWC) and Sabatier reaction, i.e. carbon dioxide methanation. TWC and Sabatier reaction represent two distinct ways to tackle the problem of atmospheric pollution, seen from two different perspectives. The first one mainly deals with automotive engine emissions in the atmosphere, with the precise aim to reduce the concentration of Unburnt HydroCarbons (UHCs), carbon monoxide (CO) and nitrogen oxides (NO_x), since they represent the major noxious gases in the exhaust of internal combustion engines. The name comes from the three processes taking place: reduction to nitrogen oxides to nitrogen, oxidation of hydrocarbons and carbon monoxide to carbon dioxide. Stringent regulations in the emission levels permitted impose their elimination before they reach the outer environment. Generally, emission control devices allow to convert simultaneously the abovementioned toxic gases into harmless carbon dioxide, nitrogen and water, according to the following equations:

$UHC + O_2 \rightarrow CO_2 + H_2O$

$2CO + O_2 \rightarrow 2CO_2$

$UHC + NO \rightarrow 0.5\ N_2 + CO_2 + H_2O$

$CO + NO \rightarrow 0.5\ N_2 + CO_2$

Perovskite oxides, a promising class of catalysts active in this kind of reactions, will be reported in the present thesis as valid alternatives to the commercial technology currently used, which is based on noble metals, in particular palladium and platinum, together with rhodium and iridium. Moreover industrial viewpoints will be discussed with a case study of perovskites with different compositions obtained by two relevant industrial synthesis techniques, correlating synthetic conditions, structural properties and catalytic activities.

The Sabatier reaction, on the other side, is the reaction of carbon dioxide with hydrogen to yield methane and water, according to:

$$CO_2 + 4H_2 \rightarrow CH_4 + H_2O$$

Traditionally this reaction was studied at high temperature (300-400°C) and high pressure (30 bar) in the presence of Ni catalyst (usually enriched with Ru) and it was discovered by P. Sabatier. Although quite old, this reaction has interesting applications in carbon cycling strategies and power-to-fuel approaches, as discussed later. In the present work, atmospheric or low pressures (≤6 bar) will be employed, and no precious metal will be implied in the synthesis of the catalysts used. Moreover both a conventional powder catalyst and membrane catalytic reactors will be tested.

Albeit the two strategies sound contrasting, as one produces carbon dioxide and the other uses it as a reagent, the perspective is to tackle atmospheric pollution in different applications and scenarios. While catalytic converters for automotive engines are diffuse mobile devices to avoid the emission of significative amounts of carbon monoxide and carbon soot into the atmosphere, producing a less harmful compound for health, Sabatier reaction is more oriented towards highly pollutant sources of concentrated carbon dioxide, such as factory gas outlets and other large industrial facilities. The latter are indeed punctual sources that can be engineered to provide relatively pure gas mixtures, suitable

to this catalytic conversion, very sensitive to impurity poisoning, as opposed to TWC in the automotive sector in which the exhaust gas mixture composition cannot be finely tuned.

1.1 State of the art: Three-Way Catalysis and perovskites

Catalytic conversion of exhaust emission for automotive engines is a technology that allows to control the concentration of toxic gases resulting from internal combustion engines and therefore to keep their amount in the atmosphere under precise threshold value. The protection of air quality and reduction of emissions is a priority for many supranational organizations, such as the European Commission. Emission standards are in place for all kind of fueled vehicles, and they are becoming increasingly stringent throughout the years, since the public and scientific sensitivity towards this theme is growing. In particular, in the European Union, the emissions of the following air pollutants are regulated: nitrogen oxides (commonly indicated as NOx), unburnt hydrocarbons, carbon monoxide and particulate matter (also known as soot, or carbon soot).

The first automotive emissions standards were introduced in 1963 in the US, as a response to Los Angeles' smog problems. A few years later (between 1970 and 1972) Japan, Australia, Canada and many European nations enacted their first emission regulations concerning CO and hydrocarbons. In the following five years also nitrogen oxide emissions were enacted in the several nations.

Globally speaking, the standards gradually have grown more stringent but have never ben unified, giving rise to mainly three sets of standards: US, Japanese and European.

Commercial TWC converters are usually placed as close to the engine as possible to benefit from the high temperature of the working combustion engine, they indeed require a temperature of approximately 400°C to be effective. Consequently, thermal ageing can cause sintering processes or diffusion, shortening significantly the lifetime of the catalytic converters. They are usually constructed with a substrate core made out of a ceramic monolith, featuring a honeycomb structure.

The most common material in catalytic converter cores is cordierite (a magnesium iron aluminum cyclosilicate). Cordierite is chosen because it has a low thermal expansion coefficient, useful feature to prevent cracking when thermally stressed. Monoliths are manufactured by extruding a suitable mixture of clay, talc, alumina and water with various organic additives, then dried and calcined at high temperature.[5] The shape of the final product comprises blocks of parallel channels and this particular structure avoids fouling since the pressure drop produced in the gas stream is negligible.[6]

A carrier for the catalytic material is therefore applied on top of the monolith, and it is called washcoat, to disperse the materials over a large surface area. Aluminum oxide, titanium oxide, silicon dioxide or a mixture of silica and alumina can be used. Ceria is also added as oxygen storage promoter. The active material in the converters is composed of a mix of precious metals, mostly from the platinum group (PGMs, Platinum Group Metals). Rhodium is used as a reduction catalyst and palladium as an oxidation catalyst, whereas platinum can serve for both reactions. Nickel and copper were historically also tested for TWC but they were soon abandoned as they are too sensitive to poisoning by lead and halide from additives in the fuel and also by sulfur dioxide derived from sulfur compounds originally present in fuel and lubrication oils. Moreover they have low thermal resistance and durability.[7]

The use of Critical Raw Materials (CRMs) in the automotive industry, mainly PGMs and Rare Earth Elements (RREs), accounts for 65-80% of the total European PGMs demand. The enforcement of new limits on gas and particulate emissions will require higher TWC performance, hence leading to further increase of the CRMs content in catalysts.

Because of the progressive loss of catalytic activity upon ageing and of the price and scarcity of Critical Raw Materials, there is a need to develop new strategies to reduce their amount in catalytic converters and for enhancing their tolerance to harsh operating conditions.[8]

Concerning their functioning, three main pollutants are present in the exhaust gases of combustion engines: nitrogen oxides (NOx), hydrocarbons and carbon monoxide. The unburnt hydrocarbons are

produced since the oxidation of gasoline in the engine (to carbon monoxide and water) is not perfectly efficient, leading to significant amounts of hydrocarbon residues in the outlet gases and partially combusted products like aldehydes, ketones and carboxylic acids, together with carbon monoxide. [9] Moreover the reaction between nitrogen and oxygen (present in air) to yield NO is favored at the high temperature reached in the engine cylinder. The produced NO can be further partially oxidized to NO_2 by oxygen again. This reaction reaches an equilibrium in which both NO and NO_2 are mixed, therefore it is usually referred to as NO_x. This equilibrium shows a dependency on temperature, partial pressures of the gases involved and contact time among them, changing considerably depending on the running conditions.

Among all these species, both produced in the engine and already present in the inlet, CO, hydrocarbons and NO_x shall be removed because of their negative health and environmental impact. The harmful effects of CO are related to the reduction of the amount of oxygen that can be transported in the blood stream to critical organs like the heart and the brain. NO_x has both detrimental health and environmental consequences. It is highly irritating to the airways in the human respiratory system and exposures to NO_2 over short periods can aggravate respiratory disease, particularly asthma. Longer exposures may contribute to the development of asthma and potentially increase susceptibility to respiratory infections.[10] It is also implied in reactions forming particulate matter and ozone, both harmful when inhaled due to effects on the respiratory system. NO_x can also interact with water and oxygen in the atmosphere to form acidic rain, damaging sensitive ecosystems such as lakes and forests. Finally NO_x in the atmosphere contribute to nutrient pollution in coastal waters, leading to unsustainable growth of algae in waters, decreasing water quality and available oxygen that fish and other aquatic life need to survive. This phenomenon is also known as algal blooms. Hydrocarbons such as Polycyclic Aromatic Hydrocarbons (PAH) have been extensively correlated to respiratory and cardiovascular diseases among others, and cancer risk. Moreover several hormonal problems that

can interfere with developmental and reproductive processes are caused by the presence of PAH in the atmosphere.[11]

Hence, to lower the diversified risks derived from their emission in the atmosphere, their removal is carried out by Three Way Catalytic converters placed in the vehicle tailpipe to convert CO, HCs and NOx into some other innocuous gas species.

Three reactions are mainly taking place in a TWC converter:

1) The oxidation of carbon monoxide
2) The oxidation of hydrocarbons
3) Reduction of NOx with CO and hydrocarbons, which are in turn oxidized

Other side reactions can take place in a TWC, such as the so-called water gas shift reaction (WGS) between CO and water which yields CO and H_2. Hydrogen also contributes to NO_x reduction.

Application of TWC requires some technical elements for their correct operation: (i) electronic fuel injection to provide a stoichiometric air/fuel mixture; (ii) an oxygen sensor in the exhaust and (iii) a microprocessor to control a feedback-loop using oxygen sensor signals to determine the amount of fuel to be injected under specific conditions to maintain the exhaust gas close to the stoichiometric ratio.[9]

Libby proposed a peculiar perovskite oxide compound, $LaCoO_3$, as an economic alternative for noble-metal catalyst for the treatment of gas exhaust from combustion engines. The suggested perovskite has indeed a prominent activity for hydrocarbon oxidation. This happened already in 1971 and opened the way to a new research branch, investigating the possibility to avoid precious metal compounds in TWC technology.[12] and simultaneously understand and improve the catalytic properties of perovskite-type oxides and relevant mechanisms involved in oxidation and reduction reactions in

TWC processes. In the abovementioned article, quite short but interestingly ahead of time, he stated that the cost of this catalyst would be about $1 per pound (in 1971), highlighting the potentiality of this new approach to auto exhaust treatment. Libby reported that $LaCoO_3$ could rival platinum in the gas phase aqueous oxygen electrode, arising interest in this family of metal oxides.

After Libby's contribution to the matter, Co-, Fe-, Mn- and Ru-based perovskite oxides were proven effective in oxidation carbon monoxide and reducing nitrogen oxides. Significant in this sense is the scientific production of Voorhoeve et al.[13–16] Not only as-prepared perovskites were tested towards this reactivity, but also other preparation approaches were attempted, e.g. the deposition of perovskites ($LaMnO_3$-type in particular) on monolith of cordierite ceramic, to imitate the already existing TWC devices but avoiding precious metal use.[17] A comprehensive review of the perovskite-type oxides that were proposed to replace conventional catalytic converters is not the aim of this chapter, for this reason the redox properties of these materials will be addressed instead, together with a discussion of the relevant mechanisms involved in oxidation and reduction processes.

Perovskite is a mineral of formula $CaTiO_3$, discovered in 1839 by the Prussian mineralogist Gustav Rose in mineral deposits in the Ural Mountains and named after the Russian mineralogist Count Lev Aleksevich von Petrovski. The crystal structure of this compound, initially thought to be cubic, was later shown to be orthorhombic.[18] As with many minerals, Perovskite has given its name to a family

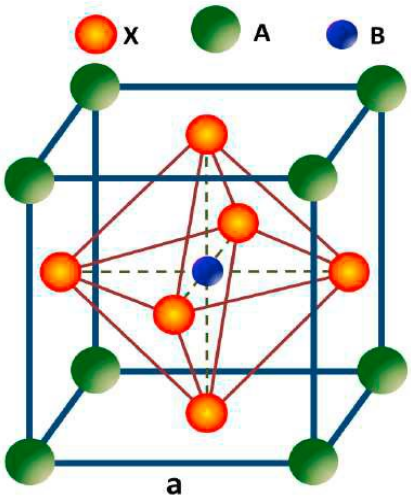

Figure 1 The ideal cubic perovskite unit cell.

of compounds called *perovskites*, with a general formula ABX_3. They can be compared to some extent with simple ionic compounds, where A is a large cation, B a medium-sized cation and X an anion. The ideal cubic structure features B cations in a 6-fold coordination, surrounded by an octahedron of anions, and the A cation in 12-fold cuboctahedral coordination. A pictorial representation of the structure is reported in Figure 1.

The overall ionic structure must be electronically neutral, oxygen bearing a -2 formal oxidation state. If we write the charges on the ion as q_A and q_B, then $q_A+q_B=6$. Frequently encountered combinations are:

$(q_A,q_B)=(1,5)$; for example $NaNbO_3$

$(q_A,q_B)=(2,4)$; for example $CaTiO_3$

$(q_A,q_B)=(3,3)$; for example $LaAlO_3$

The importance of perovskites grew with the discovery of the interesting dielectric and ferroelectric properties of $BaTiO_3$ in the 40s.[19] In the following decades it was attempted to improve the material properties, leading to an intensive research on structure-property relationships of a large number of nominally ionic ceramic perovskite phases with composition ABO_3, with a result that vast numbers of new phases were synthetized and investigated, exploring the wide flexibility in accommodating several different metal cations as A and B in the structure. This was rationalized by Goldschmidt in 1926, who suggested a formula that could be used to predict the likelihood that a pair of ions would form a perovskite structure phase.[20] It is now called the Goldschmidt's rule:

$$t = \frac{(r_A + r_X)}{\sqrt{2}(r_B + r_X)}$$

t is called the tolerance factor, r_A and r_B are the radii of the cations A and B and r_X the radius of the anion (mostly oxygen). Goldschmidt suggested that a perovskite structure phase would form if the

value of the tolerance factor is close to 1.0. Empirically a value between 0.75 and 1 is suitable to the formation of a perovskite structure.

Of course the ionic radii shall be chosen considering the coordination of the relative cation (A is 12-coordinated, B is octahedrally coordinated and the oxygen is linearly coordinated). An alternative form of this rule, calculating the observed tolerance factor, uses the measured bond lengths from crystal structures rather than ionic radii.

As said, the idealized form is a cubic structure, however not so frequent, orthorhombic and tetragonal phases are in fact more common. Also monoclinic or triclinic symmetries can be retrieved.

The variability of perovskite structures also regards the content of oxygen and defects. Usually the larger A-cation belongs to rare-earth elements, or alkaline earth or alkali metal cation. The B-site is conventionally occupied by a transition metal cation. Not only A and B can greatly vary across the periodic table, but also doping can be employed to endow the compound with a desired particular feature, getting control on the oxidation state of the cation of the structure as well as the non-stoichiometry (through anionic or cationic vacancies) in the mixed oxide based on electroneutrality arguments.

The multiplicity of oxidation states is the major responsible for the catalytic properties of perovskite catalysts.[21,22] These reasons, together with the large array of properties owned by perovskites (*e.g.* ferroelectricity, piezoelectricity, pyroelectricity, thermoelectricity, magnetism, superconductivity), account for the large number of scientific papers published every year (more than 2000) with a specific focus on perovskite preparation, structure elucidation and applications.[8]

Catalytic properties have been investigated since the 50s,[23,24] thanks to their adsorption, acid-base, as well as redox properties.[25] The first processes in which they were used as catalysts were total or partial oxidation of hydrocarbons, oxygenated compounds or halocompounds; hydrogenation of CO or CO_2; hydrogenolysis of hydrocarbons, but also photocatalytic and electrocatalytic processes.[25,26]

Empirically it has been observed that the nature of the B-site cation largely controls the catalytic activity of a perovskite-type oxide. Depending on the process, different metal occupying the B-site are more suitable than others in enhancing catalytic activity. Considering a typical TWC reaction, oxidation of hydrocarbons and CO, and excluding noble metal-based perovskites, Co- and Mn-based perovskites perform the best, as it can be seen from

Figure *2*, where B stands for B-site cation.[27] Nitadori et al. also pointed out that the role of A-cation was found to be less decisive in the studied systems.

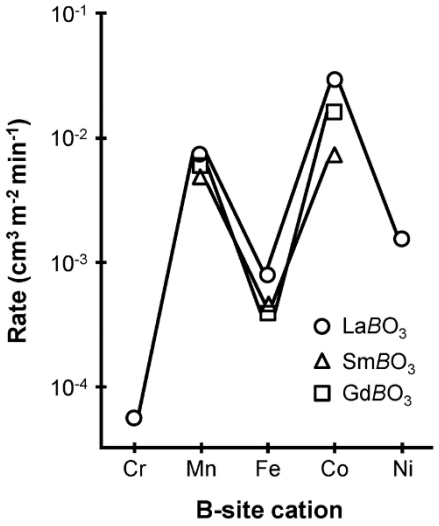

Figure 2. Influence of A- and B-site cations on the catalytic activity of perovskite-type oxides for propane oxidation at 227°C. Adapted from Nitadori et al.27

Although the nature of the A-site cation is less relevant to the catalytic activity of the compound, partial substitution (doping) with aliovalent cations can form oxygen vacancies and/or the change of oxidation state of the B-site cation. This behavior of perovskites in catalytic context will be discussed in depth in the following chapters, where Fe-, Mn- and Ni-based perovskites will be treated to investigate their catalytic, functional, morphologic and structural properties and correlations between all these aspects will be drawn.

Chapter 2 addresses a case of perovskites with diverse composition to tackle pollution abatement from the atmosphere, both in simple, mechanistical gas mixtures and more complex and realistic ones, to shed light on the reproducibility and subtle differences between industrially produced Fe- and Mn-based perovskites.

1.2 Soot oxidation and perovskites

Alongside with polluting gas removal from atmosphere, great relevance has been gained by soot abatement from diesel engine exhaust.

Diesel engines have increased in popularity compared to gasoline engines, due to better fuel efficiency, lower operating cost, higher durability and reliability.[28] Despite the large application that these engines have found in the transportation sector (commercial transport, off-road vehicles such as excavation machinery, mining equipment etc), a major environmental problem associated with diesel combustion is the emission in the atmosphere of particulate matter (PM) from the exhaust, consisting mainly of carbonaceous soot and soluble organic fraction (SOF) of hydrocarbons.[29] Their effect on environment and human health is detrimental: it absorbs sunlight contributing to the greenhouse effect, it is able to shrink cloud droplets size, brightening clouds and darkening ice and snow. Carrying several adsorbate on the surface, particular matter is able to interfere with soil, agriculture and animal physiology in a notable way.[30] Their nanoporosity (with a typical range of 2-4 nm) and large surface areas can host approximately 90 different organic pollutants, including aromatic compounds and other hydrocarbons with also heavy metals (such as lead). No doubt is left that the carcinogenic properties of aromatic compounds and photochemical effects of hydrocarbons, enhancing the hazard brought about by soot emission in the atmosphere.[31] According to the World Health Organization (WHO), particular matter (i.e. soot) is one of the main cause of cardiovascular and respiratory diseases.[32]

The term soot is given to the particulates formed during the combustion of carbon-based fuels under substoichiometric conditions (that may occur deliberately or in poor mixing conditions, which is the case of diesel engines).

The formation of soot proceeds following some fundamental steps that have been universally accepted by the scientific community: sequential nucleation, growth and coagulation. Soot inception begins in laminar diffusion flame for a range of hydrocarbons at temperatures between 1300 and 1400°C.[33,34] Uncharged radicals and molecules are the flame nucleation precursors, *i.e.* nucleation units. The growth takes place by addition of gaseous carbonaceous species and this process results in the formation of the particles comprised of spherules.[35] Many mechanicistic models are available but the prevailing ones describe acetylene and polycyclic aromatic hydrocarbons (also known as PAHs) as the suppliers of the bulk of the carbon that is incorporated into the soot spherules. Other authors suggest the involvement of polyynes ($C_{2n}H_2$, n=2,3,..) as precursor radicals, partly because their stability increases with the temperature.[36,37 38]

The process will be described according to the considerations of Richter and Howard in a systematic collection of reaction pathways for soot formation, published in 2000.[39]

The formation of molecular precursors of soot is the first stage. It starts from small molecules such as benzene to progressively larger PAHs, adding small units (such as C_2, C_3 among others) to PAH radicals. However also recombination among growing aromatic species or addition reactions may take place at the same time. Depending on the fuel each reaction contributes differently.

After this first step, nucleation or inception can start: the heaviest PAH molecules (with approximately a molecular mass of 2000 amu and an effective diameter of at least 1.5 m) can coagulate. The exact chemical details of the formation of incipient soot nuclei are still a demanding task and have not be completely unveiled and understood.

The mass of such particles then increases via the addition of gas phase species such as acetylene and PAH, including PAH radicals. This process does not affect the number of particles but only their size.

When a sufficient mass is reached, sticking collisions between particles take place and significantly (and rapidly) increase particle sizes decreasing particle number. Gas addition may still happen during this phase, but it represents a secondary process.

If the product of this multiplicity of phenomena can reside long time at high temperature, carbonization can occur: a general rearrangement of the structure leads from a mainly amorphous material to a more graphitic carbon material, by means of elimination of functional groups, cyclization, ring condensation and ring fusion reactions, together with dehydrogenation, growth and alignment of polyaromatic layers. Finally, if oxygen is present, oxidation processes are possible, competing with soot formation.[40]

Since perovskites are known for their good oxidation catalytic potentialities, they have been extensively studied in order to optimize their composition as well as preparation approaches towards the most performing material in this sense.

Their structure and properties can also be modified due to the great extent of substitution possible at both A and B sites. The oxygen adsorption and desorption properties of perovskites can play a crucial role for low temperature oxidation of soot/particulate matter. Two types of oxygen are retrieved by oxygen temperature programmed desorption studied (O_2-TPD): alpha and beta oxygen. Alpha desorbs from the perovskite, which is said to be responsible for oxidation reactions at lower and higher temperature respectively. When molecular oxygen adsorbs on the catalytic surface of perovskite, it is accommodated in the O^{2-} vacancies formed by the partial substitution of A-site cations by lower valence ions. Such alpha type weakly chemisorbed oxygen, “suprafacial” species are supposed to be responsible for soot oxidation.[41–44]

Chapter 3 will deal in depth with Mn-based perovskites for soot oxidation and there more details are given about the choice of the composition and about the mechanisms underlying the reaction of interest.

1.3 Carbon dioxide abatement

Many evidences point out that the Earth's climate and the carbon cycle are inherently linked: carbon cycle processes determine the flow of carbon between reservoirs and in the atmosphere, the carbon-based gases carbon dioxide and methane are, along with water vapor, the major greenhouse gases (GHGs).[45] Carbon dioxide, among GHGs, is very long-lived, and its atmospheric concentration has been rising at unprecedented rates due to continued intensive fossil fuel use, land use change and cement production. Concerning reports show that the concentration of atmospheric carbon dioxide has exceeded 400 ppm, and is currently at levels not seen in at least the last 800 000 years. Changes in the global carbon cycle and detectable global warming are the consequences.[46,47] As atmospheric CO_2 levels continue to rise the likelihood of "severe, pervasive, and irreversible" impacts increases. This was recognized by the United Nations Framework Convention on Climate Change, who facilitated the Paris Agreement on climate change in which countries pledged Nationally Determined Contributions (NDCs) to deliver emissions reductions. However, the emissions reductions resulting from current NDCs appear to be insufficient to limit warming to "well below 2° C above pre-industrial," the goal of the Paris Agreement. Consequently, it is increasingly likely that some form of carbon dioxide removal from the atmosphere will be needed to reach this goal.[45] For example, using an intermediate complexity Earth system model, it could be predicted that if carbon dioxide emissions were interrupted today, surface temperature would remain approximately constant for centuries (the source of this notion dates back to 2010 but we consider it still valid in the present day).[48] Other authors report that if we could set to zero the carbon dioxide emission at the middle of the twenty-first century (556 ppm according to predictions of the Hadley Center climate/carbon cycle model) the Earth surface temperature would continue to increase slightly and remain 2°C higher than the pre-industrial level for at least a century.[49]

These predictions point out the necessity of a parallel action, beside cutting carbon dioxide emission, which should always remain the primary goal in climate mitigation policies. The alternative to stopping completely CO_2 emission is not to prevent its release in the atmosphere but to exploit technologic pathways to capture it when it is already free in the atmosphere and possibly to utilize it as a source of carbon to synthesize new useful molecules: carbon-based fuels are an example and comprise methane, methanol, dimethyl ether and heavier hydrocarbons.

A double benefit to environment and economy would therefore be achieved: from one side harmful carbon dioxide emissions are reduced in amount, to the other we would be able to obtain valuable fuels and to close the carbon cycle that causes such a large number of detrimental effects on global climate. Many others have been the proposals for the utilization pathways of carbon dioxide: production of carbon dioxide-based polymers, microalgae fuels and other microalgae products, concrete building materials, CO_2 enhanced oil recovery, bioenergy with carbon capture and storage, enhanced weathering, forestry techniques (including afforestation, reforestation, forest management and wood products), land management via soil carbon sequestration techniques and biochar fabrication. A comprehensive and recent review addressing all these alternatives can be found at ref.[50], from which Figure 3 is taken. This picture summarizes in an effective way the whole scenario and the relevance of each contribution to carbon dioxide emission and natural capture (land and ocean sink respectively). The numbers below each stock is the estimates of stocks in the Earth's spheres (litosphere, biosphere, hydrosphere and atmosphere, labelled in bold) with selected stock subcategories. All estimates are based on IPCC estimates.[47]

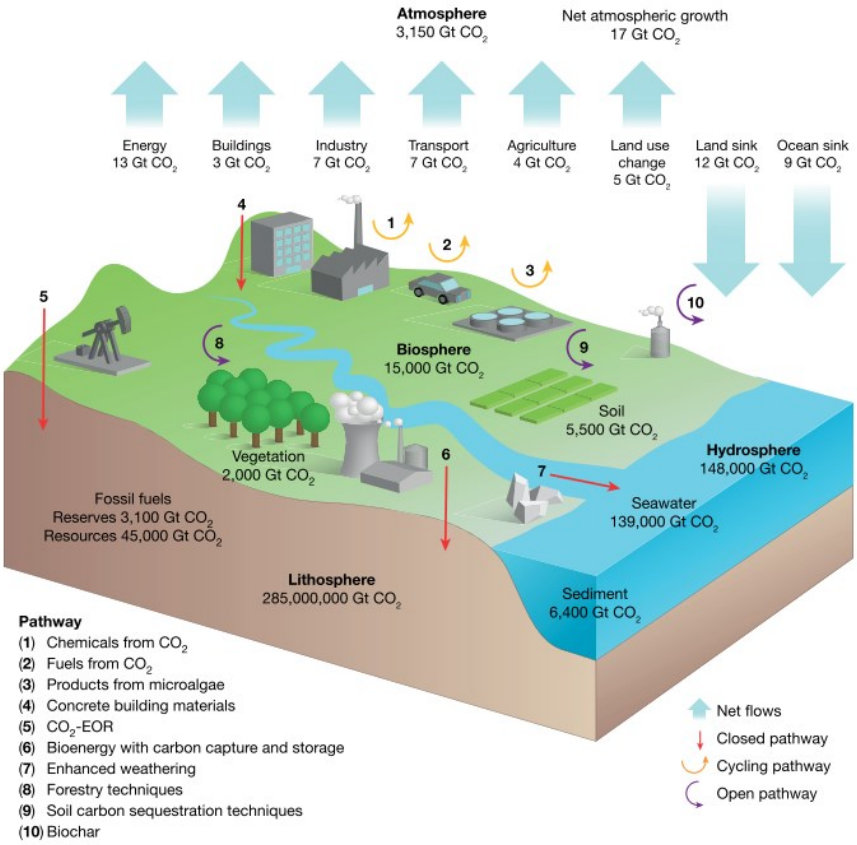

Figure 3 Stocks and net flows of CO2 including potential utilization and removal pathways. The image is taken from Hepburn et al. The Technological and Economic Prospects for CO2 Utilization and Removal. Nature 2019, 575 (7781), 87–97. Please see text for further information.

In this project we will deal with CO_2 conversion to fuels through catalytic hydrogenation processes to convert it from flue gas or other sources (punctual or diffuse) into fuels. In this case the utilization product is a CO_2-derived fuel that can be directly used (methane or methanol) or can undergo Fischer-Tropsch, that will be then used as combustion media to release energy again.

Moreover fuels derived from CO_2 are argued to be an attractive option in the decarbonization process because they can be deployed within existing transport infrastructure.[51,52] This currently represents the only pathway to decarbonize challenging sectors such as aviation, since the energy densities of hydrocarbons are orders of magnitude above those of present-day batteries.[53]

According to estimates, the potential for the scale of CO_2 utilization in fuels varies widely, from 1 to 4.2 Gt CO_2 y^{-1}, reflecting uncertainties in potential market penetration.[50] Of course the attractiveness of this solution depends also on the availability of the so-called "green" hydrogen, that means renewable retrieved hydrogen and not fossil fuel-derived one.

The production of carbon dioxide derived fuels is nowadays focusing on five main topics: (1) reverse water-gas shift, (2) hydrogenation to hydrocarbons, alcohols, dimethyl ether (DME) and formic acid, (3) reaction with hydrocarbons to syngas, (4) photo- and electrochemical/catalytic conversion and (5) thermochemical conversion.[54] We should keep in mind that currently the utilization of CO_2 as chemical feedstock is currently limited to a few processes: synthesis of urea (for nitrogen fertilizers and plastics), salicylic acid (pharmaceutical active ingredients) and polycarbonates (for plastic production). However this of course corresponds to a small share of the large potential of this inexpensive reagent. At the present day hydrogenation of CO_2 to form oxygenates and/or hydrocarbons is the most intensively investigated area of CO_2 conversion. Methanol, which is already a viable fuel, has been investigated as a potential product of such processes, together with DME, a clean-burning fuel that is a potential diesel substitute. Ethanol formation, either directly or via methanol homologation, or the conversion of CO_2 to formic acid are also potentially interesting routes. Moreover methanol, ethanol and formic acid may be used as feedstocks in fuel cells, providing a route to store energy from CO_2 and then produce electricity.

Considering again hydrogenation from green hydrogen, according to estimates, the hydrogenation to hydrocarbons consumes much more hydrogen (per unit of product) than formation of oxygenates. Therefore, this route is valuable in principle only when hydrogen is made mainly from renewable or non-fossil resources.[54]

The industrial opportunities in this field comprise attractive aspects in the development of efficient conversion routes of CO_2 to fuel and chemicals, or the use of CO_2 in chemical processes: first of all, it implies a decrease in costs for CO_2 disposal or emission reduction credits, with a consequent

improvement of the public image for the contribution in converting a greenhouse gas into valuable chemicals or fuels. This would lead to the production of liquid fuels from CO_2 which easily integrate within the existing infrastructure and having a higher energy density and easier transport/storage than competing solutions (hydrogen, in particular).

The recovery of CO_2 from flue gas to produce a high concentration feedstock is already a consolidated technology that was successfully developed in the past, usually by adsorption in suitable solvents (mainly alkanolamines) but also membranes or solid adsorbents. This technology is usually referred to as Carbon Capture.[55–58] Chemical absorption technology usually refers to ammonia process and amine scrubbing, in which acid-base properties are exploited in order to obtain carbonate salts. Physical absorption can make use of activated carbon with very high porosity in order to trap CO_2 inside pores, or in alternative membrane technology, working at refrigeration temperature to favor gas adsorption. Finally chemical looping combustion (CLC) is another viable alternative for its capture from the atmosphere.

Three main methods for capturing CO_2 are currently commercially available and they are post combustion capture, pre-combustion capture and capture by means of an oxygen rich combustive medium. In the case of post combustion capture, this technique is well-known and established in industrial setups and it allows the removal of sulphur oxides as well (namely SO_2, S_2O_3). Pre-combustion technique is also well established but needs higher concentrations of carbon dioxide to be effective, and it is sensitive to moisture presence in the gases mixture. The last technique, relying on oxygen rich combustive media, has the great advantage of excluding nitrogen from the mixture, avoiding the formation of nitrogen oxides. Moreover it works with less gas volumes than other techniques thanks to the removal of nitrogen.

Chemical looping approaches are based on a constant oxygen exchange: two reactors are coupled, in one of them metal nanoparticles are able to adsorb chemically selectively oxygen in a dissociative way forming the relative oxide. It should not be reactive towards nitrogen to avoid nitride formation

and is called carrier material. In a following step such oxides are brought into contact with the fuel that will react forming CO_2 and H_2O without traces of nitrogen or sulphur oxides since oxygen was generated and exchanged from pure feedstocks, no separation device is therefore needed.[50]

1.4 Carbon dioxide activation and Power-to-Gas approach

The process of exploiting renewable energy to produce green hydrogen to be employed in carbon dioxide hydrogenation is called Power-to-Gas process (PtG). It allows to utilized the intermittent excess of electricity, produced by renewable power sources like solar or wind, to decompose water into hydrogen and oxygen by electrolysis.[59,60] A schematic and generic scheme for the energy cycle that exploits captured or sequestered carbon dioxide and sustainable or renewable hydrogen to yield carbon-neutral or renewable carbonaceous fuels is visible in Figure 4, which is taken from ref.[51]

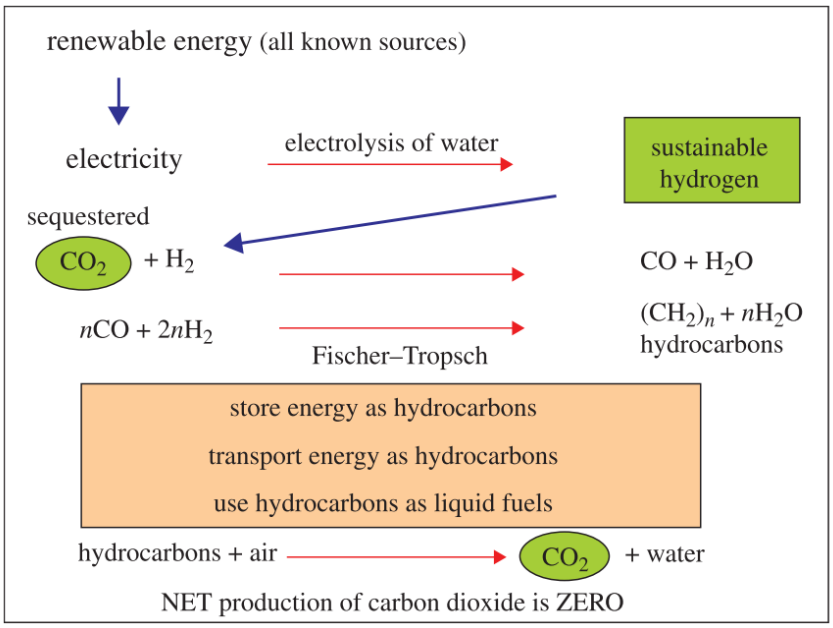

Figure 4 Generic energy cycle to yield carbon-neutral fuels from CO2. Taken from Jiang et al. Phil. Trans. R. Soc. A (2010) 368, 3343

The produced hydrogen can work as an energy carrier or used to react with carbon dioxide to give methane according to the Sabatier reaction ($CO_2 + 4H_2 \rightarrow CH_4 + 2H_2O$). One main advantage of the production of methane is its already existing distribution infrastructure. As for carbon dioxide methanation, it is an exothermic ad thermodynamically favored reaction (ΔH0=-164 kJ/mol; ΔG0 = -131 kJ/mol) but kinetically limited, being an 8-electron process occurring above 200°C in the only presence of a catalyst. The range of study of CO_2 methanation is between 200°C and 500°C to avoid the reverse water gas shift reaction ($CO_2 + H_2 \rightarrow CO + H_2O$), which takes place at higher temperatures. Moreover one of the main interests of this research is to minimize critical raw material use and to develop a simple and sustainable synthetic methodology to obtain such materials.

Thermodynamically speaking, CO_2 activation is not an easy task. Its Gibbs free energy is quite low (-394.39 kJ/mol)[61] (see also Figure 5): high energy is required to the formation of carbon dioxide and the kinetics is unfavored. The entropic term included in the Gibbs free energy makes little or no contribution to the thermodynamic driving force for any reaction involving carbon dioxide.[51] Therefore enthalpy can be conveniently considered as a good initial guide for assessing thermodynamic stability and feasibility of any CO_2 conversion.

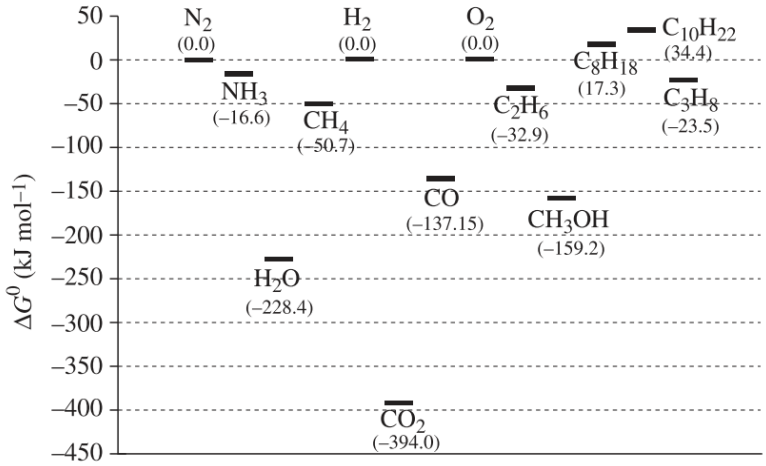

Figure 5 Gibbs free energy of formation for selected chemicals. Here the free energy of formation for the constituent elements is taken as the reference point. Taken from Jiang et al. Phil.Trans. R. Soc. A (2010) 368, 3343

Comparing the enthalpy of the methane steam-reforming, a well-known and common reaction, with the one of CO_2 dry reforming (both to obtain syngas), the former requires just 20% more energy input than the latter, giving the general impression of a feasible process, as long as the working temperature is adequate.[51,62] From Figure 5 it is therefore possible to conclude that it would be thermodynamically easier to carry out reactions using CO_2 as a co-reactant with another substance that has a higher (less negative) Gibbs free energy, *e.g.* H_2 and CH_4.

To conveniently activate the stable carbon dioxide molecule, the double C=O bonds should be weakened by the interaction with a suitable support.[63] Often transition metal supports were proposed for the formation of a surface carbonate, but the weakening effect was not enough effective. Other supports induce a bridge coordination of carbon dioxide between the metal atoms of the surface, this phenomenon electronically depletes the C-O bond from the π system and deform the O-C-O bond angle away from the initial 180°. Since the carbon sp^2 orbital is not overlapping with the sp^3 of oxygen as well as before, also the σ bond system becomes less strong. All these circumstances finally lower the activation energy for the overall molecule hydrogenation. If the support is also prone to dissociatively bind hydrogen on the surface, then both reagents are kinetically favored to react together, and a catalytic effect of the support is observed.[64]

CO_2 dry reforming is the process of formation of CO and H_2O starting from a hydrogen and carbon dioxide. It is a thermodynamically unfavored reaction and to get kinetically acceptable performances high pressures and high temperatures are required. Its main drawback is the possibility for side reaction to occur, in particular carbon deposition (*i.e.* coking) is always possible and the complete reduction of carbon dioxide to carbon is called Boudouard reaction. It is particularly favored at temperatures higher than 700°C. The main catalysts employed for CO_2 dry reforming are noble metals, non noble transition metal (especially Ni), perovksites, zeolites or clays with large surface areas.[65,66]

Regarding the production of methanol, a fuel whose worldwide annual production exceeds 40 Mt, a direct reaction between CO_2 and hydrogen is possible and can be viewed as a mechanism for "liquefying" hydrogen chemically using carbon dioxide. The pioneer of the so-called *methanol economy* was George Olah (1927-2017), a Hungarian chemist. In his comprehensive works he advanced the concept and potential widespread adoption of methanol (or DME) obtained by the chemical recycling of CO_2.[52,67] A real attraction of such an approach is that one could envisage the catalytic hydrogenation of CO_2 focused at small, delocalized production sites as an alternative to the current large-scale, localized sites producing methanol by steam reforming of CH_4.[51,68] The critical issues of this approach center on the following points: first of all the separation and availability of carbon dioxide at adequate concentrations, the development of high performances, robust and inexpensive catalysts to activate the implied small molecules, the operation that needs to be carried out at mild temperature and pressure conditions and finally the availability of sustainable hydrogen. Detailed analysis of the energetic cost of methanol synthesis from atmospheric CO_2 highlight the greatest role of the energy requirement of hydrogen production as determining factor for the viability of this route.[69]

Solar photocatalytic reduction of CO_2 is another option that can simultaneously recycle CO_2 and store intermittent solar energy in synthetic carbon-neutral fuels suitable for storage. However, to the present day, this represents one of the most challenging tasks in environmental catalysis: already in 1979 Inoue and colleagues reported the photocatalytic reduction of CO_2 in aqueous solutions to produce a mixture of formaldehyde, formic acid, methanol and methane using various wide-band-gap semiconductors (such as the conventional titania, ZnO, CdS among others).[70] The primary task of photocatalysis in this case is to convert the absorbed photons into electron-hole pairs, which needs to be separated to drive chemical oxidation and reduction half-reactions at the semiconductor-electrolyte interface. In other words the absorption process must be coupled with multi-electron redox reactions,

often occurring simultaneously. The properties of potential photocatalysts are determined by the redox potential of the rate-limiting steps of water oxidation and CO_2 reduction:

$$2H_2O_{(l)} \rightarrow O_{2(g)} + 4H^+_{(aq)} + 4e^- \qquad E^0_{ox} = -1.23\ V,$$

$$CO_{2(aq)} + e^- \longrightarrow CO_2^-\ (aq) \qquad E^0_{red} = -1.65\ V.$$

These values allow to recognize the minimum threshold for the energy levels of the conduction and valence bands of a photocatalyst. Wide-band-gap semiconductors are the most suitable photocatalysts for CO_2 reduction because photo-generated electrons in the bottom of the conduction band can have sufficient negative redox potential to drive CO_2 reduction, while the photo-generated holes in the valence band can be sufficiently energetic (positive holes) to act as acceptors and oxidize water to O_2. The main drawback of such systems is the inability to use visible light efficiently.

Several groups of novel efficient photocatalysts have recently been discovered, including oxynitrides (*e.g.* $Ga_{1-x}Zn_xO_{1-y}N_y$;[71–73]), tantalates (*e.g.* $NaTaO_3$ and others;[74]), bismuth-based photocatalysts (*e.g.* $BiVO_4$;[75–77]) and some others.[74]

1.5 Sabatier reaction

Chapter 4, 5 and 6 will deal with carbon dioxide methanation approaches by means of very different supports and catalysts. The recurring theme for these three chapters will be the use of nickel as catalyst for the reaction and the repeated attempt to support it on various substrates, let them be simple oxides, mixed oxides or carbon matrixes.

The CO_2 hydrogenation to methane is called Sabatier reaction and could be easily employed in industrial applications and the product can be used as a fuel or raw material for the production of

chemicals. Paul Sabatier (1854-1941) was a French chemist that together with Jean-Baptiste Senderens discovered the reaction in 1897. He was awarded the Nobel Prize in Chemistry in 1992 along with Victor Grignard for their work improving the hydrogenation of organic species in the presence of metals.

One of the most interesting application of this reaction, beside the removal of unwanted carbon dioxide from the atmosphere, is its use in future manned space colonization on Mars.[78] Bringing hydrogen from the Earth to Mars would make it possible to convert the Martian carbon dioxide atmosphere into methane and water for fuel and astronaut life-support systems.[79]

In the authentic Sabatier process the reaction $CO_2 + 4H_2 \rightarrow CH_4 + 2H_2O$ is conducted at 300-400°C and high pressures (30 bar) in the presence of a nickel catalyst.[80] Already at Sabatier's time Ni was suggested as an active catalyst for this reaction, but also the performances of ruthenium on alumina were known. Nickel is a very attractive solution, however, due to its high selectivity and low cost.

CO_2 methanation studies stemmed from CO methanation research, a field that gained importance for the production of Synthetic Natural Gas during the oil crisis in the late 1970s.[81] Later in the 80s some new studies focused on the use of coke oven gas or blast furnace gas for downstream methanation.[59] Only in the following years, as a result of an ever-growing environmental awareness and the urgency to reduce anthropogenic greenhouse gas emissions, CO_2 methanation gained new popularity in the scientific and technologic community. At the same time a new need for electricity storage was rising and Power-to-Gas approaches were considered as promising solutions.

The challenges about this reaction are nowadays reducing the pressure needed to carry out the process (and in this thesis atmospheric pressure or 6 bar will be set as working pressures) and the activation temperature. However temperature is a critical parameter, that cannot be indistinctly increased with the aim of accelerating the kinetics. The reverse water gas shift reaction (rWGS) is indeed occurring at temperatures higher than 500°C and produces CO which is then a byproduct needing a further separation step at the end: $CO_2 + H_2 \rightarrow CO + H_2O$.[82]

Despite the simplicity of the reaction, the accurate description of the mechanism can be challenging. Debates are still active about the nature of the intermediate compound(s) in the process and two main schools of thought include in one case the conversion of CO_2 to CO and in the other involves the formate intermediate.[83–86] There is a general agreement on the fact that CO is implied in the reaction. A great number of studies have been conducted to shed light on the adsorption and activation of CO_2 on metal surfaces such as Cu, Pt, Pd and Fe, sometimes with the help of computational techniques like density functional theory DFT calculations, but still no universal consensus could be achieved.[87–90] As reported by Aziz et al. DFT calculations were for instance performed to investigate the complete hydrogenation mechanisms for CO_2 on Ni(110)surface[91], with the result that it passes via various stable intermediates and namely carbon monoxide, methoxy, formate and eventually yield methane. The authors suggest that methane formation via hydroxyl carbonyl intermediate requires a lower energy barrier than via monoxide and formate intermediates.

According to the CO route, supported by *in situ* FTIR investigations on CO_2 adsorbing, a dissociation of CO_2 to adsorbed CO and O occurs, over a variety of noble metal-based catalyst.[86] The direct dissociation of CO_2 was evidenced by Karelovic and colleagues.[92] The fate of CO_{ads} is also debated: it is known that it must proceed by dissociation but two pathways are actually likely to occur. The first is a direct CO dissociation and the second is a H-assisted CO dissociation. The first mechanism is proposed to occur over group VIII metal-based catalysts, however the second route is being proposed by other authors.[93–97] Figure 6 reports from ref.[86] a schematic summary of the mentioned reaction pathway that lead to methane formation from the mixture of carbon dioxide and hydrogen.

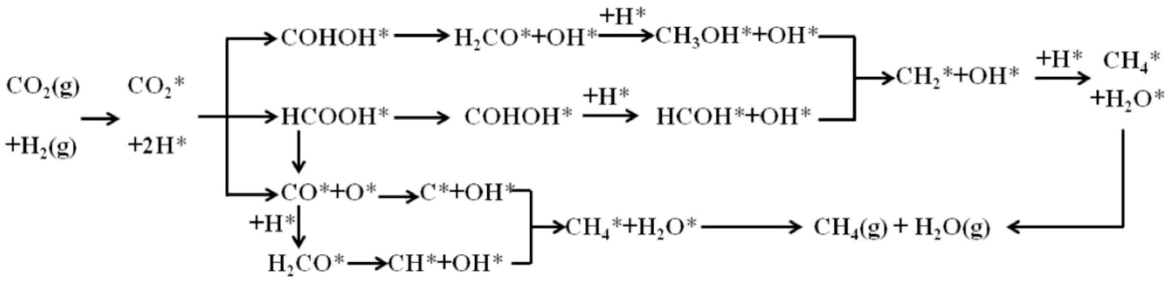

Figure 6 Representation of possible reaction pathways of carbon dioxide methanation. Image taken from Su et al. J. Energy Chem (2016) 26, 4, 553

References

(1) IPCC. IPCC Special Report on the Ocean and Cryosphere in a Changing Climate; 2019.

(2) Cattaneo, C.; Beine, M.; Fröhlich, C. J.; Kniveton, D.; Martinez-Zarzoso, I.; Mastrorillo, M.; Millock, K.; Piguet, E.; Schraven, B. Human Migration in the Era of Climate Change. *Rev. Environ. Econ. Policy* **2019**, *13* (2), 189–206. https://doi.org/10.1093/reep/rez008.

(3) Core Writing Team, R. K. P. and L. A. M. (eds. . IPCC, 2014: Climate Change 2014: Synthesis Report. Contribution of Working Groups I, II and III to the Fifth Assessment Report of the Intergovernmental Panel on Climate Change; Geneva, Switzerland, 2014. https://doi.org/https://www.ipcc.ch/report/ar5/syr/.

(4) Shi, R.; Waterhouse, G. I. N.; Zhang, T. Recent Progress in Photocatalytic CO 2 Reduction Over Perovskite Oxides. *Sol. RRL* **2017**, *1* (11), 1700126. https://doi.org/10.1002/solr.201700126.

(5) Avila, P.; Montes, M.; Miró, E. E. Monolithic Reactors for Environmental Applications. *Chem. Eng. J.* **2005**, *109* (1–3), 11–36. https://doi.org/10.1016/j.cej.2005.02.025.

(6) Nijhuis, T. A.; Beers, A. E. W.; Vergunst, T.; Hoek, I.; Kapteijn, F.; Moulijn, J. A. Preparation of Monolithic Catalysts. *Catal. Rev.* **2001**, *43* (4), 345–380. https://doi.org/10.1081/CR-120001807.

(7) Gandhi, H. S.; Graham, G. W.; McCabe, R. W. Automotive Exhaust Catalysis. *J. Catal.* **2003**, *216* (1–2), 433–442. https://doi.org/10.1016/S0021-9517(02)00067-2.

(8) Keav, S.; Matam, S. K.; Ferri, D.; Weidenkaff, A. Structured Perovskite-Based Catalysts and Their Application as Three-Way Catalytic Converters-a Review. *Catalysts*. MDPI AG July 1, 2014, pp 226–255. https://doi.org/10.3390/catal4030226.

(9) Guillén-Hurtado, N.; Rico-Pérez, V.; García-García, A.; Lozano-Castelló, D.; Bueno-López, A. Three-Way Catalysts: Past, Present and Future. *DYNA* **2012**, *79* (175 E), 114–121.

(10) Kampa, M.; Castanas, E. Human Health Effects of Air Pollution. *Environ. Pollut.* **2008**, *151* (2), 362–367. https://doi.org/10.1016/j.envpol.2007.06.012.

(11) Srivastava, M.; Srivastava, A.; Yadav, A.; Rawat, V. Source and Control of Hydrocarbon Pollution. In *Hydrocarbon Pollution and its Effect on the Environment*; IntechOpen, 2019. https://doi.org/10.5772/intechopen.86487.

(12) Libby, W. F. Promising Catalyst for Auto Exhaust. *Science (80-.).* **1971**, *171* (3970), 499–500. https://doi.org/10.1126/science.171.3970.499.

(13) Voorhoeve, R. J. H.; Remeika, J. P.; Freeland, P. E.; Matthias, B. T. Rare-Earth Oxides of Manganese and Cobalt Rival Platinum for the Treatment of Carbon Monoxide in Auto Exhaust. *Science (80-.).* **1972**, *177* (4046), 353–354. https://doi.org/10.1126/science.177.4046.353.

(14) Voorhoeve, R. J. H.; Remeika, J. P.; Johnson, D. W. Rare-Earth Manganites: Catalysts with Low Ammonia Yield in the Reduction of Nitrogen Oxides. *Science (80-.).* **1973**, *180* (4081), 62–64. https://doi.org/10.1126/science.180.4081.62.

(15) Voorhoeve, R. J. H.; Remeika, J. P.; Trimble, L. E. Perovskites Containing Ruthenium as Catalysts for Nitric Oxide Reduction. *Mater. Res. Bull.* **1974**, *9* (10), 1393–1404. https://doi.org/10.1016/0025-5408(74)90064-6.

(16) Voorhoeve, R. J. H.; Trimble, L. E.; Khattak, C. P. Exploration of Perovskite-like Catalysts: Ba2CoWO6 and Ba2FeNbO6 in NO Reduction and CO Oxidation. *Mater. Res. Bull.* **1974**, *9* (5), 655–666. https://doi.org/10.1016/0025-5408(74)90136-6.

(17) Gallagher, P. K.; Johnson, D. W.; Schrey, F. Studies of Some Supported Perovskite Oxidation Catalysts. *Mater. Res. Bull.* **1974**, *9* (10), 1345–1352. https://doi.org/10.1016/0025-5408(74)90057-9.

(18) Tilley, R. J. D. *Perovskites: Structure-Property Relationships*; John Wiley & Sons, Ed.; 2016.

(19) Roberts, S. Dielectric and Piezoelectric Properties of Barium Titanate. *Phys. Rev.* **1947**, *71* (12), 890–895. https://doi.org/10.1103/PhysRev.71.890.

(20) Goldschmidt, V. M. Die Gesetze Der Krystallochemie. *Naturwissenschaften* **1926**, *14* (21), 477–485. https://doi.org/10.1007/BF01507527.

(21) Weidenkaff, A.; Ebbinghaus, S. G.; Lippert, T.; Montenegro, M. J.; Soltmann, C.; Wessicken, R. Phase Formation and Phase Transition of Ln1–XCaxCoO3–δ (Ln= La, Er) Applied for Bifunctional Air Electrodes. *Cryst. Eng.* **2002**, *5* (3–4), 449–457. https://doi.org/10.1016/S1463-0184(02)00056-4.

(22) Weidenkaff, A. Preparation and Application of Nanostructured Perovskite Phases. *Adv. Eng. Mater.* **2004**, *6* (9), 709–714. https://doi.org/10.1002/adem.200400098.

(23) Parravano, G. Ferroelectric Transitions and Heterogenous Catalysis. *J. Chem. Phys.* **1952**, *20* (2), 342–343. https://doi.org/10.1063/1.1700412.

(24) Dickens, P. G.; Whittingham, M. S. Recombination of Oxygen Atoms on Oxide Surfaces. Part 2.—Catalytic Activities of the Alkali Metal Tungsten Bronzes. *Trans. Faraday Soc.* **1965**, *61*, 1226–1231. https://doi.org/10.1039/TF9656101226.

(25) Peña, M. A.; Fierro, J. L. G. Chemical Structures and Performance of Perovskite Oxides. *Chemical Reviews*. American Chemical Society July 2001, pp 1981–2017. https://doi.org/10.1021/cr980129f.

(26) Lago, R.; Bini, G.; Peña, M. A.; Fierro, J. L. G. Partial Oxidation of Methane to Synthesis Gas Using LnCoO3 Perovskites as Catalyst Precursors. *J. Catal.* **1997**, *167* (1), 198–209. https://doi.org/10.1006/jcat.1997.1580.

(27) Nitadori, T.; Ichiki, T.; Misono, M. Catalytic Properties of Perovskite-Type Mixed Oxides (ABO 3) Consisting of Rare Earth and 3d Transition Metals. The Roles of the A- and B-Site Ions. *Bull. Chem. Soc. Jpn.* **1988**, *61* (3), 621–626. https://doi.org/10.1246/bcsj.61.621.

(28) Mishra, A.; Prasad, R. Preparation and Application of Perovskite Catalysts for Diesel Soot Emissions Control: An Overview. *Catal. Rev.* **2014**, *56* (1), 57–81. https://doi.org/10.1080/01614940.2014.866438.

(29) Abdullah, A. Z.; Abdullah, H.; Bhatia, S. Improvement of Loose Contact Diesel Soot Oxidation by Synergic Effects between Metal Oxides in K2O–V2O5/ZSM-5 Catalysts. *Catal. Commun.* **2008**, *9* (6), 1196–1200. https://doi.org/10.1016/j.catcom.2007.11.003.

(30) Prasad, R.; Bella, V. R. A Review on Diesel Soot Emission, Its Effect and Control. *Bull. Chem. React. Eng. Catal.* **2011**, *5* (2). https://doi.org/10.9767/bcrec.5.2.794.69-86.

(31) Lu, P.; Li, C.; Zeng, G.; Xie, X.; Cai, Z.; Zhou, Y.; Zhao, Y.; Zhan, Q.; Zeng, Z. Research on Soot of Black Smoke from Ceramic Furnace Flue Gas: Characterization of Soot. *J. Hazard. Mater.* **2012**, *199–200*, 272–281. https://doi.org/10.1016/j.jhazmat.2011.11.004.

(32) Davidson, C. I.; Phalen, R. F.; Solomon, P. A. Airborne Particulate Matter and Human Health: A Review. *Aerosol Sci. Technol.* **2005**, *39* (8), 737–749. https://doi.org/10.1080/02786820500191348.

(33) Martin, J. W.; Salamanca, M.; Kraft, M. Soot Inception: Carbonaceous Nanoparticle Formation in Flames. *Prog. Energy Combust. Sci.* **2022**, *88*, 100956. https://doi.org/10.1016/j.pecs.2021.100956.

(34) Glassman, I.; Nishida, O.; Sidebotham, G. Critical Temperatures of Soot Formation. *Springer Ser. Chem. Phys.* **1994**, No. 59, 316–324. https://doi.org/10.1007/978-3-642-85167-4_18.

(35) Hall-Roberts, V. J.; Hayhurst, A. N.; Knight, D. E.; Taylor, S. G. The Origin of Soot in Flames: Is the Nucleus an Ion? *Combust. Flame* **2000**, *120* (4), 578–584. https://doi.org/10.1016/S0010-2180(99)00116-9.

(36) Frenklach, M. ON SURFACE GROWTH MECHANISM OF SOOT PARTICLES. **1996**, 2285–2293.

(37) Krestinin, A. V. Detailed Modeling of Soot Formation in Hydrocarbon Pyrolysis. **2000**.

(38) Donnet, J.-B. Fifty Years of Research and Progress on Carbon Black. *Carbon N. Y.* **1994**, *32* (7), 1305–1310. https://doi.org/10.1016/0008-6223(94)90116-3.

(39) Richter, H.; Howard, J. . Formation of Polycyclic Aromatic Hydrocarbons and Their Growth to Soot—a Review of Chemical Reaction Pathways. *Prog. Energy Combust. Sci.* **2000**, *26* (4–6), 565–608. https://doi.org/10.1016/S0360-1285(00)00009-5.

(40) Lahaye, J.; Prado, G. Morphology and Internal Structure of Soot and Carbon Blacks. In *Particulate Carbon*; Springer US: Boston, MA, 1981; pp 33–55. https://doi.org/10.1007/978-1-4757-6137-5_2.

(41) Dhakad, M.; Rayalu, S. S.; Kumar, R.; Doggali, P.; Bakardjieva, S.; Subrt, J.; Mitsuhashi, T.; Haneda, H.; Labhsetwar, N. Low Cost, Ceria Promoted Perovskite Type Catalysts for Diesel Soot Oxidation. *Catal. Letters* **2008**, *121* (1–2), 137–143. https://doi.org/10.1007/s10562-007-9310-7.

(42) Tran, Q. N.; Martinovic, F.; Ceretti, M.; Esposito, S.; Bonelli, B.; Paulus, W.; Di Renzo, F.; Deorsola, F. A.; Bensaid, S.; Pirone, R. Co-Doped LaAlO3 Perovskite Oxide for NOx-Assisted Soot Oxidation. *Appl. Catal. A Gen.* **2020**, *589*, 117304. https://doi.org/10.1016/j.apcata.2019.117304.

(43) Díaz, C.; Urán, L.; Santamaria, A. Preparation Method Effect of La0.9K0.1Co0.9Ni0.1O3 Perovskite on Catalytic Soot Oxidation. *Fuel* **2021**, *295*, 120605. https://doi.org/10.1016/j.fuel.2021.120605.

(44) Xiao, P.; Zhong, L.; Zhu, J.; Hong, J.; Li, J.; Li, H.; Zhu, Y. CO and Soot Oxidation over Macroporous Perovskite LaFeO3. *Catal. Today* **2015**, *258*, 660–667. https://doi.org/10.1016/j.cattod.2015.01.007.

(45) Keller, D. P.; Lenton, A.; Littleton, E. W.; Oschlies, A.; Scott, V.; Vaughan, N. E. The Effects of Carbon Dioxide Removal on the Carbon Cycle. *Curr. Clim. Chang. Reports* **2018**, *4* (3), 250–265. https://doi.org/10.1007/s40641-018-0104-3.

(46) IPCC. IPCC. Climate Change 2013: The Physical Science Basis. Contribution of Working Group I to the Fifth Assessment Report of the Intergovernmental Panel on Climate Change; 2013.

(47) Field, C.B., V.R. Barros, D.J. Dokken, K. J. C. IPCC. Climate Change 2014: Impacts, Adaptation, and Vulnerability. Part A: Global and Sectoral Aspects. Contribution of Working Group II to the Fifth Assessment Report of the Intergovernmental Panel on Climate Change; 2014.

(48) Cao, L.; Caldeira, K. Atmospheric Carbon Dioxide Removal: Long-Term Consequences and Commitment. *Environ. Res. Lett.* **2010**, *5* (2), 024011. https://doi.org/10.1088/1748-9326/5/2/024011.

(49) Lowe, J. A.; Huntingford, C.; Raper, S. C. B.; Jones, C. D.; Liddicoat, S. K.; Gohar, L. K. How Difficult Is It to Recover from Dangerous Levels of Global Warming? *Environ. Res. Lett.* **2009**, *4* (1), 014012. https://doi.org/10.1088/1748-9326/4/1/014012.

(50) Hepburn, C.; Adlen, E.; Beddington, J.; Carter, E. A.; Fuss, S.; Mac Dowell, N.; Minx, J. C.; Smith, P.; Williams, C. K. The Technological and Economic Prospects for CO2 Utilization and Removal. *Nature* **2019**, *575* (7781), 87–97. https://doi.org/10.1038/s41586-019-1681-6.

(51) Jiang, Z.; Xiao, T.; Kuznetsov, V. L.; Edwards, P. P. Turning Carbon Dioxide into Fuel. *Philos. Trans. R. Soc. A Math. Phys. Eng. Sci.* **2010**, *368* (1923), 3343–3364. https://doi.org/10.1098/rsta.2010.0119.

(52) Olah, G. A.; Goeppert, A.; Prakash, G. K. S. *Beyond Oil and Gas: The Methanol Economy*; Wiley, 2009. https://doi.org/10.1002/9783527627806.

(53) Shih, C. F.; Zhang, T.; Li, J.; Bai, C. Powering the Future with Liquid Sunshine. *Joule* **2018**, *2* (10), 1925–1949. https://doi.org/10.1016/j.joule.2018.08.016.

(54) Centi, G.; Perathoner, S. Opportunities and Prospects in the Chemical Recycling of Carbon Dioxide to Fuels. *Catal. Today* **2009**, *148* (3–4), 191–205. https://doi.org/10.1016/j.cattod.2009.07.075.

(55) Shafeeyan, M. S.; Daud, W. M. A. W.; Houshmand, A.; Arami-Niya, A. Ammonia Modification of Activated Carbon to Enhance Carbon Dioxide Adsorption: Effect of Pre-Oxidation. *Appl. Surf. Sci.* **2011**, *257* (9), 3936–3942. https://doi.org/10.1016/j.apsusc.2010.11.127.

(56) Mishra, A. K.; Ramaprabhu, S. Carbon Dioxide Adsorption in Graphene Sheets. *AIP Adv.* **2011**, *1* (3), 032152. https://doi.org/10.1063/1.3638178.

(57) Walton, K. S.; Millward, A. R.; Dubbeldam, D.; Frost, H.; Low, J. J.; Yaghi, O. M.; Snurr, R. Q. Understanding Inflections and Steps in Carbon Dioxide Adsorption Isotherms in Metal-Organic Frameworks. *J. Am. Chem. Soc.* **2008**, *130* (2), 406–407. https://doi.org/10.1021/ja076595g.

(58) Yong, Z.; Mata, V.; Rodrigues, A. Adsorption of Carbon Dioxide at High Temperature—a Review. *Sep. Purif. Technol.* **2002**, *26* (2–3), 195–205. https://doi.org/10.1016/S1383-5866(01)00165-4.

(59) Rönsch, S.; Schneider, J.; Matthischke, S.; Schlüter, M.; Götz, M.; Lefebvre, J.; Prabhakaran, P.; Bajohr, S. Review on Methanation – From Fundamentals to Current Projects. *Fuel* **2016**, *166*, 276–296. https://doi.org/10.1016/j.fuel.2015.10.111.

(60) Stangeland, K.; Kalai, D.; Li, H.; Yu, Z. CO 2 Methanation: The Effect of Catalysts and Reaction Conditions. *Energy Procedia* **2017**, *105*, 2022–2027. https://doi.org/10.1016/j.egypro.2017.03.577.

(61) Nohra, M.; Woo, T. K.; Alavi, S.; Ripmeester, J. A. Molecular Dynamics Gibbs Free Energy Calculations for CO2 Capture and Storage in Structure I Clathrate Hydrates in the Presence of SO2, CH4, N2, and H2S Impurities. *J. Chem. Thermodyn.* **2012**, *44* (1), 5–12. https://doi.org/10.1016/j.jct.2011.08.025.

(62) Lutz, A.; Bradshaw, R.; Keller, J.; Witmer, D. Thermodynamic Analysis of Hydrogen Production by Steam Reforming. *Int. J. Hydrogen Energy* **2003**, *28* (2), 159–167. https://doi.org/10.1016/S0360-3199(02)00053-8.

(63) Álvarez, A.; Borges, M.; Corral-Pérez, J. J.; Olcina, J. G.; Hu, L.; Cornu, D.; Huang, R.; Stoian, D.; Urakawa, A. CO2 Activation over Catalytic Surfaces. *ChemPhysChem* **2017**, *18* (22), 3135–3141. https://doi.org/10.1002/cphc.201700782.

(64) Sahebdelfar, S.; Takht Ravanchi, M. Carbon Dioxide Utilization for Methane Production: A Thermodynamic Analysis. *J. Pet. Sci. Eng.* **2015**, *134*, 14–22. https://doi.org/10.1016/j.petrol.2015.07.015.

(65) Lavoie, J.-M. Review on Dry Reforming of Methane, a Potentially More Environmentally-Friendly Approach to the Increasing Natural Gas Exploitation. *Front. Chem.* **2014**, *2*. https://doi.org/10.3389/fchem.2014.00081.

(66) Aresta, M.; Dibenedetto, A.; Angelini, A. Catalysis for the Valorization of Exhaust Carbon: From CO2 to Chemicals, Materials, and Fuels. Technological Use of CO2. *Chem. Rev.* **2014**, *114* (3), 1709–1742. https://doi.org/10.1021/cr4002758.

(67) Olah, G. A. Beyond Oil and Gas: The Methanol Economy. *Angew. Chemie Int. Ed.* **2005**, *44* (18), 2636–2639. https://doi.org/10.1002/anie.200462121.

(68) Dias, Y. R.; Perez-Lopez, O. W. Carbon Dioxide Methanation over Ni-Cu/SiO2 Catalysts. *Energy Convers. Manag.* **2020**, *203*, 112214. https://doi.org/10.1016/J.ENCONMAN.2019.112214.

(69) Langdon, R. J.; Yousefi, P. D.; Relton, C. L.; Suderman, M. J. Gasoline-Ethanol-Methanol Tri-Fuel Vehicle Development and Its Role in Expediting Sustainable Organic Fuels for Transport. *Clin. Epigenetics* **2009**. https://doi.org/10.2/JQUERY.MIN.JS.

(70) Inoue, T.; Fujishima, A.; Konishi, S.; Honda, K. Photoelectrocatalytic Reduction of Carbon Dioxide in Aqueous Suspensions of Semiconductor Powders. *Nature* **1979**, *277* (5698), 637–638. https://doi.org/10.1038/277637a0.

(71) Maeda, K.; Teramura, K.; Lu, D.; Takata, T.; Saito, N.; Inoue, Y.; Domen, K. Photocatalyst Releasing Hydrogen from Water. *Nature* **2006**, *440* (7082), 295–295. https://doi.org/10.1038/440295a.

(72) Luo, N.; Jiang, Z.; Shi, H.; Cao, F.; Xiao, T.; Edwards, P. Photo-Catalytic Conversion of Oxygenated Hydrocarbons to Hydrogen over Heteroatom-Doped TiO2 Catalysts. *Int. J. Hydrogen Energy* **2009**, *34* (1), 125–129. https://doi.org/10.1016/j.ijhydene.2008.09.097.

(73) Varghese, O. K.; Paulose, M.; LaTempa, T. J.; Grimes, C. A. High-Rate Solar Photocatalytic Conversion of CO 2 and Water Vapor to Hydrocarbon Fuels. *Nano Lett.* **2009**, *9* (2), 731–737. https://doi.org/10.1021/nl803258p.

(74) Kudo, A.; Miseki, Y. Heterogeneous Photocatalyst Materials for Water Splitting. *Chem. Soc. Rev.* **2009**, *38* (1), 253–278. https://doi.org/10.1039/B800489G.

(75) Long, M.; Cai, W.; Cai, J.; Zhou, B.; Chai, X.; Wu, Y. Efficient Photocatalytic Degradation of Phenol over Co 3 O 4 /BiVO 4 Composite under Visible Light Irradiation. *J. Phys. Chem. B* **2006**, *110* (41), 20211–20216. https://doi.org/10.1021/jp063441z.

(76) Shang, M.; Wang, W.; Zhou, L.; Sun, S.; Yin, W. Nanosized BiVO4 with High Visible-Light-Induced Photocatalytic Activity: Ultrasonic-Assisted Synthesis and Protective Effect of Surfactant. *J. Hazard. Mater.* **2009**, *172* (1), 338–344. https://doi.org/10.1016/j.jhazmat.2009.07.017.

(77) Jiang, Z.; Yang, F.; Yang, G.; Kong, L.; Jones, M. O.; Xiao, T.; Edwards, P. P. The Hydrothermal Synthesis of BiOBr Flakes for Visible-Light-Responsive Photocatalytic Degradation of Methyl Orange. *J. Photochem. Photobiol. A Chem.* **2010**, *212* (1), 8–13. https://doi.org/10.1016/j.jphotochem.2010.03.004.

(78) Lunde, P. J.; Kester, F. L. Carbon Dioxide Methanation on a Ruthenium Catalyst. *Ind. Eng. Chem. Process Des. Dev.* **1974**, *13* (1), 27–33. https://doi.org/10.1021/i260049a005.

(79) Marconi, E.; Tuti, S.; Luisetto, I. Structure-Sensitivity of CO 2 Methanation over Nanostructured Ni Supported on CeO 2 Nanorods. *Catalysts* **2019**, *9* (4), 375. https://doi.org/10.3390/catal9040375.

(80) Kagan, H. B. Victor Grignard and Paul Sabatier: Two Showcase Laureates of the Nobel Prize for Chemistry. *Angew. Chemie Int. Ed.* **2012**, *51* (30), 7376–7382. https://doi.org/10.1002/anie.201201849.

(81) Kopyscinski, J.; Schildhauer, T. J.; Biollaz, S. M. A. Production of Synthetic Natural Gas (SNG) from Coal and Dry Biomass – A Technology Review from 1950 to 2009. *Fuel* **2010**, *89* (8), 1763–1783. https://doi.org/10.1016/j.fuel.2010.01.027.

(82) le Saché, E.; Pastor-Pérez, L.; Haycock, B. J.; Villora-Picó, J. J.; Sepúlveda-Escribano, A.; Reina, T. R. Switchable Catalysts for Chemical CO 2 Recycling: A Step Forward in the Methanation and Reverse Water–Gas Shift Reactions. *ACS Sustain. Chem. Eng.* **2020**, *8* (11), 4614–4622. https://doi.org/10.1021/acssuschemeng.0c00551.

(83) Aldana, P. A. U.; Ocampo, F.; Kobl, K.; Louis, B.; Thibault-Starzyk, F.; Daturi, M.; Bazin, P.; Thomas, S.; Roger, A. C. Catalytic CO2 Valorization into CH4 on Ni-Based Ceria-Zirconia. Reaction Mechanism by Operando IR Spectroscopy. *Catal. Today* **2013**, *215*, 201–207. https://doi.org/10.1016/j.cattod.2013.02.019.

(84) Ocampo, F.; Louis, B.; Roger, A. C. Methanation of Carbon Dioxide over Nickel-Based Ce0.72Zr0.28O2 Mixed Oxide Catalysts Prepared by Sol–Gel Method. *Appl. Catal. A Gen.* **2009**, *369* (1–2), 90–96. https://doi.org/10.1016/J.APCATA.2009.09.005.

(85) Frontera, P.; Macario, A.; Ferraro, M.; Antonucci, P. L. Supported Catalysts for CO2 Methanation: A Review. *Catalysts* **2017**, *7* (12), 59. https://doi.org/10.3390/catal7020059.

(86) Su, X.; Xu, J.; Liang, B.; Duan, H.; Hou, B.; Huang, Y. Catalytic Carbon Dioxide Hydrogenation to Methane: A Review of Recent Studies. *Journal of Energy Chemistry*. Elsevier B.V. July 1, 2016, pp 553–565. https://doi.org/10.1016/j.jechem.2016.03.009.

(87) Krause, J.; Borgmann, D.; Wedler, G. Photoelectron Spectroscopic Study of the Adsorption of Carbon Dioxide on Cu(110) and — as Compared with the Systems And. *Surf. Sci.* **1996**, *347* (1–2), 1–10. https://doi.org/10.1016/0039-6028(95)00964-7.

(88) Berko, A.; Solymosi, F. INTERACTION OF CO2 AND HCOOH WITH Pd(100) SURFACE. *Vacuum* **1987**, *37* (1–2), 196. https://doi.org/10.1016/0042-207X(87)90149-7.

(89) Liao, B.; Wei, Q.; Wang, K.; Liu, Y. Study on CuO-BaTiO3 Semiconductor CO2 Sensor. *Sensors Actuators, B Chem.* **2001**, *80* (3), 208–214. https://doi.org/10.1016/S0925-4005(01)00892-9.

(90) Ding, X.; Pagan, V.; Peressi, M.; Ancilotto, F. Modeling Adsorption of CO2 on Ni(110) Surface. *Mater. Sci. Eng. C* **2007**, *27* (5-8 SPEC. ISS.), 1355–1359. https://doi.org/10.1016/J.MSEC.2006.06.024.

(91) Hahn, K. R.; Iannuzzi, M.; Seitsonen, A. P.; Hutter, J. Coverage Effect of the CO 2 Adsorption Mechanisms on CeO 2 (111) by First Principles Analysis. *J. Phys. Chem. C* **2013**, *117* (4), 1701–1711. https://doi.org/10.1021/jp309565u.

(92) Karelovic, A.; Ruiz, P. Mechanistic Study of Low Temperature CO2 Methanation over Rh/TiO2 Catalysts. *J. Catal.* **2013**, *301*, 141–153. https://doi.org/10.1016/J.JCAT.2013.02.009.

(93) Zhen, W.; Li, B.; Lu, G.; Ma, J. Enhancing Catalytic Activity and Stability for CO2 Methanation on Ni@MOF-5 via Control of Active Species Dispersion. *Chem. Commun.* **2015**, *51* (9), 1728–1731. https://doi.org/10.1039/C4CC08733J.

(94) Solymosi, F.; Erdöhelyi, A.; Bánsági, T. Methanation of CO2 on Supported Rhodium Catalyst. *J. Catal.* **1981**, *68* (2), 371–382. https://doi.org/10.1016/0021-9517(81)90106-8.

(95) Weatherbee, G. D.; Bartholomew, C. H. Hydrogenation of CO2 on Group VIII Metals. II. Kinetics and Mechanism of CO2 Hydrogenation on Nickel. *J. Catal.* **1982**, *77* (2), 460–472. https://doi.org/10.1016/0021-9517(82)90186-5.

(96) Andersson, M. P.; Abild-Pedersen, F.; Remediakis, I. N.; Bligaard, T.; Jones, G.; Engbæk, J.; Lytken, O.; Horch, S.; Nielsen, J. H.; Sehested, J.; Rostrup-Nielsen, J. R.; Nørskov, J. K.; Chorkendorff, I. Structure Sensitivity of the Methanation Reaction: H2-Induced CO Dissociation on Nickel Surfaces. *J. Catal.* **2008**, *255* (1), 6–19. https://doi.org/10.1016/j.jcat.2007.12.016.

(97) Karelovic, A.; Ruiz, P. Improving the Hydrogenation Function of Pd/γ-Al2O 3 Catalyst by Rh/γ-Al2O3 Addition in CO2 Methanation at Low Temperature. *ACS Catal.* **2013**, *3* (12), 2799–2812. https://doi.org/10.1021/CS400576W.

2. Industrially Produced Fe- and Mn-based perovskites: Effect of Synthesis on Reactivity in Three-Way Catalysis

In this chapter the results of a joint project between Johnson Matthey, Lurederra and IMPACT Group at the Department of Chemical Sciences at the University of Padova will be presented. Johnson Matthey is a company from the United Kingdom, global leader in sustainable technologies, with a focus on the preparation and testing of catalysts for the automotive sector. Lurederra is a Spanish technological center carrying out research and applied technological development activities in the fields of nanotechnology and innovative materials for environmental applications. This project is placed in the broader framework of the European project Partial PGM, created to propose an integrated approach for the development of nanostructured automotive exhaust treatment with reduced Partial Platinum Group Metals (PGMs) content. It was financially supported by the European Union's H2020 under grant agreement no. 686086 PARTIAL PGMs.

The results of this shared project gave rise to two published scientific articles, whose content is here reported. [1,2]

As discussed in the introduction, the development of innovative catalysts for pollutants control focused on perovskites as versatile materials, which allow the incorporation of different cations in their structure to tune activity and selectivity.[3] Adding inexpensive and largely available, catalytically active transition metal cations can represent a novel approach for Three-Way Catalysis (TWC)[4] that allows minimizing noble metal utilization. TWC is the commonly used exhaust emission control technology to deal with toxic pollutants in exhaust gases from automotive engines. In particular they

are optimized to combine oxygen with carbon monoxide and unburned hydrocarbon to produce carbon dioxide and water and, simultaneously, to reduce oxides of nitrogen (NOx) to gaseous nitrogen.

Perovskite oxides have a general formula ABO_3, in which the A-site ion is usually an alkaline earth or rare-earth element, whereas B-site ion is usually a transition metal ion. The aliovalent doping of the perovskite A and B sites induces the formation of structural defects and different oxidation states, together with cationic redox couples. [5–8]

A relevant problem, when developing complex formulations, is the synthesis of the catalysts both in terms of reproducibility, and scale-up. There are several routes for the synthesis of perovskites.[9–15] Coprecipitation (COP) and Flame Spray Pyrolysis (FSP) are among the most industrially adopted methods. In COP the precipitation of the hydroxide precursors is induced by pH change and is followed by calcination treatments to obtain the final phase. FSP is appreciated for scale-up, being a continuous process in which the precursors solution is kept at high temperature for a very short time to assure the formation of the desired phase while avoiding the decrease of specific surface area. The first reports of perovskite synthesis using flame spray pyrolysis were by Brewster and Kodas in 1997 who prepared $BaTiO_3$ by spraying an aqueous Ba acetate/Ti lactate feed into a H_2/air flame.[16] This was followed by Leanza et al. who prepared $La_{1-x}M_xCoO_3$ (M=Ce, Eu) by spraying an aqueous metal acetate/nitrate/citrate feed into a H_2/O_2 flame. [17]

The aim of the project was to investigate the effects of industrial scale-up on functional properties of the catalysts, and therefore two different sets of materials are considered: Fe-based Cu-doped and Mn-based K-doped perovskites, to shine light on the differences and similarities between varied composition when subjected to diversified synthetic approaches. We indeed suppose that the differences in the synthesis carried out may be more influent on the results when the composition is more complex, depending also on the cations involved.

The first article published deals with undoped (LF) and Ca,Cu-doped (LCFC) under stoichiometric lanthanum ferrites synthetized by COP and FSP. The interest on ferrite perovskites has recently grown in literature. [18,19,28–31,20–27] It was found that oxidation reactions and thermal stability of the materials are enhanced in the case of La-deficient compositions. [32–35] Moreover computational calculations also concluded that calcium inclusion can enhance oxygen conductivity in $LaFeO_3$. [36] In the second article an analogous work is presented regarding Mn-based K-doped perovskites, prepared with the same approach described.

Literature data suggest that good activities can be obtained considering Fe, Co, and Mn in the B site.[37–39] Cobalt is very active in the abatement of pollutants, with particular reference to oxidation [6,40,41] but also activity in reduction can be enhanced through doping and tuning of the nanocomposition.[42,43] However, its use on industrial scale is not an easy task; because of this we focused on Co-doped $LaMnO_3$ in which only a minimum amount of cobalt is included.

Mn-based perovskites already proved to be promising by literature [14,44–47] in TWC applications. In particular Mn insertion in perovskite B-site is beneficial, especially for oxidation of hydrocarbons and CO.[48–50] A-site doping is found to be less decisive, however partial substitution at the A-site by a cation of different valence (such as K^+ instead of La^{3+}) induces the formation of oxygen vacancies and/or changes of the oxidation state of the B-site cation, increasing the catalytic properties of the materials. [47,49,51] K^+ is considered to be able to activate both gas pollutants and soot. The behavior of K-doped manganites with respect to soot oxidation will be the topic of a following Chapter of the present thesis. For these materials the commonly accepted mechanism is based on structural defects and vacancies which affect oxygen uptake and release. This phenomenon goes under the name of Mars-van-Krevelen mechanism and it implies the presence of two distinct types of catalytically active oxygen species in perovskites: suprafacial oxygen species (commonly denoted as α) and intrafacial oxygen (β). At lower temperature (i.e. below 600°C) suprafacial oxygen is available and reacts,

whereas at higher temperatures bulk β oxygen is activated and takes place to the catalytic oxidation, being replenished by dissociation of molecular oxygen (or NO) from the gas phase. [52]

Catalysts obtained by FSP and by COP have been compared considering TWC as a potential application (automotive exhaust treatment, in fact, is a very demanding form of catalysis). Doped ferrites and manganites have been considered because of their good fresh activity in TWC reactions, low cost and absence of noble metals.[32,34,53] Given that FSP is a continuous process, samples obtained in successive stages of the synthesis procedure have been characterized.

The catalytic activity of the samples in TWC reactions is correlated with XRD (X-Ray Diffraction), XPS (X-Ray Photoelectron Spectroscopy), H_2-TPR (Temperature Programmed Reduction), BET surface area measurements (Brunauer-Emmett Teller), SEM (Scanning Electron Microscopy), EDX (Energy Dispersive X-Ray analysis) and ICP-OES (Inductively Coupled Plasma Optical Emission Spectrometry) results.

2.1 Synthesis of the samples: Flame Spray Pyrolysis and Coprecipitation

The FSP perovskites were produced by Flame Spray Pyrolysis technology, with a small-scale flame reactor owned by Lurederra which allows a production capacity of 0.1 kg/h. The FSP technology consists of simple one-step aerosol combustion process where a mixture of metal precursors, dissolved in an appropriate solvent (specifically xylene) is sprayed with an oxidizing gas (specifically air) into a high temperature flame zone where the aerosol droplets generated are individually evaporated and oxidized, turning the mixture of metal precursors into nanosized particles with perovskite structure. Properties such as high purity, low aggregation and small nanoparticle size are typically obtained following this process, and can be controlled depending on the operational parameters, namely, precursor feed flow, amount of dispersant gas, nozzle pressure, flame morphology, etc. [16,17]

The production of LCFC has been distributed over several days, to assess the variability of the product and process after several operation phases, including cycles of start-up and shut-down, and variable duration of the stable operations.

Being an industrial machinery the detailed knowledge of the synthesis parameters (Temperature, Pressure) is not possible but the main differences among the batches are summarized as follows. LCFC A is collected after saturation of filters, following an initial tuning of the process, in terms of temperature and pressure at the nozzle. LCFC B is collected on the filters after a following stable operation step, at the same conditions as case A; the temperature on the filters (where particles are collected) and ducts may rise, but it is always below 200°C; even if the residence time of the material is longer, we do not expect this temperature to affect the material composition or structure. After phase B, phase C attempted to stabilize the operating conditions in the flame to approach case A, with stable operation. The sample LCFC D is the last material extracted from the equipment and LCFC E is a duplicate sample of LCFC A. Each material (A, B, C, D, and E) is sampled in the same way: the nanopowders are retained as aggregates on the filters tissue and periodically discharged (by shaking the bag filters with compressed air) into a container, that is emptied before each phase, to limit cross-contamination. The collection of materials D and E, at the final stage, requires mechanical abrasion of the filters, because of a more compact deposition onto the tissue.

The coprecipitation approach belongs to the vast family of wet synthesis methods. Salts of the required metals are dissolved in the same medium (water usually). They are coprecipitated either by concentrating the solution or by adding a precipitating reagent (such as increasing the pH). [54]

For the synthesis of LCFC COP the following procedure was followed: KOH (>85%, 750 g, 11.4 mol) was dissolved in water (7 L) and the solution was stirred and heated to 60°C. Lanthanum nitrate hexahydrate (649.5 g, 1.5 mol), calcium nitrate (118 g, 0.5 mol), iron nitrate nonahydrate (808 g, 2 mol) and copper nitrate trihydrate (120.8 g, 0.5 mol) were dissolved in water to give 1.5 L total volume of solution. The salt solution was added to the base at 10 mL/min. When the addition was

complete the precipitate was aged with stirring for 30 minutes at 60°C. The material was collected by vacuum filtration, washed to remove adsorbed ions and dried at 105°C. The sample was fired at 700°C for 2 hours in air to form the perovskite phase.

For the synthesis of the Mn-based samples KOH (>85%, 795 g, 12 mol) was dissolved in water (7 L) and the solution was stirred and heated to 60°C. Lanthanum nitrate hexahydrate (974.3 g, 2.25 mol), potassium nitrate (25.3 g, 0.25 mol), manganese nitrate (50 wt./w% solution, 805.3 g, 2.25 mol) and cobalt nitrate hexahydrate (72.8 g, 0.25 mol) were dissolved in water to give 1.5 L total volume of solution. The salt solution was added to the base at 10 ml/min. When the addition was complete the precipitate was aged with stirring for 30 minutes at 60°C. The material was collected by vacuum filtration, washed to remove adsorbed ions and dried at 105°C. The sample was calcinated at 700°C for 2 hours in air to form perovskite phase.

2.2 Characterization

XPS measurements were carried out with a Perkin Elmer 5600 ci Multi Technique System. The spectrometer is calibrated by assuming the Binding Energy (BE) of the Au 4f7/2 line to be 84.0 eV with respect to the Fermi level. Both extended spectra (survey, 187.85 eV pass energy, 0.5 eV/step, 0.05 s/step) and detailed spectra (for La 3d, O1s, C1s, Fe 2p, Ca 2p, Cu 2p - 23.5 eV pass energy, 0.1 eV/step, 0.1s/step) are collected with a standard Al Kα source working at 200 W. The standard deviation in BE values of the XPS line is 0.10 eV. The atomic percentage, after a Shirley-type background subtraction,[55] is evaluated by using the PHI sensitivity factors.[56] The peak positions are corrected for the charging effects by considering the C1s peak at 284.8 eV and evaluating the BE differences.[57] All fitting procedures are carried out on normalized spectra.

XRD analyses are performed with a Bruker D8 Advance diffractometer with Bragg–Brentano geometry using a Cu Ka radiation (40 kV, 40 mA, k = 0.154 nm).

Field emission-scanning electron microscopy and energy dispersive X-ray spectroscopy (EDX) measures are carried out on a Zeiss SUPRA 40VP. Both morphological and compositional analyses are carried out setting the acceleration voltages at 20 kV. The main difference between XPS and EDX compositional results lies in the different sampling depth reached by the two techniques, as further explained below: XPS is a surface analysis technique, whereas EDX results depend on a deeper penetration in the bulk of the material analyzed.

Temperature Programmed Reduction (TPR) is performed with an Autochem II 2920 Micromeritics, equipped with a TCD detector. TPR measurements are carried out in a quartz reactor by using 50 mg of sample and heating from RT to 900 °C at 10 °C/min under a constant flow of H_2 5% in Ar. TPR samples were previously outgassed with He (50 ml·min−1) at RT. The surface area of all samples is determined by Asap 2020 Plus from Micromeritics. The measurements are carried out at liquid nitrogen temperature (77K). The specific surface area is calculated using the Brunauer-Emmet-Teller (BET) equation. Prior to N_2-sorption, all samples are degassed at 200 °C for 16 hours.

The samples for ICP analysis were prepared by dissolving the powder (about 20 mg exactly weighted) in a solution of 10 mL of HCl (Sigma-Aldrich, ≥37%) and 10 mL HNO_3 (Sigma Aldrich, ≥65%) under stirring at about 80°C for 2 h.

2.3 Activity test

Two series of catalytic activity tests were carried out, at atmospheric pressure, on simple and more complex feed mixtures. All the inlet compositions and GHSV(Gas Hourly Space Velocity) data are summarized in Table 1.

The first set of measurements is based on a model reaction, NO + CO. Stoichiometric CO and NO (1% each) are fed with Ar, to a quartz reactor (6 mm internal diameter) hosting a packed bed of catalyst as powder (50 mg); the temperature was monitored by a thermocouple inserted right upstream

of the bed. The inert carrier was always He (Table 1). The flows were controlled by thermal mass flowmeters (Vögtlin Instruments). The temperature of the bed was varied between room temperature and 500°C with a stepped temperature program. The reaction products were monitored with an Agilent 7890A gas chromatograph, equipped with a TCD detector. The columns are a molecular sieve 13X (60/80 mesh, 1.8 m) and a Porapak Q (1.8 m). The calibration was done using standard gases containing known concentrations of the components.

The second set of catalytic activity measurements aimed at resembling the actual conditions of an automotive exhaust. The gas feed composition is reported in Table 1. In addition to a larger number of species, 10 vol% of steam and 15 vol% of CO_2 were always used, reflecting actual conditions, quite challenging for the catalysts. A different quartz tube flow reactor, 8 mm internal diameter, was used, in which the catalytic bed is placed. The electrically heated quartz reactor contains a shallow bed of catalyst as powder (200 mg of sample), sieved in the size 250-350 μm. The temperature is monitored upstream the bed; it was varied between RT and 600°C. The flow rates were controlled by mass flow meters (Brooks Instruments and Bronkhorst High-Tech). Steam was generated by an isothermal bubbler. Each catalyst was tested at both fuel-rich and stoichiometric conditions; stoichiometric O_2 is determined from total oxidation of the fuels (CO, H_2, HCs), accounting also for the O_2 expected from NO reduction. The vapor in the outlet gas was condensed and the dry mixture analyzed. The following gases were determined: H_2, CO_2, O_2, N_2, CO, HCs by GC (Agilent 7820, with Porapak Q and MS5A using TCD and FID in series), at a frequency of 1/9 sample/min. CO, CO_2, NO and NO_2 are measured by FTIR (Shimadzu IRTracer-100), at a frequency of 1 sample/min. CO and CO_2 reported in the results are taken from GC, which from past experience has shown to be more accurate than IR in detecting these gases. The set-up is summarized in the scheme in Figure 7.

The standard testing sequence in the second set of measurements is: (1) heating the catalyst at 10°C/min to 600°C in air, (2) 2 hours of pre-conditioning at 600°C in air, (3) 2 hours of conditioning at 600°C with the reaction mixture, (4) slow temperature decrease (-2°C/min) to measure the catalyst

activity at different temperatures, down to 90°C, a temperature at which no catalytic activity is detected. It has been verified that the selected cooling rate of -2°/min is sufficiently slow to achieve steady-state operation of the catalyst, at each temperature scanned. Since the test is basically conducted at small isothermal plateaux, the exothermicity of the reactions involved (such as CO, H_2 and HC oxidations) does not represent a noticeable issue for the accuracy of the testing.

The simple mixture was tested at rising temperature, on a catalyst without any pretreatment (to understand the effect of surface composition and active sites), while the complex mixture was tested from 600°C during controlled cooling, after a pretreatment of the catalyst in air, at high temperature (following protocols suggested by industry for automotive catalysts). Reactant conversion and product yield are defined with molar fractions x (mixtures are very diluted) as:

Conversion of i = $100*(x_i/x_i°)$

Yield of i from j = $100*(\Delta x_i/\Delta x_j)$

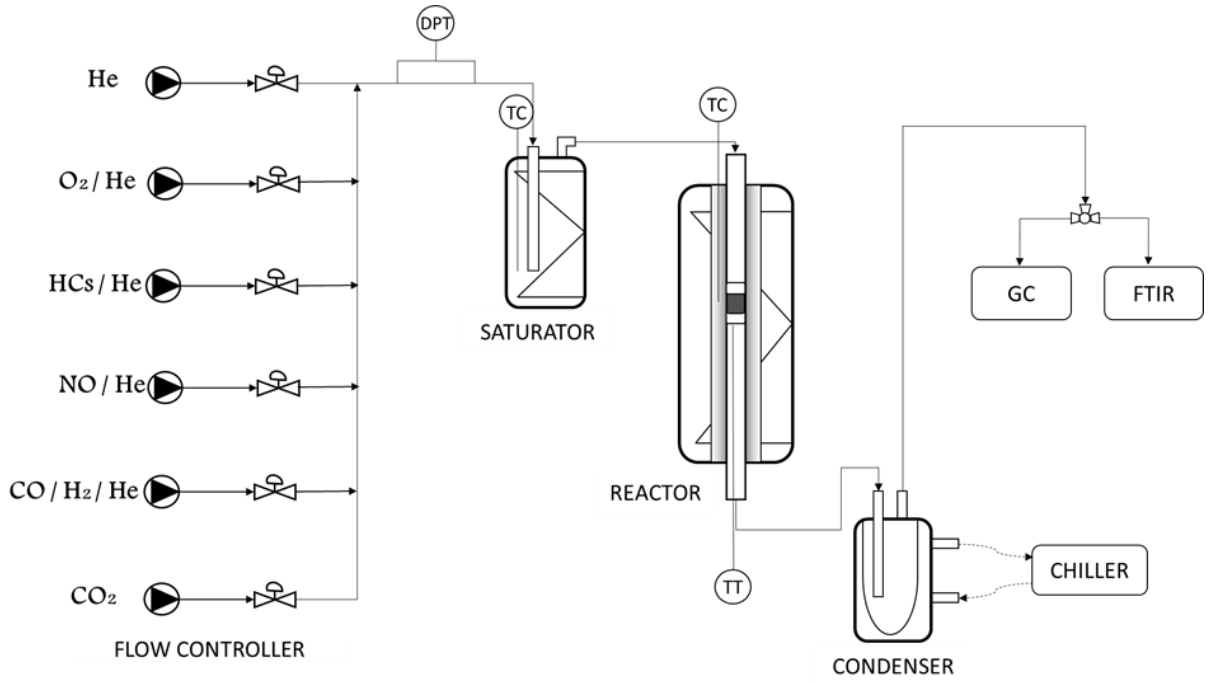

Figure 7 Catalytic setup for complex mixture testing.

Inert	CO_2	H_2O	O_2	CO	NO	H_2	CH_4	C_3H_6	C_3H_8	λ		m_{cat}	Flow rate	WHSV
	%	%	%	%	%	%	ppm	Ppm	ppm			mg	SmL/ min	(SmL/h)/ g_{cat}
He	-	-	-	1	1	-	-	-	-	-		50	100	150000
He	15	10	0.777	0.7	0.1	0.233	230	450	230	1.0	Stoich	200	200	60000
He	15	10	0.609	0.9	0.1	0.300	300	600	300	0.6	Rich	200	200	60000

Table 1 Feed composition of all the measurements ($\lambda = O_2$ fed/O_2 stoich = $[O_2]/(0.5\,[CO] + 0.5\,[H_2] + 2\,[CH_4] + 4.5\,[C_3H_6] + 5\,[C_3H_8] - 0.5\,[NO])$).

2.4 Results and discussion: characterization and catalytic assessment

The report of the results will be organized as follows: first the Fe-based perovskites (at different production stages and doped/undoped) will be dealt with, and in the following part the results (both in terms of characterization and catalytic assessment) for the Mn-based perovskite will be presented. Common conclusions will end the chapter.

2.4.1 Different production stages for LCFC

Firstly the results of the characterization of the samples obtained during different phases of the FSP production is reported. Significant differences have been found comparing $La_{0.6}Ca_{0.2}Fe_{0.8}Cu_{0.2}O_3$ obtained by FSP (in consecutive production stages) and by co-precipitation (LCFC COP).

Five $La_{0.6}Ca_{0.2}Fe_{0.8}Cu_{0.2}O_3$ samples (LCFC A, B, C, D and E respectively) show significant differences in morphology, composition and structural features. LCFC A diffraction pattern (Figure 8), unlike B, C and D, shows a lower degree of crystallinity, suggesting incomplete formation of the perovskite phase. In LCFC B, C, and E, the most relevant diffraction peak shifts from 32.25° to higher values (32.3°-32.5°) suggesting the change in the unit cell size due to the different radius of the cations [58] and confirms the incorporation of A-site dopants into the perovskite unit cell. Sample, D, in contrast, shows a decrease in the 2θ value of the peak at 32° consistent with an inefficient insertion of Ca.

XP spectra obtained for the different samples are compared in Figure 9 while atomic compositions (XPS and EDX) are summarized in Table 2. The O1s XPS signal has two components perovskite lattice (528.7 eV) and surface oxygen species, e.g. OH-(530.8 eV). A difference is observed only in LCFC A in which a component centered at 529.0 eV is relevant; the peak position corresponds to

oxygen in La_2O_3 and Fe_2O_3. [59] The peak shape indicates a high degree of hydroxylation of the surfaces.

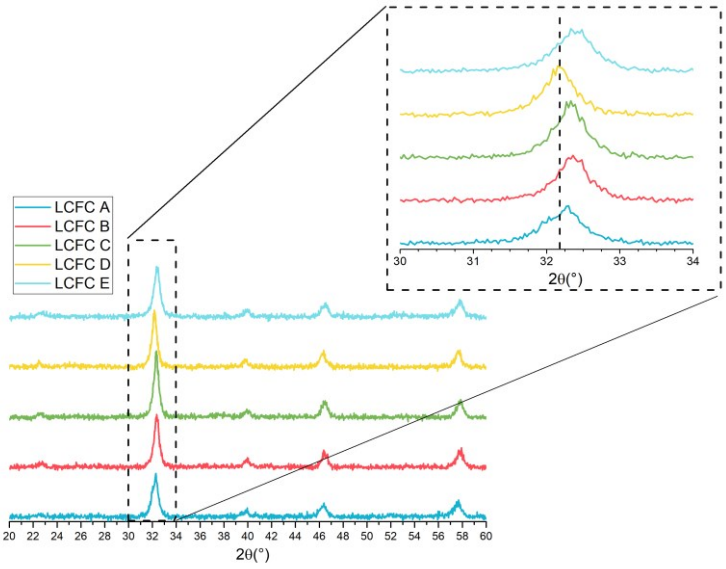

Figure 8 XRD patterns for LCFC A, B, C, D and E. Inset: the most intense peak.

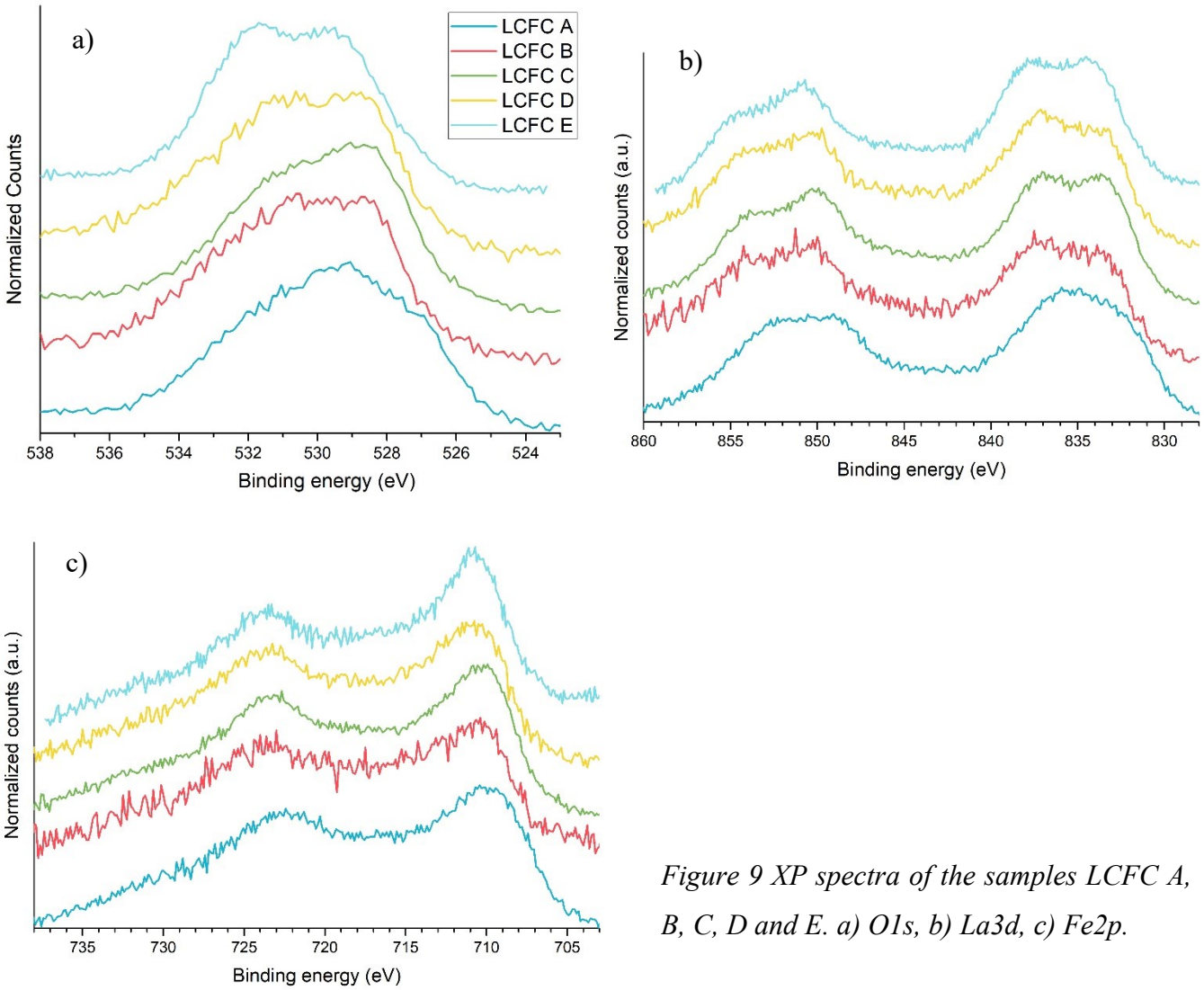

Figure 9 XP spectra of the samples LCFC A, B, C, D and E. a) O1s, b) La3d, c) Fe2p.

O1s peak confirms that the first stage of the synthesis does not allow the complete formation of the perovskite structure, but instead an additional mixture of La and Fe oxides (contribution at about 529.5-530 eV), likely giving a contribution to the amorphous feature of the XR diffractograms of the initial samples.

The change of the O1s peak shape is evident as we move from sample A to E: in sample D lattice and hydroxyl oxygen are in comparable amounts. The La3d XP spectra are quite similar for all samples and agree (peak position 832.8-833.2 eV and shake-up contribution at 835.9-837.5 eV) with lanthanum (III) in perovskites. The broadened shape of $La3d_{5/2}$ peak in sample A suggests the presence of another contribution, assigned to $La(OH)_3$/LaOOH species (834.5 eV).[39,58,67–71,59–66] This last contribution is less evident in the samples B, C, and D.

The Fe2p XP spectra are significant, as they show a progressive shift towards higher BE going from sample A to E. $Fe2p_{3/2}$ peak centered at 709.4 eV in sample LCFC A, is typical of Fe(II). For sample D the peak position tends to reach the value of 710.2-710.5 eV, typical of $Fe2p_{3/2}$ in the Fe(III) form.[72] A further confirmation comes from the deconvolution of the spectra in the region of Fe2p (carried out setting the typical values for Fe(II) and Fe(III) reported in [6]): the Fe(II)/Fe(III) atomic ratio being 1.8 in sample A and ca. zero in the other ones.

Different oxidation states for iron are also confirmed by TPR analysis, as reported below. Fe(IV), suggested by TPR, cannot be confirmed by XPS.[5]

Quantitative analysis (Table 3) shows that oxygen is always over stoichiometric confirming the presence of surface oxygen species. Iron is also relevant in surface even if it is slightly more abundant under the few external monolayers of samples A and C. Ca is near the nominal value only with EDX whereas Cu is more abundant in surface but always under-stoichiometric.

Cu2p XP spectra do not show any change in the oxidation state of copper, Cu(II). Ca2p XP spectra do not give any further insight about the surface structure and composition of the samples, this being quite similar for all samples and corresponding to the expected Ca(II).

Sample	*Type*	*La*	*Ca*	*Fe*	*Cu*	*O*	*La**	*Ca**	*Fe**	*Cu**	*Ca/La*	*Cu/Fe*	*(Fe+Cu)/ (La+Ca)*	*O/ (La+Ca+Fe+Cu)*	*O lattice/O surface*[a]
LCFC A	XPS	14.4	2.6	15.7	2.2	65.0	41.2	7.5	44.9	6.4	0.18	0.14	1.05	1.86	5.5
LCFC B	XPS	14.3	2.5	18.5	3.5	61.1	36.8	6.5	47.4	8.9	0.18	0.19	1.30	1.57	1.0
LCFC C	XPS	15.0	3.8	17.2	3.6	60.4	37.9	9.6	43.5	9.0	0.25	0.21	1.11	1.53	2.1
LCFC D	XPS	13.9	3.0	19.2	3.7	60.3	35.0	7.5	48.4	9.2	0.21	0.19	1.36	1.52	1.3
LCFC E	XPS	15.8	2.3	17.0	0.9	63.9	43.9	6.4	47.2	2.5	0.15	0.05	0.99	1.77	1.9
LCFC	Nominal	12.5	4.2	16.6	4.2	62.5	33.0	11.0	44.0	11.0	0.33	0.3	1.22	1.67	

Sample	*Type*	*La*	*Ca*	*Fe*	*Cu*	*O*	*La**	*Ca**	*Fe**	*Cu**	*Ca/La*	*Cu/Fe*	*(Fe+Cu)/ (La+Ca)*	*O/ (La+Ca+Fe+Cu)*	*O lattice/O surface*[a]
LCFC A	EDX	8.0	2.2	9.9	1.2	78.8	37.8	10.2	46.6	5.8	0.27	0.12	1.09	3.72	
LCFC B	EDX	8.3	2.7	11.3	1.7	76.1	34.7	11.2	47.1	6.9	0.32	0.15	1.18	3.18	
LCFC C	EDX	11.0	3.2	14.4	1.9	69.6	36.1	10.4	47.4	6.1	0.29	0.13	1.15	2.29	
LCFC D	EDX	9.8	2.9	12.6	1.5	73.3	36.5	11.0	47.1	5.4	0.30	0.12	1.11	2.75	
LCFC E	EDX	10.7	2.9	12.9	1.6	71.9	38.0	10.4	45.9	5.6	0.27	0.12	1.06	2.56	
LCFC	Nominal	12.5	4.2	16.6	4.2	62.5	33.0	11.0	44.0	11.0	0.33	0.3	1.22	1.67	

Table 2 XPS and EDX compositions (atomic concentrations) obtained for the doped LCFC obtained by Flame Spray Pyrolysis (FSP). The compositions obtained without considering oxygen (*) are reported in order to emphasize the cation surface segregation phenomena. The last column refers to the ratio between the integrated peak area contribution at 529 eV and the integrated peak area contribution at 532 eV.

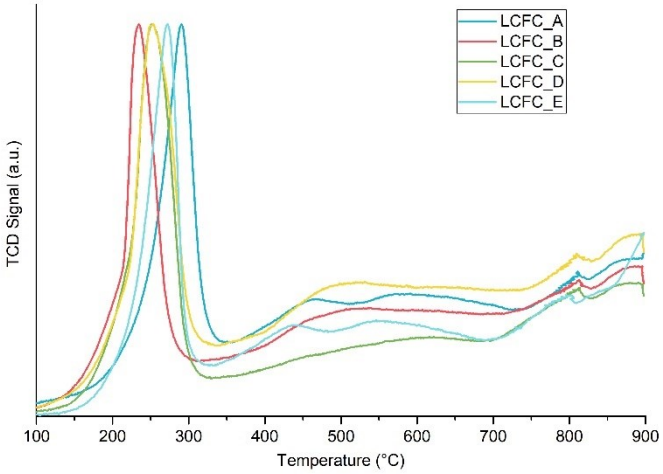

Figure 10. H2-TPR profile for LCFC FSP obtained during different production moments (A–E).

Furthermore, EDX/XPS cation-only compositional analysis point out a trend of marked segregation of La on the surface, probably as oxide, whereas Fe surface segregates only in LCFC D. The B/A cations atomic ratio is near the expected value (being slightly higher only in the surface of sample B and D).

The bulk reducibility of the solids was investigated by H_2-Temperature Programmed Reduction experiments (H_2-TPR). TPR profile of the different LCFC (Figure 10, Table 3) samples, A-E, shows the presence of two, in some cases three, signals at 224-286°C, 465°C and 582°C. The peak at lower temperature is ascribed to the reduction from Cu(II) to Cu(0) as reported in literature.[6] This assignment is in good agreement with the calculated hydrogen consumption (Table 3). The Cu(II) reduction temperature shifts throughout the different samples; the highest temperature is observed for sample A, which contains, beside the desired perovskite, a mixture of metal oxides (as shown by XPS and EDX). We can rationalize the different reduction temperature as the synthetic process conditions give rise to catalysts characterized by slightly different size and degree of crystallinity. In analogous samples obtained by FSP, Rossetti et al. [73] reported that highly reducible B^{3+} is evident for samples prepared with lower pressure drop across the nozzle, suggesting that a slightly higher crystal order

induces higher reducibility. Furthermore, a better ordering leads to more energetically uniform redox species. This can be compared with Isupova et al. [74] who found that the tuning of B-O interaction strength correlates with the concentration of phase boundaries, and a higher reducibility is expected with increasing the concentration of phase boundaries. So, beside the inclusion of dopants, the reducibility of the sample depends also on the FSP synthetic conditions which may alter the morphological and crystalline character of the obtained materials.

	T max (°C)	mol H_2 consumed/expected	Assignment	Fe(IV)/((Fe(IV)+Fe(III))
LCFC FSP A				0.27
Low T peak	290	0.68	Cu(II) - Cu (0)	
Broad signal	450-650	0.04	Fe(IV)-Fe(III); Fe(III)-Fe(II)	
LCFC FSP B				0.55
Low T peak	234	0.83	Cu(II) - Cu (0)	
Broad signal	450-650	0.09	Fe(IV)-Fe(III); Fe(III)-Fe(II)	
LCFC FSP C				0.13
Low T peak	252	0.89	Cu(II) - Cu (0)	
Broad signal	450-650	0.03	Fe(IV)-Fe(III); Fe(III)-Fe(II)	
LCFC FSP D				0.54
Low T peak	253	0.78	Cu(II) - Cu (0)	
Broad signal	450-650	0.05	Fe(IV)-Fe(III); Fe(III)-Fe(II)	
LCFC FSP E				0.47
Low T peak	272	0.65	Cu(II)-Cu(0)	
Broad signal	450-650	0.02	Fe(IV)-Fe(III); Fe(III)-Fe(II)	

Table 3 H_2-TPR results. The third column (mol H_2 consumed/expected) refers to the experimental and theoretical amount of H_2 to be consumed during the TPR, in correlation to the stoichiometric composition of the samples.

Sample – Synthesis	Composition	Specific Surface Area (m^2/g)
LCFC A – FSP	$La_{0.6}Ca_{0.2}Fe_{0.8}Cu_{0.2}O_3$	61.1
LCFC B – FSP	$La_{0.6}Ca_{0.2}Fe_{0.8}Cu_{0.2}O_3$	59.1
LCFC C – FSP	$La_{0.6}Ca_{0.2}Fe_{0.8}Cu_{0.2}O_3$	57.0
LCFC D – FSP	$La_{0.6}Ca_{0.2}Fe_{0.8}Cu_{0.2}O_3$	59.0
LCFC E – FSP	$La_{0.6}Ca_{0.2}Fe_{0.8}Cu_{0.2}O_3$	60.8

Table 4 Specific Surface Area (in m2/g) of the samples LCFC A, B, C, D and E.

The peak at higher temperature behaves differently: in some cases, two different contributions are clearly recognizable (e.g. LCFC A), in other cases they are merged into one single broad peak. The higher temperature region is attributed to iron species, in particular the reduction from Fe(IV) to Fe (III) (465 °C) and Fe(III) to Fe(II) (582 °C). [34,57]

The results of the deconvolution are summarized by the ratio of the integrated areas of the corresponding peaks in Table 3.

Samples B and D have a similar ratio Fe(IV)/Fe(III), compared to samples A, C and E which show almost no reduction of Fe(IV). Note that samples A and C were collected at similar operating conditions in the FSP set up.

SEM images (Figure 11) point out the homogeneity of the samples and underline the formation of highly dispersed particles and, progressively with the production process advancement, also of globular particles (diameter of about 100 nm), most likely combustion residues (carbon). For instance, sample A does not show any combustion residue, whereas the other samples progressively have more carbon particles on their surface.

The specific surface areas obtained for this samples are reported in

Table *4*: no significant differences are observed for the specific surface area of the catalysts obtained at different stages of the FSP process that range from 57 to 61 m^2/g testifying to the morphological homogeneity of the catalysts. In fact, focusing on FSP, the main influence seems to derive from the doping (LFC FSP specific surface area is about 32 m^2/g). To help understanding the effect of Ca-doping, $La_{0.6}Ca_{0.2}Fe_{0.8}Cu_{0.2}O_3$ was compared with the Ca-free $La_{0.7}Fe_{0.8}Cu_{0.2}O_3$ (LFC FSP) both obtained by FSP.

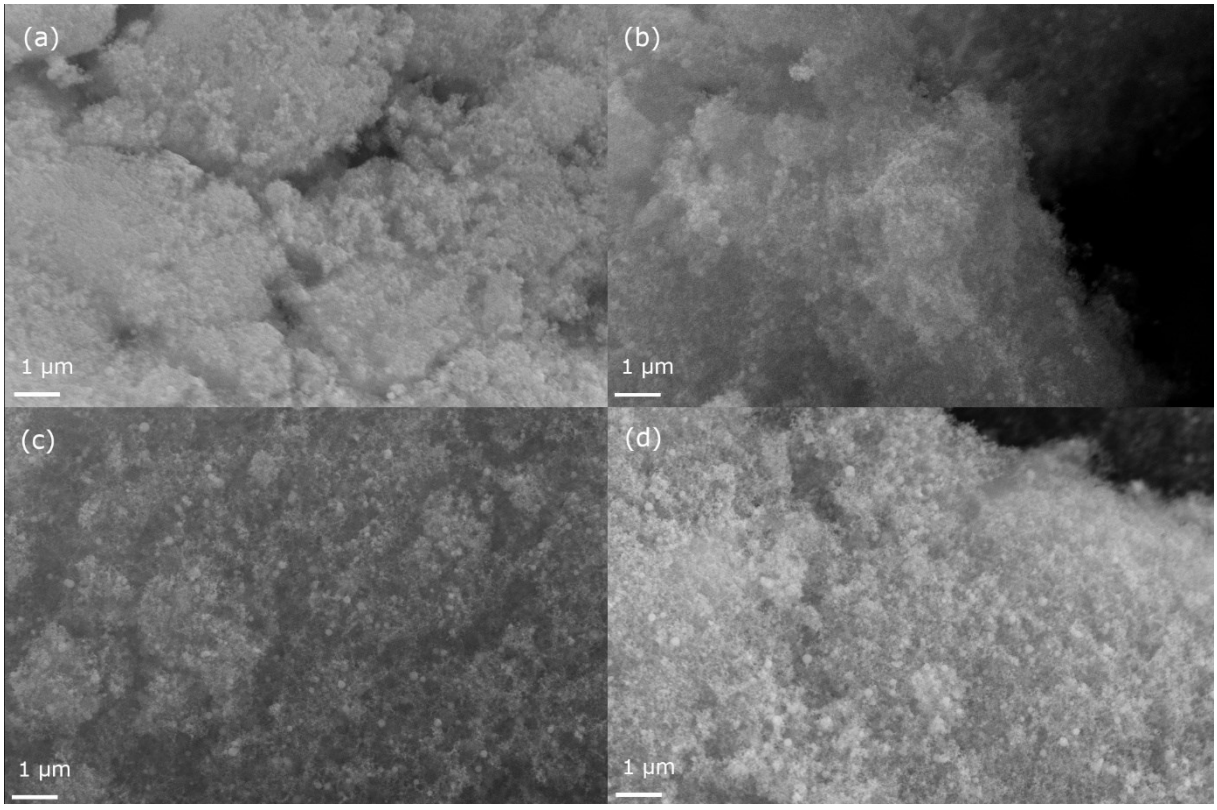

Figure 11 SEM images for LCFC A sample (a), LCFC B (b), LCFC CC (c), LCFC D (d).

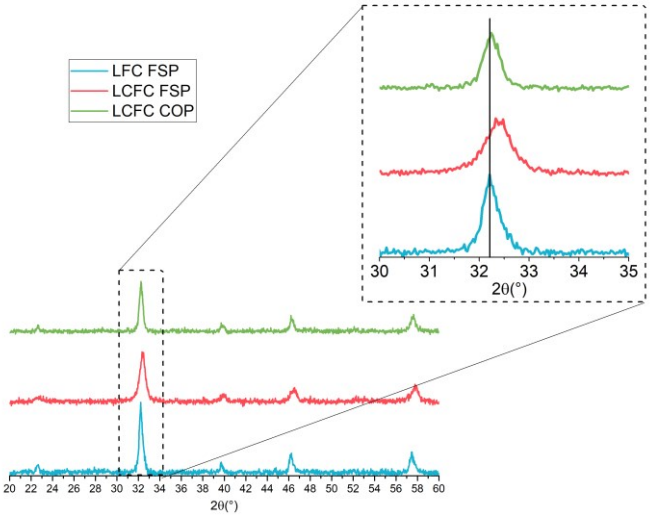

Figure 12 XRD patterns of the samples LFC FSP, LCFC FSP, LCFC COP.

2.4.2 Comparison of LCFC FSP and COP

The XRD patterns, Figure 12, show the expected perovskite phase (orthorhombic lattice symmetry). The intense X-ray diffraction peaks at 2θ values of 32.21°, 39.65°, 46.25° and 57.44° correspond to the typical (121), (220), (202), and (240) reflection plans, thus relating it to the orthorohombic crystal structure with a space group Pbmm (JCPDS PDF 37-1493). The non-doped sample LFC obtained by FSP and the doped sample obtained by coprecipitation, LCFC COP, are very similar in terms of crystalline composition. The LCFC FSP pattern, in contrast, is shifted towards higher 2θ values (Figure 12, inset) due to the contraction of the unit cell volume consequent to the inclusion of Ca. The ionic radii of La(III) and Ca(II) are very near and no significant variation of the unit cell is expected as a consequence of the substitution; the Fe(IV) small radius ($r_{Ca(II)}$=134 pm, $r_{La(III)}$ =136 pm) can account for the cell contraction ($r_{Fe(III)}$=64.5 pm, $r_{Fe(IV)}$=58.5 pm). The formation of of Fe(IV) was observed to be induced by Ca doping [32,53,75] and confirmed in perovskites by Mossbauer Spectroscopy [60]. Beside Fe(IV), also oxygen vacancies can result from electric charge compensation [76] and cause the lattice restriction. Barbero et al. observed that the formation of oxygen vacancies becomes significant for x>0.2 in stoichiometric $La_{1-x}Ca_xFeO_3$ [77] but the A-site substoichiometry and the presence of Cu is expected to favor also their formation [32,34]. The shift of the XRD signals suggests the un-complete inclusion of Ca in the perovskite lattice for sample obtained by COP and its inclusion in the FSP one. Rietveld refinement studies on similar samples corroborate this hypothesis [32].

In Figure 13 XP spectra are reported. O1s spectra indicate two distinct contributions, lattice oxygen (at about 529 eV) and surface oxygen species (532.0 eV). [6,57,67–69,59–66] Fitting procedure reveals that FSP samples are characterized by a higher amount of surface oxygen species with respect to the COP ones. $La3d_{5/2}$ and $La3d_{3/2}$ are consistent with the presence of La (III) (shake-up signals at 837.3 and 838.5 eV), $La(OH)_3$ and LaOOH (about 835 eV) are observed (833.5 for $La3d_{5/2}$ in perovskites) 39,41,52–56,44–51. [39,58,67–71,59–66]

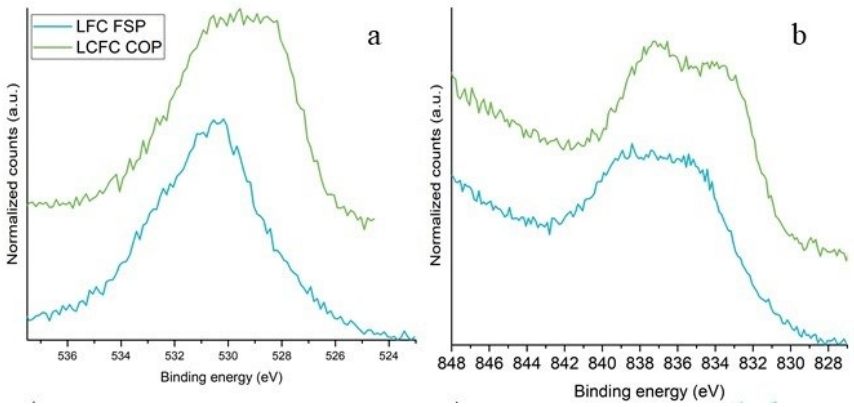

Figure 13 XP spectra of the samples LFC FSP and LCFC COP. a) O1s, b) La3d.

Sample	*Type*	*La*	*Ca*	*Fe*	*Cu*	*O*	*La**	*Ca**	*Fe**	*Cu**	*Ca/La*	*Cu/Fe*	*(Fe+Cu)/ (La+Ca)*	*O/ (La+Ca+Fe+Cu)*	*O lattice/O surface[a]*
LCFC COP	XPS	16.3	2.2	20.0	3.2	58.3	39.0	5.3	48.0	7.6	0.14	0.16	1.25	1.40	3.6
LFC FSP	XPS	13.9		17.1	3.6	65.4	40.1		49.5	10.4		0.21	1.49	1.89	0.2
LCFC	Nominal	12.5	4.2	16.6	4.2	62.5	33.0	11.0	44.0	11.0	0.33	0.3	1.22	1.67	
LFC	Nominal	14.9		17.0	4.3	63.8	35.0		40.0	25.0		0.6	1.86	1.76	

Sample	*Type*	*La*	*Ca*	*Fe*	*Cu*	*O*	*La**	*Ca**	*Fe**	*Cu**	*Ca/La*	*Cu/Fe*	*(Fe+Cu)/ (La+Ca)*	*O/ (La+Ca+Fe+Cu)*	*O lattice/O surface[a]*
LCFC COP	EDX	12.9	1.4	12.9	3.6	69.2	41.9	4.5	41.9	11.7	0.11	0.28	1.16	2.25	
LFC FSP	EDX	12.1		14.6	1.8	71.5	42.4		51.2	6.4		0.13	1.36	2.51	
LCFC	Nominal	12.5	4.2	16.6	4.2	62.5	33.0	11.0	44.0	11.0	0.33	0.3	1.22	1.67	
LFC	Nominal	14.9		17.0	4.3	63.8	35.0		40.0	25.0		0.6	1.86	1.76	

Table 5 XPS and EDX compositions (atomic concentrations) obtained for the doped and un-doped LFC obtained by Flame Spray Pyrolysis (FSP) and by Co-precipitation (COP). The compositions obtained without considering oxygen (*) are reported in order to emphasize the cation surface segregation phenomena. The last column refers to the ratio between the integrated peak area contribution at 529 eV and the integrated peak area contribution at 532 eV.

Ca2p region is identical for the two Ca-doped samples. Fe2p peaks (710.5 eV) are characteristic of Fe(III). [16,23,32,34] $Cu2p_{3/2}$ XP spectrum is centered at 933.5 eV, a position characteristic of Cu in oxides; the presence of Cu(II) is confirmed by the shake-up at 941.8 eV.[6,69]

Oxygen is over stoichiometric and is more abundant in the FSP samples. Table 5 shows that in the LFC sample Fe and La are surface segregated, whereas Cu is less than expected (even if more abundant in XPS than in EDX). The same observation applies to samples LCFC FSP and COP as regards to La, but Ca doping causes further decrease of surface Cu. Only in the COP sample (and with EDX) the amount of Cu gets closer to the expected value. Ca is present in significantly lower amounts in the COP catalyst.

TPR curves for each sample have been compared in Figure 14 and quantitative results are reported in Table 6. Three peaks are identified at 205-278°C (Cu(II) to Cu(0)) and 422-481°C, Fe(IV) to Fe(III), and about 650°C, (Fe(III) to Fe(II)).[11,53] The two contributions of iron oxide reduction are very weak in the LCFC FSP sample with respect to LFC FSP (2 to 4% of the value expected from the composition to be compared with the 65% of the Ca-free catalyst). This is an evidence for the stabilization of Fe (III) and Cu(II) (whose reduction temperature increases by about 100 °C) in the lattice structure or of a low ion mobility. Calcium doping has proved to be effective in decreasing the reducibility of the FSP-sample. Wu et al.[32] compared the behavior of stoichiometric and under stoichiometric, doped and un-doped $LaFeO_3$. No significant reduction is observed in stoichiometric sample whereas a broad signal due to the reduction of segregated α-Fe_2O_3 is observed in under-stoichiometric one. After doping the reduction of iron oxide is not anymore observed and the reduction of Cu(II) to Cu(0) is evident. The insertion of calcium into the perovskite stabilizes Cu inside the unit cell un-favoring its segregation as CuO and its reduction. In COP sample the apparently incomplete inclusion of Ca in the structure seems to confirm this hypothesis: a double spiked peak that accounts for the reduction of two distinct species of Cu (II) agrees with the presence of segregated

easily reducible CuO and less reducible Cu(II) inserted into the perovskite unit cell. In fact, the low temperature contribution seems to agree with the FSP sample without Ca whereas the high temperature contribution is consistent with the LCFC FSP catalyst (E). The ratio between these two contributions is around 1:3.

SEM images are reported in *Figure 15*. For the FSP materials the pictures highlight the presence of the combustion residues (small white particles) and a homogeneous morphology with dispersed particles. LCFC COP sample reveals a more compact morphology with larger aggregates. The catalyst produced by co-precipitation, LCFC COP, (Table 7) shows a specific surface area of 22 m^2/g, about one third of the corresponding catalyst obtained by FSP, consistently with the more compact morphology; this can be due to the harsh calcination treatment. The different preparation procedure plays a role: in a Ca,Cu-doped perovskite of identical composition but obtained by citric acid procedure a specific surface area of 21.3 m^2/g was obtained. The specific surface area is mainly affected by doping: in the LCFC FSP, indeed, it is around 60 (57.0 to 61.1 m^2/g in the samples obtained at different synthesis steps) whereas it is 32.5 m^2/g in LFC FSP. This was attributed, by Andoulsi et al. [78] to the increased nucleation sites resulting from higher stacking fault energy due to calcium incorporation into the perovskite lattice. [79]

General considerations on the ICP compositional analytic results can be made. This concerns only the metal composition and does not make any difference between perovskite, oxide or other phases that could be present on the surface. The overall trend is that the experimental composition approaches more the nominal one for the samples obtained by COP method. In Table 8 the samples collected at different phases of the FSP process are progressively converging to the nominal throughout the process, however La never reaches the nominal composition. In Table 9 LFC FSP shows that the copper content is roughly half of the nominal expected, meaning that copper is not perfectly included in the structure. Unlike Cu, La and Fe are in agreement with the expected results. Comparing LCFC obtained by COP with the analogous samples by FSP, COP sample includes Cu better than FSP, whereas Ca has been included in a lower amount that expected.

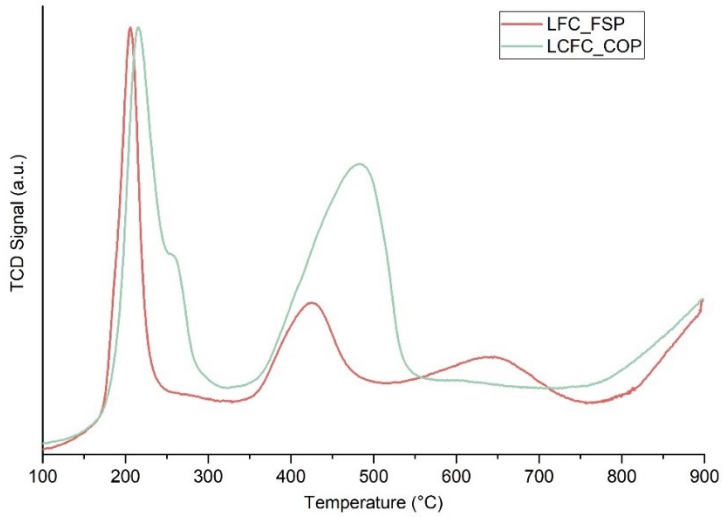

Figure 14 H_2-TPR profile for LFC FSP and LCFC COP.

	T max (°C)	mol H_2 consumed/expected	Assignment	Fe(IV)/ ((Fe(IV)+Fe(III))
LCFC FSP				0.47
Low T peak	272	0.65	Cu(II)-Cu(0)	
Broad signal	450-650	0.02	Fe(IV)-Fe(III); Fe(III)-Fe(II)	
LFC FSP				0.27
Low T peak	206	0.54	Cu(II) - Cu (0)	
Broad signal	450-650	0.65	Fe(IV)-Fe(III); Fe(III)-Fe(II)	
LCFC COP				0.42
Low T peak	216-250	1.02	Cu(II)-Cu(0)	
Broad signal	450-650	0.18	Fe(IV)-Fe(III); Fe(III)-Fe(II)	

Table 6 H_2-TPR results for FSP and COP samples. The third column (mol H2 consumed/expected) refers to the experimental and theoretical amount of H2 to be consumed during the TPR, in correlation to the stoichiometric composition of the samples.

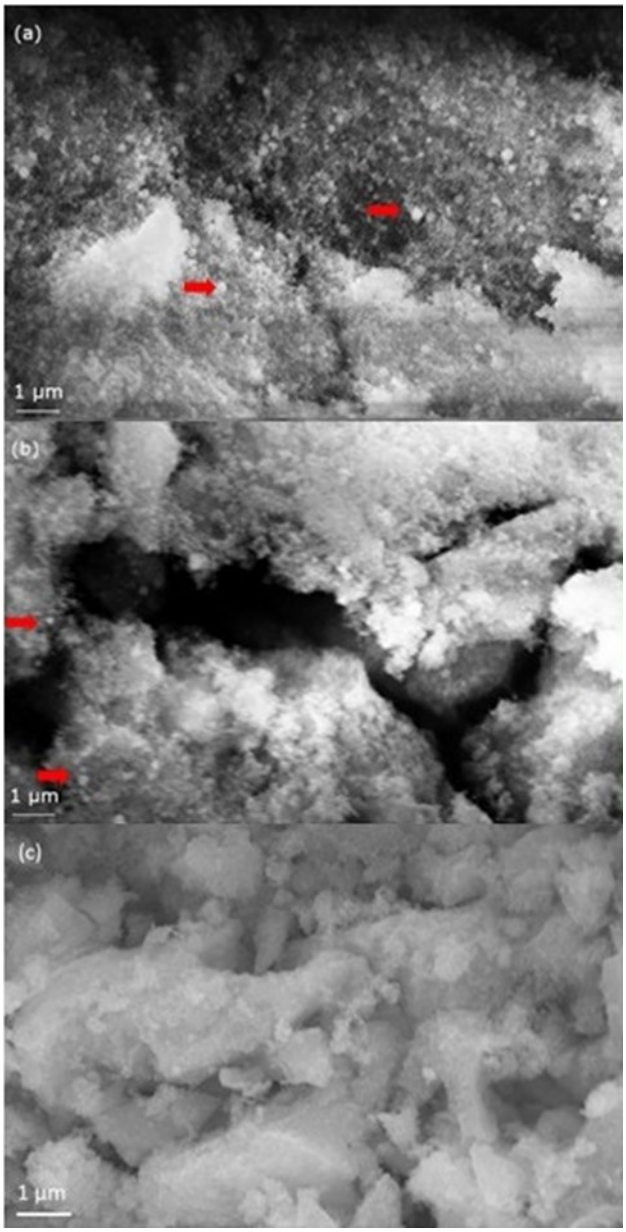

Figure 15. SEM images for LFC sample (a), LCFC FSP E (b) and LCFC COP (c).

Sample – Synthesis	**Composition**	**Specific Surface Area (m^2/g)**
LFC – FSP	$La_{0.7}Fe_{0.8}Cu_{0.2}O_3$	32.5
LCFC – COP	$La_{0.6}Ca_{0.2}Fe_{0.8}Cu_{0.2}O_3$	22.0

Table 7 Composition and specific surface area of the analyzed samples.

		ICP results (%)					
	Nominal	LCFC A	LCFC B	LCFC C	LCFC D	LCFC E	LCFC COP
La	54.26	61.95	58.63	59.99	62.07	61.75	60.62
Ca	8.34	4.08	4.75	5.99	4.48	4.22	2.17
Cu	8.29	3.99	5.88	3.77	3.66	4.06	7.99
Fe	29.12	29.98	30.74	30.25	29.78	29.97	29.22

Table 8 ICP composition of the samples compared to the nominal composition (only metals). LCFC samples

		ICP results (%)
	Nominal	LFC FSP
La	62.93	64.25
Cu	8.22	4.59
Fe	28.85	31.16

Table 9 ICP composition of the samples compared to the nominal composition (only metals). LFC sample

2.4.3 Catalytic results: CO-NO mixture

Each sample has been tested for CO assisted NO reduction (Figure 16) and with a complex mixture simulating the automotive exhaust under rich and lean conditions (Figure 17 to Figure 19). The light-off temperature for CO oxidation and NO reduction is quite low for a non-PGM catalyst, approx. 250°C, and is lower for LCFC COP; this is the best sample being able to approach full conversion of CO and NO below 400°C. Both samples from FSP (LFC FSP and LCFC FSP) behave very similarly, despite the different doping and the differences highlighted by the characterization. These preliminary results suggest that the catalyst characterized by higher activity, in spite of the lower specific surface area, is the one obtained by co-precipitation.

CO conversion starts at 100 °C lower temperatures with respect to NO. It is widely accepted that CO oxidation can proceed via Mars-van Krevelen mechanism,[52] using oxygen from the material. CO molecularly adsorbs on Lewis surface acidic sites and reacts with oxygen species near neighbors of the Lewis acidic sites, originating carbon dioxide that desorbs. The result is a partially reduced site (oxygen vacancy) that may be re-oxidized by gas phase oxygen (if available),
by bulk oxygen (if mobility is enough) or be the site for another CO chemisorption. In the catalyst without or with small amount of Ca, this phenomenon is more evident. The activity profiles suggest that CO conversion evolves with a change in the mechanism around 200-250 °C. At this temperature the conversion of NO also begins suggesting that NO contributes to the CO oxidation.

The comparison between the CO conversion and CO_2 yield curves suggests that, particularly at temperatures higher than 350-400 °C, part of the carbon dioxide remains on the catalyst surface as an adsorbate. The insertion of calcium into the cell modifies the catalytic activity at lower temperature: in LFC FSP the light-off temperature is around 150 °C, in LCFC FSP is around 225 °C; moreover, the start of the light-off curve is steeper. For LCFC COP, the light-off temperature is around 125°C. For LCFC FSP a step-like increment is observed (around 200 °C) when the oxidation starts involving

NO. The N_2 production starts at higher temperature then the NO consumption and it remains always less than the expected from NO reduction. That suggests that some N_2O (not measured but calculated) might form at lower temperature; although N_2O is evidently less at higher temperature, there is always some in the products.

The higher reactivity of the COP sample can be related to the higher amount of iron observed on the surface and the lower amount of oxygen, which could favor the formation of oxygen vacancies capable of activating NO and chemisorbing CO. The relevance of Fe (IV) on catalytic activity of $LaFeO_3$-based perovskites was already underlined.[32,53,75,77]

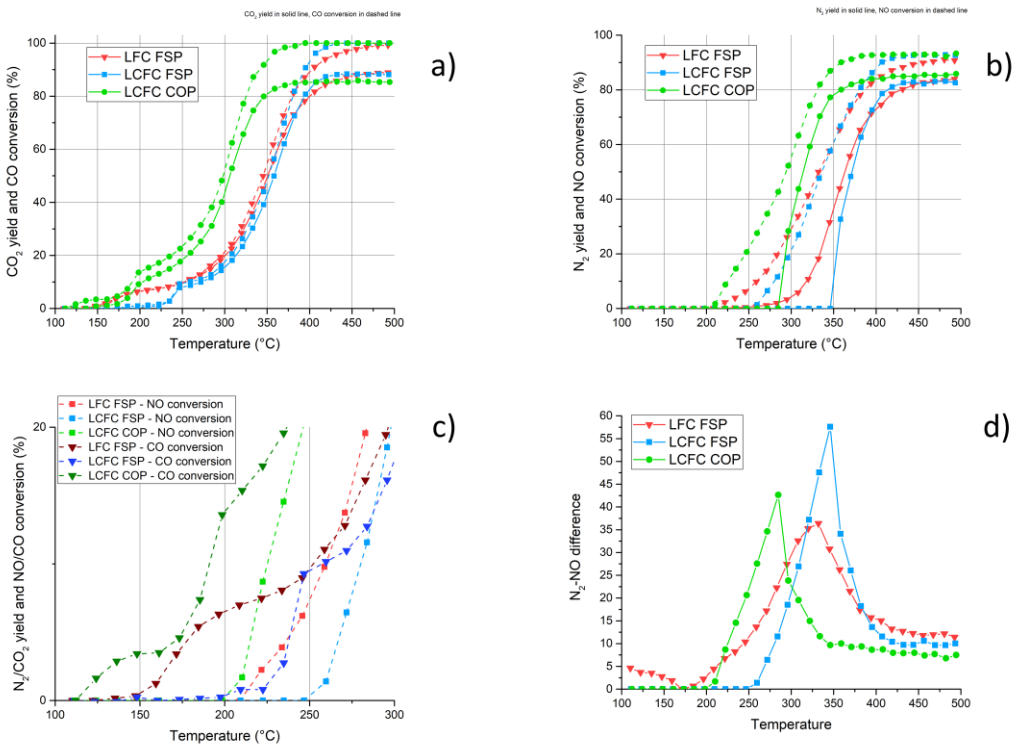

Figure 16 CO-NO mixture reactivity for samples LFC FSP; LCFC FSP E; LCFC COP. (a) CO conversion (dashed), and CO2 yield (solid); b) NO conversion (dashed), and N2 yield (solid); c) N2/CO2 yield and NO/CO conversion between 100 and 300 °C. d) N2O determined by the difference by NO conversion and N2 yield.

2.4.4 Catalytic results: complex TWC mixture

The activity of these catalysts under a complex TWC mixture, either stoichiometric or rich, is reported in Figure 17 to Figure 19. Figure 17 shows the conversion of all reactants for LCFC COP under stoichiometric conditions, to highlight the sequential onset of reactivity. The sequence does not change for the other catalysts. CO is always oxidized first, and then H_2, followed by HCs, with CH_4 seldom activated.

Materials that differ by synthesis and Ca-doping are compared in terms of single-reactant conversion with the stoichiometric mixture in Figure 18. All the materials are good oxidation catalysts, sequentially activating the oxidation of CO (between 120 and 170°C on the different materials), H_2 (~170-200°C), unsaturated (~250°C) and then saturated (~350°C) C3s, and finally CH_4 (~400-450°C), as anticipated in Figure 17. In presence of O_2, CO is oxidized at lower temperature (slightly above 100°C on LFC) compared to the simpler CO+NO mixture, Figure 16. Consistently, CO conversion approaches 100% at 300°C (or below, for LFC), again significantly lower than the CO+NO mixture. While this lowering of the range of temperature to achieve the same activity might also be an effect of a longer contact time with the gases (i.e. lower WHSV, see Table 1), the ranking of activity in CO oxidation of the materials appears very different with the complex TWC mixture vs. the simple CO+NO. Now the LFC appears markedly more active than LCFC's, and the production route does not make a difference on the activity of the latter. With just CO and NO, the oxidation of CO was found to be more effective on LCFC prepared by coprecipitation, while both materials prepared by FSP (LFC and LCFC) behave similarly. Note that reactant conversion on the same mass of catalyst does not account for differences in specific surface of the materials, see

Table *4* and Table 7, where there is a factor of up to 3 among measured values. The same measurements of Figure 18 reformulated through an estimate of turn-over frequency, thus accounting for the specific surface, is reported Figure 20. An addendum about the comparison based on the turn-

over rate is included at the end of the chapter for further clarification. They unambiguously suggest a specific activity ranking as LCFC-COP>LFC-FSP>LCFC-FSP, (the reverse order of specific surface). NO reduction is negligible in the presence of stoichiometric O_2; some activity (not reported in Figure 18) was observed between 350°C and 500°C, with a maximum conversion of 7% and 2.7% for FSP and COP LCFCs, respectively. Comparing the different catalysts, a large role of Ca-doping, particularly in the oxidation of CO, C_3H_6 and CH_4, is observed. The activation of methane is more affected by the synthesis, achieving 61% conversion at 600°C for LCFC- FSP, whereas only 31% is converted on LCFC-COP. It also appears that the undoped ferrite LCF makes the ignition easier, specifically of CO and C_3H_6, suggesting that Ca-doping is not effective. There is an abundance of O_2 in the gas phase; it is extremely large at low temperature where oxidations did not start yet, but also at high temperature some O_2 remains, being difficult to complete the CH_4 oxidation, see Figure 18.

NO reduction was not observed because of two facts, i) the testing procedure, that fully oxidizes the materials with air at 600°C; reagents are fed starting from this step, at 600°C, where the catalysts are expected to lack oxygen vacancies; ii) the abundance of O_2 mentioned, that increases during cooling, prevents the formation of enough vacancies; iii) adsorption of other gases might be preferred over the adsorption of NO on the perovskite surface.

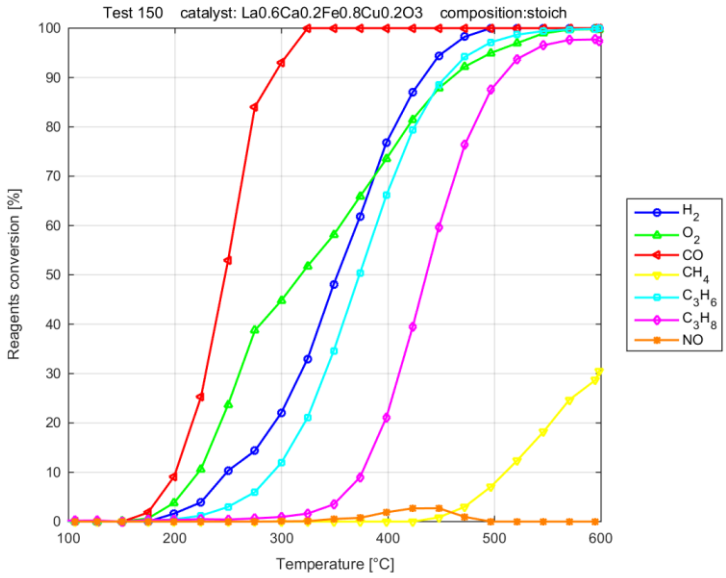

Figure 17 Activity of LCFC COP. Stoichiometric TWC mixture.

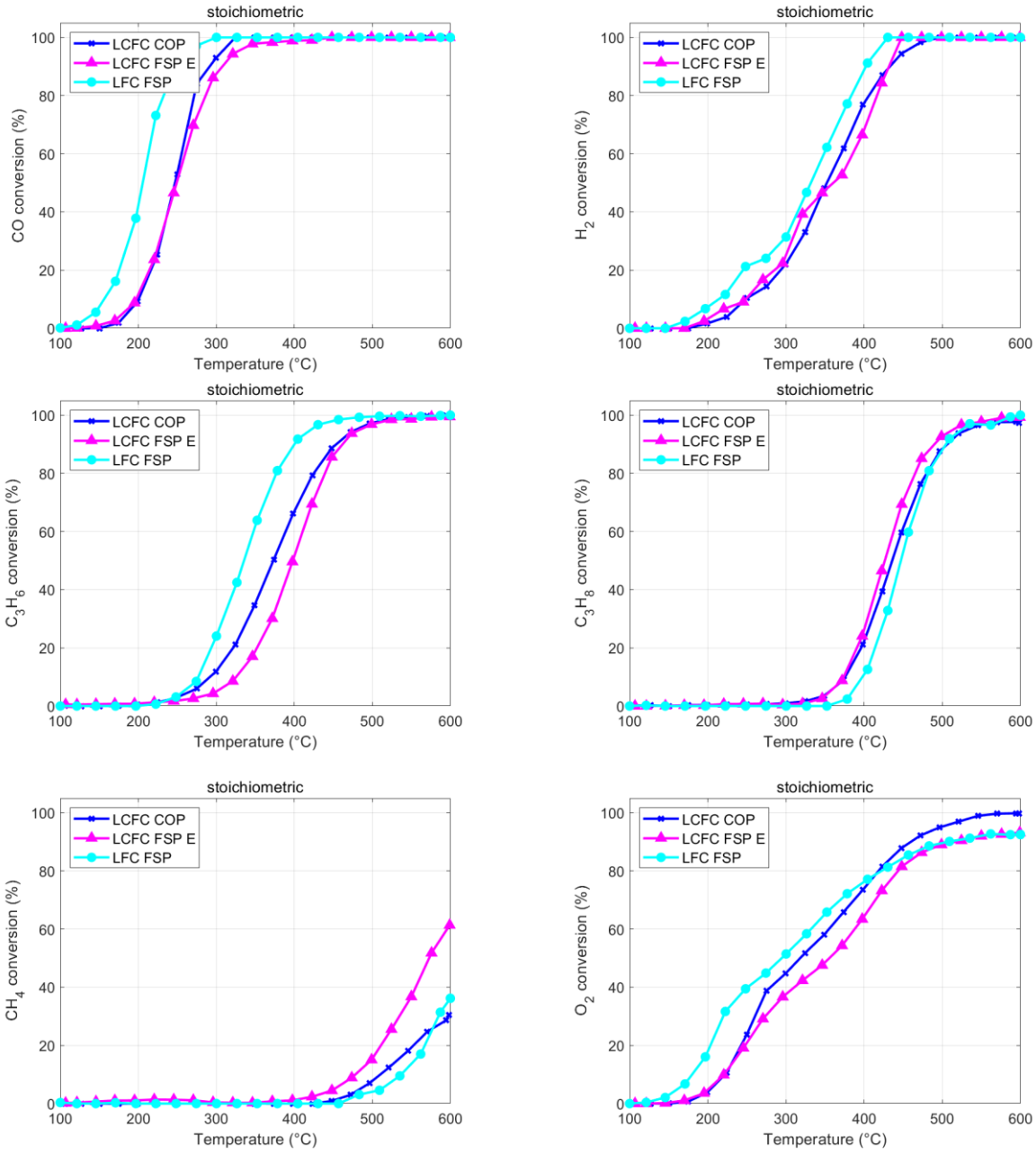

Figure 18 LCFC FSP E, LCFC COP. Stoichiometric TWC mixture.

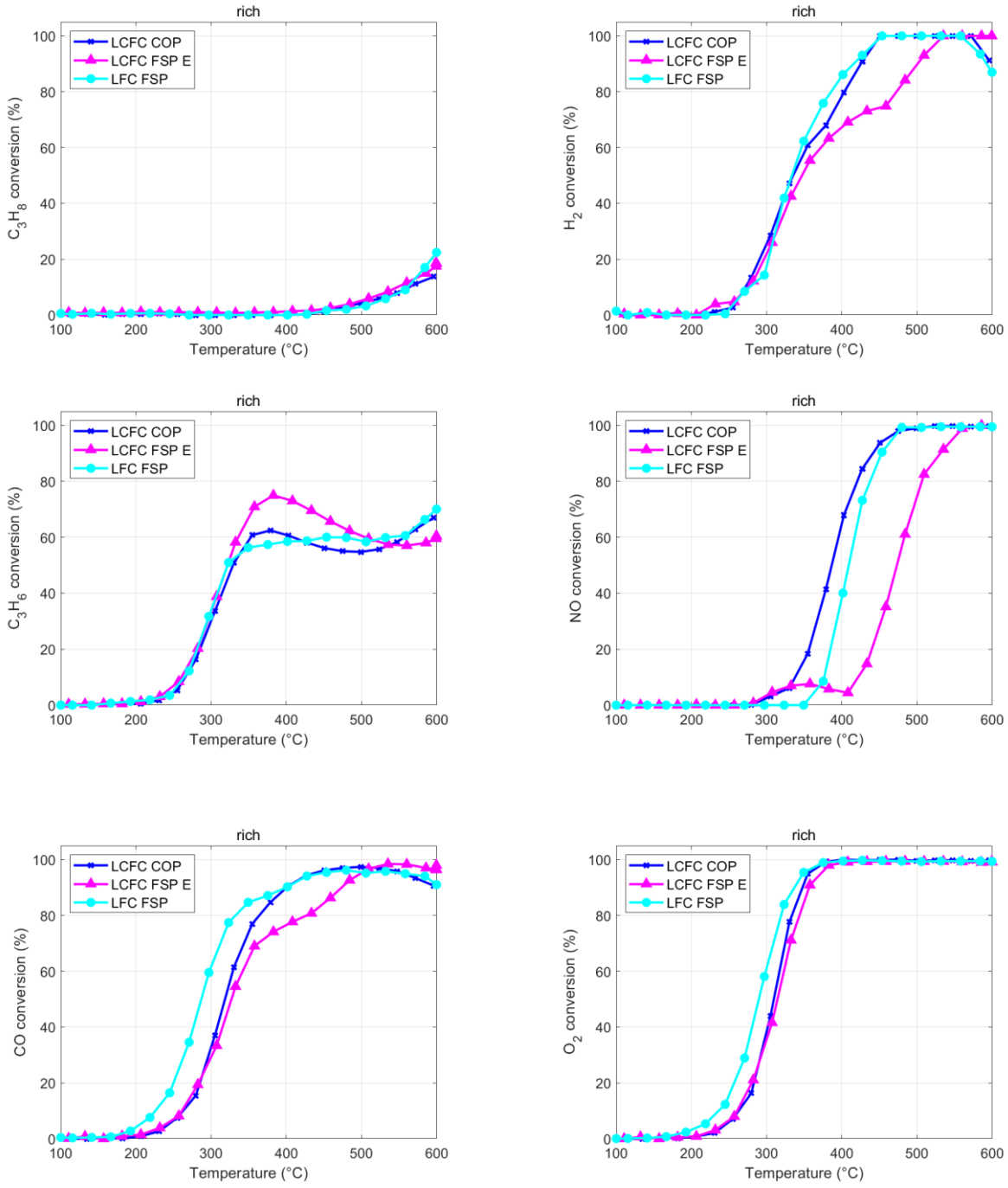

Figure 19 Activity of LFC FSP, LCFC FSP, LCFC COP. Rich TWC mixture.

The activity with the rich mixture is quite different, Figure 19. First, the evolution of CO, H_2, and HC is the result of two mechanisms, oxidation and reforming, the latter emerging at high temperature, where the O_2 is completely consumed, in the first part of the catalyst bed. Secondly, the phase in which oxygen is completely consumed allows a significant (up to quantitative) conversion of NO. That is a confirmation of the results of the CO+NO mixture, where the mechanism of NO reduction based on vacancy formation was suggested, but it requires reaching the extinction of O_2 in the gas phase to recreate vacancies, after the oxidative pretreatment of the catalysts at high temperature. Indeed, NO reduction occurs above the temperature where the O_2 is totally consumed. We did not observe any activation of CH_4 oxidation (not shown). We clearly see that both CO and H_2 are still available when the O_2 is totally consumed (>350°C), likely supporting the NO reduction. The NO reduction is better on COP sample compared to the FSP, supposedly by the larger amount of lattice oxygen identified by XPS for COP prepared materials. Moreover, the two copper species detected by TPR seem to work consequently, with a first activation in CO conversion at 350°C and a second rise in reactivity a 400-450°C°.

Between 200°C and 350°C we observe the activation of CO, H_2 and propene oxidation. C_3H_8 oxidation is surprisingly very weak in rich conditions, compared to the stoichiometric mixture, perhaps due to the different propane/oxygen ratio. A maximum in C_3H_6 conversion is reached when O_2 in the gas feed approaches the total consumption, at about 380°C. At higher temperatures (>400°C), production of CO and H_2 conversion ceases to increase, because of the activation of the reforming reactions; that is especially clear for COP sample. For temperatures higher than 500°C, the CO and H_2 conversion stabilizes, although O_2 is not available anymore. This indicates that C_3H_6 consumption is correlated to the action of another oxidizing agent, such as NO. An interesting mechanism is occurring for sample LCFC – FSP; NO starts to convert at 290°C for both LCFC catalysts, but in the case of the LCFC-FSP sample, the reaction seems to follow a two-step mechanism: the first at low temperature, with a maximum at 350°C (7% conversion), whereas after

the total O_2 consumption, NO conversion increases, reaching the total reduction at 590°C. LCFC-COP sample does not exhibit such a behavior, neither LFC. The comparison of catalysts with the rich TWC, reformulated to account for the specific surface area is reported in the Figure 21.

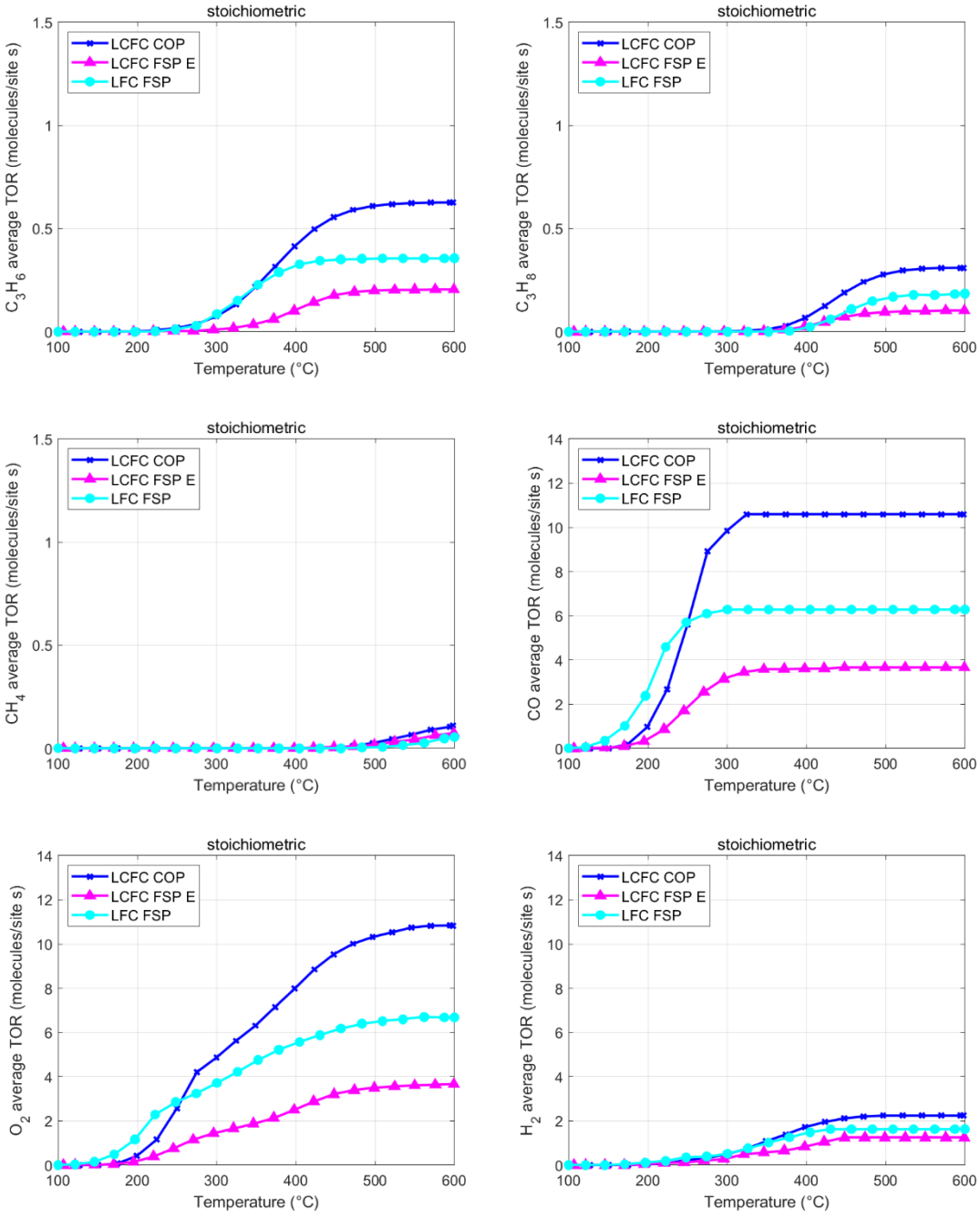

Figure 20 LCFC FPS E, LCFC COP. Stoichiometric TWC mixture (Turn Over Rate).

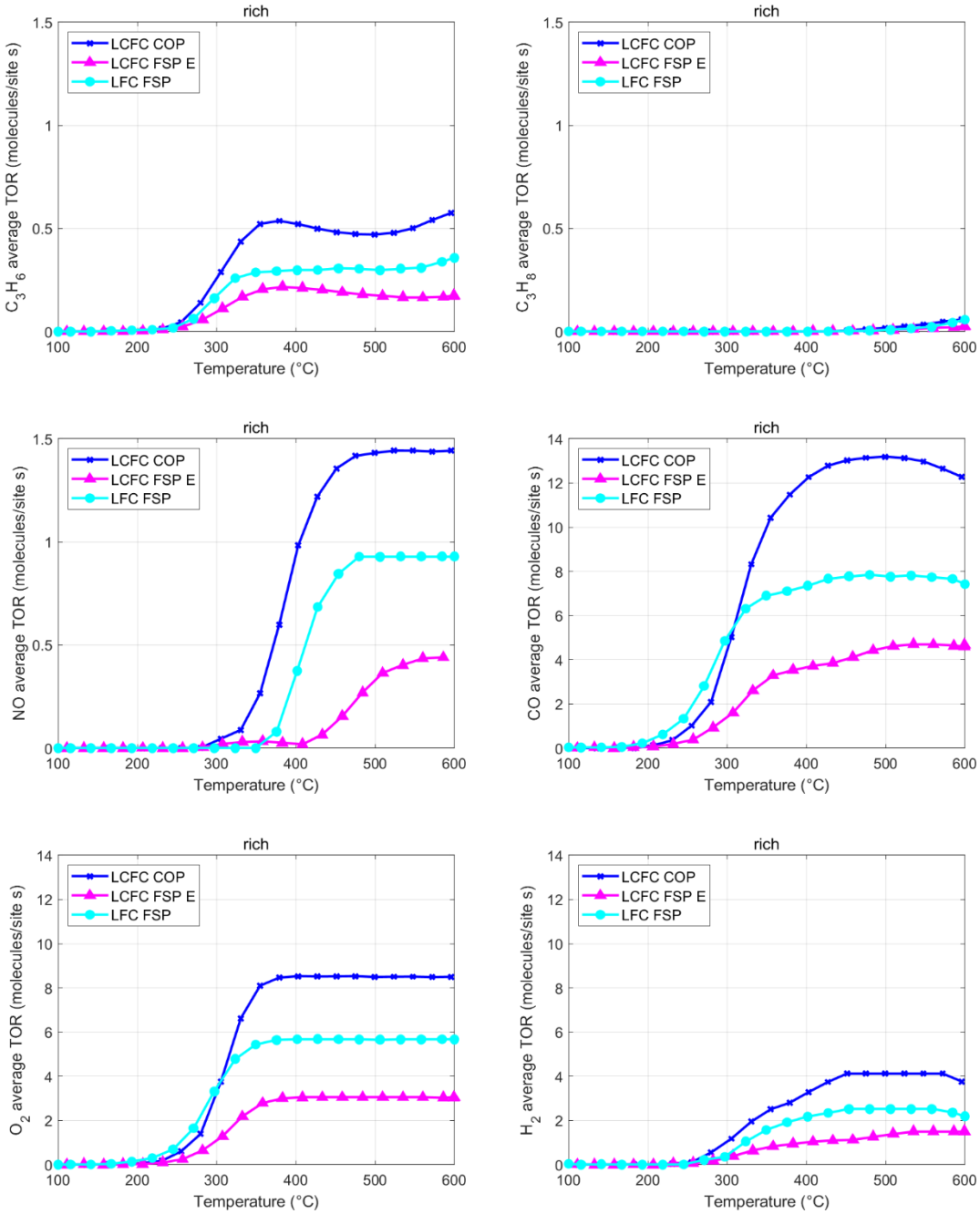

Figure 21 Activity of LFC FSP, LCFC FSP E, LCFC COP. Rich TWC mixture (Turn Over Rate).

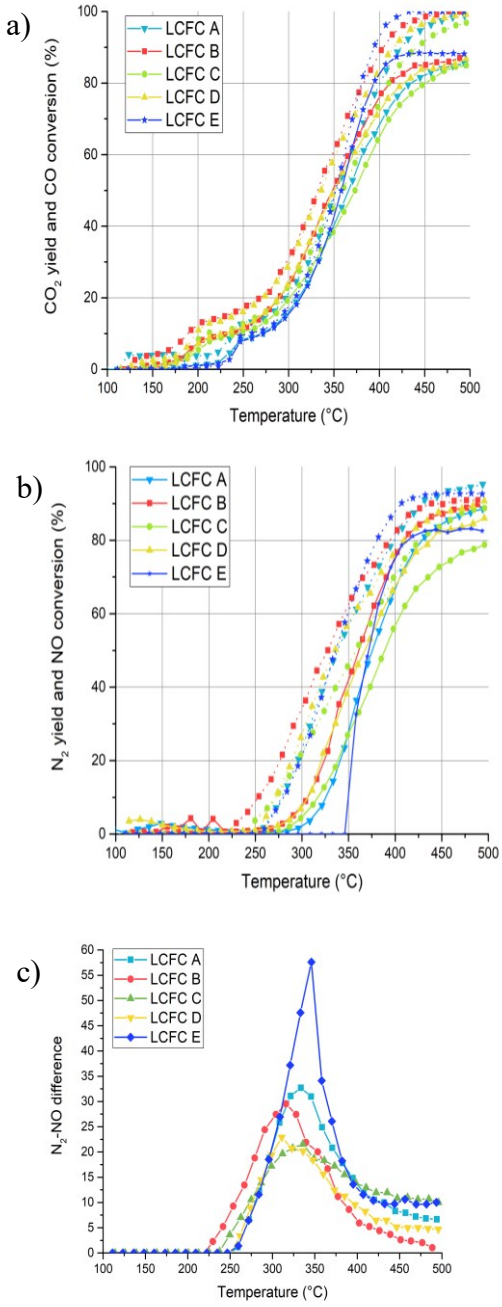

Figure 22 Activity during CO+NO reaction. Samples LCFC A, B, C, D and E. a) and b) CO and NO conversion (dashed), and CO2 and N2 yields (solid); c) N2O determined by the difference between NO conversion and N2 yield.

The results of the activity test with the complex TWC mixture for LFC FSP, very similar to LCFC-COP ones, confirm the hypothesis that LCFC-COP was not effectively doped with Ca. Comparing LFC FSP and LCFC FSP (i.e. the same composition with and without Ca-doping), the undoped sample appears more active in NO reduction. For this reason, we can conclude that the inclusion of Ca has a negative impact on the catalytic reductive activity under these conditions, rearranging the perovskite lattice in such a way that compromises the reducibility of the transition metals (as seen by H_2-TPR) with particular reference to Cu. Comparing the XPS and EDX composition it is evident that the LCFC COP is not the sample with the highest amount of Fe and Cu and thus the surface composition does not appear to play a fundamental role under this reaction condition (i.e. from high to low temperature after pretreatment). In contrast the possible formation of oxygen vacancies capable of activating HCs seems to play a fundamental role. Oxygen vacancies can form thanks mainly to the understoichiometry and are not observed to have undergo cluster formation with Ca inserted into the unit cell. [36]

Concerning the variability in LCFC synthesis by FSP, also these samples were thoughtfully studied with respect to their catalytic behavior in CO assisted NO reduction (Figure 22).

Samples A, C and E have also been tested with complex mixture (see Figure 23and Figure 24, respectively stoichiometric and rich mixture), given their remarkable differences in properties as revealed by the structural and compositional analysis.

The two-steps in the CO conversion that we have seen in Figure 16 are confirmed, supporting the evidence of a Mars-van Krevelen mechanism under these conditions (no O_2) and testing procedure (increasing temperature, from room temperature). LCFC B and D are the more active catalysts, slightly better than A, C, and E. The conversions of both CO and NO are in excess of 80-85% above 450°C. Samples B and D are characterized by the higher (Fe+Cu)/(La+Ca) atomic ratio (1.3 and 1.4, respectively – see Table 2). The efficiency of Ca insertion does not seem to enhance reactivity: the

activity of catalysts B and D are very similar whereas the XRD patterns suggest a different insertion. This supports the hypothesis that at lower temperature the surface active sites are more relevant for catalytic performances, than bulk mobility. TPR revealed that the sample B is characterized by the lower Cu(II) reduction temperature (Figure 10). We observe a notable difference in N_2 yield of sample D, which was characterized by a different crystallographic feature, although the CO oxidizes almost like the other materials; that is consistent with a higher N_2O production, even at high temperature.

Considering stoichiometric TWC feed mixture, Figure 23, sample C is clearly less effective than A and its replica E, in CO (and partially in C_3H_6) oxidation, while A and E confirm a very good reproducibility of the synthetic process. To get a clearer picture of the performances of the catalysts, a table of comparison with a commercially available compound is reported (

Table *10*).

That is further confirmed by the O_2 consumption, a useful parameter to summarize the total activity of each catalyst; it defines which reactions take place and the environment in which the reactions occur. As already seen above, oxygen conversion is never complete; at the maximum temperature of the test (600°C) reaches 93%.

Accordingly, the materials are always in the presence of some oxygen. The apparent two phases indicated by the oxygen conversion curve reflect the early activation of CO and H_2, quite separate from the activation of HCs. Apparently, propene oxidation begins after the complete consumption of CO is achieved (> 350°C), suggesting that the same active sites are used. At very high temperatures, the differences among samples disappears, not only because some species (CO, C3s) are totally consumed, but also the mild CH_4 conversion is very similar for all the samples. Also, NO, which is poorly reduced in a stoichiometric mixture, does not differentiate the samples. It appears that a lower crystallinity, together with the residual presence of metal oxides, (sample A) turns out to be helpful to enhance catalytic activity.

In rich conditions, Figure 24, we see similar activity in all the samples, regardless of the production phase. Now oxygen is the limiting reagent, mostly for low temperature oxidations, when NO is not yet activated (to produce O_2). All samples catalytically activate the combustion at about 180°C for CO, H_2 and propene oxidation. After O_2 total consumption, propene reforming reaction occurs at about 400°C, causing an increase of CO concentration (conversion decreases) very clear at high temperature (>530°C). NO is reduced easily at 290°C, but only at total O_2 consumption NO conversion boosts. Again, the reaction apparently follows a two-step mechanism, in the presence (300°C < T < 400°C) or absence (>400°C) of O_2, finally leading to NO total conversion. These observations agree with how observed by Barbero et al. [77] that attributed the activity in ethanol oxidation to the Fe(IV) surface sites and that of hydrocarbons to the surface oxygen vacancies (not probable in presence of oxygen).

While differences among samples collected at different production phases are small, and the reproducibility at the same production phase (A vs E) is excellent, we see some residual variability, with sample C slightly less effective in CO and NO, while samples A and E activate C_3H_6 at lower temperature. Considering the characterization, the higher activity of sample A, richer in lattice oxygen than in surface oxygen species, suggests a bulk effect on the functional tests, rather than a surface phenomenon.

The main differences between samples A and C is the lower amount of Fe+Cu and the very low inclusion of Ca in the unit cell observed for A. An explanation of the higher catalytic activity of A, which also support the idea of a higher contribution of the bulk to the reactivity, may be the decrease of oxygen ion mobility due to the inclusion of calcium into the perovskite lattice.

The larger presence of Fe(II) indicated by TPR should also be considered. The testing procedure, with a pretreatment in oxygen at high temperature, may be responsible for its oxidation to Fe(III) and Fe(IV), more active in oxidation. That is consistent with the activity in the simple mixture, and with the CO oxidation two-step mechanism.

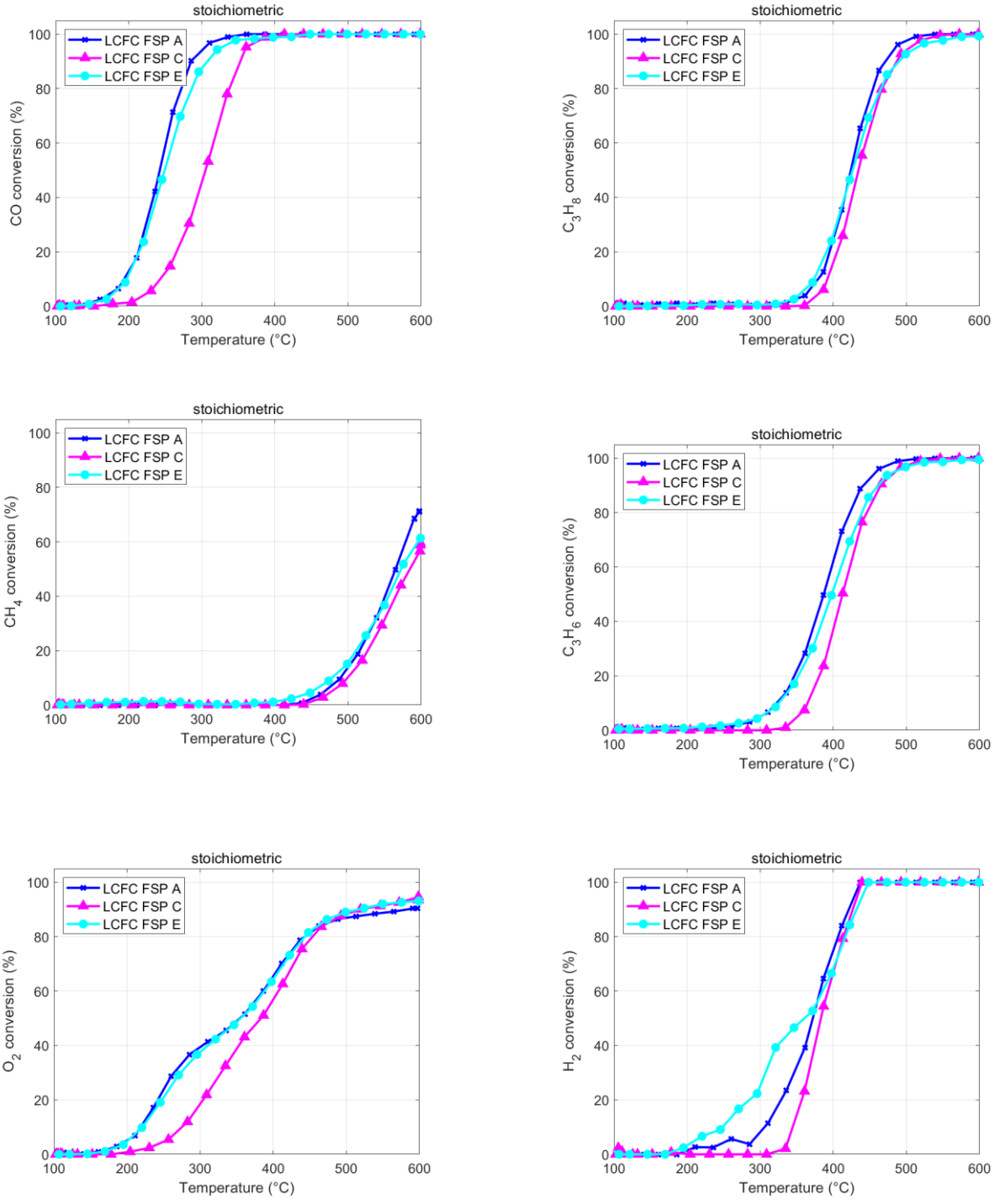

Figure 23 Activity of LCFC FSP A, C and E. Stoichiometric TWC mixture.

	Temperature of half conversion (°C) commercial sample	Temperature of half conversion (°C) LCFC A	Temperature of half conversion (°C) LCFC C	Temperature of half conversion (°C) LCFC E	Temperature of half conversion (°C) LCFC COP	Temperature of half conversion (°C) LFC FSP
CO conversion	217	235	305	240	242	211
C_3H_6 conversion	262	378	410	398	366	331
NO conversion	455	326	352	329	289	327

Table 10 Comparison with a commercial catalyst (data taken from reference 34), stoichiometric complex mixture.

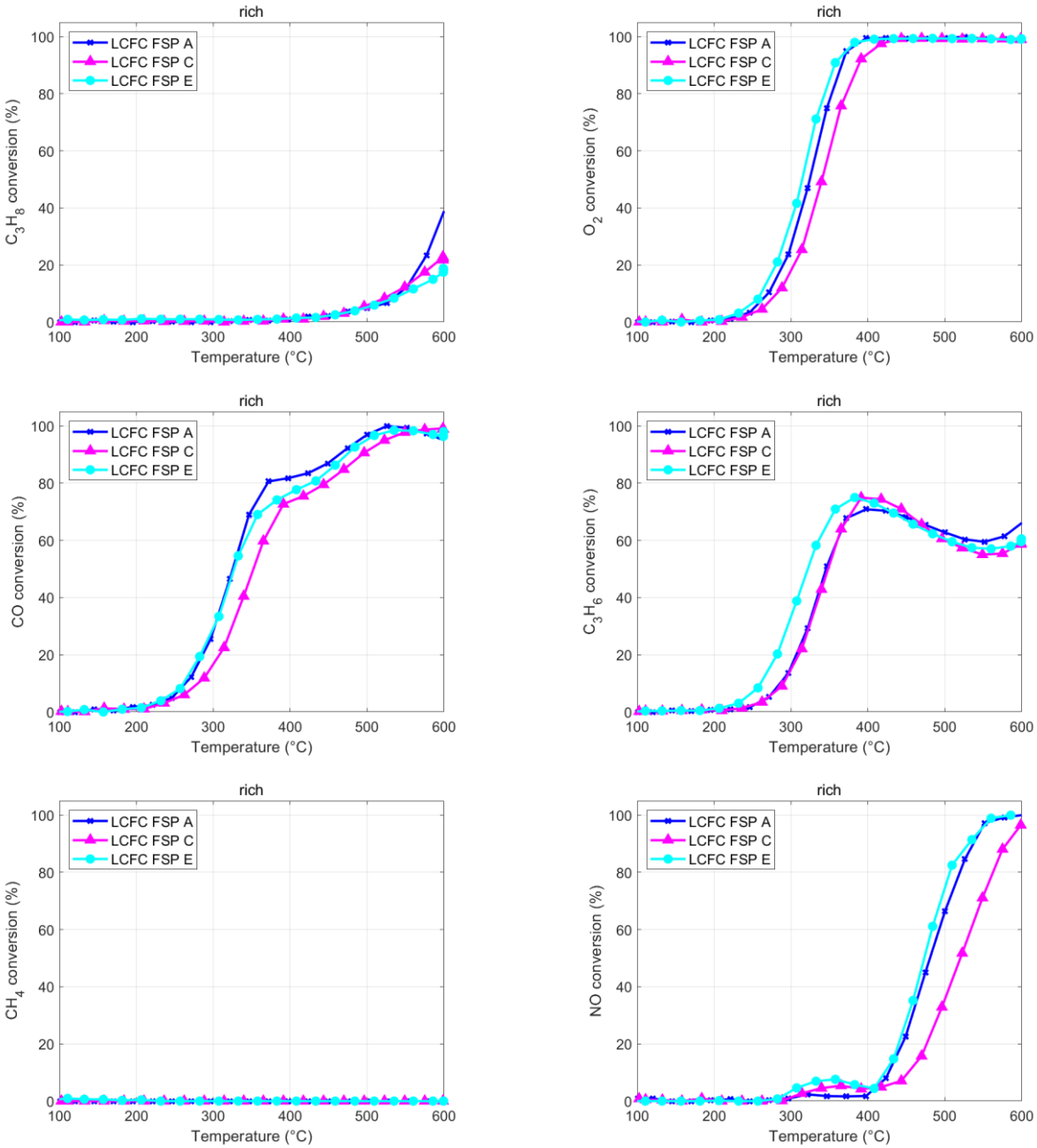

Figure 24 Activity of LCFC FSP A, C, and E. Rich TWC mixture.

2.4.5 Comparison between LKMC FSP and COP

The Mn-based composition is discussed below in terms of the results of the characterization and of the catalytic tests.

The Specific Surface Area of the $La_{0.9}K_{0.1}Mn_{0.9}Co_{0.1}O_3$ prepared by FSP (LKMC FSP) is 64.9 m^2/g; for the one obtained by coprecipitation (LKMC COP) a lower value, 29.0 m^2/g, has been observed. The diffraction patterns (Figure 25) agree with expectations for this perovskite; a slight shift toward lower angles for the diffraction peaks of LKMC COP, suggests a different level of dopant inclusion, as *e.g.* an uncomplete inclusion of K.

XP spectra (Figure 26) underline a significant effect of the preparation method on the surface composition. At first, beside lattice oxygen (components around 529-530 eV), a significant contribution due to other surface oxygen species can be observed. This is particularly evident for FSP sample, in which surface oxygen species contribute with a broad signal centered at 532-533 eV; the peak position and shape suggest attributing this component to surface active oxygen species. In the COP catalyst the relative amount of active oxygen seems less relevant and originates a tail at higher Binding Energies. The different shape can also be caused by the presence of non-perovskite oxides (contributing around 530 eV), since different oxygen species are responsible for different contributions in the O1s XP spectrum range.

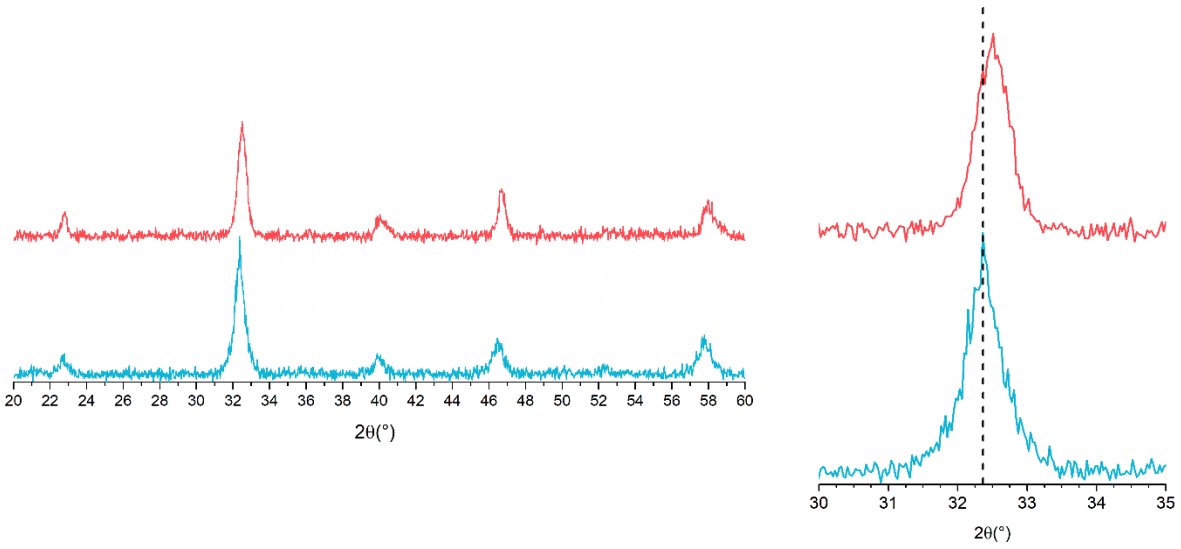

Figure 25 a) XRD pattern of samples LKMC FSP (blue) and LKMC COP (red). B) inset of the most intense peak.

La3d peaks positions (834.2 and 838.2 eV) and shape (shake-up contributions at higher Binding Energies) indicate that lanthanum ions are present in the 3+ oxidation state;[67] whereas a slight broadening for $La3d_{5/2}$ in the COP sample suggests the presence, beside perovskite, of La (833.9-834.4 eV) of hydroxylic species, ($La(OH)_3$, LaOOH at about 835 eV).

Mn2p region was recorded to identify Mn oxidative state and the experimental evidence supports the presence mainly of Mn (III) as the $2p_{3/2}$ is centered at 641.7-642.1 eV.[80] The spin-orbit splitting is compatible with the species considered, with a Δ=11.3 eV.[59] Presence of the Mn (IV) ion cannot be well established due to the proximity of its peak to that of the Mn (III) ion, however H_2-TPR tests suggest its presence, see later. [81]

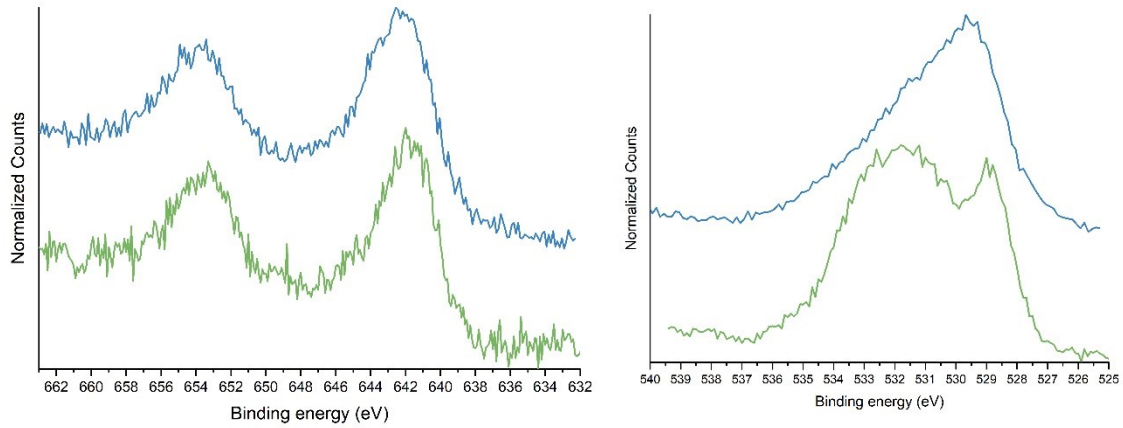

Figure 26 Mn 2p (left) and O 1s (right) XP spectra for the samples LKMC FSP (green) and COP (in blue).

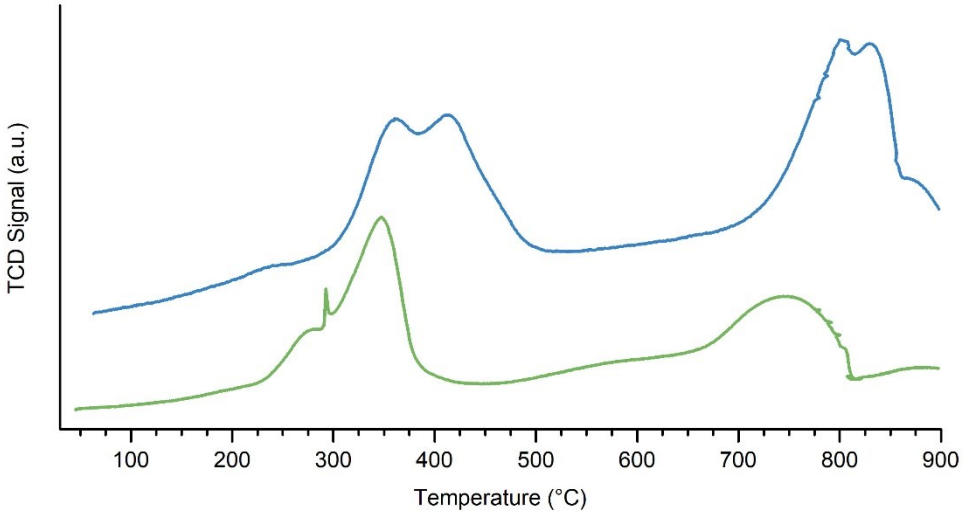

Figure 27 H_2-TPR profile of the samples: in green LKMC FSP, in blue LKMC COP.

The Co2p peak shape and position are consistent with the presence of Co(III). No trace of K is visible from XP spectra in the samples, probably due to the low potassium amount. The fitting procedure was performed through a Shirley type background subtraction and considering Voigt fitting curves.[82] The amount of surface oxygen is higher than the nominal value for both samples; this is consistent with the presence of hydroxyl groups and surface-active species suggested by the peak shape. Consistently with the peak shape, the surface over stoichiometry is more relevant in the FSP sample. The preparation procedure strongly affects the surface composition: La is segregated on the surface independently on production procedure but COP favors Mn surface segregation and FSP the presence of cobalt. Interestingly, the presence of K is only observed in the COP sample (by means of EDX) and it is not detected by XP spectroscopy. A comparison of the compositions obtained with XPS (surface analysis) and EDX (bulk analysis) techniques is reported in

Table *11* and shows that the results are similar for FSP sample, although differing from the nominal composition. The reason for such behavior lies in the surface segregation of Co and the trend of K to accumulate in the bulk rather that in the surface. Unlike the FSP sample, the COP one shows a different tendency in the metal cation distribution due to the poor inclusion of K in the structure.

H_2-TPR analysis was carried out to assess information about the reducibility of surface and bulk cations. As depicted in Figure 27 and reported in the quantitative

Table *12*, H_2-TPR profiles differ from one sample to the other, giving the general impression that LKMC COP is less reducible than its analogue prepared by FSP. H_2-TPR curves show a group of peaks around 300-450 °C and another one around 700-850°C (Figure 27). The signals at lower temperature, according to literature sources, are assigned to the reduction of Mn (IV) to Mn (III)[83] those at higher temperature are related to the extensive reduction of Mn (III) to Mn (II).[83] Cobalt reduction was observed to occur in two steps: from Co(III) to Co(II) around 440°C, and from Co(II) to Co(0) at about 600°C [8,84–88]; reduction temperature, however, is deeply affected by the perovskite composition and the preparation procedure. [89,90]

Sample	Type	La	K	Mn	Co	O	K/La	Co/ Mn	(Mn+Co)/ (La+K)	O/(La+K+Mn+Co)	Ratio lattice oxygen : surface oxygen (by XPS integration)
LKMC FSP	XPS	11.8 50.2	0.0 0.0	9.6 40.6	2.2 9.2	76.5	0.0	0.2	1.0	3.3	0.2
	EDX	12.1 48.7	0.4 1.6	10.2 41.0	2.3 9.3	75.1	0.0	0.2	1.0	3.0	
LKMC COP	XPS	19.1 51.2	0.0 0.0	18.2 48.8	0.0 0.0	62.6	0.0	0.0	1.0	1.7	0.5
	EDX	12.5 50.9	0.0 0.0	10.8 44.1	1.2 5.0	75.4	0.0	0.1	1.0	3.1	
Nominal		18.0 45.0	2.05 .0	18.0 45.0	2.05 .0	60.0	0.1	0.1	1.0	1.5	

Table 11 XPS and EDX atomic compositions (%) obtained for LKMC FSP and COP. In the cation columns, the first value is the one obtained considering also oxygen, the second one is obtained as cation-only compositions. These are reported in order to emphasize the cation surface segregation phenomena.

	T max (°C)	H_2 mol consumed ($\cdot 10^{-3}$)	Species being reduced	Stoichiometric coefficient	Electrons involved	n of cation/mole perovskite($\cdot 10^{-3}$)	n of H_2/g expected($\cdot 10^{-3}$)
LKMC FSP			Mn(III)	0.8+0.9(Mn^{4+})	1	3.87	1.94
peak 1	309.7 348.3	0.97 0.64	Mn(IV)	0.1	1	0.431	0.22
peak 2	646.5 745.8	0.44 0.60	Co(III)	0.1	3	0.431	0.65 0.22 0.43
SUM		2.65	SUM				2.80
LKMC COP							
peak 1	351.4 414.4	0.36 0.70					
peak 2	803.3 837.6	0.84 0.08					
SUM		1.98					

Table 12 H_2-TPR results: experimental hydrogen uptake compared with the expected and fitting (italics) results. The calculation for the expected amounts is reported on the right-hand side of the table.

The expected hydrogen consumption is determined considering the reduction of Mn(IV) to Mn(II) and of Co(III) to Co(0), and the relative quantities of such cations are obtained by stoichiometry (Mn^{4+} is present due to K substituting La) and it is equal to 2.80 mol/g (see right-hand side of Table *12*). This value is compared to experimental hydrogen consumption, reported as number of moles consumed. From a first comparison between hydrogen consumed and expected (being this last value constant for both samples), FSP sample shows an almost perfect agreement (the difference is approx. 5%), whereas COP sample consumes only 75% of the hydrogen theoretically needed to reduce it completely (1.98 mmol vs 2.80). This incomplete reduction together with the shift of the reductive reactions to higher temperatures suggests that COP is less reducible than FSP. The shape of the peaks, as well as their position, change with the preparation method and their broadness indicates the presence of multiple species not equivalent in terms of reducibility [73]. The different thermal stories of the samples have led to a different morphology of the samples, and therefore a different behavior when reduction is performed. Indeed FSP approach usually does not imply a following thermal treatment, which is instead very common in COP preparation. COP decreased reducibility might thus be the result not only of a different composition (different amount of K into the perovskite cell, different surface composition), but also of sintering phenomena occurred during calcination.

Table *12* includes both the information about the peak (temperature, hydrogen consumption and comparison between experimental and theoretical values) and the results of a fitting procedure performed on the peaks obtained (as reported in the Figure 28). The relative areas reported below show that the first peak, compatible with Mn(IV), Mn(III) and Co(III) reduction, is actually made up by two distinct components, not directly assigned to any of such species because of the non-correspondence between stoichiometric coefficients and the relative areas. For this reason, we can conclude that the same species is actually present in different chemical environment and so suffers from differs thermal behaviors in a reductive atmosphere. However, since the area of the first peak is

quite large, and not compatible with the small actual content of Mn (IV), Mn (III) is thought to reduce at a lower temperature than expected, because Mn (IV) activates Mn (III) reduction. Moreover, since the first peak is attributed to easily reducible species, the larger area is observed for FSP sample, therefore richer in Mn(IV). Also some active oxygen species can contribute to a small amount of the first reduction processes observed at low temperature (approximately 200°C and below), as reported in literature [91]. Such species are more abundant in FSP sample, as confirmed by XP spectra of O1s region.

Representative SEM images are reported in Figure 29. The pictures show the formation of macro-aggregates with a diameter of several microns, covered with small particles which are homogeneous in size (few nanometers) and distribution in both samples. A significant difference is the tendency of LKMC FSP sample to form aggregates of considerable size, whereas LKMC COP sample tends to form both big and small aggregates. In particular, small aggregates appear as a surface decoration on more compact, bigger particles. This can be due to the different thermal treatment which the samples have undergone in the preparation (*i.e.* higher temperatures for LKMC FSP sample).

LKMC experimental ICP composition is in good agreement with the nominal one in both cases. Among dopants, Co is also more efficiently included in the structure as compared to K (see Table 13).

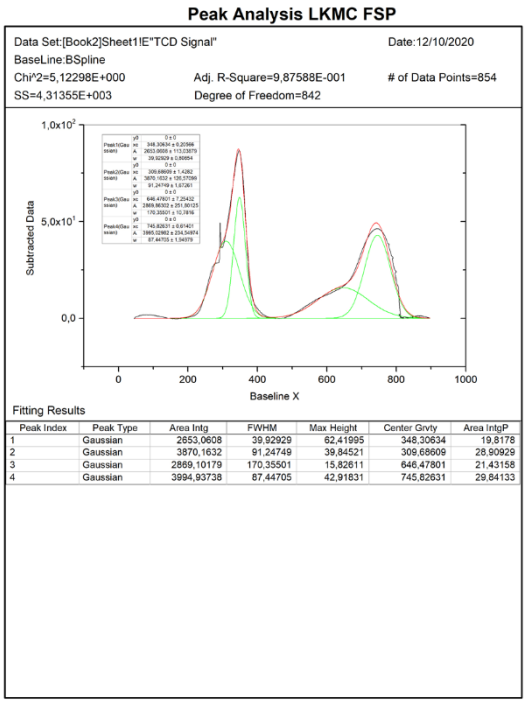

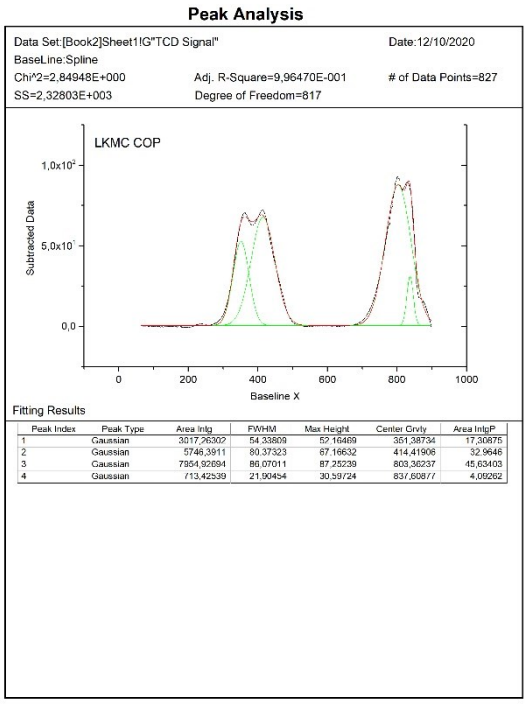

Figure 28 H_2-TPR fitting results for LKMC FSP and COP.

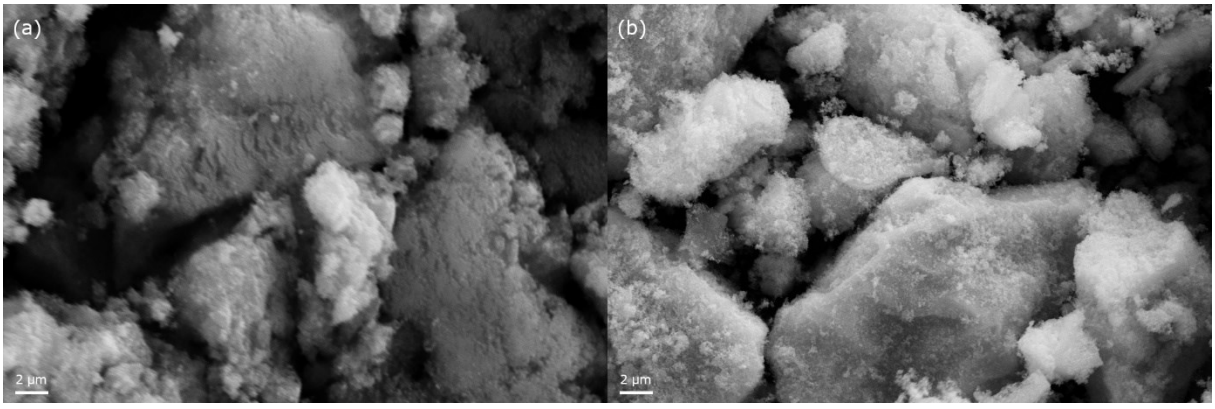

Figure 29 SEM images of LKMC FSP (a) and LKMC COP (b).

		ICP results (%)	
	Nominal	LKMC FSP	LKMC COP
La	67.91	70.40	69.35
K	2.12	1.64	1.28
Mn	26.76	23.73	26.57
Co	3.21	4.23	2.79

Table 13 ICP composition of the LKMC samples compared to the nominal composition (only metals).

2.4.5 Catalytic results: CO-NO mixture

The catalytic test suggests that the FSP sample gives better results in CO assisted NO reduction (Figure 30) due to the inclusion of K in the structure, which leads to Co, instead of Mn, surface segregation. Catalytic activity starts being noticeable after 300°C if we consider NO conversion. However when observing CO oxidation, a plateau of activity is seen in the same low temperature region (below 300°C), with no significant NO reduction. This behavior suggests the involvement of surface oxygen species in CO oxidation, with no intervention from NO as oxidant (suprafacial oxidation mechanism). As long as NO is not used as oxidant (no appreciable conversion is detected) such mechanism is believed to take place when CO is actually converted to CO_2. When also NO conversion is detected, suprafacial oxidation mechanism decreases in favor of the mechanism commonly known as CO-assisted NO reduction.

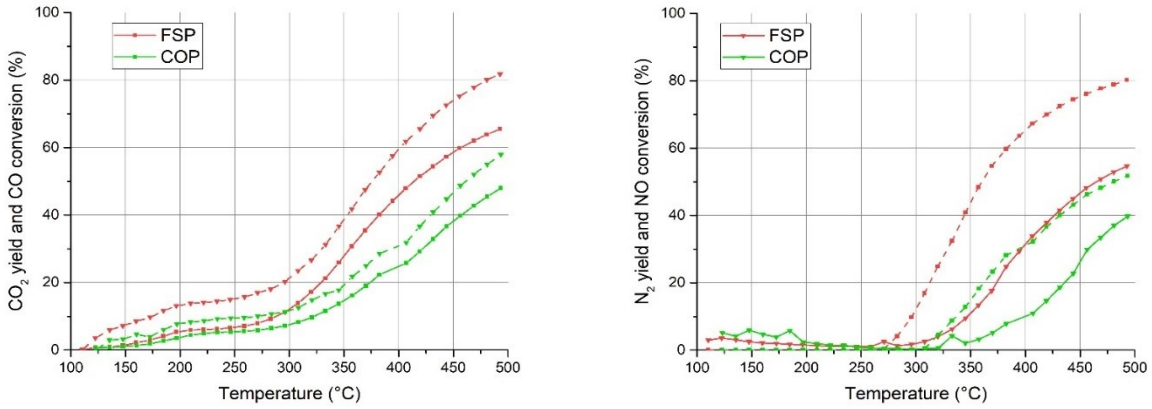

Figure 30 CO-NO mixture reactivity. CO_2 and N_2 yields are in solid lines and CO and NO conversion in dashed lines.

2.4.6 Catalytic results: complex TWC mixture

Also in the stoichiometric complex mixture the two catalysts show different activity but the LKMC sample synthesized by COP has a high activity compared to the one synthesized in FSP. (see Figure 31 and Figure 32, O_2 consumption is reported separately in Figure 33). [92]

COP sample surface, in contrast to FSP sample one, is richer in Mn (IV) (according to XPS – Table *11*, surface composition), a well working oxidant, which, indeed, allows to achieve good performances in a complex mixture. Propene is being converted at 270°C for sample LKMC COP, whereas the other sample converts it above 350°C. A positive effect of temperature on reaction rate is evident for propane oxidation between 300-450°C, resulting in an enhancement of approximately 30% in conversion for LKMC FSP. Interestingly, in stoichiometric conditions, LKMC synthetized via FSP and COP shows a comparable temperature effect on the methane oxidation reaction rate.

As regards NO, the presence of O_2 in stoichiometric amount prevents any significant NO reduction: it is occurring between 350°C and 500°C, reaching a maximum conversion of 9% for FSP sample and 2.5% for COP. This is consistent with the mechanism proposed for perovskite that considers the interaction between NO and the oxygen vacancies present on the perovskite surface as the rate determining step for NO reduction. [6]

The profile of O_2 consumption indicates the minimum temperature at which the catalyst is active, that is approximately 200°C for both samples in stoichiometric conditions. Above 400 °C, as regards COP sample, oxidation of the HCs, H_2 and CO is overall higher than that synthesized via flame spray and the available O_2 is totally consumed, not supplemented by NO reduction, activated in negligible way.

Concerning rich mixture testing conditions, in the range between 200 °C and 300 °C the activated reactions are the oxidation of CO, H_2 and C_3H_6. LKMC COP sample looks much more active than its FSP obtained counterpart. In particular, a lower ignition temperature for C3 is observed for COP sample. This sample is able to light off for C3 reagents at approximately 250°C, whereas FSP sample

exhibits ignition temperatures of 350°C for C_3H_6 and 394°C for C_3H_8. In COP activity profiles, propylene is totally converted at 491°C, whereas FSP reaches maximum conversion at 545°C. At 417°C, propane conversion is 78% for COP sample, and only 17% for FSP. The conversion of propene is well below the values achieved in the stoichiometric case, explained by the total consumption of O_2 that limits the oxidation of the hydrocarbons surviving that temperature.

Above 400°C in the COP catalysts all the available oxygen is exhausted, conversely, LKMC FSP sample achieves the complete conversion of oxygen at 500°C.

When the total consumption of oxygen is achieved, NO is reduced and it reaches complete conversion at 600°C for LKMC COP, while LKMC FSP remains rather limited compared to the other catalysts (conversion of approximately 43%).

As regards rich conditions, evaluating O_2 consumption is a useful way to sum up the activity of each sample and define which reactions are taking place. For LKMC COP sample, at temperatures below 250°C the prevalent reaction is CO oxidation. Raising the reaction temperature other oxidations are involved, such as H_2, C_3H_6 and C_3H_8. Over 400°C all the oxygen available is depleted and the catalyst is exposed to a gaseous mixture containing oxidation products and unconverted CO, H_2 and hydrocarbons, together with a high amount of steam (10%) and CO_2 (15%). Therefore, at this temperature (400°C), NO reduction begins and is completely accomplished at 600°C. For LKMC FSP sample, oxygen conversion starts at 200°C with CO oxidation. At temperatures higher than 300°C H_2 and C_3H_6 are also reduced.

Summing up the behavior of the samples, since the mixture has run out of oxygen over 400°C, the oxidation occurs exploiting oxygen deriving from NO, which acts as an oxidant while getting reduced. This rationalization also explains the two-step oxidation of hydrogen, probably due to this shift in the oxidant used. Methane does not get oxidized in rich conditions by any samples, which are therefore inactive to such a reagent in slightly reducing environment (defect of oxygen according to reaction stoichiometry).

Specific surface area has been measured for each sample, but it does not actually affect the performance as expected: COP sample suffers from aggregation and sintering due to thermal treatment resulting in low surface areas, whereas FSP sample area is roughly twice as much. This

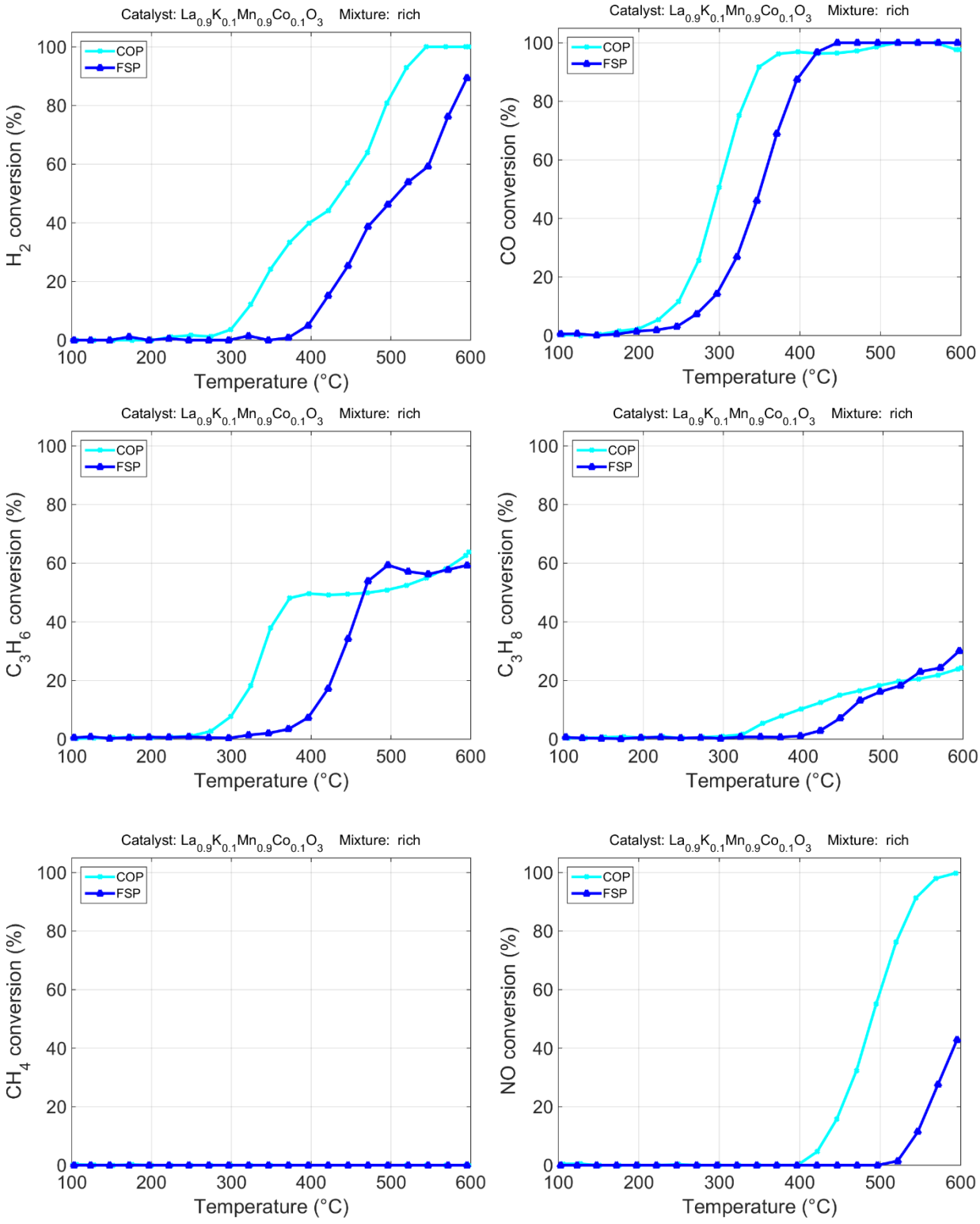

Figure 31 Rich mixture catalytic tests for LKMC FSP and COP.

means that catalytic performance trend mainly depends on chemical and structural features of both material surface and bulk.

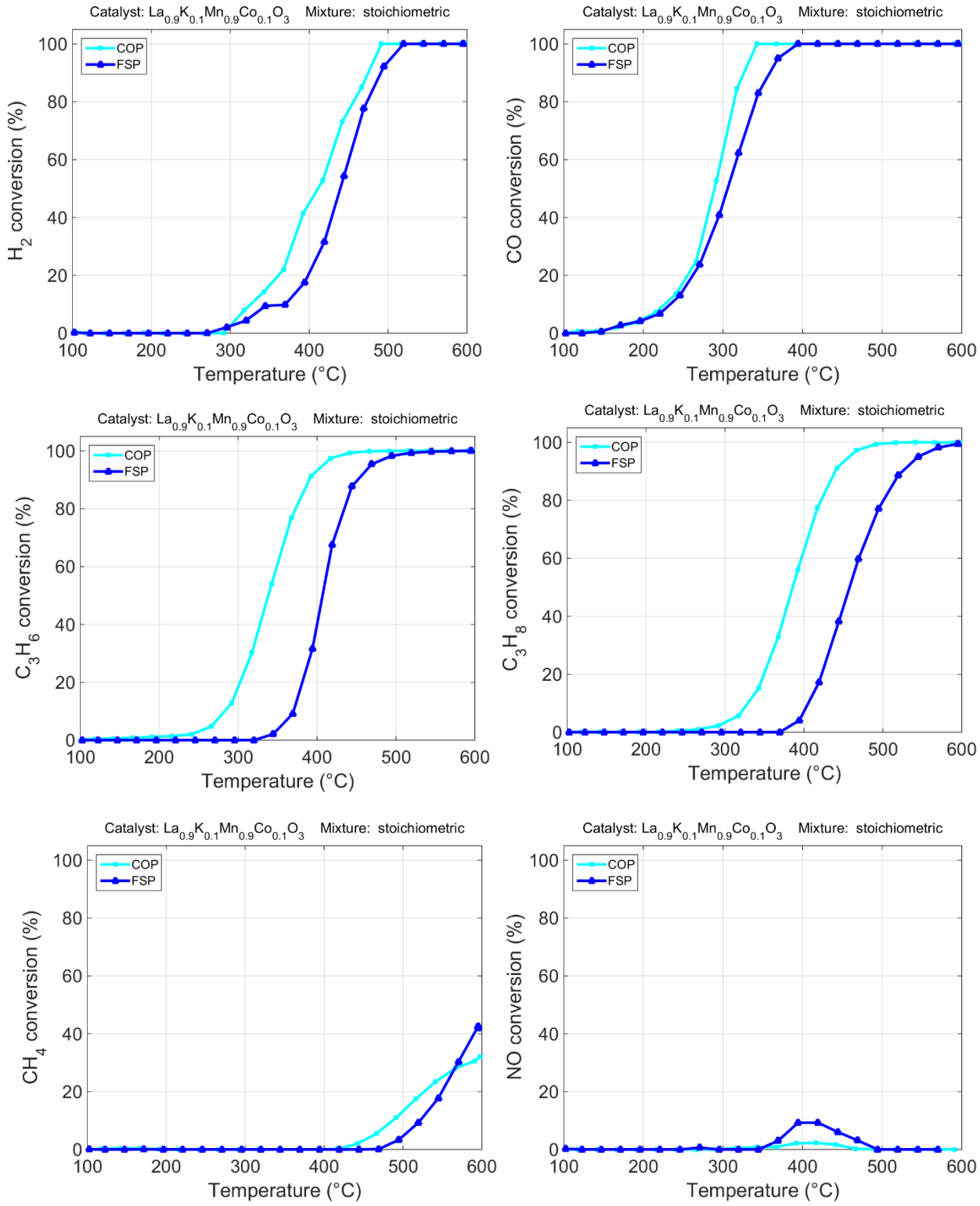

Figure 32 Stoichiometric mixture catalytic tests for LKMC FSP and COP.

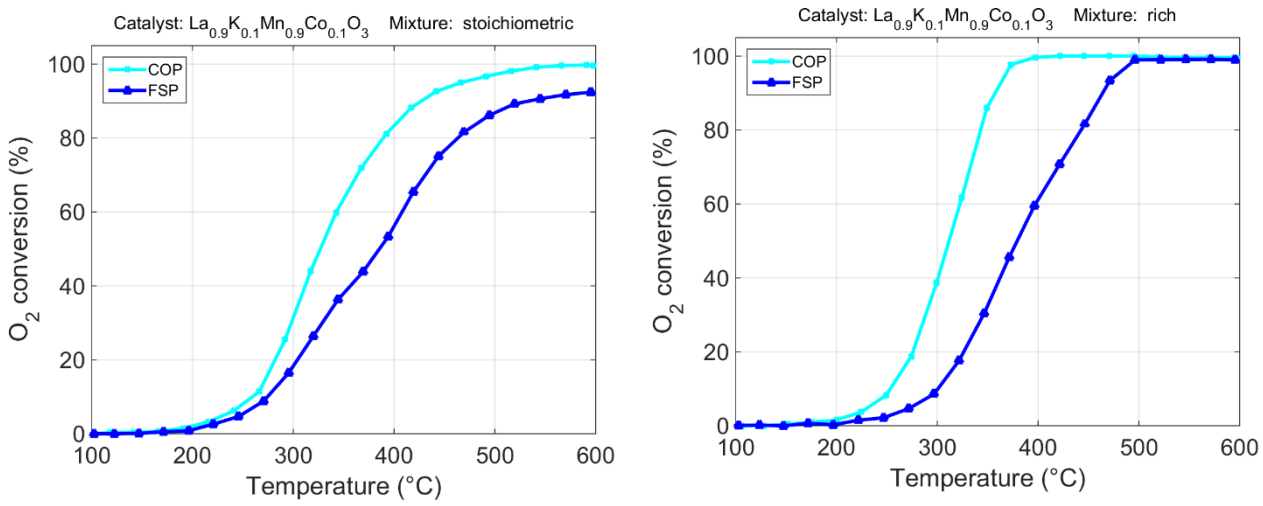

Figure 33 Stoichiometric (a) and rich (b) mixture catalytic tests for LKMC FSP and COP.

2.5 Functional chemisorption tests

A selection of the Fe-based samples, and namely LFC FSP, LCFC E FSP and LCF COP, underwent also some functional behavior tests in order to determine their chemisorption activities towards oxygen, an important feature in Mars-Van Krevelen mechanism-mediated oxidations. These samples were selected to perform both a H_2-TPR and an O_2-TPD (Temperature Programmed Desorption) characterization with the specific conditions encountered in complex mixture catalytic test, i.e. an oxidizing pretreatment carried out in air (O_2 20%) at 600°C for 2 hours. In the following section the results will be reported.

In LCFC FSP (reported in Figure 34) the overall trend is a decreased reducibility after the oxidizing treatment, even if counterintuitive, we might justify this as the result of the sintering of the particles. In particular, for the sample that underwent the pretreatment, the area under the curve in this region 600-900°C is more extended when compared to the area under the peak in the same region for the sample without pretreatment. Since no peak in the region 400-600°C is evident, it is reasonable to suppose that the two peaks for the blue curve (Fe(IV) and Fe(III) reduction) are merged into one single peak for the pretreated sample with a maximum at 786°C (red curve).

Firstly reduction results are presented. In LCFC FSP E (see Figure 35), instead, the reducibility increases: a shift towards lower reduction temperature is seen in the reduction profile. Moreover in the first highlighted region, which corresponds to Cu(II)-Cu(0) reduction and ranges between 100 and 300°C, we can observe that after the oxidizing treatment of Cu reduction peak is double-spiked, accounting for a double-step reduction of Cu(II) to Cu(I) and then Cu(I) to Cu(0). Similarly to the as-prepared sample (red curve), Fe reduction is barely visible, not giving clear indication about the reduction temperature of the process. For this reason we can assume that iron reducibility has not been actually altered by the oxidizing treatment.

As seen in the homologous FSP-obtained sample, LCFC COP experiences an increased reducibility after the oxidizing treatment, even if not so remarked as in the first case. Another substantial difference observed after the pretreatment is the disappearing of the double spike in the Cu reduction, which means that probably the reduction from Cu(I) to Cu(0) is the one more subjected to the shift to lower reduction temperature. The main peak is indeed shifting only from 217 to 196°C, whereas the double peak is shifting from a much higher temperature, namely 258°C. The Fe reduction does not show as many changes: the Fe(IV) peak appears slightly broader after the pretreatment, with a similar shift downwards in temperature (from 481 to 462°C) and lastly Fe (III) is reduced at very high temperature, with a broad peak that is probably extending over the investigated temperature range (up to 900°C, conventionally).

From the comparison of the trend of the two samples and the analysis of the complex mixture catalytic results, the first impression is that for LFC FSP sample, Fe is the species that is being altered the most by the oxidizing treatment, as Cu only shifts its position but remains quantitatively unchanged. As a matter of fact, after each reducing treatment metallic Cu was visible on the walls of the reactor, showing a complete reduction of the metal. LFC FSP sample show a great difference in H_2-TPR if subjected to the pretreatment. When looking at the catalytic test results in a complex mixture, LFC FSP appears to be the more active compound, unlike its performances in the simple mixture tests.

This behavioral difference (from simple to complex gas mixture) might be explained by the change in Fe coordination environment that is experienced after the pretreatment, the same that was carried out before the complex mixture catalytic assessment. Indeed LCFC FSP does not seem to be deeply affected by the oxidizing treatment, showing only changes in the Cu region (room temperature up to 300°C). The same reasoning applies to LCFC COP, which exhibits no significant change in Fe reduction region, but only a shift for Cu reduction.

Oxygen desorption was investigated as well after the oxidizing pretreatment. The samples were heated at 900°C in 100% O_2 to saturate all the adsorption sites of the material and kept at the constant temperature of 900°C for 2 hours, then they were cooled down to room temperature (again in an O_2 100% flow) with a descending ramp of 90°C/min. Finally the oxygen flow was interrupted and a TCD signal was recorded. The investigated temperature range goes from room temperature to 900°C, with a ramp of 10°C/min.

O_2-TPD tests have been performed to understand the different behavior of the samples in the case of an oxidizing pretreatment (such as the treatment before the complex mixture test). The pretreatment in this case was different as respect to the one performed for H_2-TPR in the previous section, because a complete oxidation allowed the investigation of all adsorption sites on the surface and not only a fraction of them. The obtained profiles are in Figure 37, Figure 38 and Figure 39, respectively for LFC FSP, LCFC FSP E and LCFC COP. They show a single peak at very high temperature, much higher than those reached during the catalytic activity tests. It is worth reminding that, as demonstrated by XRD analysis, LCFC FSP sample was effectively Ca doped. The behavior shown in Figure 38 is indicative of an initial release of surface oxygen species, followed by the temperature activated release of structure oxygen. Noteworthy, LFC FSP sample behaves differently (see Figure 37): Ca did not enter the lattice, and the release of oxygen is continuous from the beginning of the Temperature Programmed Reduction. When a particular temperature is reached (774°C), oxygen from a particular lattice position is released, as shown by the peak in Figure 37. Another

demonstration of the incomplete inclusion of Ca in LCFC COP sample lattice is its O_2-TPD reported in Figure 39: the trend is indeed identical to that of LFC FSP sample, Ca-free by design. Also the temperature for oxygen release is quite similar to the one of LFC sample.

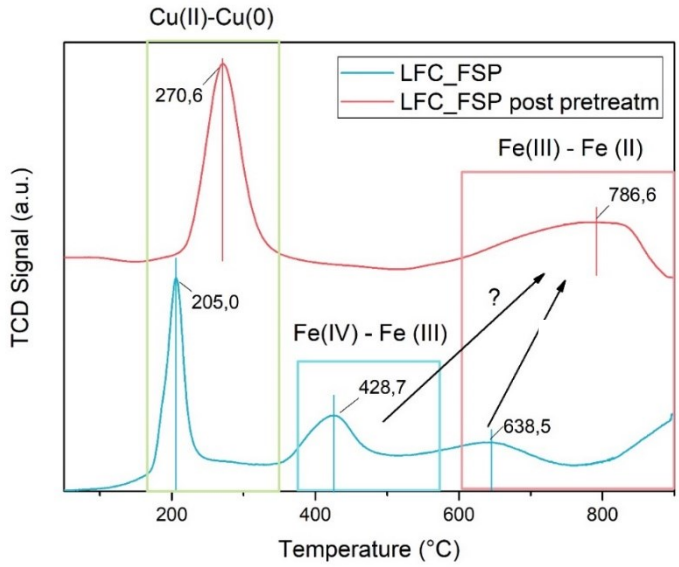

Figure 34 H_2-TPR profile of LFC FSP, without (blue) and with (red) oxidizing pretreatment in O_2 20% at 600°C for 2 hours.

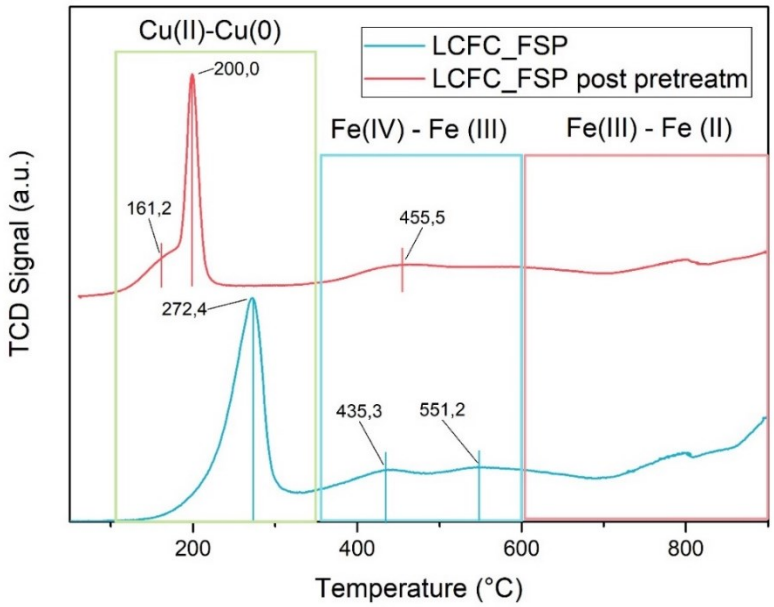

Figure 35 H_2-TPR profiles of LCFC FSP E, without (blue) and with (red) oxidizing pretreatment in O_2 20% at 600°C for 2 hours.

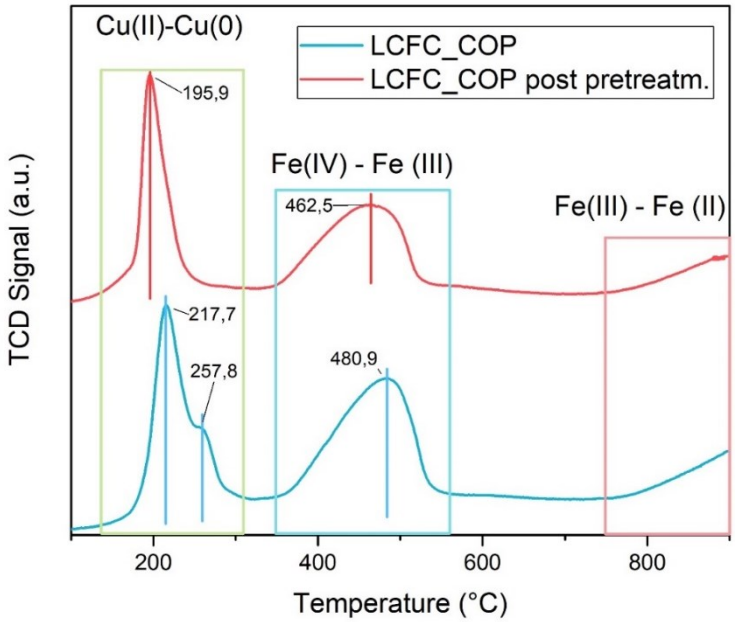

Figure 36 H_2-TPR profiles of LCFC COP, without (blue) and with (red) oxidizing pretreatment in O2 20% at 600°C for 2 hours.

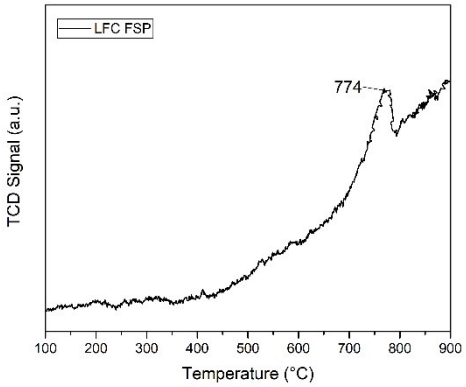

Figure 37 O_2-TPD profile for LFC FSP sample.

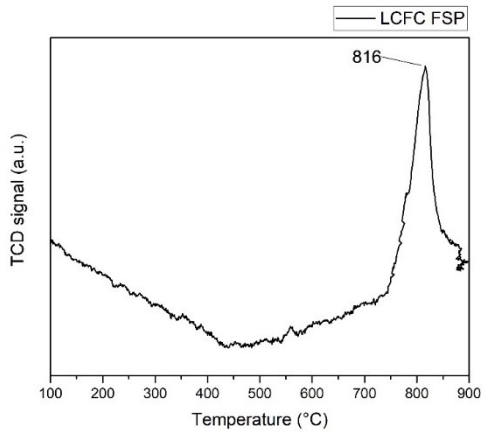

Figure 38 O_2-TPD profile for LCFC FSP E sample.

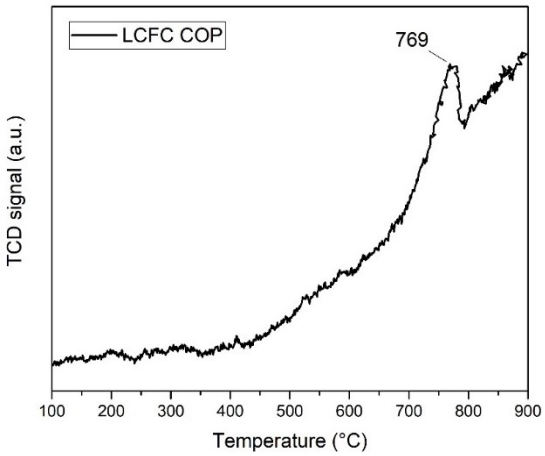

Figure 39 O_2-TPD profile for LCFC COP sample.

2.6 Conclusions

The problem of industrial production of perovskite-based complex catalysts was here dealt focusing on the effect of preparation procedure and of reproducibility. $La_{0.8}Ca_{0.2}Fe_{0.8}Cu_{0.2}O_3$ (LCFC), a Ca,Cu-doped Fe-based perovskite, is industrially synthesized by means of two different methods: co-precipitation (COP) and Flame Spray Pyrolysis (FSP). FSP powders obtained at successive moments have been compared, as well as a Ca-free catalyst ($LaFe_{0.8}Cu_{0.2}O_3$, LFC).

XRD patterns suggest that the Ca-insertion depends on the synthesis procedure (being more efficient in FSP) and, focusing on FSP, on the specific production moment. XPS and EDX underline a different surface composition and different segregation phenomena for COP and FSP catalysts. In COP catalyst, in fact, the amount of surface oxygen is lower but the B-cations, particularly Cu, are more abundant. Morphological differences are highlighted by SEM, in the COP sample is more compact.

Consistently with the different chemical, structural, and morphological characteristics, the catalysts exhibit different activity and selectivity. For these reasons, the composition of bulk and surface are quite significant for the catalytic performance; this holds, in particular, for the concentration of active oxygen species, able to undergo Mars-van Krevelen oxidation mechanism, and B cation distribution along the material depth. Interestingly, doping of the A-site deeply alters the mobility of ions throughout the structure, resulting in different, and in some cases, worse catalytic activity. Moreover, the effect of surface area is not directly related to the catalytic activity under these conditions, since the most active samples are the ones with the lowest surface area values, evidencing the paramount role of surface/bulk composition and reducibility. In particular, the surface composition seems to play a more significant role at lower temperatures whereas at higher temperature the reducibility is more relevant. Therefore, it is important to test not only simple gas mixes (e.g. CO+NO), but also more complex mixtures under relevant conditions (e.g. stoich. or rich), especially for industrial applications.

This comparison allowed to better clarify the role of calcium doping in catalytic activity, which is depending on the reactants mixture and the reaction conditions. As a general trend, coprecipitation technique results in a less efficient inclusion of Ca in the perovskite lattice and seems less suitable for the industrial approach. The insertion of Ca into the perovskite crystalline cell enhance the formation of Fe(IV) active sites for molecules oxidation. The presence of Ca inside the lattice, however, also affects the perovskite lattice stabilizing copper with respect to the segregation of Cu(II) as copper oxide. In general, this decreases the reducibility of the catalyst. Oxygen vacancies are observed to prevail with amount of doping Ca higher than the ones characterizing the samples presented in this contribution. Because of this reason it is probable that they can contribute to the activation of HCs only at higher temperature when oxygen is not anymore present in the reaction mixture being consumed in the oxidation of non-HCs species.

In the second part we have compared the chemical, structural, morphological properties of $La_{0.9}K_{0.1}Mn_{0.9}Co_{0.1}O_3$ catalyst powders which were industrially obtained with two different processes: Flame Spray Pyrolysis (FSP) and Co-Precipitation (COP). Roughly speaking the catalysts seem very similar for composition and structure. A detailed comparison, however, reveals that the degree of K insertion inside the perovskite cell is process-dependent and the effects are expected on cell deformation, ion mobility, surface composition. La and Mn segregate in the surface in the COP catalysts while Co is surface-accumulated in the FSP catalyst. The different surface composition affects the reactivity; BET specific surface area differences, moreover, cannot be claimed as the reason for the different activity.

In the CO-assisted NO reduction, LKMC FSP is performing better than LKMC COP whereas in the complex mixture the opposite is observed. The higher activity of FSP is related to the presence of oxygen active species on the perovskite surface and to a suprafacial oxidation mechanism. In the complex mixture, in contrast, the surface composition and the Mn-segregation seems to play a major role. Consistently, the results of the catalytic testing reveal that activity is quite different among the

two catalysts, with a lower ignition temperature for CO, N_2 and propene oxidation by COP-obtained sample.

As regards NO reduction, the presence of O_2 in stoichiometric amount prevents any significant NO reduction. The profile of O_2 consumption indicates the minimum temperature at which the catalyst is active, that is approximately 200°C for both samples in stoichiometric conditions.

Concerning rich mixture testing conditions, the most relevant result is the NO reduction that is measured in the presence of depleted O_2, considered the actual obstacle for NO: when the total consumption of oxygen is achieved, NO is reduced and it reaches complete conversion at 600°C for LKMC COP.

A final remark on economic considerations must be given. In general, production cost estimates in FSP manufacture are difficult due to the variability of the raw material prices and geographically varying labor costs, being the uncertainties in raw material price estimates the main influent factor on the total production costs, which can be estimated below 100 EUR/kg , according to previous works in literature.[93] Possible optimization margins therefore imply raw material supply costs, as well as low-cost precursor solutions with higher metal-to-carbon rations, a better utilization of the heat generated during combustion and strategies for more efficient flame quenching.[93] Considering one of the main costs of commercial catalyst is noble metals, perovskites provide a cheap alternative in terms of materials cost and production.

The catalysts in this paper have been tested in their fresh state, but commercially viable catalysts must survive harsh hydrothermal ageing conditions at high temperature (>950°C). Therefore, we consider that the next step is to optimize these materials to survive these ageing conditions utilizing the characterization methods described in this paper to better understand the ageing process.

As a general conclusion, valid both for Fe- and Mn-based perovskites, COP approach seems less effective in delivering an efficient dopant inclusion, probably due to the difficulty in regulating finely the pH in a complex system of many different metallic cations in solution. This leads to important

consequences in the composition distribution and therefore in the catalytic activity and selectivity. However the extent of structural modifications due to the preparation approach greatly varies between different compositions.

Addendum: Comparison based on Turn-Over Rate

With the purpose of accounting for the dramatic differences in specific surface among the same materials produce by different synthetic routes, we tried to reformulate the comparison in terms of turn-over rate (TOR), defined as the number of reagent molecules consumed per single site, in the unit time. Unfortunately, that require knowledge of the surface site availability for several species in the complex mixture, without a precise knowledge of the reaction mechanism. In addition, TOR is expected to vary along the catalyst bed. Given these uncertainties, we recast Figure 18 and Figure 19 in terms of TOR for each species, averaged over the entire catalyst bed, calculated as

$$TOR = \frac{-\Delta \dot{N}_i}{(\Gamma/\mathrm{NR})\, SSA\, m_{cat}}$$

Where $\dot{N}_i$ is the molar flow rate (moles/s) of each reactant i=1..NR=H_2, O_2, CO, CH_4, C_3H_6, C_3H_8, NO, $\Delta \dot{N}_i$ is the difference between outlet and inlet, Γ/NR the surface site density (moles/m^2) and SSA the specific surface areas (m^2/gcat). The sites are assumed to be shared among the NR reactants (including O_2); their surface density estimated as 1.5 10^{-5} moles/m^2. While the above assumptions on the available sites (surface density and occupancy) can be arbitrary, the estimated TOR introduces the active surface of the materials in their comparison.

The ranking among the 3 LCFC based materials is much sharper, because of the differences in the SSA. For all the reactants, the ranking is unambiguously LCFC-COP>LFC-FSP>LCFC-FSP for both stoichiometric and rich mixtures, simply because of the reverse order in the specific surface areas, i.e. LCFC-FSP>LFC-FSP > LCFC-COP. TOR plots also allow to reveal that the activity of each site follows the order CO≈O_2 > H_2 >> HCs in stoichiometric mixtures, and CO > O_2 > H_2 > NO > C_3H_6 in the rich one.

Notwithstanding the approximation, the order of TOR calculated, between 10^{-1} and 10^{1} molecules/(site s) is perfectly in line with the indications of Somorjai[94] for this interval of temperature.

References

(1) Brusamarello, E.; Blonda, C.; Salazar-Castro, C.; Canu, P.; Glisenti, A. Industrially Produced Fe- and Mn-Based Perovskites: Effect of Synthesis on Reactivity in Three-Way Catalysis: Part 2. *ACS Omega* **2021**, acsomega.1c02132. https://doi.org/10.1021/ACSOMEGA.1C02132.

(2) Brusamarello, E.; Blonda, C.; Salazar-Castro, C.; Pascui, A. E.; Canu, P.; Glisenti, A. Industrially Produced Fe- and Mn-Based Perovskites: Effect of Synthesis on Reactivity in Three-Way Catalysis: Part 1. *ACS Omega* **2021**, acsomega.1c02133. https://doi.org/10.1021/ACSOMEGA.1C02133.

(3) Libby, W. F. Promising Catalyst for Auto Exhaust. *Science (80-.).* **1971**, *171* (3970), 499–500. https://doi.org/10.1126/science.171.3970.499.

(4) Royer, S.; Duprez, D.; Can, F.; Courtois, X.; Batiot-Dupeyrat, C.; Laassiri, S.; Alamdari, H. Perovskites as Substitutes of Noble Metals for Heterogeneous Catalysis: Dream or Reality. *Chem. Rev.* **2014**, *114* (20), 10292–10368. https://doi.org/10.1021/cr500032a.

(5) Sorenson, S. C.; Wronkiewicz, J. A.; Sis, L. B.; Wirtz, G. P. Properties of LaCoO3 as a Catalyst in Engine Exhaust Gases. *Ceram. Bull.* **1974**, *53* (5), 446–449.

(6) Glisenti, A.; Pacella, M.; Guiotto, M.; Natile, M. M.; Canu, P. Largely Cu-Doped LaCo1-XCuxO3 Perovskites for TWC: Toward New PGM-Free Catalysts. *Appl. Catal. B Environ.* **2016**, *180*, 94–105. https://doi.org/10.1016/j.apcatb.2015.06.017.

(7) Koirala, R.; Pratsinis, S. E.; Baiker, A. Synthesis of Catalytic Materials in Flames: Opportunities and Challenges. *Chem. Soc. Rev.* **2016**, *45* (11), 3053–3068. https://doi.org/10.1039/c5cs00011d.

(8) Peña, M. A.; Fierro, J. L. G. Chemical Structures and Performance of Perovskite Oxides. *Chemical Reviews*. American Chemical Society July 2001, pp 1981–2017. https://doi.org/10.1021/cr980129f.

(9) Schwarz, J. A.; Contescu, C.; Contescu, A. Methods for Preparation of Catalytic Materials. *Chem. Rev.* **1995**, *95* (3), 477–510. https://doi.org/10.1021/cr00035a002.

(10) Szabo, V.; Bassir, M.; Van Neste, A.; Kaliaguine, S. Perovskite-Type Oxides Synthesized by Reactive Grinding Part II: Catalytic Properties of LaCo(1-x)FexO3 in VOC Oxidation. *Appl. Catal. B Environ.* **2002**, *37* (2), 175–180. https://doi.org/10.1016/S0926-3373(01)00328-9.

(11) Li, Z.; Lv, L.; Ao, X.; Li, J. G.; Sun, H.; An, P.; Xue, X.; Li, Y.; Liu, M.; Wang, C.; Liu, M. An Effective Method for Enhancing Oxygen Evolution Kinetics of LaMO3 (M = Ni, Co, Mn) Perovskite Catalysts and Its Application to a Rechargeable Zinc–Air Battery. *Appl. Catal. B Environ.* **2020**, *262*, 118291. https://doi.org/10.1016/j.apcatb.2019.118291.

(12) Levasseur, B.; Kaliaguine, S. Effects of Iron and Cerium in La1-YCeyCo1-XFexO3 Perovskites as Catalysts for VOC Oxidation. *Appl. Catal. B Environ.* **2009**, *88* (3–4), 305–314. https://doi.org/10.1016/j.apcatb.2008.11.007.

(13) Fang, F.; Feng, N.; Wang, L.; Meng, J.; Liu, G.; Zhao, P.; Gao, P.; Ding, J.; Wan, H.; Guan, G. Fabrication of Perovskite-Type Macro/Mesoporous La1-XKxFeO3-Δ Nanotubes as an Efficient Catalyst for Soot Combustion. *Appl. Catal. B Environ.* **2018**, *236*, 184–194. https://doi.org/10.1016/j.apcatb.2018.05.030.

(14) Giannakas, A. .; Ladavos, A. .; Pomonis, P. . Preparation, Characterization and Investigation of Catalytic Activity for NO+CO Reaction of LaMnO3 and LaFeO3 Perovskites Prepared via Microemulsion Method. *Appl. Catal. B Environ.* **2004**, *49* (3), 147–158. https://doi.org/10.1016/j.apcatb.2003.12.002.

(15) Safakas, A.; Bampos, G.; Bebelis, S. Oxygen Reduction Reaction on La0.8Sr0.2CoxFe1-XO3-Δ Perovskite/Carbon Black Electrocatalysts in Alkaline Medium. *Appl. Catal. B Environ.* **2019**, *244*, 225–232. https://doi.org/10.1016/j.apcatb.2018.11.015.

(16) Brewster, J. H.; Kodas, T. T. Generation of Unagglomerated, Dense, BaTiO3 Particles by Flame-Spray Pyrolysis. *AIChE J.* **1997**, *43* (S11), 2665–2669. https://doi.org/10.1002/aic.690431310.

(17) Leanza, R.; Rossetti, I.; Fabbrini, L.; Oliva, C.; Forni, L. Perovskite Catalysts for the Catalytic Flameless Combustion of Methane. Preparation by Flame-Hydrolysis and Characterisation by TPD-TPR-MS and EPR. *Appl. Catal. B Environ.* **2000**, *28* (1), 55–64. https://doi.org/10.1016/S0926-3373(00)00163-6.

(18) Petrović, S.; Terlecki-Baričević, A.; Karanović, L.; Kirilov-Stefanov, P.; Zdujić, M.; Dondur, V.; Paneva, D.; Mitov, I.; Rakić, V. LaMO3 (M = Mg, Ti, Fe) Perovskite Type Oxides: Preparation, Characterization and Catalytic Properties in Methane Deep Oxidation. *Appl. Catal. B Environ.* **2008**, *79* (2), 186–198. https://doi.org/10.1016/j.apcatb.2007.10.022.

(19) Faye, J.; Baylet, A.; Trentesaux, M.; Royer, S.; Dumeignil, F.; Duprez, D.; Valange, S.; Tatibouët, J. M. Influence of Lanthanum Stoichiometry in La 1-XFeO 3-δ Perovskites on Their Structure and Catalytic Performance in CH 4 Total Oxidation. *Appl. Catal. B Environ.* **2012**, *126*, 134–143. https://doi.org/10.1016/j.apcatb.2012.07.001.

(20) Wang, H.; Dong, X.; Zhao, T.; Yu, H.; Li, M. Dry Reforming of Methane over Bimetallic Ni-Co Catalyst Prepared from La(CoxNi1-x)0.5Fe0.5O3 Perovskite Precursor: Catalytic Activity and Coking Resistance. *Appl. Catal. B Environ.* **2019**, *245*, 302–313. https://doi.org/10.1016/j.apcatb.2018.12.072.

(21) Garcia-Muñoz, P.; Lefevre, C.; Robert, D.; Keller, N. Ti-Substituted LaFeO3 Perovskite as Photoassisted CWPO Catalyst for Water Treatment. *Appl. Catal. B Environ.* **2019**, *248*, 120–128. https://doi.org/10.1016/j.apcatb.2019.02.030.

(22) Pang, S.; Xu, J.; Su, Y.; Yang, G.; Zhu, M.; Cui, M.; Shen, X.; Chen, C. The Role of A-Site Cation Size Mismatch in Tune the Catalytic Activity and Durability of Double Perovskite Oxides. *Appl. Catal. B Environ.* **2020**, *270*, 118868. https://doi.org/10.1016/j.apcatb.2020.118868.

(23) Tian, C.; Zhang, H.; Zhu, X.; Lin, B.; Liu, X.; Chen, H.; Zhang, Y.; Mullins, D. R.; Abney, C. W.; Shakouri, M.; Chernikov, R.; Hu, Y.; Polo-Garzon, F.; Wu, Z.; Fung, V.; Jiang, D. en; Liu, X.; Chi, M.; Liu Jimmy, J.; Dai, S. A New Trick for an Old Support: Stabilizing Gold Single Atoms

on LaFeO3 Perovskite. *Appl. Catal. B Environ.* **2020**, *261*, 118178. https://doi.org/10.1016/j.apcatb.2019.118178.

(24) Taran, O. P.; Ayusheev, A. B.; Ogorodnikova, O. L.; Prosvirin, I. P.; Isupova, L. A.; Parmon, V. N. Perovskite-like Catalysts LaBO3 (B=Cu, Fe, Mn, Co, Ni) for Wet Peroxide Oxidation of Phenol. *Appl. Catal. B Environ.* **2016**, *180*, 86–93. https://doi.org/10.1016/j.apcatb.2015.05.055.

(25) Grabowska, E. Selected Perovskite Oxides: Characterization, Preparation and Photocatalytic Properties-A Review. *Applied Catalysis B: Environmental*. 2016, pp 97–126. https://doi.org/10.1016/j.apcatb.2015.12.035.

(26) Li, P.; Zhang, R.; Liu, N.; Royer, S. Efficiency of Cu and Pd Substitution in Fe-Based Perovskites to Promote N2 Formation during NH3 Selective Catalytic Oxidation (NH3-SCO). *Appl. Catal. B Environ.* **2017**, *203*, 174–188. https://doi.org/10.1016/j.apcatb.2016.10.021.

(27) Zhang, Q.; Huang, Y.; Peng, S.; Zhang, Y.; Shen, Z.; Cao, J. ji; Ho, W.; Lee, S. C.; Pui, D. Y. H. Perovskite LaFeO3-SrTiO3 Composite for Synergistically Enhanced NO Removal under Visible Light Excitation. *Appl. Catal. B Environ.* **2017**, *204*, 346–357. https://doi.org/10.1016/j.apcatb.2016.11.052.

(28) Afzal, S.; Quan, X.; Zhang, J. High Surface Area Mesoporous Nanocast LaMO3 (M = Mn, Fe) Perovskites for Efficient Catalytic Ozonation and an Insight into Probable Catalytic Mechanism. *Appl. Catal. B Environ.* **2017**, *206*, 692–703. https://doi.org/10.1016/j.apcatb.2017.01.072.

(29) Wang, M.; Zhao, T.; Dong, X.; Li, M.; Wang, H. Effects of Ce Substitution at the A-Site of LaNi0.5Fe0.5O3 Perovskite on the Enhanced Catalytic Activity for Dry Reforming of Methane. *Appl. Catal. B Environ.* **2018**, *224*, 214–221. https://doi.org/10.1016/j.apcatb.2017.10.022.

(30) Gong, S.; Xie, Z.; Li, W.; Wu, X.; Han, N.; Chen, Y. Highly Active and Humidity Resistive Perovskite LaFeO3 Based Catalysts for Efficient Ozone Decomposition. *Appl. Catal. B Environ.* **2019**, *241*, 578–587. https://doi.org/10.1016/j.apcatb.2018.09.041.

(31) Sun, W.; Wei, H.; yang An, L.; Jin, C.; Wu, H.; Xiong, Z. ang; Pu, C.; Sun, C. Oxygen Vacancy Mediated La1-XCexFeO3-Δ Perovskite Oxides as Efficient Catalysts for CWAO of Acrylic Acid by A-Site Ce Doping. *Appl. Catal. B Environ.* **2019**, *245*, 20–28. https://doi.org/10.1016/j.apcatb.2018.12.024.

(32) Wu, J.; Dacquin, J. P.; Cordier, C.; Dujardin, C.; Granger, P. Optimization of the Composition of Perovskite Type Materials for Further Elaboration of Four-Way Catalysts for Gasoline Engine. *Top. Catal.* **2019**, *62* (1–4), 368–375. https://doi.org/10.1007/s11244-018-1083-2.

(33) Emmerlich, J.; Linke, B. M.; Music, D.; Schneider, J. M. Towards Designing La1 - XSrxCoyFe 1 - YO3 - D with Enhanced Phase Stability: Role of the Defect Structure. *Solid State Ionics* **2014**, *255*, 108–112. https://doi.org/10.1016/j.ssi.2013.11.047.

(34) Schön, A.; Dacquin, J. P.; Granger, P.; Dujardin, C. Non Stoichiometric La1-YFeO3 Perovskite-Based Catalysts as Alternative to Commercial Three-Way-Catalysts? – Impact of Cu and Rh Doping. *Appl. Catal. B Environ.* **2018**, *223*, 167–176. https://doi.org/10.1016/j.apcatb.2017.06.026.

(35) Wu, Y.; Ni, X.; Beaurain, A.; Dujardin, C.; Granger, P. Stoichiometric and Non-Stoichiometric Perovskite-Based Catalysts: Consequences on Surface Properties and on Catalytic Performances in the Decomposition of N 2O from Nitric Acid Plants. *Appl. Catal. B Environ.* **2012**, *125*, 149–157. https://doi.org/10.1016/j.apcatb.2012.05.033.

(36) Pushpa, R.; Daniel, D.; Butt, D. P. Electronic Properties of Ca Doped LaFeO3: A First-Principles Study. *Solid State Ionics* **2013**, *249–250*, 184–190. https://doi.org/10.1016/j.ssi.2013.08.007.

(37) Shen, S. T.; Weng, H. S. Comparative Study of Catalytic Reduction of Nitric Oxide with Carbon Monoxide over the La1-XSrxBO3 (B = Mn, Fe, Co, Ni) Catalysts. *Ind. Eng. Chem. Res.* **1998**, *37* (7), 2654–2661. https://doi.org/10.1021/ie970691g.

(38) Lindstedt, A.; Strömberg, D.; Milh, M. A. High-Temperature Catalytic Reduction of Nitrogen Monoxide by Carbon Monoxide and Hydrogen over La1-XSrxMO3 Perovskites (M = Fe, Co) during Reducing and Oxidising Conditions. *Appl. Catal. A, Gen.* **1994**, *116* (1–2), 109–126. https://doi.org/10.1016/0926-860X(94)80283-1.

(39) Gunasekaran, N.; Rajadurai, S.; Carberry, J. J.; Bakshi, N.; Alcock, C. B. Surface Characterization and Catalytic Properties of La1-XAxMO3 Perovskite Type Oxides. Part I. Studies on La0.95Ba0.05MO3 (M = Mn, Fe or Co) Oxides. *Solid State Ionics* **1994**, *73* (3–4), 289–295. https://doi.org/10.1016/0167-2738(94)90046-9.

(40) Grillo, F.; Natile, M. M.; Glisenti, A. Low Temperature Oxidation of Carbon Monoxide: The Influence of Water and Oxygen on the Reactivity of a Co3O4 Powder Surface. *Appl. Catal. B Environ.* **2004**, *48* (4), 267–274. https://doi.org/10.1016/j.apcatb.2003.11.003.

(41) Pinto, D.; Glisenti, A. Pulsed Reactivity on LaCoO3-Based Perovskites: A Comprehensive Approach to Elucidate the CO Oxidation Mechanism and the Effect of Dopants. *Catal. Sci. Technol.* **2019**, *9* (11), 2749–2757. https://doi.org/10.1039/c9cy00210c.

(42) Pacella, M.; Garbujo, A.; Fabro, J.; Guiotto, M.; Xin, Q.; Natile, M. M.; Canu, P.; Cool, P.; Glisenti, A. PGM-Free CuO/LaCoO3 Nanocomposites: New Opportunities for TWC Application. *Appl. Catal. B Environ.* **2018**, *227* (November 2017), 446–458. https://doi.org/10.1016/j.apcatb.2018.01.053.

(43) Carollo, G.; Garbujo, A.; Xin, Q.; Fabro, J.; Cool, P.; Canu, P.; Glisenti, A. CuO/La0.5Sr0.5CoO3 Nanocomposites in TWC. *Appl. Catal. B Environ.* **2019**, *255*, 117753. https://doi.org/10.1016/j.apcatb.2019.117753.

(44) Tarjomannejad, A.; Niaei, A.; Gómez, M. J. I.; Farzi, A.; Salari, D.; Albaladejo-Fuentes, V. NO + CO Reaction over LaCu0.7B0.3O3 (B = Mn, Fe, Co) and La0.8A0.2Cu0.7Mn0.3O3 (A = Rb, Sr, Cs, Ba) Perovskite-Type Catalysts. *J. Therm. Anal. Calorim.* **2017**, *129* (2), 671–680. https://doi.org/10.1007/s10973-017-6264-x.

(45) He, H.; Liu, M.; Dai, H.; Qiu, W.; Zi, X. An Investigation of NO/CO Reaction over Perovskite-Type Oxide La0.8Ce0.2B0.4Mn0.6O3 (B = Cu or Ag) Catalysts Synthesized by Reverse Microemulsion. *Catal. Today* **2007**, *126* (3-4 SPEC. ISS.), 290–295. https://doi.org/10.1016/j.cattod.2007.06.004.

(46) Giannakas, A. E.; Leontiou, A. A.; Ladavos, A. K.; Pomonis, P. J. Characterization and Catalytic Investigation of NO + CO Reaction on Perovskites of the General Formula LaxM1 - XFeO3 (M = Sr and/or Ce) Prepared via a Reverse Micelles Microemulsion Route. *Appl. Catal. A Gen.* **2006**, *309* (2), 254–262. https://doi.org/10.1016/j.apcata.2006.05.016.

(47) Keav, S.; Matam, S. K.; Ferri, D.; Weidenkaff, A. Structured Perovskite-Based Catalysts and Their Application as Three-Way Catalytic Converters-a Review. *Catalysts*. MDPI AG July 1, 2014, pp 226–255. https://doi.org/10.3390/catal4030226.

(48) Tascón, J. M. D.; González Tejuca, L. Catalytic Activity of Perovskite-Type Oxides LaMeO3. *React. Kinet. Catal. Lett.* **1980**, *15* (2), 185–191. https://doi.org/10.1007/BF02062430.

(49) Nitadori, T.; Ichiki, T.; Misono, M. Catalytic Properties of Perovskite-Type Mixed Oxides (ABO 3) Consisting of Rare Earth and 3d Transition Metals. The Roles of the A- and B-Site Ions. *Bull. Chem. Soc. Jpn.* **1988**, *61* (3), 621–626. https://doi.org/10.1246/bcsj.61.621.

(50) Panich, N. M.; Pirogova, G. N.; Korosteleva, R. I.; Voronin, Y. V. Oxidation of CO and Hydrocarbons over Perovskite-Type Complex Oxides. *Russ. Chem. Bull.* **1999**, *48* (4), 694–697. https://doi.org/10.1007/BF02496248.

(51) Voorhoeve, R. J. H.; Remeika, J. P.; Trimble, L. E.; Cooper, A. S.; Disalvo, F. J.; Gallagher, P. K. Perovskite-like La1-XKxMnO3 and Related Compounds: Solid State Chemistry and the Catalysis of the Reduction of NO by CO and H2. *J. Solid State Chem.* **1975**, *14* (4), 395–406. https://doi.org/10.1016/0022-4596(75)90061-4.

(52) Mars, P.; van Krevelen, D. W. Oxidations Carried out by Means of Vanadium Oxide Catalysts. *Chem. Eng. Sci.* **1954**, *3*, 41–59. https://doi.org/10.1016/S0009-2509(54)80005-4.

(53) Ciambelli, P.; Cimino, S.; Lisi, L.; Faticanti, M.; Minelli, G.; Pettiti, I.; Porta, P. La, Ca and Fe Oxide Perovskites: Preparation, Characterization and Catalytic Properties for Methane Combustion. *Appl. Catal. B Environ.* **2001**, *33* (3), 193–203. https://doi.org/10.1016/S0926-3373(01)00163-1.

(54) Schubert, U.; Huesing, N. *Synthesis of Inorganic Materials*; Wiley-VCH, 2012.

(55) Shirley, D. A. High-Resolution x-Ray Photoemission Spectrum of the Valence Bands of Gold. *Phys. Rev. B* **1972**, *5* (12), 4709–4714. https://doi.org/10.1103/PhysRevB.5.4709.

(56) Briggs, D. Handbook of X-Ray Photoelectron Spectroscopy C. D. Wanger, W. M. Riggs, L. E. Davis, J. F. Moulder and G. E.Muilenberg Perkin-Elmer Corp., Physical Electronics Division, Eden Prairie, Minnesota, USA, 1979. 190 Pp. $195; Chastain, J., Ed.; Eden Prairie, 1981; Vol. 3. https://doi.org/10.1002/sia.740030412.

(57) Umbach, E. *Practical Surface Analysis*; Wiley: New York, 1992; Vol. 11. https://doi.org/10.1016/0165-9936(92)87016-d.

(58) Garbujo, A.; Pacella, M.; Natile, M. M.; Guiotto, M.; Fabro, J.; Canu, P.; Glisenti, A. On A-Doping Strategy for Tuning the TWC Catalytic Performance of Perovskite Based Catalysts. *Appl. Catal. A Gen.* **2017**, *544* (July), 94–107. https://doi.org/10.1016/j.apcata.2017.07.009.

(59) Naumkin, V. A.; Kraut-Vass, A.; Gaarenstroom, S. W.; J., P. C. NIST X-Ray Photoelectron Spectroscopy Database. *Meas. Serv. Div. Natl. Inst. Stand. Technol.* **2012**, *20899* (20), 20899. https://doi.org/10.18434/T4T88K.

(60) Galenda, A.; Natile, M. M.; Nodari, L.; Glisenti, A. La0.8Sr0.2Ga0.8Fe0.2O3-δ: Influence of the Preparation Procedure on Reactivity toward Methanol and Ethanol. *Appl. Catal. B Environ.* **2010**, *97* (3–4), 307–322. https://doi.org/10.1016/j.apcatb.2010.04.004.

(61) Tabata, K.; Matsumoto, I.; Kohiki, S. Surface Characterization and Catalytic Properties of La1-x-SrxCoO3. *J. Mater. Sci.* **1987**, *22* (5), 1882–1886. https://doi.org/10.1007/BF01132422.

(62) Tejuca, L. G.; Fierro, J. É. L. G. XPS and TPD Probe Techniques for the Study of LaNiO3 Perovskite Oxide. *Thermochim. Acta* **1989**, *147* (2), 361–375. https://doi.org/10.1016/0040-6031(89)85191-3.

(63) Kang, Z.; Li, L.; Wei, Q. An XPS Study of Perovskite Oxides RECrO3. *Chem. Res. Chinese Univ.* **1996**, *12* (3), 280–284.

(64) Haber, J.; Stoch, J.; Ungier, L. X-Ray Photoelectron Spectra of Oxygen in Oxides of Co, Ni, Fe and Zn. *J. Electron Spectros. Relat. Phenomena* **1976**, *9* (5), 459–467. https://doi.org/10.1016/0368-2048(76)80064-3.

(65) Mullica, D. F.; Perkins, H. O.; Lok, C. K. C.; Young, V. The X-Ray Photoemission Spectra of La(OH)3. *J. Electron Spectros. Relat. Phenomena* **1993**, *61* (3–4), 337–355. https://doi.org/10.1016/0368-2048(93)80024-G.

(66) Sunding, M. F.; Hadidi, K.; Diplas, S.; Løvvik, O. M.; Norby, T. E.; Gunnæs, A. E. XPS Characterisation of in Situ Treated Lanthanum Oxide and Hydroxide Using Tailored Charge Referencing and Peak Fitting Procedures. *J. Electron Spectros. Relat. Phenomena* **2011**, *184* (7), 399–409. https://doi.org/10.1016/j.elspec.2011.04.002.

(67) Natile, M. M.; Poletto, F.; Galenda, A.; Glisenti, A.; Montini, T.; De Rogatis, L.; Fornasiero, P. La0.6Sr0.4Co1-YFeyO 3-δ Perovskites: Influence of the Co/Fe Atomic Ratio on Properties and Catalytic Activity toward Alcohol Steam-Reforming. *Chem. Mater.* **2008**, *20* (6), 2314–2327. https://doi.org/10.1021/cm703329k.

(68) Galenda, A.; Natile, M. M.; Krishnan, V.; Bertagnolli, H.; Glisenti, A. LaSrCoFeO and Fe2O3/LaSrCoFeO Powders: Synthesis and Characterization. *Chem. Mater.* **2007**, *19* (11), 2796–2808. https://doi.org/10.1021/cm062742i.

(69) Natile, M. M.; Ponzoni, A.; Concina, I.; Glisenti, A. Chemical Tuning versus Microstructure Features in Solid-State Gas Sensors: LaFe1-XGaxO3, a Case Study. *Chem. Mater.* **2014**, *26* (4), 1505–1513. https://doi.org/10.1021/cm4018858.

(70) Guiotto, M.; Pacella, M.; Perin, G.; Iovino, A.; Michelon, N.; Natile, M. M.; Glisenti, A.; Canu, P. Washcoating vs. Direct Synthesis of LaCoO3 on Monoliths for Environmental Applications. *Appl. Catal. A Gen.* **2015**, *499*, 146–157. https://doi.org/10.1016/j.apcata.2015.04.013.

(71) Perin, G.; Fabro, J.; Guiotto, M.; Xin, Q.; Natile, M. M.; Cool, P.; Canu, P.; Glisenti, A. Cu@LaNiO3 Based Nanocomposites in TWC Applications. *Appl. Catal. B Environ.* **2017**, *209* (7), 214–227. https://doi.org/10.1016/j.apcatb.2017.02.064.

(72) McIntyre, N. S.; Zetaruk, D. G. X-Ray Photoelectron Spectroscopic Studies of Iron Oxides. *Anal. Chem.* **1977**, *49* (11), 1521–1529. https://doi.org/10.1021/ac50019a016.

(73) Rossetti, I.; Biffi, C.; Forni, L. Oxygen Non-Stoichiometry in Perovskitic Catalysts: Impact on Activity for the Flameless Combustion of Methane. *Chem. Eng. J.* **2010**, *162* (2), 768–775. https://doi.org/10.1016/j.cej.2010.06.003.

(74) Isupova, L. A.; Yakovleva, I. S.; Rogov, V. A.; Alikina, G. M.; Sadykov, V. A. Oxygen States in Oxides with a Perovskite Structure and Their Catalytic Activity in Complete Oxidation Reactions: System La 1 - XCa XFeO 3 - y (x = 0-1). *Kinet. Catal.* **2004**, *45* (3), 446–453. https://doi.org/10.1023/B:KICA.0000032182.48410.e2.

(75) Pecchi, G.; Jiliberto, M. G.; Buljan, A.; Delgado, E. J. Relation between Defects and Catalytic Activity of Calcium Doped LaFeO 3 Perovskite. *Solid State Ionics* **2011**, *187* (1), 27–32. https://doi.org/10.1016/j.ssi.2011.02.014.

(76) Shannon, R. D. Revised Effective Ionic Radii and Systematic Studies of Interatomic Distances in Halides and Chalcogenides. *Acta Crystallogr. Sect. A* **1976**, *32* (5), 751–767. https://doi.org/10.1107/S0567739476001551.

(77) Barbero, B. P.; Gamboa, J. A.; Cadús, L. E. Synthesis and Characterisation of La1-XCaxFeO3 Perovskite-Type Oxide Catalysts for Total Oxidation of Volatile Organic Compounds. *Appl. Catal. B Environ.* **2006**, *65* (1–2), 21–30. https://doi.org/10.1016/j.apcatb.2005.11.018.

(78) Andoulsi, R.; Horchani-Naifer, K.; Férid, M. Structural and Electrical Properties of Calcium Substituted Lanthanum Ferrite Powders. *Powder Technol.* **2012**, *230* (3), 183–187. https://doi.org/10.1016/j.powtec.2012.07.026.

(79) Pillai, S. K.; Sikhwivhilu, L. M.; Hillie, T. K. Synthesis, Characterization and Photoluminescence Properties of Dy3+-Doped Nano-Crystalline SnO2. *Mater. Chem. Phys.* **2010**, *120* (2–3), 619–624. https://doi.org/10.1016/j.matchemphys.2009.12.010.

(80) Wang, Y.; Ren, J.; Wang, Y.; Zhang, F.; Liu, X.; Guo, Y.; Lu, G. Nanocasted Synthesis of Mesoporous LaCoO3 Perovskite with Extremely High Surface Area and Excellent Activity in Methane Combustion. *J. Phys. Chem. C* **2008**, *112* (39), 15293–15298. https://doi.org/10.1021/jp8048394.

(81) Alifanti, M.; Kirchnerova, J.; Delmon, B. Effect of Substitution by Cerium on the Activity of LaMnO3 Perovskite in Methane Combustion. *Appl. Catal. A Gen.* **2003**, *245* (2), 231–244. https://doi.org/10.1016/S0926-860X(02)00644-0.

(82) Sherwood, P. M. A. The Use and Misuse of Curve Fitting in the Analysis of Core X-ray Photoelectron Spectroscopic Data. *Surf. Interface Anal.* **2019**, *51* (6), 589–610. https://doi.org/10.1002/sia.6629.

(83) Cihlar, J.; Vrba, R.; Castkova, K.; Cihlar, J. Effect of Transition Metal on Stability and Activity of La-Ca-M-(Al)-O (M = Co, Cr, Fe and Mn) Perovskite Oxides during Partial Oxidation of Methane. *Int. J. Hydrogen Energy* **2017**, *42* (31), 19920–19934. https://doi.org/10.1016/j.ijhydene.2017.06.075.

(84) Lago, R.; Bini, G.; Peña, M. A.; Fierro, J. L. G. Partial Oxidation of Methane to Synthesis Gas Using LnCoO3 Perovskites as Catalyst Precursors. *J. Catal.* **1997**, *167* (1), 198–209. https://doi.org/10.1006/jcat.1997.1580.

(85) Fierro, J. L. G. Structure and Composition of Perovskite Surface in Relation to Adsorption and Catalytic Properties. *Catal. Today* **1990**, *8* (2), 153–174. https://doi.org/10.1016/0920-5861(90)87016-V.

(86) Bedel, L.; Roger, A. C.; Estournes, C.; Kiennemann, A. Co0 from Partial Reduction of La(Co,Fe)O3 Perovskites for Fischer-Tropsch Synthesis. *Catal. Today* **2003**, *85* (2–4), 207–218. https://doi.org/10.1016/S0920-5861(03)00388-2.

(87) Sis, L. B.; Wirtz, G. P.; Sorenson, S. C. Structure and Properties of Reduced LaCoO3. *J. Appl. Phys.* **1973**, *44* (12), 5553–5559. https://doi.org/10.1063/1.1662195.

(88) Echchahed, B.; Kaliaguine, S.; Alamdari, H. Well Dispersed Co0 by Reduction of LaCoO3 Perovskite. *Int. J. Chem. React. Eng.* **2006**, *4* (1), 1–14. https://doi.org/10.2202/1542-6580.1332.

(89) Wu, S.; Song, C.; Bin, F.; Lv, G.; Song, J.; Gong, C. La1-XCexMn1-YCoyO3 Perovskite Oxides: Preparation, Physico-Chemical Properties and Catalytic Activity for the Reduction of Diesel Soot. *Mater. Chem. Phys.* **2014**, *148* (1–2), 181–189. https://doi.org/10.1016/j.matchemphys.2014.07.029.

(90) Royer, S.; Alamdari, H.; Duprez, D.; Kaliaguine, S. Oxygen Storage Capacity of La1−xA′xBO3 Perovskites (with A′=Sr, Ce; B=Co, Mn)—Relation with Catalytic Activity in the CH4 Oxidation Reaction. *Appl. Catal. B Environ.* **2005**, *58* (3–4), 273–288. https://doi.org/10.1016/j.apcatb.2004.12.010.

(91) Yi, Y.; Liu, H.; Chu, B.; Qin, Z.; Dong, L.; He, H.; Tang, C.; Fan, M.; Bin, L. Catalytic Removal NO by CO over LaNi0.5M0.5O3 (M = Co, Mn, Cu) Perovskite Oxide Catalysts: Tune Surface Chemical Composition to Improve N2 Selectivity. *Chem. Eng. J.* **2019**, *369*, 511–521. https://doi.org/10.1016/j.cej.2019.03.066.

(92) Simmance, K.; Thompsett, D.; Wang, W.; Thiebaut, B. Evaluation of Perovskite Catalysts Prepared by Flame Spray Pyrolysis for Three-Way Catalyst Activity under Simulated Gasoline

Exhaust Feeds. *Catal. Today* **2019**, *320* (October 2017), 40–50. https://doi.org/10.1016/j.cattod.2017.12.035.

(93) Wegner, K.; Schimmöller, B.; Thiebaut, B.; Fernandez, C.; Rao, T. N. Pilot Plants for Industrial Nanoparticle Production by Flame Spray Pyrolysis. *KONA Powder Part. J.* **2011**, *29* (29), 251–265. https://doi.org/10.14356/kona.2011025.

(94) Somorjai, G. A.; Li, Y. *Introduction to Surface Chemistry and Catalysis*, 2nd Editio.; Wiley, 2010.

3. Mn-based perovskites for carbon soot oxidation

In a similar fashion as in the previous chapter, Mn-based perovskites have been considered towards catalytic oxidation of soot and considering different dopings both in the A- and B-site of the perovskite structure. In this chapter the activity in soot oxidation will be the main considered aspect, due to the peculiar Mn-based composition, suitable for such application. In the first part of the chapter (section 3.1) K-doping in the A-site and Co-doping in the B-site will be addressed, whereas in section 3.2 the effect of Ni-doping in the structure will be evaluated. A general conclusion will summarize the results of the two investigations underlying similarities and differences in the behavior and features of differently doped Mn-based perovskites.

Soot is a danger for human health and climate change [1]. To prevent soot emission different and complementary approaches are possible: the design of reactors or engines may be optimized, highly efficient filters can be applied and/or catalysts can be used to lower the ignition temperature of soot.

Commercially, the current solution employed for Diesel engines in automotive sector is the use of the so-called Diesel Particulate Filters (DPFs). DPFs are fabricated in a similar way as Three-Way Catalytic converters (TWC): they comprise a monolith (traditionally in cordierite, or silicon carbide for higher mechanical resistance at high temperature) with a honeycomb intrinsic structure characterized by high surface areas. Through the mechanism called surface filtration or coke filtration, soot is deposited on the surface of the device and periodically combusted.[2] Technologic progress in this field brought also the use of the so-called Continuous Regeneration Trap (CRT), patented by Johnson Matthey; this device combines a DPF filter with a Pt-based pre-oxidizer which converts CO, hydrocarbons and NO_x to CO_2, H_2O and NO_2. NO_2 is then used to rapidly oxidize soot to carbon dioxide. Later also a Four Way Catalyst was developed, again in the attempt of combining in a single device the TWC features with soot oxidation activity. The main drawback of such devices is still the massive use of noble metals in the active phase (e.g. Pt, Pd and Rh), and the project

described in this chapter is an endeavor to investigate the possibility of using non-noble metal based perovskites, already known for their TWC activity, in soot oxidation reactions.

The use of noble metal free catalysts could be of significant help in obtaining low cost and sustainable soot abatement devices. Perovskites type oxides are among promising catalysts[3] because of their capability of activating the simultaneous removal of NO_x and diesel soot in the presence of oxygen.[4–7]

3.1 Mn-based Co-doped perovskites for soot oxidation

Among the perovskites, $LaMnO_3$-based ones are characterized by the higher efficiency. Catalysts activation by means of alkali and alkali-metals is observed to assure higher performance to oxide-based catalysts:[8–11] K seems to be the more efficient also in activation of perovskites. [7,12] The mechanisms through which activation is obtained are not yet fully understood but a relevant role seems to be played by electron exchange, soot morphology modification, decreased stability of surface carbonates.[13] Other authors in literature postulate various motivation behind the promoting effect of K in soot oxidation catalysis; some of them are mentioned: an electron donor activity with surface oxygen as the electron acceptor (and subsequent formation of phenoxide species or gaseous K),[14–16] the decrease of the stability of carbonates induced by K, which leads to lower decomposition temperatures of carbonates,[15,17,18] redox-type oxygen- or electron-transfer mechanisms or a combination of both,[19–28] promotion of a dissociative chemisorption of oxygen,[15,19,20,29–31] K is also discussed to be the active phase in K-bearing (oxidic) catalysts, The active phase could either be free K^+ ions and/or clusters of alkali metals, which might be anchored through alkali metal phenolate groups on the surface, but the latter do not really contribute to the active species.[27,31,32]

The contribution of all these phenomena can differ for the specific type of catalyst. In the present contribution we focused on cobalt-doped manganese-based perovskites. Cobalt is an effective oxidant in perovskite structures, but the tendency is that of minimizing this employment due to its cost and

toxicity, since a large-scale application is always the primary goal. In particular, the effect of K on $LaMn_{0.9}Co_{0.1}O_3$ and $SrMn_{0.9}Co_{0.1}O_3$ is studied; moreover, the insertion of K into the crystalline cell and, on the other side, its deposition on the surface, have been compared in terms of catalytic efficiency.

3.1.1 Materials and methods

The samples were prepared by citrate method[33] starting from La_2O_3 (Sigma-Aldric, pure), $Sr(NO_3)_2$ (Aldrich ≥98%), Manganese(II) acetate tetra hydrate (Sigma-Aldrich ≥99%), K_2CO_3 (Aldrich 95%) and $Co(NO_3)_2 \cdot 6H_2O$ (Sigma-Aldrich 98%). Carbonate and nitrate precursors were dissolved in an aqueous solution while lanthanum solution was obtained by mineralizing the corresponding oxide with nitric acid. A solution of monohydrate citric acid (Sigma Aldrich ≥99.0%) was added: its molar ratio was 1.9:1 with respect to the total amount of cations. The solution is then heated up to 80°C in air to promote water evaporation and to obtain a pink wet-get. The gel is slowly heated up to 400°C for 2 hours in air to decompose the organic framework and the obtained powder samples were ground and calcined at 700°C ($LaMn_{0.9}Co_{0.1}O_3$ – LMC, $La_{0.9}K_{0.1}Mn_{0.9}Co_{0.1}O_3$ – LKMC) and 800°C ($Sr_{0.9}K_{0.1}Mn_{0.9}Co_{0.1}O_3$ – SKMC) for 6 hours to obtain the perovskite. The nanocomposite, $KO_x/LaMn_{0.9}Co_{0.1}O_3$ – K/LMC, was obtained by wet impregnation of the LMC perovskite powder with a solution of K^+ obtained by dissolving the carbonate in order to reach the same atomic composition of the LKMN catalyst. The suspension was stirred 24 hours and then the solvent was slowly removed by heating at 90°C. The final heat treatment was carried out at 500°C for 3 hours (the desorption of K was observed at temperatures higher than 600°C).[28,34]

Impregnation, which will be addressed also in the following chapters, is a largely used technique in the production of supported catalysts, as it is able to provide a physical interaction between support and catalyst with an efficient and homogeneous dispersion of the active sites of the catalyst on a material with different chemical and mechanical features. In this case LMC, acting as a support, is catalytically active in K/LMC composite, thanks to its properties of ionic and electronic mobility,

with K_2O acting as an alkaline promoter. Moreover this method was applied also thanks to its easy application in an industrial production scale.

The XPS measurements were carried out with a Perkin Elmer Φ 5600ci Multi Technique System. The spectrometer was calibrated by assuming the binding energy (BE) of the Au $4f_{7/2}$ line to be 84.0 eV with respect to the Fermi level. Both extended spectra (survey - 187.85 eV pass energy, 0.8 eV·step^{-1}, 0.05 s·step^{-1}) and detailed spectra (for Mn 2p, Co 2p, La 3d, Sr 2p, K 1s, O 1s and C 1s – 23.50 eV pass energy, 0.1 eV·step^{-1}, 0.1 s·step^{-1}) were collected with a standard Al Kα source working at 200 W. The standard deviation in the BE values of the XPS line is 0.10 eV. The atomic percentage, after a Shirley-type background subtraction,[35] was evaluated by using the PHI sensitivity factors.[36] The peak positions were corrected for the charging effects by considering the C 1s peak at 285.0 eV and evaluating the BE differences.[37]

The XRD analyses were performed with a Bruker D8 Advance diffractometer with Bragg-Brentano geometry using a Cu Kα radiation (40 kV, 40 mA, λ = 0.154 nm). The data were collected at 0.03°, with a counting time of 7 s/step in the (2θ) range from 20° to 70°. The crystalline phases were identified by the search-match method using the ICDD (International Centre for Diffraction Data) database.

Temperature Programmed Reduction (TPR), and specific surface area (BET, Brunauer-Emmett-Teller) measurements were performed with an Autochem II 2920 Micromeritics, equipped with a TCD detector. The H_2-TPR measurements were carried out in a quartz reactor by using 50 mg of sample and heating from RT to 900°C at 10°C min^{-1} under a constant flow of H_2 5% in Ar (50 ml·min^{-1}). TPR samples were previously outgassed with He (50 ml·min^{-1}) at RT.

In BET measurements 100 mg of sample were used; before measurement the sample was treated at 350°C for 2 h under a constant flow of He (50 ml·min^{-1}); each surface area value obtained was the average of three consecutive measurements.

Field emission-scanning electron microscopy and EDX measures were carried on a Zeiss SUPRA 40VP. Morphological analysis and EDX analysis were carried out setting the acceleration voltages at 20 kV.

The catalytic tests are carried out in a quartz reactor (6 mm ID) with a packed bed of powders; the temperature was monitored by a thermocouple right upstream of the bed. The inert carrier was always Ar. The flow rates were controlled by thermal mass flow meters (Vögtlin). The composition of the gas mixture (before and after reaction) was measured by Gas Chromatography (Agilent 7890A), with a TCD detector and 13X (60/80 mesh, 1.8 m) and Porapak Q (1.8 m) columns. Temperature ramp involved a fast heating (10°C/min) until 150°C, which should favor CO_2 desorption from the sample, and a slow ramp (1°C/min) until 450°C. Injection of the products at the GC was carried out every eight minutes, allowing us to detect also the possible production of CO in competition to CO_2 from the combustion, an occurrence that, however, was never detected. Soot was added in 1:10 ratio in tight contact mode. If an oxygen-transfer step is involved, then the contact between catalyst and soot and, experimentally, the method used to bring them in contact, is crucial to the catalytic activity.

Sample	Acronym	BET Specific Surface Area (m^2/g)	Crystalline Structure	H_2 up-take	Total	Mn(III)/Mn(II) Co(II)/Co(0)	Mn(IV)/Mn(III) Co(III)/Co(II)
$LaMn_{0.9}Co_{0.1}O_3$	LMC	25	rhombohedral	Theoretical Experimental	0.60 0.59	8 41	92 59
$La_{0.9}K_{0.1}Mn_{0.9}Co_{0.1}O_3$	LKMC	21	rhombohedral	Theoretical Experimental	0.65 0.54	23 46	77 54
$K10\%/LaMn_{0.9}Co_{0.1}O_3$	K/LMC	20	rhombohedral	Theoretical Experimental	0.60 0.40	8 43	92 57
$Sr_{0.9}K_{0.1}Mn_{0.9}Co_{0.1}O_3$	SKMC	6	hexagonal	Theoretical Experimental	1.05 0.97	48 81	52 19

Table 14 Composition of the studied catalyst, crystalline structure and H_2-up-take data obtained by means of H_2-TPR. The up-take data are expressed as mol H_2/mol sample; the attribution to the reduction phenomena (determined by fitting the experimental curves) are compared with the theoretical ones determined considering that all K is inserted into the crystalline cell and determined the formation of Mn (IV).

Mul et al.[32] identified two different procedures to test soot oxidation in presence of a catalyst: loose and tight contact. Loose contact represents a situation closer to the real one, as catalyst and soot are simply mixed together with a spatula; tight mode prescribes instead a much more intimate contact between the two species, obtained by crushing them in a mortar. Standard Printex-U carbon black is used to simulate soot. To enhance the catalyst answer and emphasize the difference in the behaviors, tight contact was preferred. This allows a better evaluation of the effect of the different dopant (K vs Sr) and of their insertion into the perovskite cell with respect to the surface deposition.

3.1.2 Results and discussion

The materials prepared are listed in Table 14, together with the results of XRD and H_2-TPR analysis. All diffraction peaks of the La-containing perovskites can be assigned to the rhombohedral geometry. (JCPDS 72-1156 (C)), (Figure 40) while the hexagonal one is observed in SKMC. Doping with K(I) causes the shift of the signals toward lower angles (because of the difference in ionic radii K(I) = 1.38 Å, La(III) =1.061 Å)[38] confirming the insertion of K into the perovskite cell. No secondary phases are observed.

BET surface area values are summarized in Table 14. The values obtained in the catalysts containing K are only slightly lower than that of LMC. The specific surface area of SKMC is, in contrast, significantly lower; this result is probably a consequence of the higher calcination temperature (800 instead of 700°C) necessary to obtain the perovskite phase.

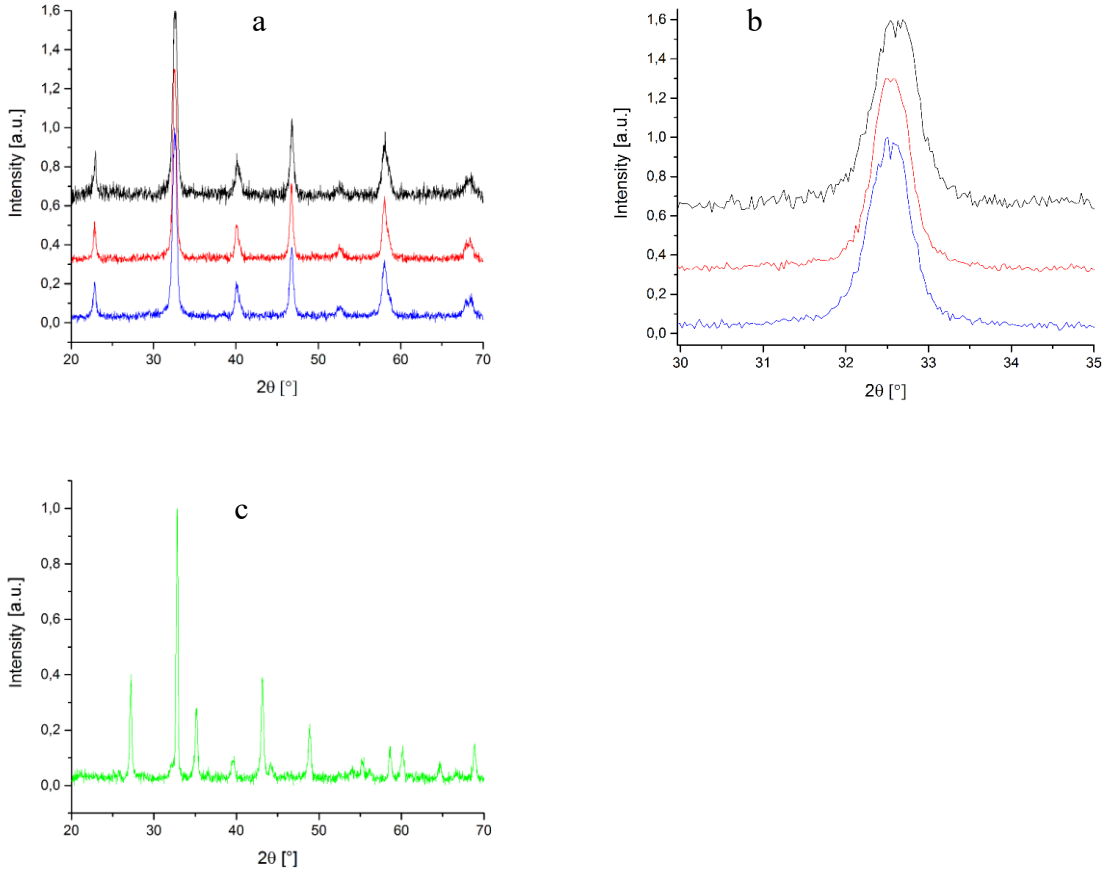

Figure 40 XRD patterns of: a) $LaMn_{0.9}Co_{0.1}O_3$ (blue), $La_{0.9}K_{0.1}Mn_{0.9}Co_{0.1}O_3$ (red), $0.1K/LaMn_{0.9}Co_{0.1}O_3$ (black), b) Detail 30-35°; c) $Sr_{0.9}K_{0.1}Mn_{0.9}Co_{0.1}O_3$ (green).

The XP spectra are compared in Figure 41. The Mn 2p XP peaks are centered at 642.2-642.5 and 653.6 – 654.0 eV for the 3/2 and 1/2 components, respectively, a position which is typical of Mn in oxides; it is difficult, however, to distinguish between Mn(III) and Mn(IV).[39] No significant differences are observed when K is also present or when Sr substitutes La. La 3d peak position (834.2-834.6 and 851.0-851.4 eV, for $3d_{5/2}$ and $3d_{3/2}$, respectively) and shape (shake-up contributions at 840 and 858 eV) are consistent with how expected for La(III) in perovskites and are not modified by doping or by the deposition of K. Sr 3d peak shows two doublets whose 5/2 positions, at 132.8 and 133.6 eV, respectively, suggest the presence, beside the perovskite, of carbonate species, compatible with C1s spectra. Two main signals compose the O 1s spectra: the peak at 529.5-530.0 eV is due to the perovskite oxygen whereas the one at about 532.0 eV at oxygen in hydroxides and carbonates; this last contribution is more evident in SKMC. [37,39–41]

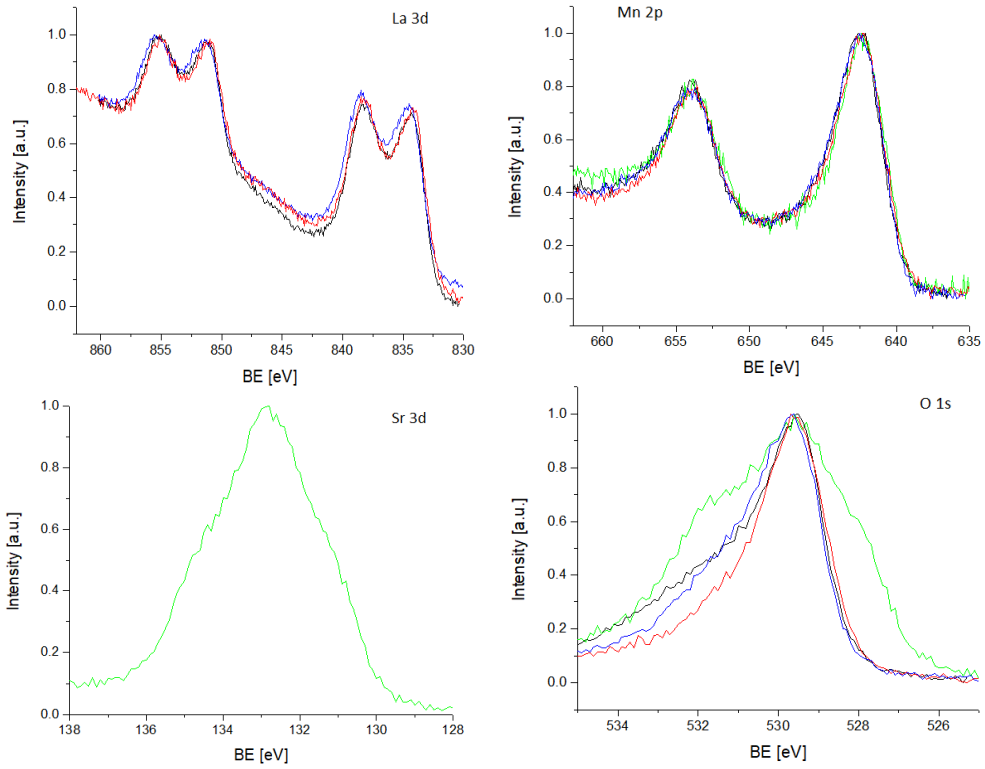

Figure 41 XP spectra obtained for $LaMn_{0.9}Co_{0.1}O_3$ (blue), $La_{0.9}K_{0.1}Mn_{0.9}Co_{0.1}O_3$ (red), $0.1K/LaMn_{0.9}Co_{0.1}O_3$ (black), $Sr_{0.9}K_{0.1}Mn_{0.9}Co_{0.1}O_3$ (green).

In all catalysts, XPS quantitative analysis (Table 15) reveals the surface segregation of oxygen, consistent with the formation of hydroxyl and carbonate groups, as denoted by qualitative analysis. In LMC surface segregation of Mn is evident, and it is not significantly affected by the insertion of K. Also K shows an attitude to surface segregation. It is noteworthy that, in K/LMC, K is less present in surface than expected, consistently with its frequently reported desorption trend.[42] The "after reaction" compositional values are discussed below, together with reactivity results.

		La	K	Mn	Co	O	K/La	Mn/La	(Co+Mn)/(K+La)
LMC	XPS	15.7 (42.2)	- -	21.0 (56.5)	0.5 (1.3)	62.9	-	1.3	1.4
	EDX	18.1	-	16.7	3.0	62.2	-	0.9	1.1
		(47.9)	-	(44.2)	(7.9)				
	Nominal After reaction	20.0 (50.0) 12.6 (45.2)	- - -	18.0 (45.0) 11.9 (42.6)	2.0 (5.0) 3.4 (12.2)	60.0 72.1	- -	0.9 0.9	1.0 1.2
LKMC	XPS	11.6 (28.3)	5.8 (14.2)	23.1 (56.3)	0.5 (1.2)	59.0	0.5	2.0	1.4
	EDX	16.0	1.9	18.1	2.0	62.0	0.1	1.1	1.1
		(42.1)	(5.0)	(47.6)	(5.4)				
	Nominal After reaction	18.0 (45.0) 2.2 (4.9)	2.0 (5.0) 26.0 (57.5)	18.0 (45.0) 7.2 (15.9)	2.0 (5.0) 9.8 (21.7)	60.0 54.8	0.1 11.8	1.0 3.3	1.0 0.6
K/LMC	XPS	12.4 (37.1)	2.5 (7.6)	18.2 (54.6)	0.3 (0.7)	66.6	0.2	1.5	1.2
	EDX	14.7	1.1	14.9	1.9	67.3	0.1	1.0	1.1
		(45.1)	(3.4)	(45.7)	(5.8)				
	Nominal After reaction	18.0 (45.0) 3.1 (5.4)	2.0 (5.0) 32.6 (57.1)	18.0 (45.0) 8.5 (14.9)	2.0 (5.0) 12.9 (22.6)	60.0 42.9	0.1 10.5	1.0 2.7	1.0 0.6
		Sr	K	Mn	Co	O	K/Sr	Mn/Sr	(Co+Mn)/(K+Sr)
SKMC	XPS	15.1 (39.3)	8.1 (20.9)	13.7 (35.6)	1.7 (4.3)	61.4	0.5	0.9	0.7
	EDX	13.7	0.8	11.4	1.3	72.9	0.1	0.8	0.9
		(50.4)	(3.0)	(42.0)	(4.6)				
	Nominal After reaction	18.0 (45.0) 13.1 (23.7)	2.0 (5.0) 29.3 (52.9)	18.0 (45.0) 9.5 (17.1)	2.0 (5.0) 3.5 (6.3)	60.0 44.6	0.1 2.2	1.0 0.7	1.0 0.3

Table 15 XPS and EDX quantitative analysis of the catalysts; the nominal compositions obtained from the weighted amounts are reported for comparison. "After reaction" values are taken post soot oxidation test by XPS. Values in brackets indicate the percentage without considering oxygen contributions.

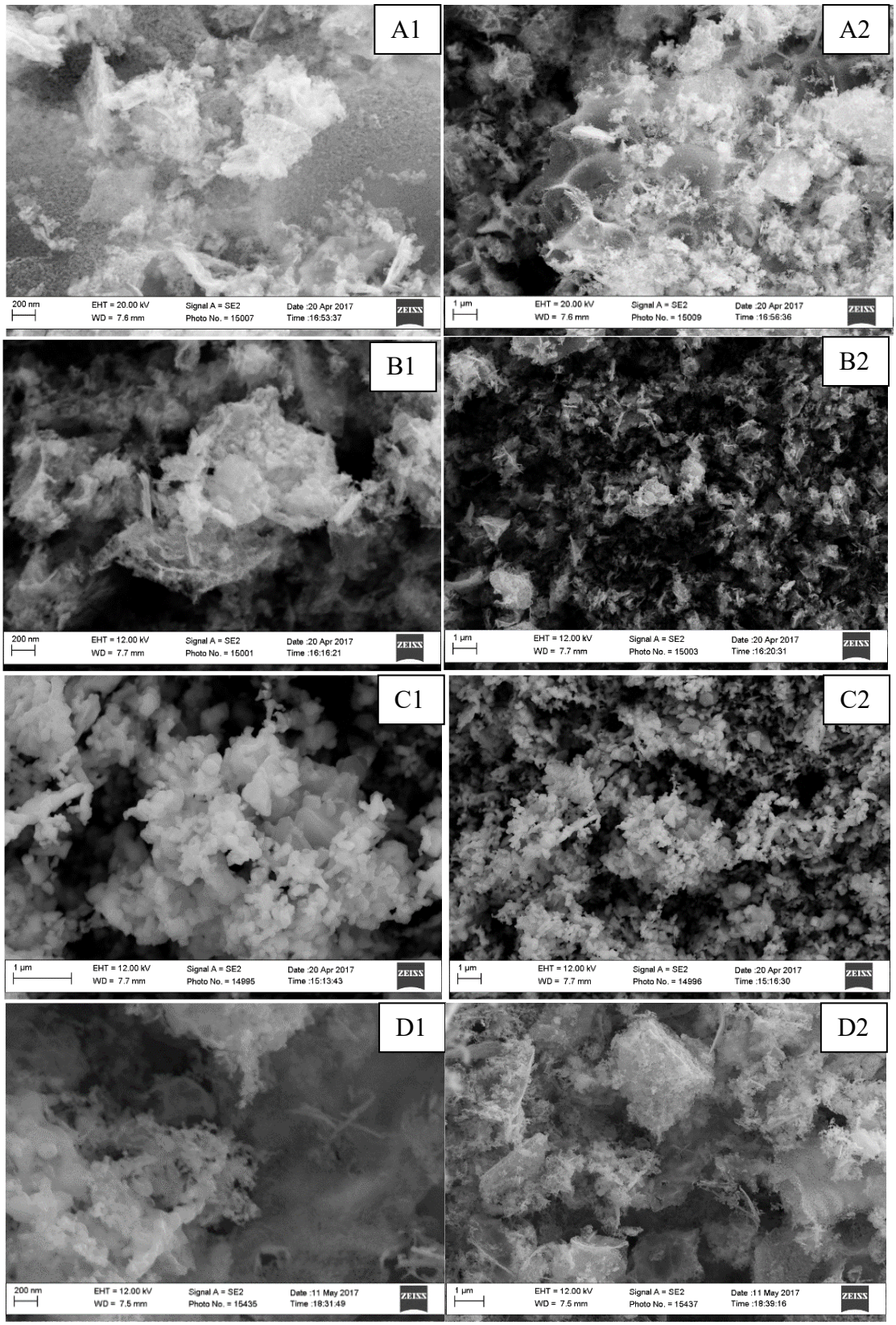

Figure 42 SEM images: A: K/LMC; B: LMC; C: SKMC; D: LKMC. Images labelled with "1" are acquired at 10^5K magnification, images labelled with "2" at 10^4K magnification.

SEM images are grouped in Figure 42. Qualitatively it can be appreciated the higher dimension of SKMC particles compared with samples from the same group, identified to reach about 100 nm. It is not clearly distinguishable the presence of K_2O in K/LMC from the simple visual analysis, but the surface presents a higher variability and irregularity that can be a trace for the presence of different phases not homogeneously distributed.

The H_2-TPR curves of the different catalysts are compared in Figure 43. In all cases the presence of two groups of signals centered around 300-400 °C (Mn(IV) to Mn(III)) and 600-800 °C (Mn(III) to Mn(II)) is evident. The reduction of cobalt is expected to contribute in a low amount to both the groups of signals (Co(III) to Co(II) around 440°C and Co(II) to Co(0) around 500-600 °C).[43]

Focusing on the lower temperature signals two main contributions are observed in LMC at 320 and 388 °C, whereas at higher temperature a broad signal is observed around 800 °C. The fitting procedure reveals, in the low temperature signals group, minor contributions around 157, 218, and 270 °C. The comparison with literature data suggests to attribute these last signals to the reduction of surface oxygen species.[44] Oxygen species contribute less than 10% to the total H_2-consumption. The signals at 321 and 388 °C, consistent with the reduction of Mn(IV), contributes for about 30% of hydrogen consumption. The remaining consumption is observed around 800°C and corresponds to the reduction of Mn(III).[45,46] The H_2-uptake corresponds to 0.24 mol H_2/mol LMC at low temperature and 0.35 mol H_2/mol LMC at higher temperature. According to literature, the hydrogen consumption below 500°C was attributed to the reduction Mn(IV) to Mn(III) of some Mn(IV) present in the perovskite structure, however, based on the hydrogen consumption values, it is possible that the reduction process of Mn(III) to Mn(II) partially occurred in that temperature range. The reducibility of Mn(III) at lower temperature was observed to depend on the amount of complexing agent (citric acid) and on the textural properties of the catalyst.[47] In particular, the Mn(III) reduction seems to be favored by higher specific surface area and lower size of the particles. The H_2 uptake between 150 and 400 °C (which

can give a rough idea of the reducibility) is 0.24 mol H_2/mol (Mn+Co) which corresponds to 40% of the Mn+Co ions in 1 mol of perovskite.

The insertion of K into the perovskite cell determines a slight increment of the surface oxygen species which contribute to the total consumption for 12.5 %. The H_2-uptake at higher temperature decreases from 0.35 to 0.29 mol H_2/mol perovskite. Also the total uptake decreases from 0.59 to 0.54 mol H_2/mol (Mn+Co). The H_2 uptake at lower temperature is 37% of the expected. The reducibility decreases even more when K is deposited on the surface of LMC (28 %). The insertion of Sr inside the perovskite cell in substitution of La is expected to favor the formation of Mn(IV) and thus the reducibility. Consistently the H_2-uptake at low temperature is 0.78 mol H_2/mol (Mn+Co) and the reducibility is 74%. Noteworthy in the K/LMC and SKMC catalysts no traces of surface oxygen species (reduced at temperature lower than 300 °C) are observed.

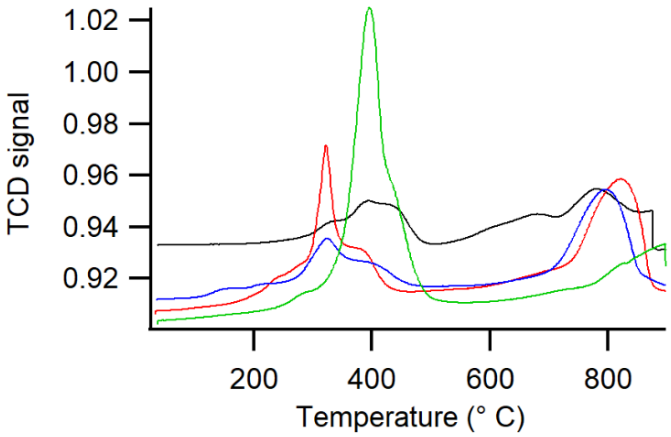

Figure 43 H_2-TPR curves obtained for $LaMn_{0.9}Co_{0.1}O_3$ (blue), $La_{0.9}K_{0.1}Mn_{0.9}Co_{0.1}O_3$ (red), $0.1K/LaMn_{0.9}Co_{0.1}O_3$ (black), $Sr_{0.9}K_{0.1}Mn_{0.9}Co_{0.1}O_3$ (green).

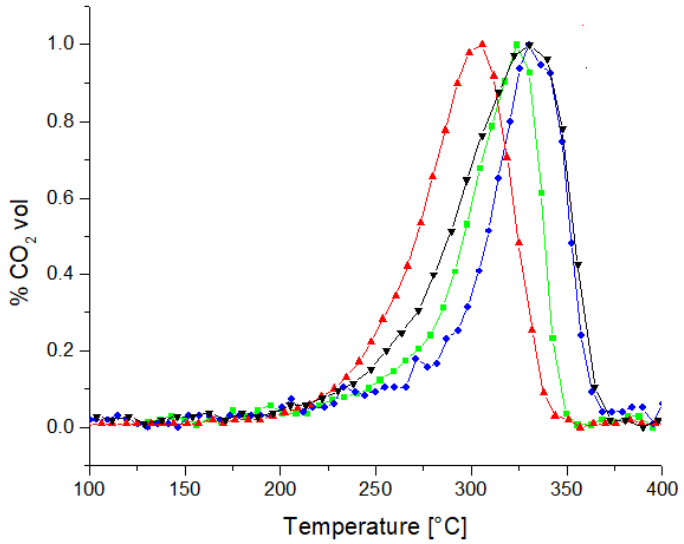

Figure 44 CO_2 formed from soot oxidation, as a function of temperature, for the different catalysts: $LaMn_{0.9}Co_{0.1}O_3$ (blue), $La_{0.9}K_{0.1}Mn_{0.9}Co_{0.1}O_3$ (red), $0.1K/LaMn_{0.9}Co_{0.1}O_3$ (black), $Sr_{0.9}K_{0.1}Mn_{0.9}Co_{0.1}O_3$ (green).

The catalytic behavior in the soot oxidation is compared in Figure 44. The temperature of maximum conversion of soot and the CO_2 production curve shape underline that the insertion of K into the perovskite cell is the more efficient way to activate the catalyst toward soot oxidation. The worst results are obtained with the un-activated LMC. In all cases, however, the presence of a catalyst favors the soot oxidation.

The soot oxidation in absence of catalyst is suggested to proceed through the following steps: firstly, molecular oxygen is chemisorbed onto the soot surface; the dissociative chemisorption allows oxygen atoms to interact with the surface carbon atoms and form a solid complex. At the end the solid complex desorbs subtracting a carbon atom from the soot particle. [48]

The adsorption of the oxidant on the surface-active site of carbon and the desorption of the products strongly depend on the oxidant concentration, on the amount of active sites, on the coverage degree and sticking fault. It is reasonable to consider the dissociative chemisorption of oxygen as the rate determining step. The reactivity of NO_2 is higher with respect to that of O_2; it is suggested that NO_2

can form surface complex molecules of the type C-NO_2 and C-ONO capable of decomposing with increasing temperature forming CO, CO_2 and NO. [48]

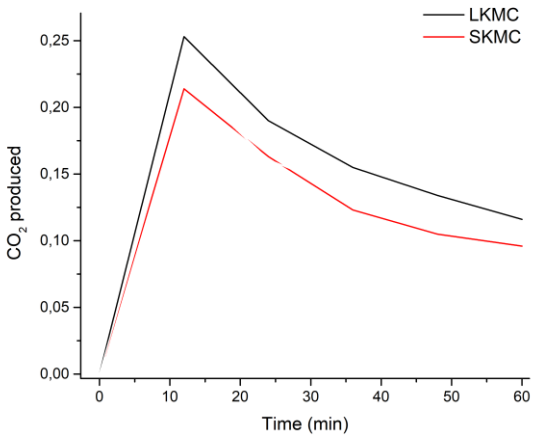

Figure 45 CO_2 formed from CO oxidation after 1 hour of oxidation treatment at 300°C as a function of time: LKMC (black) and SKMC (red).

In presence of oxide-based catalysts the reaction mechanism is more complicated and involves the interaction of perovskite and soot particles. It is suggested that several steps follow: adsorption of oxygen on the catalyst, exchange of activated oxygen species (such as O^- and O^{2-}) from catalyst to the carbon surface, formation of surface oxygen containing (SOC) complex molecules, desorption of SOCs. The catalytic activity is, in this case, affected by the capability of the catalyst to promote the formation and exchange of SOCs.[49]

Li et al. suggest four reaction mechanisms that simultaneously occur during soot combustion: soot oxidation in the soot/catalyst interface carried out by the active species O^{2-} and O^- formed by interaction of oxygen with the surface oxygen vacancies; catalytic oxidation of NO to NO_2 on the catalyst surface; N-containing species adsorb on the catalyst surface and can migrate toward the soot particles; NO oxidation to nitrates and nitrites that can oxidize soot giving rise to CO_2 and N_2; adsorption of NO_2 on the soot surface and direct reaction (of NO_2 or NOx resulting from decomposition) with surface carbon.[50]

All catalysts are active in the soot oxidation: the temperature of maximum combustion, considered as a value to compare the catalytic activity, T_m, decreases of, at least, 60°C with respect of the case without catalyst. The more active catalyst, however, is LKMC with a T_m of 306 °C whereas the worst is LMC. The substitution of La with Sr moves toward lower values (around 250°C) the temperature at which the catalysts start its activity but the T_m is similar to that of LMC (323 vs 330 °C). It is interesting to observe that when K is deposited on the LMC surface the catalyst seems to activate at a temperature similar to that of the LKMC but the T_m is almost coincident to that of LMC).

LKMC is the catalyst characterized by the higher surface segregation of the B-Cations; moreover, the TPR reveals the higher relative amounts of species reduced at lower temperatures (280-320 °C) so suggesting the contribution of surface oxygen active species to switch the reaction and of Mn(IV) species. Mn(IV) is present in higher amount in the SKMC catalysts but the reduction temperature is

shifted at higher temperature (around 400°C). In this last case the almost complete absence of oxygen surface active species is underlined by fitting procedure.

The XPS analysis carried out on the catalysts after reaction reveals a significant surface segregation of Co in LMC; in the other catalysts the surface segregation of K is even more evident. The surface segregation of cobalt in SKMC, is less marked while no particular difference is observed between LKMC and K/LMC. A possible explanation of the phenomenon of Co segregation after reaction is that the more reducible Co is drawn to the surface by the reducing surface potential imposed by contact with the soot.

Figure 45 shows the carbon dioxide profiles obtained on the K-doped catalysts tested for their Oxygen Storage Capacity (OSC), described as follows.

The OSC test was carried out in the same setup, employing 50 mg of catalyst, and composed of two steps. In the first one, the catalyst was subjected to 1 hour of oxidation treatment in synthetic air (80% N_2/20% O_2) at the fixed temperature of 300 °C. The second step, spaced with 2 min He flow, was a CO-TPR reaction at the same fixed temperature, using a 5%CO/He atmosphere. Gas flow was always kept at 100 ml/min.

Hydrogen-TPR had denoted a faster reduction kinetic when K was present in the structure. In this particular test, the first maximum, sampled at 12 min from the beginning of the test, is related to the most reactive oxygen, and the degree of convergence towards 0 yield can instead give insights on the transport and active replenish of the surface oxygen species. We already argued that K insertion mainly affects surface reactivity, increasing oxygen retention on the surface, whereas Sr employment can help in stabilizing the structure and increase oxygen supply to the reaction sites.

LKMC significantly outperforms SKMC, suggesting that with combined K-doping, helping chemisorption of oxidant species, and Co, that has already proven to induce higher oxygen mobility and structural modifications, the material can find a good balance between the two paths of activated oxygen species creation: surface chemisorption of oxygen and transport from the bulk. Transport

contribution becomes more important when doping with Sr. Cobalt was found by Royer et al. to present a good redox activity even at low temperatures.[51] SKMC benefits from the presence of Co, but its transport activity is undermined by K presence.

3.1.3 Partial conclusions

The scope of this project is the investigation and development of innovative perovskite catalysts with the aim of a possible application in the abatement of carbon soot from diesel engines in the automotive sector. The employment of novel materials, such as the ones suggested from the present work, with a reduced content of noble metals is a challenging yet urgent task in this technologic branch. Therefore, the materials here proposed have been tested for soot oxidation in presence of oxygen and NO, with an excess of oxygen to emulate as much as possible the conditions of a real diesel engine exhaust mixture, and for their oxygen storage capacity, to get a deeper insight on their mechanistic aspects in the abovementioned reaction. Testing with different inlet gas mixtures could open the way to other applications such as Gasoline Particulate Filters or Four Way Catalysts.

The compositions chosen arise from redox considerations: Mn, stable both in reducing and oxidizing environments, is a good oxygen donating element in perovskite oxides. In the B-site, furthermore, Co was chosen since it is known from literature its beneficial contribution for soot and NO oxidation. In the A-site the K-doping resulted in an increased catalytic activity both for soot oxidation and NOx conversion. K deposition was also investigated to shed light on its significance when outside the structure. The synthetic approach used is particularly sustainable, since it avoids very high temperature and noxious solvents. A deep structural, morphological and compositional characterization campaign allowed to highlight that Co and K dopings are not responsible for significant surface segregation and/or perovskite structure desegregation. From Temperature Programmed Reaction the reducibility of the materials was tested with the following result: it decreases when La is substituted by Sr. The explanation for this behavior can be found by means of

XPS analysis: Sr-doped samples tend to easily form carbonates and alkaline elements are prone to slight segregation on the surface, whereas Co migrates to the bulk.

Temperature Programmed Oxidation test (*i.e.* catalytic activity assessment) in presence of NO, oxygen and soot showed that the double doping (Co and K) increases notably the catalytic activity of the material in the oxidation reaction: LKMC is able to fully oxidize soot at 306°C, a considerably lower temperature than without any catalyst. Sr-doped samples are still quite active, but less than the counterpart without Sr. Another interesting result is the different behavior for the K-doped sample and the K-deposited one: it is likely that K-doping only is able to promote oxygen vacancies formation.

Considering all these aspects as a whole, both from compositional points of view and from catalytic and OSC tests, LKMC seems to be a good integration of the surface activity guaranteed by K with the importance of oxygen from the lattice thanks to the presence of Co.

3.2 Mn-based Ni-doped perovskites for soot oxidation

Similarly to the previous section, $LaMnO_3$-based perovskites will be the main character of this story. However in this case, Ni-doping was exploited as a strategy to enhance catalytic activity in soot oxidation. Ni reportedly deactivates upon carbon deposition on its surface, as it catalyzes the cracking of carbon containing molecules.[52,53] However, when combined with other reducible transition elements into complex oxide structures, it can significantly boost the activity thanks to the good NOx storage capacity as well as its redox behavior.[54,55]

A set of Ni-based perovskite samples are presented to tackle with environmental issues. The approach followed in this case is the doping with Sr on the A-site of the perovskite and with Ni on the B-site. Ni-based catalysts are often used in the methane steam reforming and are a valid alternative to noble metals as catalysts in this process. However, they often suffer from deactivation since they are sensitive to coke deposition (giving rise to fouling phenomena) due to side processes taking place at

the same time as the main reaction. With proper formulation, nevertheless, Ni can be inserted as a doping element in the perovskite structure and be active as a catalyst in soot oxidation. [56] For this reason the following formulations have been considered: $La_{0.75}K_{0.25}Mn_{0.7}Ni_{0.3}O_3$ (LKMN), $La_{0.75}Sr_{0.25}Mn_{0.7}Ni_{0.3}O_3$ (L25MN), and $La_{0.5}Sr_{0.5}Mn_{0.7}Ni_{0.3}O_3$ (LS50MN).

3.2.1 Materials and methods

The synthetic approach used is the same as in the previous section: the samples were prepared by citrate method[33] starting from La_2O_3 (Sigma-Aldric, pure), $Sr(NO_3)_2$ (Aldrich ≥98%), Manganese(II) acetate tetra hydrate (Sigma-Aldrich ≥99%), K_2CO_3 (Aldrich 95%) and $Ni(NO_3)_2 \cdot 6H_2O$ (Sigma-Aldrich 98%). Carbonate and nitrate precursors were dissolved in an aqueous solution while lanthanum solution was obtained by mineralizing the corresponding oxide with nitric acid. A solution of monohydrate citric acid (Sigma Aldrich ≥99.0%) was added: its molar ratio was 1.9:1 with respect to the total amount of cations. Then solution is then heated up to 80°C in air to promote water evaporation and to obtain a pink wet-gel. The gel is slowly heated up to 400°C for 2 hours in air to decompose the organic framework and the obtained powder samples were ground and calcined at 1000°C for 6 hours to obtain the perovskite.

Each characterization procedure and technique used in this case is identical to the ones described in the previous section, and the catalytic assessment was as well carried out with the same abovementioned protocols.

3.2.2 Results and discussion

BET measurement for specific surface area determination are reported in Table 16. The values are quite low since the high calcination temperatures very likely resulted in a sintering process that reduced considerably the surface area. Sr doping can improve surface area with respect to K doping. Increase in surface area obviously might improve catalytic activity, however the importance of

surface in perovskite catalysis only reaches a certain limit, as transport properties – and the structural and electronic factors that can influence it – gain more importance.[57]

Sample	Specific surface area (m^2/g) obtained by BET
LKMN	12.0
LS50MN	24.0
LS25MN	16.0

Table 16 Specific surface areas of the Ni-doped samples (in m^2/g).

The XRD patterns (Figure 46) are typical for a rhombohedral perovskite phase for the samples LKMN, LS25MN and LS50MN [50-0308 (C)]. The 30% Ni doping also caused segregation of NiO with rhombohedral structure [44-1159 (C)]. In the formulation of the perovskite, a doping element with different ionic radius (Mn(VII) and Ni(II) are respectively 0.46 Å and 0.69 Å) can be the cause for the presence of impurities in the crystalline phase of the perovskite.

The position of the most intense peak shows an angle shift of 0.5° towards higher values from LKMN and LS50MN. The cell shrinks due to the different ionic radius of Sr (1.12 Å) and K (1.38 Å) and therefore the whole pattern is affected by a constant shift.

These structure deformations are relevant as they affect redox and transport properties. In general, the increase in free cell volume of a perovskite can be linked to an enhancement of ionic conductivity even at temperatures as low as 350 °C. Correlations are available in literature that link increased cell free volume with increased oxygen mobility and, consequently, a boost in oxidation performances.[58,59]

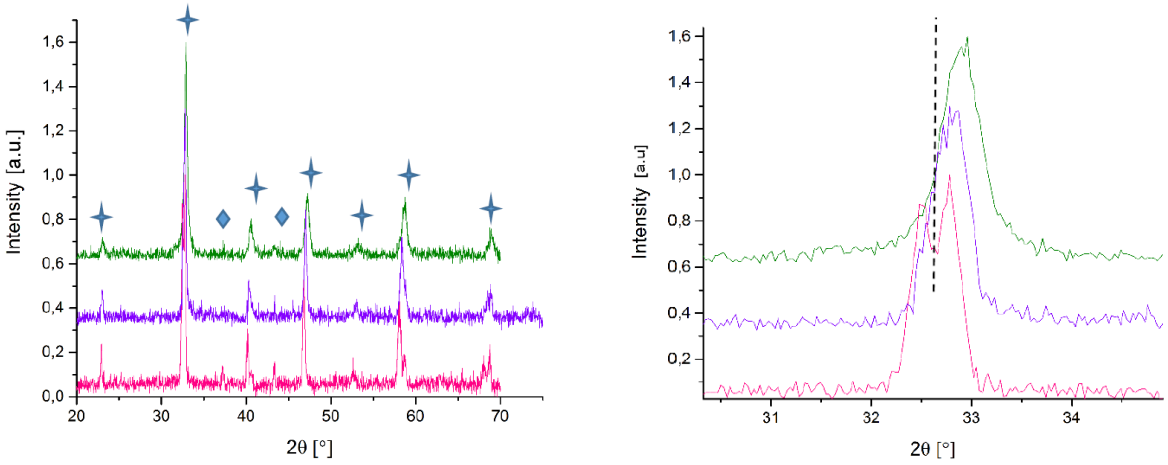

Figure 46 XRD patterns for LKMN (pink), LS25MN (violet) and LS50MN (green). The cross symbol indicates the perovskite phase, the diamond shape the NiO. On the right-hand side of the figure, the inset for the most intense peak in the interval 30°-35°.

From the inspection of XPS surface composition analysis (reported in Table 17), a specific trend is notable: an excess of oxygen on the surface in the samples doped with Sr (LS25MN and LS50MN) evidences the formation of carbonates and hydroxide species and a surface excess of Mn. In the case of LKMN oxygen is slightly substoichiometric. Ni shows a tendency to diffuse in the bulk of the structure, since in all samples the experimental value is lower than the nominal one. In LKMN the over-stoichiometric noticeable for La suggests instead a migration to the surface of the cation, whereas in the sample LS25MN and LS50MN this is not detectable.

Table 17 also compares EDX compositional analysis and the nominal composition as atomic percentage. The advantage of this kind of comparison lies in the different sampling depth of XPS and EDX techniques, the former strictly superficial (a few nm of depth) and the latter more bulk-related (up to 100 nm).

The global B-site/A-site ratio is lower for LKMN and LSMN25. EDX data, conversely, evidence the opposite trend. Increasing Sr doping equilibrates the relative amounts, also causing a decrease of ionic mobility. If we consider the possible non-stoichiometry δ of these perovskite formulations, namely the difference between the theoretical six negative charges brought by oxygen and the sum of the positive charges belonging to cations, we find the following range of values (depending if we consider Mn as 3+ or 4+):

- 5.5-6.2 for LKMN
- 5.75-6.45 for LSMN25
- 5.5-6-2 for LSMN50

Despite the same values of theoretical non-stoichiometry, LKMN and LSMN50 exhibit opposite trends as far as surface and bulk segregations are concerned, meaning that the nature of the cations involved (ionic radius, electronegativity, mutual interactions) matters more than simple compensation of charges.

Oxygen is significantly over-stoichiometric in the surface of Sr-containing samples and this correlates with the O1s XP spectrum, indicating the presence of carbonates.

Ni is generally more concentrated in the bulk of the material. After reaction data show that the concentration of the dopant on the surface is significantly increased in LSMN25 and LSMN50. This does not happen at the expenses of Mn concentration, which is more than doubled as well, indicating a comparable redox response to the reaction environment for these two elements. La instead diminishes (particularly notable from Mn/La ratio column), as dramatically does oxygen, despite the high presence of oxidant species in the reaction atmosphere. This corroborates the assumption that contact with soot imposes a reducing surface potential to the catalysts.

		La	K/Sr	Mn	Ni	O	K(Sr)/La	Mn/La	(Ni+Mn)/(K(Sr)+La)
LKMN	XPS	19.8	5.1	14.1	3.3	57.7	0.3	0.7	0.7
		(46.8)	(12.1)	(33.4)	(7.8)				
	EDX	12.9	5.3	19.1	7.4	55.3	0.4	1.5	1.5
		(28.9)	(11.9)	(42.7)	(16.5)				
	Nominal	15.0	5.0	14.0	6.0	60.0	0.3	0.9	1.0
		(37.5)	12.5	(35.0)	(15.0)				
	After reaction	-	-	-	-	-	-	-	-
		-	-	-	-				
LSMN25	XPS	9.5	8.6	13.3	2.7	66.0	0.9	1.4	0.9
		(27.9)	(25.2)	(39.0)	(7.2)				
	EDX	19.2	5.6	19.4	9.2	46.6	0.3	1.0	1.2
		(36.0)	(10.5)	(36.3)	(17.2)				
	Nominal	15.0	5.0	14.0	6.0	60.0	0.3	0.9	1.0
		(37.5)	(5.0)	(35.0)	(15.0)				
	After reaction	7.1	9.5	24.0	14.3	45.1	1.34	3.4	2.3
		(12.9)	(17.3)	(43.7)	(26.1)				
LSMN50	XPS	8.7	9.0	16.2	4.7	66.6	1.0	1.9	1.2
		(22.5)	(23.3)	(42.0)	(12.2)				
	EDX	9.2	10.4	12.7	5.5	62.1	1.1	1.4	0.9
		(24.3)	(27.4)	(33.5)	(14.5)				
	Nominal	10.0	10.0	14.0	6.0	60.0	1.0	1.4	1.0
		(25.0)	(25.0)	(35.0)	(15.0)				
	After reaction	7.5	8.8	24.8	13.5	45.3	1.2	3.3	2.35
		(13.7)	(16.1)	(45.3)	(24.7)				

Table 17 Compositional analysis (atomic percentages) obtained via XPS and EDX on the Ni-doped series of samples. "After reaction" values are taken post the soot oxidation test by XPS. Values in brackets indicate the percentage without considering oxygen contributions.

Sample	Sr $3d_{5/2}$	Sr $3d_{3/2}$	$Mn2p_{3/2}$	Mn $2p_{1/2}$	O 1s (lattice)	O 1s (OH^-, CO_3^{2-})
LKMN	-	-	641.4	652.9	529.9	530.7
LS50MN	132.5	134.0	642.4	653.9	529.4	532.2
LS25MN	133.1	134.1	642.1	653.9	529.7	531.5

Table 18 Position (Binding Energies, in eV) of the main XPS signals observed in the (as prepared) samples.

In Figure 47 XP spectra obtained for LKMN (pink), LS25MN (purple) and LS50MN (green). the survey does not show the presence of unexpected elements (except for adventitious carbon): indeed only Ni, Mn, La, K and Sr are present. Core levels 3/2 and 1/2 of the Mn 2p peak show Binding Energy values that are lower for LKMN (1 eV approximately) as compared to LS(25/50)MN. From the Binding Energy range comparison reported in Table 18 for manganese oxides it can be assumed that Mn in LKMN is predominantly present in the Mn (III) oxidation state, although Mn (III) and Mn (IV) result in the same photoelectronic peak but with slight differences in shape. Lower oxidation states (*e.g.* Mn^{2+}) can be excluded since MnO profile shows a satellite peak (at approximately 647 eV) placed between the two core levels as compared to the other oxides. [60]

Oxygen 1s photoelectronic peak is typical for lattice oxygen (peak at lower Binding Energy) and for metal carbonates and hydroxylic groups on the surface (531.5-532.2 eV); in the case of the Sr-doped samples, $SrCO_3$ is also present, as confirmed by the contribution on the Sr 3d photoelectronic spectrum at 134.4 eV. [39]

XP spectra recorded after reaction for the sample LKMN show some significant alteration of the structure of the catalyst: $La3d_{3/2}$ peak shifts towards higher BE, possibly due to the presence of hydroxide species on the surface. $Mn2p_{3/2}$ shifts instead to lower BE, indicating a likely alteration of the oxidation state from Mn(IV) to Mn(III) or even Mn(II). Finally O1s peak, heavily contaminated by the signal for SiO_2, used during the reaction and still present on the surface as trace, highlights a new contribution to the main peak at 530.9 eV, very typical for carbonates and hydroxides on the surface.

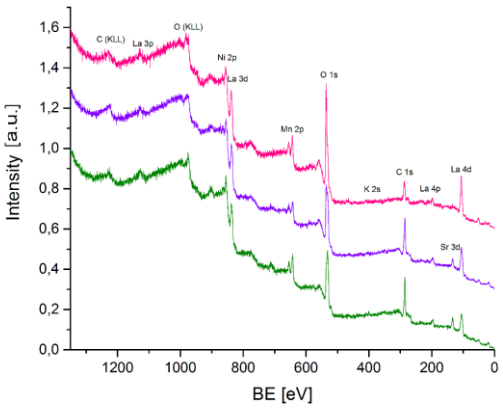

Figure 47 XP spectra obtained for LKMN (pink), LS25MN (purple) and LS50MN (green).

H_2-TPR tests are reported in Figure 48 and reduction peaks for Mn and Ni are recognizable. La and Sr reduction processes take place at temperature that are higher than 900°C.

Comparing the reduction profile with literature data ($LaMn_{1-x}Ni_xO_3$) [61] the identification of the reduction peaks was made possible: the main peaks, placed in the temperature range 300-450°C, are indicative of Mn (IV) reduction to Mn (III) (signal 1 and 2), in the same interval Ni (III) is reduced to Ni (II). Between 450 and 600°C Ni (II) is reduced to Ni (0) (signal 3). Over 650°C it is noticeable the reduction signal of Mn (III) to Mn (II) (signal 4) that causes the decay of the perovskite structure. In this case doping is able to affect the chemical environment of the elements in the perovskite:[62] the reduction peak for Mn(IV)/Mn(III). The K doping in LKMN shifts the reduction peaks towards higher temperature as compared to similar compounds, decreasing the reducibility of the compound, and making the reduction profile sharper (due to the higher relative intensity, see signal 2). This enhancement of the intensity can be caused by the absence of strontium carbonate on the surface, as highlighted by XPS, which enables the reductive mechanism of Mn and Ni by H_2, on the other side the same species in LSMN TPR profile give peaks with lower resolution.

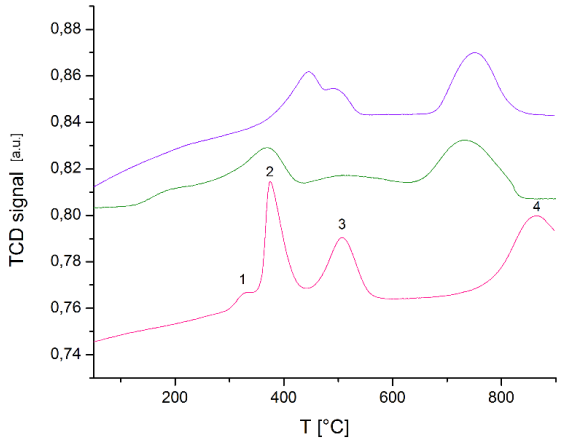

Figure 48 H_2-TPR profiles for LKMN (pink), LS25MN (purple) and LS50MN (green) in the range 50-900°C.

LS25MN and LKMN show poor agreement between the experimental and the expected hydrogen consumption; the case of LS25MN is particularly significant since the presence of strontium carbonate hindered bulk reduction, as detected by XPS surface composition analysis. Unlike the other samples, for LS50MN expected consumption and experimental data are converging, indeed Sr surface percentage is lower. Moreover, in LKMN reduction profile, the last reduction peak is not complete under 900°C, significantly decreasing the experimental hydrogen consumption, which is obtained by integration of the reduction profile curve and instrumental TCD detector calibration. Considering the reduced species and the reduction peaks, it was possible to calculate the average theoretical oxidation number of Mn for each sample, and it was equal 3.5. for LKMN and LS50MN and 3.3 for LS25MN. Nickel reduction contribution is expected to appear in the intermediate temperature range (450 °C-600 °C).[63] The clearer Ni contribution is displayed by LKMN, whereas Sr doping seems to undermine Ni reducibility at a point where in LSMN50 the Ni reduction peak is re-shaped in a broad and weak signal. Generally, in both series K-doping produces intense and narrow signals, seemingly accelerating the scavenging of the active oxygen, whereas Sr doping, or no A-site doping, in this order, expand that reduction in time and temperature range. Nevertheless, it is interesting the fact that K-doped samples present a certain high-temperature shift of the second Mn(III) reduction process, more likely to depend upon structural properties of the material, than readily available surface sites. TPR data suggest that the insertion of K points towards maximizing surface activity, whereas Sr doping can improve the overall redox behavior of the structure as well as its stability (Ni is less prone to undergo reduction).

SEM magnified pictures show a homogeneous surface morphology for each sample: the particles form aggregates with communicating porous cavities. LKMN and LS25MN particles are more dispersed than LS50MN. The diameter of the aggregates for LKMN and LS50MN is wider, while the finer granulometry caused a higher packing for LS25MN sample. The diameter of the particles in LKMN and LS25MN is around 100 nm, see Figure 49.

The oxidation of soot in presence of oxygen but without any catalytic species implied takes place between 600 and 800°C,[64] depending on the different experimental conditions, able to interfere with the kinetics of the reaction. Similar mechanistic considerations as the previous section hold true also in this case, given the oxygen adsorption-mediated process that features soot oxidation. Among the most known mechanisms for soot oxidation by oxidizing agents as O_2, NO, NO_2 or other species, Marsh and Kuo [48] suggested a mechanism that implies mainly three stages. Firstly O_2 undergoes chemisorption on the surface of the carbon nanoparticles and then an oxygen atom is transferred from the oxidizing gas to carbon to form a solid complex, which will be eventually desorbed, subtracting a carbon atom from the surface of solid.

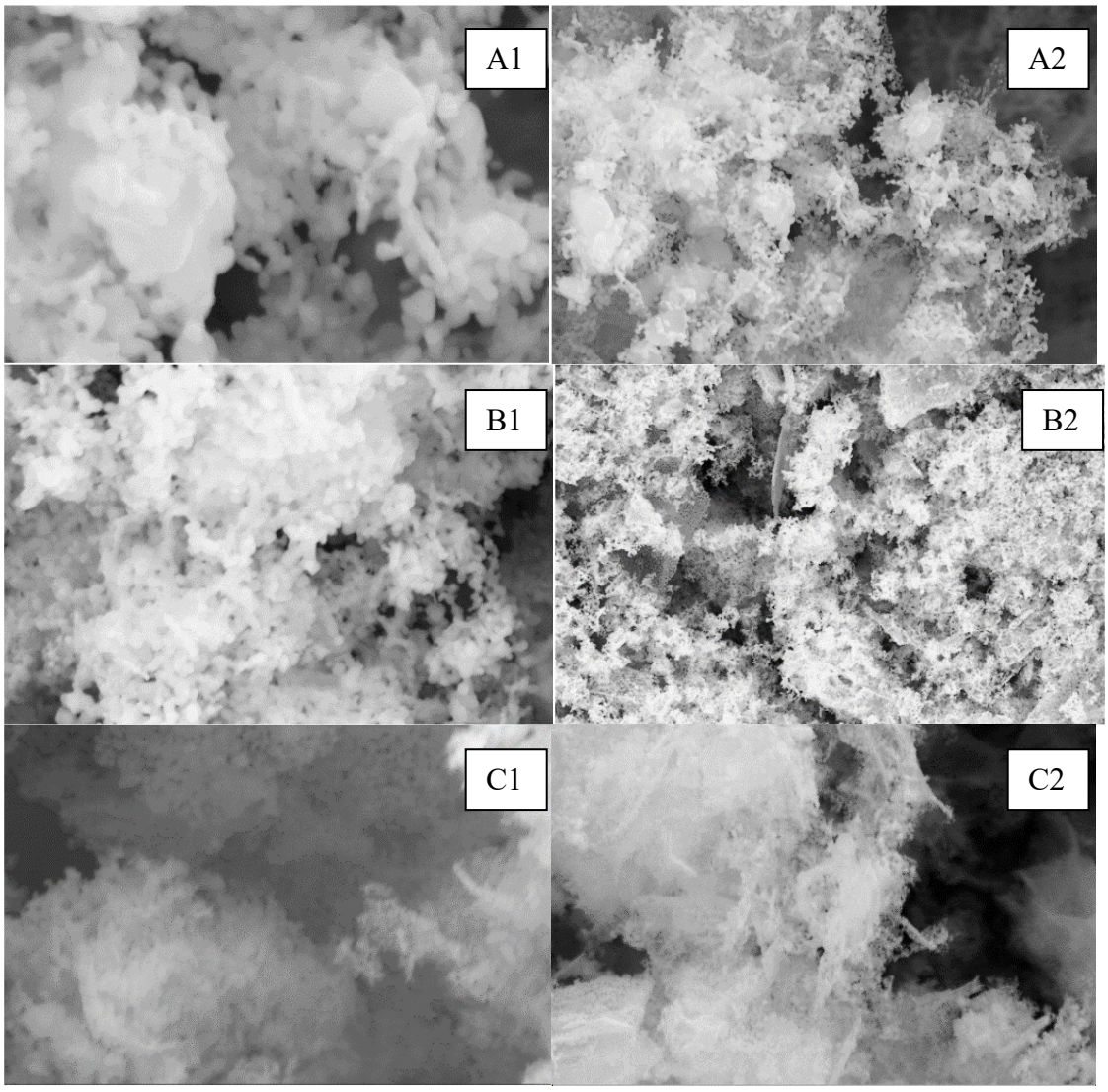

Figure 49 SEM images: A: LKMN; B: LS25MN; C: LS50MN. Images labelled with "1" are taken at 10^5K magnification, images labelled with "2" at 10^4K magnification.

The adsorption of the oxidizing molecule on the free sites of carbon and the desorption of the produced gases (CO and CO_2) depends on the concentration of the gas, as well as on the degree of surface coating and on the temperature. The adsorption represents the rate determining step of the process and the desorption rate increases as temperature and coating degree increase. NO_2 reactivity is higher than O_2 towards soot, especially below 600-800°C, the typical temperature at which oxygen reacts. It is thought that NO_2 can form surface complexes with carbon such as C-NO_2 and C-ONO, later decomposed increasing the temperature to CO and/or CO_2 releasing NO. Mixture with carbon, NO and O_2 were studied at high temperatures (850°C) with results that suggest that the favored reaction path is the interaction of gaseous NO with the surface complexes containing nitrogen and oxygen to form N_2.

A preliminary test has been performed without the catalyst in presence of only NO+O_2 mixture with soot in the same reaction conditions. It is known that the excess of oxygen and the temperature range 100-500°C is favoring the oxidation of NO to NO_2 which oxidizes the soot.[48] In the described conditions, no CO or any other byproduct was detected. This excludes the possible formation of N_2O from NO disproportion at low temperatures.[64] CO_2 is produced during the reaction when the temperature increases and its concentration has a peak around 390°C. This demonstrates that the oxidation in presence of NO_2 is activated in a lower temperature range than the process with only O_2. In Figure 50 the catalytic tests for Temperature Programmed Oxidation are reported, between 100 and 400°C. The results are summarized in Table 19. K-doped sample (LKMN) shows the highest activity with the lowest T_m (temperature at which the combustion rate is at its highest, 310°C), while the T_m for Sr-doped sample is roughly 30°C higher. K-doping enhances the oxidative activity of the perovskite since it increases Mn in the IV oxidation state, favoring therefore the formation of oxygen vacancies. Sr instead tends to react to form $SrCO_3$ on the surface of the perovskite (as demonstrated by XPS analysis), deactivating the catalyst. In particular, the deactivation rises from the interruption

of the contact points between soot and catalyst, which are fundamental to the mobility of oxygen vacancies.

The OSC test, as described previously, was carried out in the same setup, employing 50 mg of catalyst, and composed of two steps. In the first one, the catalyst was subjected to 1 hour of oxidation treatment in synthetic air (80% N_2/20% O_2) at the fixed temperature of 300 °C. The second step, spaced with 2 min He flow, was a CO-TPR reaction at the same fixed temperature, using a 5%CO/He atmosphere. Gas flow was always kept at 100 ml/min.

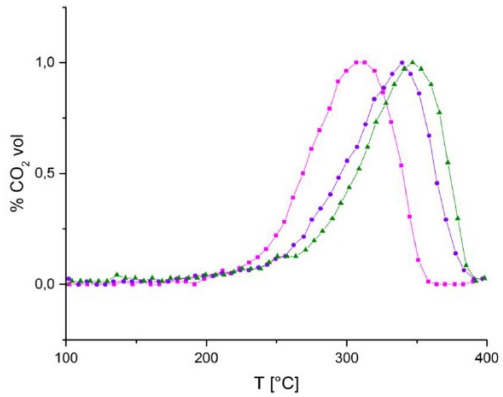

Figure 50 Catalytic TPO tests for LKMN (purple), LS50MN (green) and LS25MN (dark purple).

Sample	T_m (°C)
LKMN	310
LS25MN	347
LS50MN	340

Table 19 Temperature of maximum conversion for soot in LKMN; LS25MN and LS50MN.

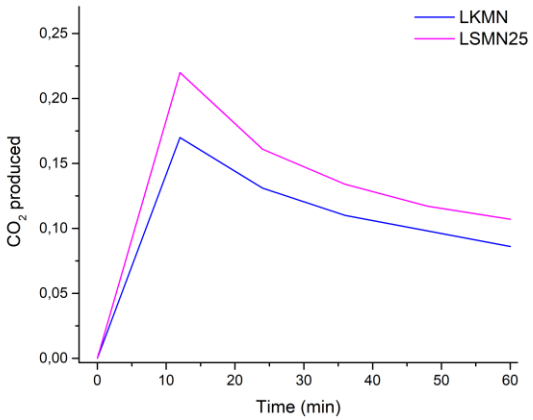

Figure 51 CO_2 formed from CO oxidation after 1 hour of oxidation treatment at 300 °C as a function of time: $La_{0.75}K_{0.25}Mn_{0.7}Ni_{0.3}O_3$ (blue) and $La_{0.75}Sr_{0.25}Mn_{0.7}Ni_{0.3}O_3$ (purple).

Figure 51 shows the carbon dioxide production profiles obtained on two selected catalysts, LKMN and LS25MN. In this test the first peak, sampled at 12 minutes from the beginning of the test, is related to the most active oxygen, and the degree of convergence toward zero yield can give insights on the transport and active replenishment of the surface oxygen species. LKMN, a K-doped sample, features a faster decay of carbon dioxide production than LS25MN. K insertion indeed mainly affects surface reactivity, increasing oxygen retention on the surface, whereas Sr employment can help in stabilizing the structure and increase oxygen supply to the reaction sites. Accordingly, LKMN is the least performing sample in OSC testing. Therefore, Sr insertion is useful as regards transport contribution but conversely the sample suffer from the presence of Ni, not highly reducible. Indeed, studies on the structural effect of Ni insertion in a $LaMnO_3$ lattice indicate an increase in the Oxygen Storage Capacity thanks to the adsorption activity on Ni(III) sites but Ni presence itself can undermine the oxygen transport mechanism. [61] Even if LKMN is not performing better than the Sr-doped sample in the OSC, its catalytic performances in soot oxidation are satisfactory: unlike CO oxidation, soot conversion seems to require a higher involvement of all the surface species present, meaning that the present of potassium is proving crucial to increase the surface oxygen activation.

3.2.3 Partial conclusion

A set of perovskites with different A-site doping, and constant B-site doping, were synthetized, extensively characterized, and compared in soot oxidation by oxygen and NO, as well as OSC via CO-TPR in the steady state. K-doping proved to induce a higher contribution of reactive surface oxygen species, as it was evidenced by H_2-TPR comparisons as well as catalytic results. Sr-instead, despite the tendency to segregate on the surface, has the positive effect of improving oxygen mobility from the inner layers of the lattice. However, this was not enough to achieve satisfactory results in soot oxidation, due to both the presence of unreactive strontium carbonate on the surface and the relatively lower adsorption activity as compared to potassium. A heavier doping can likely cause a higher concentration of oxygen vacancies on the surface. Oxygen vacancies are also important site for the activation of NO, that must be oxidized to NO_2 and extract carbon atoms from the soot matrix. At the same time it is possible that oxygen vacancies activate the decomposition to N_2O, rather than NO_2, on which active species act towards N_2 production.

However, the comparison of results between LSMN25 and LSMN50 reveals how increasing Sr doping does not necessarily lead to better performances. In the latter case, B-site elements are much more concentrated on the surface than the less-doped sample, and also with respect to K-doped samples. Interestingly, the B-site dopant Ni tends to remain inside the bulk material, despite being attracted towards the surface during reaction, as it can be imposed by the contact with soot, that can most certainly be viewed as a reducing agent.

In conclusion perovskite catalysts prove to be effective and comparable to noble metal catalyst in this strictly redox reaction:[65–68] active participation of cations of the catalyst, their ability to reduce and coordinate oxygen and possibly to let oxygen itself migrate throughout the structure are well known properties of perovskite catalysts.

3.3 Final remarks

These two distinct sets of perovskites allowed to shed light on the similarities and differences that different B-site doping exert on the structures and catalytic performances of the samples, with a specific focus on catalytic soot oxidation. Both dopants, Co and Ni, exhibit a marked tendency to accumulate in the bulk of the material, rather than segregating onto the surface, despite the reducing character of soot.

Moreover K-doping, as compared to K deposition, was proved to be a crucial feature inducing structure modifications that could enhance catalytic performances, thanks to a “redox-driven” design of the material.

If we compare the catalytic performances of both sets, LKMC series appear to be more active in soot oxidation, but the least active in Oxygen Storage Capacity tests. This pronounced activity can be ascribed to the K helping the surface activity of the material and Co acting in the bulk as a generator of oxygen vacancies that result in an increased ability of binding oxygen, with its counterpart, Ni, being less active to this extent.

References

(1) Jacobson, M. Z. Short-Term Effects of Controlling Fossil-Fuel Soot, Biofuel Soot and Gases, and Methane on Climate, Arctic Ice, and Air Pollution Health. *J. Geophys. Res. Atmos.* **2010**, *115* (14), 14209. https://doi.org/10.1029/2009JD013795.

(2) Lu, J.-H.; Chen, Y.-S. The Regeneration of Diesel Particulates Filter (DPF) with Hydrogen; 2013. https://doi.org/10.4271/2013-01-0090.

(3) Hernández-Giménez, A. M.; Castelló, D. L.; Bueno-López, A. Diesel Soot Combustion Catalysts: Review of Active Phases. *Chem. Pap.* **2014**, *68* (9), 1154–1168. https://doi.org/10.2478/s11696-013-0469-7.

(4) Peng, X.; Lin, H.; Shangguan, W.; Huang, Z. A Highly Efficient and Porous Catalyst for Simultaneous Removal of NOx and Diesel Soot. *Catal. Commun.* **2007**, *8* (2), 157–161. https://doi.org/10.1016/j.catcom.2006.04.015.

(5) Teraoka, Y.; Nakano, K.; Shangguan, W.; Kagawa, S. Simultaneous Catalytic Removal of Nitrogen Oxides and Diesel Soot Particulate over Perovskite-Related Oxides. *Catal. Today* **1996**, *27* (1–2), 107–113. https://doi.org/10.1016/0920-5861(95)00177-8.

(6) Teraoka, Y.; Nakano, K.; Kagawa, S.; Shangguan, W. F. F. Simultaneous Removal of Nitrogen Oxides and Diesel Soot Particulates Catalyzed by Perovskite-Type Oxides. *Appl. Catal. B Environ.* **1995**, *5* (3), L181–L185. https://doi.org/10.1016/0926-3373(94)00059-X.

(7) Teraoka, Y.; Kanada, K.; Kagawa, S. Synthesis of La□K□Mn□O Perovskite-Type Oxides and Their Catalytic Property for Simultaneous Removal of NOx and Diesel Soot Particulates. *Appl. Catal. B Environ.* **2001**, *34* (1), 73–78. https://doi.org/10.1016/S0926-3373(01)00202-8.

(8) Legutko, P.; Kaspera, W.; Jakubek, T.; Stelmachowski, P.; Kotarba, A. Influence of Potassium and NO Addition on Catalytic Activity in Soot Combustion and Surface Properties of Iron and Manganese Spinels. *Top. Catal.* **2013**, *56* (9–10), 745–749. https://doi.org/10.1007/s11244-013-0026-1.

(9) Li, Q.; Wang, X.; Xin, Y.; Zhang, Z.; Zhang, Y.; Hao, C.; Meng, M.; Zheng, L. L.; Zheng, L. L. A Unified Intermediate and Mechanism for Soot Combustion on Potassium-Supported Oxides. *Sci. Rep.* **2015**, *4* (1), 4725. https://doi.org/10.1038/srep04725.

(10) Pacultová, K.; Draštíková, V.; Chromčáková; Bílková, T.; Kutláková, K. M.; Kotarba, A.; Obalová, L. On the Stability of Alkali Metal Promoters in Co Mixed Oxides during Direct NO Catalytic Decomposition. *Mol. Catal.* **2017**, *428*, 33–40. https://doi.org/10.1016/j.molcata.2016.11.038.

(11) Shang, Z.; Sun, M.; Che, X.; Wang, W.; Wang, L.; Cao, X.; Zhan, W.; Guo, Y.; Guo, Y.; Lu, G. The Existing States of Potassium Species in K-Doped Co3O4 Catalysts and Their Influence on the Activities for NO and Soot Oxidation. *Catal. Sci. Technol.* **2017**, *7* (20), 4710–4719. https://doi.org/10.1039/c7cy01444a.

(12) Bin, F.; Song, C.; Lv, G.; Song, J.; Gong, C.; Huang, Q. La1-XKxCoO3 and LaCo 1-YFeyO3 Perovskite Oxides: Preparation, Characterization, and Catalytic Performance in the Simultaneous Removal of NOx and Diesel Soot. *Ind. Eng. Chem. Res.* **2011**, *50* (11), 6660–6667. https://doi.org/10.1021/ie200196r.

(13) Rinkenburger, A.; Toriyama, T.; Yasuda, K.; Niessner, R. Catalytic Effect of Potassium Compounds in Soot Oxidation. *ChemCatChem* **2017**, *9* (18), 3513–3525. https://doi.org/10.1002/cctc.201700338.

(14) Wen, W.-Y. Mechanisms of Alkali Metal Catalysis in the Gasification of Coal, Char, or Graphite. *Catal. Rev.* **1980**, *22* (1), 1–28. https://doi.org/10.1080/03602458008066528.

(15) Jimenez, R.; Garcia, X.; Cellier, C.; Ruiz, P.; Gordon, A. Soot Combustion with K/MgO as Catalyst. *Appl. Catal. A Gen.* **2006**, *297* (2), 125–134. https://doi.org/10.1016/j.apcata.2005.08.042.

(16) Ura, B.; Trawczyński, J.; Kotarba, A.; Bieniasz, W.; Illán-Gómez, M. J.; Bueno-López, A.; López-Suárez, F. E. Effect of Potassium Addition on Catalytic Activity of SrTiO3 Catalyst for Diesel

Soot Combustion. *Appl. Catal. B Environ.* **2011**, *101* (3–4), 169–175. https://doi.org/10.1016/j.apcatb.2010.09.018.

(17) Zhang, Y.; Zou, X. The Catalytic Activities and Thermal Stabilities of Li/Na/K Carbonates for Diesel Soot Oxidation. *Catal. Commun.* **2007**, *8* (5), 760–764. https://doi.org/10.1016/j.catcom.2006.09.008.

(18) Querini, C. A.; Ulla, M. A.; Requejo, F.; Soria, J.; Sedrán, U. A.; Miró, E. E. Catalytic Combustion of Diesel Soot Particles. Activity and Characterization of Co/MgO and Co,K/MgO Catalysts. *Appl. Catal. B Environ.* **1998**, *15* (1–2), 5–19. https://doi.org/10.1016/S0926-3373(97)00032-5.

(19) Aneggi, E.; de Leitenburg, C.; Dolcetti, G.; Trovarelli, A. Diesel Soot Combustion Activity of Ceria Promoted with Alkali Metals. *Catal. Today* **2008**, *136* (1–2), 3–10. https://doi.org/10.1016/J.CATTOD.2008.01.002.

(20) Wu, X.; Radovic, L. R. Catalytic Oxidation of Carbon/Carbon Composite Materials in the Presence of Potassium and Calcium Acetates. *Carbon N. Y.* **2005**, *43* (2), 333–344. https://doi.org/10.1016/j.carbon.2004.09.025.

(21) McKee, D. W.; Chatterji, D. The Catalytic Behavior of Alkali Metal Carbonates and Oxides in Graphite Oxidation Reactions. *Carbon N. Y.* **1975**, *13* (5), 381–390. https://doi.org/10.1016/0008-6223(75)90006-8.

(22) McKee, D. W. Mechanisms of the Alkali Metal Catalysed Gasification of Carbon. *Fuel* **1983**, *62* (2), 170–175. https://doi.org/10.1016/0016-2361(83)90192-8.

(23) Kikuchi, E.; Adachi, H.; Momoki, T.; Hirose, M.; Morita, Y. Supported Alkali Catalysts for Steam Gasification of Carbonaceous Residues from Petroleum. *Fuel* **1983**, *62* (2), 226–230. https://doi.org/10.1016/0016-2361(83)90204-1.

(24) Kapteijn, F.; Abbel, G.; Moulijn, J. A. CO2 Gasification of Carbon Catalysed by Alkali Metals. *Fuel* **1984**, *63* (8), 1036–1042. https://doi.org/10.1016/0016-2361(84)90184-4.

(25) Moulijn, J. A.; Cerfontain, M. B.; Kapteijn, F. Mechanism of the Potassium Catalysed Gasification of Carbon in CO2. *Fuel* **1984**, *63* (8), 1043–1047. https://doi.org/10.1016/0016-2361(84)90185-6.

(26) Nishiyama, Y. Catalytic Gasification of Coals — Features and Possibilities. *Fuel Process. Technol.* **1991**, *29* (1–2), 31–42. https://doi.org/10.1016/0378-3820(91)90015-5.

(27) Wood, B. J.; Fleming, R. H.; Wise, H. Reactive Intermediate in the Alkali-Carbonate-Catalysed Gasification of Coal Char. *Fuel* **1984**, *63* (11), 1600–1603. https://doi.org/10.1016/0016-2361(84)90234-5.

(28) You, R.; Zhang, Y.; Liu, D.; Meng, M.; Jiang, Z.; Zhang, S.; Huang, Y. A Series of Ceria Supported Lean-Burn NOx Trap Catalysts LaCoO3/K2CO3/CeO2 Using Perovskite as Active Component. *Chem. Eng. J.* **2015**, *260*, 357–367. https://doi.org/10.1016/j.cej.2014.09.016.

(29) Jiménez, R.; García, X.; López, T.; Gordon, A. L. Catalytic Combustion of Soot. Effects of Added Alkali Metals on CaO–MgO Physical Mixtures. *Fuel Process. Technol.* **2008**, *89* (11), 1160–1168. https://doi.org/10.1016/j.fuproc.2008.05.013.

(30) Chen, S. G.; Yang, R. T. Unified Mechanism of Alkali and Alkaline Earth Catalyzed Gasification Reactions of Carbon by CO 2 and H 2 O. *Energy & Fuels* **1997**, *11* (2), 421–427. https://doi.org/10.1021/ef960099o.

(31) Chen, S. G.; Yang, R. T. The Active Surface Species in Alkali-Catalyzed Carbon Gasification: Phenolate (C□O□M) Groups vs Clusters (Particles). *J. Catal.* **1993**, *141* (1), 102–113. https://doi.org/10.1006/jcat.1993.1122.

(32) Mul, G.; Neeft, J. P. A.; Kapteijn, F.; Makkee, M.; Moulijn, J. A. Soot Oxidation Catalyzed by a Cu/K/Mo/Cl Catalyst: Evaluation of the Chemistry and Performance of the Catalyst. *Appl. Catal. B, Environ.* **1995**, *6* (4), 339–352. https://doi.org/10.1016/0926-3373(95)00027-5.

(33) Marcilly, C.; Courty, P.; Delmon, B. Preparation of Highly Dispersed Mixed Oxides and Oxide Solid Solutions by Pyrolysis of Amorphous Organic Precursors. *J. Am. Ceram. Soc.* **1970**, *53* (1), 56–57. https://doi.org/10.1111/j.1151-2916.1970.tb12003.x.

(34) Gálvez, M. E.; Ascaso, S.; Stelmachowski, P.; Legutko, P.; Kotarba, A.; Moliner, R.; Lázaro, M. J. Influence of the Surface Potassium Species in Fe–K/Al2O3 Catalysts on the Soot Oxidation Activity in the Presence of NOx. *Appl. Catal. B Environ.* **2014**, *152–153*, 88–98. https://doi.org/10.1016/j.apcatb.2014.01.041.

(35) Shirley, D. A. High-Resolution x-Ray Photoemission Spectrum of the Valence Bands of Gold. *Phys. Rev. B* **1972**, *5* (12), 4709–4714. https://doi.org/10.1103/PhysRevB.5.4709.

(36) Briggs, D. Handbook of X-Ray Photoelectron Spectroscopy C. D. Wanger, W. M. Riggs, L. E. Davis, J. F. Moulder and G. E.Muilenberg Perkin-Elmer Corp., Physical Electronics Division, Eden Prairie, Minnesota, USA, 1979. 190 Pp. $195; Chastain, J., Ed.; Eden Prairie, 1981; Vol. 3. https://doi.org/10.1002/sia.740030412.

(37) Umbach, E. *Practical Surface Analysis*; Wiley: New York, 1992; Vol. 11. https://doi.org/10.1016/0165-9936(92)87016-d.

(38) Shannon, R. D. Revised Effective Ionic Radii and Systematic Studies of Interatomic Distances in Halides and Chalcogenides. *Acta Crystallogr. Sect. A* **1976**, *32* (5), 751–767. https://doi.org/10.1107/S0567739476001551.

(39) Naumkin, V. A.; Kraut-Vass, A.; Gaarenstroom, S. W.; J., P. C. NIST X-Ray Photoelectron Spectroscopy Database. *Meas. Serv. Div. Natl. Inst. Stand. Technol.* **2012**, *20899* (20), 20899. https://doi.org/10.18434/T4T88K.

(40) Galenda, A.; Natile, M. M.; Krishnan, V.; Bertagnolli, H.; Glisenti, A. LaSrCoFeO and Fe 2 O 3 /LaSrCoFeO Powders: Synthesis and Characterization. *Chem. Mater.* **2007**, *19* (11), 2796–2808. https://doi.org/10.1021/cm062742i.

(41) Galenda, A.; Natile, M. M.; Nodari, L.; Glisenti, A. La0.8Sr0.2Ga0.8Fe0.2O3-δ: Influence of the Preparation Procedure on Reactivity toward Methanol and Ethanol. *Appl. Catal. B Environ.* **2010**, *97* (3–4), 307–322. https://doi.org/10.1016/j.apcatb.2010.04.004.

(42) Madey, T. E.; Yakshinskiy, B. V.; Ageev, V. N.; Johnson, R. E. Desorption of Alkali Atoms and Ions from Oxide Surfaces: Relevance to Origins of Na and K in Atmospheres of Mercury and the Moon. *J. Geophys. Res. E Planets* **1998**, *103* (E3), 5873–5887. https://doi.org/10.1029/98JE00230.

(43) Glisenti, A.; Pacella, M.; Guiotto, M.; Natile, M. M.; Canu, P. Largely Cu-Doped LaCo1-XCuxO3 Perovskites for TWC: Toward New PGM-Free Catalysts. *Appl. Catal. B Environ.* **2016**, *180*, 94–105. https://doi.org/10.1016/j.apcatb.2015.06.017.

(44) Onrubia, J. A.; Pereda-Ayo, B.; De-La-Torre, U.; González-Velasco, J. R. Key Factors in Sr-Doped LaBO3 (B = Co or Mn) Perovskites for NO Oxidation in Efficient Diesel Exhaust Purification. *Appl. Catal. B Environ.* **2017**, *213*, 198–210. https://doi.org/10.1016/j.apcatb.2017.04.068.

(45) Ramesh, K.; Chen, L.; Chen, F.; Liu, Y.; Wang, Z.; Han, Y. F. Re-Investigating the CO Oxidation Mechanism over Unsupported MnO, Mn2O3 and MnO2 Catalysts. *Catal. Today* **2008**, *131* (1–4), 477–482. https://doi.org/10.1016/j.cattod.2007.10.061.

(46) Sihaib, Z.; Puleo, F.; Garcia-Vargas, J. M.; Retailleau, L.; Descorme, C.; Liotta, L. F.; Valverde, J. L.; Gil, S.; Giroir-Fendler, A. Manganese Oxide-Based Catalysts for Toluene Oxidation. *Appl. Catal. B Environ.* **2017**, *209*, 689–700. https://doi.org/10.1016/j.apcatb.2017.03.042.

(47) Sihaib, Z.; Puleo, F.; Pantaleo, G.; La Parola, V.; Valverde, J. L.; Gil, S.; Liotta, L. F.; Giroir-Fendler, A. The Effect of Citric Acid Concentration on the Properties of LaMnO3 as a Catalyst for Hydrocarbon Oxidation. *Catalysts* **2019**, *9* (3), 226. https://doi.org/10.3390/catal9030226.

(48) Marsh, H.; Kuo, K. Kinetics and Catalysis of Carbon Gasification; 1989; pp 107–151.

(49) Prasad, D. H.; Park, S. Y.; Oh, E. O.; Ji, H.; Kim, H. R.; Yoon, K. J.; Son, J. W.; Lee, J. H. Synthesis of Nano-Crystalline La1-XSrxCoO 3-δ Perovskite Oxides by EDTA-Citrate Complexing

Process and Its Catalytic Activity for Soot Oxidation. *Appl. Catal. A Gen.* **2012**, *447–448*, 100–106. https://doi.org/10.1016/j.apcata.2012.09.008.

(50) Li, Z.; Meng, M.; Zha, Y.; Dai, F.; Hu, T.; Xie, Y.; Zhang, J. Highly Efficient Multifunctional Dually-Substituted Perovskite Catalysts La 1-XK XCo 1-YCu YO 3-δ Used for Soot Combustion, NOx Storage and Simultaneous NOx-Soot Removal. *Appl. Catal. B Environ.* **2012**, *121–122*, 65–74. https://doi.org/10.1016/j.apcatb.2012.03.022.

(51) Royer, S.; Duprez, D.; Kaliaguine, S. Oxygen Mobility in LaCoO3 Perovskites. *Catal. Today* **2006**, *112* (1–4), 99–102. https://doi.org/10.1016/J.CATTOD.2005.11.020.

(52) La Cava, A. I.; Bernardo, C. A.; Trimm, D. L. Studies of Deactivation of Metals by Carbon Deposition. *Carbon N. Y.* **1982**, *20* (3), 219–223. https://doi.org/10.1016/0008-6223(82)90024-0.

(53) Pawar, V.; Ray, D.; Subrahmanyam, C.; Janardhanan, V. M. Study of Short-Term Catalyst Deactivation Due to Carbon Deposition during Biogas Dry Reforming on Supported Ni Catalyst. *Energy & Fuels* **2015**, *29* (12), 8047–8052. https://doi.org/10.1021/acs.energyfuels.5b01862.

(54) Li, Z.; Meng, M.; Dai, F.; Hu, T.; Xie, Y.; Zhang, J. Performance of K and Ni Substituted La 1-XK XCo 1-YNi YO 3-δ Perovskite Catalysts Used for Soot Combustion, NO x Storage and Simultaneous NO x-Soot Removal. *Fuel* **2012**, *93*, 606–610. https://doi.org/10.1016/j.fuel.2011.10.040.

(55) Zhang, S.; Zhu, X.; Zheng, C.; Hu, D.; Zhang, J.; Gao, X. Study on Catalytic Soot Oxidation over Spinel Type ACo2O4 (A = Co, Ni, Cu, Zn) Catalysts. *Aerosol Air Qual. Res.* **2017**, *17* (9), 2317–2327. https://doi.org/10.4209/aaqr.2016.12.0564.

(56) Zhaoqiang, L.; Ming, M.; Fangfang, D.; Tiandou, H.; Yaning, X.; Jing, Z. Performance of K and Ni Substituted La1−xKxCo1−yNiyO3−δ Perovskite Catalysts Used for Soot Combustion, NOx Storage and Simultaneous NOx-Soot Removal. *Fuel* **2012**, *93*, 606–610. https://doi.org/https://doi.org/10.1016/j.fuel.2011.10.040.

(57) Doshi, R.; Alcock, C. B.; Carberry, J. J. Effect of Surface Area on CO Oxidation by the Perovskite Catalysts La1?X Sr x MO3-? (M = Co, Cr). *Catal. Letters* **1993**, *18* (4), 337–343. https://doi.org/10.1007/BF00765279.

(58) Nair, M. M.; Abanades, S. Correlating Oxygen Mobility with Thermochemical CO 2 - Splitting Efficiency in A-Site Substituted Manganite Perovskites. *Sustain. Energy Fuels* **2021**. https://doi.org/10.1039/D1SE00950H.

(59) Taskin, A. A.; Lavrov, A. N.; Ando, Y. Fast Oxygen Diffusion in A-Site Ordered Perovskites. *Prog. Solid State Chem.* **2007**, *35* (2–4), 481–490. https://doi.org/10.1016/j.progsolidstchem.2007.01.014.

(60) Biesinger, M. C.; Payne, B. P.; Grosvenor, A. P.; Lau, L. W. M. M.; Gerson, A. R.; St, R.; Smart, C.; Smart, R. S. C. Applied Surface Science Resolving Surface Chemical States in XPS Analysis of First Row Transition Metals , Oxides and Hydroxides : Cr , Mn , Fe , Co and Ni. *Appl. Surf. Sci.* **2011**, *257* (7), 2717–2730. https://doi.org/10.1016/j.apsusc.2010.10.051.

(61) Ran, R.; Wu, X.; Weng, D.; Fan, J. Oxygen Storage Capacity and Structural Properties of Ni-Doped LaMnO 3 Perovskites. *J. Alloys Compd.* **2013**, *577*, 288–294. https://doi.org/10.1016/j.jallcom.2013.05.041.

(62) Peña, M. A.; Fierro, J. L. G. Chemical Structures and Performance of Perovskite Oxides. *Chemical Reviews*. American Chemical Society July 2001, pp 1981–2017. https://doi.org/10.1021/cr980129f.

(63) Ran, R.; Wu, X.; Weng, D.; Fan, J. Oxygen Storage Capacity and Structural Properties of Ni-Doped LaMnO3 Perovskites. *J. Alloys Compd.* **2013**, *577*, 288–294. https://doi.org/10.1016/j.jallcom.2013.05.041.

(64) Stanmore, B. R.; Brilhac, J. F.; Gilot, P. The Oxidation of Soot: A Review of Experiments, Mechanisms and Models. *Carbon N. Y.* **2001**, *39* (15), 2247–2268. https://doi.org/10.1016/S0008-6223(01)00109-9.

(65) Lee, J. H.; Jo, D. Y.; Choung, J. W.; Kim, C. H.; Ham, H. C.; Lee, K. Y. Roles of Noble Metals (M = Ag, Au, Pd, Pt and Rh) on CeO2 in Enhancing Activity toward Soot Oxidation: Active Oxygen Species and DFT Calculations. *J. Hazard. Mater.* **2021**, *403*, 124085. https://doi.org/10.1016/J.JHAZMAT.2020.124085.

(66) Wu, Q.; Jing, M.; Wei, Y.; Zhao, Z.; Zhang, X.; Xiong, J.; Liu, J.; Song, W.; Li, J. High-Efficient Catalysts of Core-Shell Structured Pt@transition Metal Oxides (TMOs) Supported on 3DOM-Al2O3 for Soot Oxidation: The Effect of Strong Pt-TMO Interaction. *Appl. Catal. B Environ.* **2019**, *244*, 628–640. https://doi.org/10.1016/J.APCATB.2018.11.094.

(67) Xiong, J.; Mei, X.; Liu, J.; Wei, Y.; Zhao, Z.; Xie, Z.; Li, J. Efficiently Multifunctional Catalysts of 3D Ordered Meso-Macroporous Ce0.3Zr0.7O2-Supported PdAu@CeO2 Core-Shell Nanoparticles for Soot Oxidation: Synergetic Effect of Pd-Au-CeO2 Ternary Components. *Appl. Catal. B Environ.* **2019**, *251*, 247–260. https://doi.org/10.1016/J.APCATB.2019.03.078.

(68) Guo, X.; Meng, M.; Dai, F.; Li, Q.; Zhang, Z.; Jiang, Z.; Zhang, S.; Huang, Y. NOx-Assisted Soot Combustion over Dually Substituted Perovskite Catalysts La1−xKxCo1−yPdyO3−δ. *Appl. Catal. B Environ.* **2013**, *142–143*, 278–289. https://doi.org/10.1016/J.APCATB.2013.05.036.

4. CO_2 methanation over supported nickel catalysts: effect of preparation on the catalytic performances

4.1 General context and state of the art of carbon dioxide methanation

CO_2 utilization is receiving increasing interest from both scientific and industrial community, partly due to climatic change considerations and because the use of carbon dioxide could eventually be the starting point for a cheaper and cleaner production of synthetic fuel less impacting than conventional fossil fuels. However this is only possible if the cost of such processes becomes more convenient and if the overall sustainability is preserved.[1] Carbon dioxide is produced and released in industrial processes, energy production, biomass combustion and gasification, cement kilns and oil refinery. The concentration of carbon dioxide in the atmosphere has increased from approx. 277 ppm in 1750, the beginning of the industrial era, to 405 ppm in 2017; moreover the flux of carbon from fossil fuels and industry to atmosphere has reached a concerning value of 34 Gt CO_2 yr^{-1}. The drastic increase in CO_2 concentration was deemed the main culprit for the increase in earth temperature. [2] This urgency impacts on scientific research whose community is now called to provide an efficient solution to this universal problem. One of the approaches that have been proposed is the so-called Power-to-Gas.

Power-to-Gas (PtG) is an option for converting energy from electricity into chemical bonds, stored in a combustible gas. Using electric power an electrolyser splits water into its two components: oxygen on the one hand and hydrogen as combustible gas on the other. Hydrogen can be now fed into a downstream methanation process. [3] This technology is currently considered worthwhile because it is the most cost-efficient long-term storage option for power, assuming that renewable sources of energy are typically discontinuous in time and often geographically far from the energy users (*e.g.* solar, wind, wave motion power sources). It also supports intersectoral decarbonization and the

substitution of fossil energy carriers. Literature shows that with renewable power generation on the increase, long-term storage with PtG will become necessary and cost-efficient. [3]

In this project, the utilization of renewable hydrogen is performed by the direct conversion of CO_2 to methane by the Sabatier reaction, which interestingly only gives water as side product ($CO_2 + H_2 \rightarrow CH_4 + 2H_2O$), in the view of obtaining a valuable fuel with a sustainable approach. The main advantage of obtaining methane is its already existing distribution infrastructure and the high energy content. Well-aware of the fact that methane belongs to the family of greenhouse gases, we assert that methane produced by carbon dioxide recycling is actually less harmful than natural fossil methane as it contributes to globally reduce greenhouse gas emissions. The methanation of carbon dioxide has a broad range of applications including the purification of synthesis gas for the production of ammonia and the production of syngas. [4] The National Aeronautics and Space Administration (NASA) is remarkably interested in applications of this reaction in manned space colonization on Mars. [5]

The reaction must be carried out between 200°C and 500°C to avoid the reverse water gas shift reaction ($CO_2 + H_2 \rightarrow CO + H_2O$), which takes place at higher temperatures. A calculation of the thermodynamical constraints to the reaction conditions has been performed by our collaborators, Prof. Canu's group at the Dept. of Industrial Engineering at the University of Padova. The results are reported in the graph below, Figure 52. As it can be seen, CO concentration starts to rise over 500°C

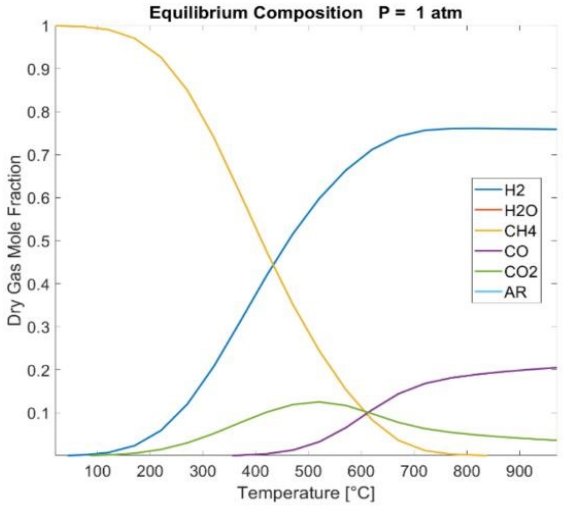

Figure 52 Theoretical equilibrium composition of the mixture of reactants for CO_2 methanation at 1 atm.

in a dry mixture of reactants and products, meaning that the reverse water gas shift reaction is favoured over the methanation, resulting in a decreased methane yield. As it will be shown later, the same behaviour was observed in the catalytic testing of the Ni-based materials obtained.

In the recent years many different catalysts have been tested towards this kind of reactivity, based on different noble or transition metals, such as Ru, Rh, Ir, Pd, Ni, Fe, Co. These metals are often used as supported catalysts on different simple or mixed oxide (as a combination of simple oxides), these include ceria, alumina, titania, silica, ceria and zirconia. [6–9] Among these options, the choice in our case was oriented excluding noble metals, a recurring theme throughout this PhD thesis, as they belong to critical raw materials that should be avoided to keep the overall sustainability of the carbon dioxide methanation process. [10] To meet several requirements, such as low cost, high activity and selectivity, the catalysts chosen for this process are Ni-based, which are also the most extensively investigated materials due to their unique properties. Unfortunately these materials are characterized by some typical drawbacks, especially carbon deposition that often occurs during exercise (coking) and the trend of sintering that has been observed in many similar systems. Carbon deposition is taking place due to the so-called Boudouard reaction which is an excessive reduction of the carbon-based molecules implied (CO_2, CO).

As many examples in literature have demonstrated, the properties of Ni as catalyst in CO_2 methanation strongly depend on the interaction with the support, in particular some properties like dispersion, reducibility and bonds to the interaction are crucial in determining the outcome of the performances of such catalyst.

As regards the choice of the support, we prepared samples based on CeO_2 support. Ceria is widely studied in the heterogeneous catalysis field thanks to its peculiar redox properties. For the same reason it is applied also in CO_2 methanation as it is reasonable to argue that its redox feature might influence the activation of both carbon dioxide and hydrogen on the surface of the composite material composed by metallic particles dispersed on a metal oxide such as ceria. Moreover, evidence in literature shows

that the higher basicity of ceria plays a role in the mechanism of the methanation favoring carbon dioxide chemisorption and activation, as well as exhibiting a strong metal-support interaction that allows a higher Ni dispersion.[11,12] The stability of ceria is also of great advantage in this reaction and if the dispersion of Ni onto the surface is carefully controlled the resistance to coking could be efficiently increased, prolonging the life span of the catalyst.

Concerning the selectivity of supported Ni towards CH_4 as only product, some authors claim that the size of the metal nanoparticles have a strong impact on such parameter: in particular if the nanoparticles are too small the resulting gas mixture might me in favor of CO concentration instead of favoring CH_4 formation. This difference was explained by the different pathways followed by the systems with different nanoparticle sizes: disregarding the metal particle size the key intermediate which is formed after reagent adsorption is monodentate m-$HCOO^-$. In the case of small nanoparticles this is decomposed in CO that, following a consecutive reaction pathway, might or not be further hydrogenated to CH_4. Whereas on particles with bigger size, the formate intermediate is readily hydrogenated without the passage through the formation of CO, thanks to the high H_2 surface coverage. Eventually more CH_4 gets formed instead of CO. This means that the control of the size is a crucial step to be considered in the preparation of CO_2 methanation catalysts: an excessive size will cut down the number of active sites which are positioned at the interface between particles and support, whereas too small particles will result in a poor selectivity in the product mixture, as also CO is formed along with the desired methane.

As a first attempt to investigate the effect of Ni loading on CeO_2, two different loading values have been selected according also to previous published work.[13] However not only the loading but also the preparation method was evaluated: along with the conventional wet impregnation technique, an innovative procedure was tested to deposit Ni on ceria. Inspired by existing literature that describes the use of ammonia to form complexes with Cu which are able to disperse copper in a very homogeneous way on an oxide surface thank to steric hindrance caused by ammonia ligands, citric

acid was here employed to perform chelation on Ni and disperse such Ni-citrate complexes on the oxidic surface. The advantages are noteworthy: firstly as an organic ligand, citric acid is easily removed by combustion and leaves no residue on the surface, secondly its complexation is easily regulated by simply controlling pH, finally and most importantly citrate ligand is significantly larger in size than ammonia, giving rise to the possibility of a finer dispersion on the surface, which eventually ends up in the formation of smaller and more sparse particles on the surface.

As many examples in literature have demonstrated [14–17], the properties of Ni as catalyst in carbon dioxide methanation strongly depends on the interaction with the support, in particular some properties like dispersion, reducibility and bonds to the interaction are crucial in determining the outcome of the performances of such catalyst. Therefore the deposition procedure strongly affects the catalytic performances of the material.

Another set of samples was prepared exploiting the exsolution technique: instead of performing the conventional impregnation procedure to prepare the already-mentioned *cermet* material (Ni/CeO_2), Ni was embedded in the structure, namely a perovskite oxide, and it emerged after a harsh reducing treatment. The exsolved nanoparticles are socketed on the surface of the perovskite, preventing agglomeration and coarsening of the nanoparticles during operation conditions. Also the controllable anchoring of the nano dispersed metal on the support represents a great advantage that makes *in situ* exsolution attractive. Moreover some authors suggested the strategy of non-stoichiometry (A-site deficiency in the ABO_3 stoichiometry) to promote exsolution as it is greatly influenced by the presence of dopants inside the perovskite structure. [24] In particular literature suggests that the co-segregation of B-site metal and oxygen vacancies play a central role in the exsolution. However the mechanism of co-segregation of doping element with oxygen vacancies still remains an open question. [24]

As suggested by literature, the active catalyst (Ni nanoparticles) is incorporated on the B site of perovskite oxide (ABO_3) during material synthesis in air and then the metal is exsolved from the

perovskite backbone as highly dispersed nanoparticles under a reducing atmosphere. To exploit the A site-deficiency strategy the composition chosen for the new set of materials was $La_{0.7}NiO_3$ as to enhance the exsolution of Ni in a reducing environment, producing $La_{0.7}NiO_3 \rightarrow La_{0.7}Ni_{0.7}O_3$+0.3 Ni. In this case metallic nickel should diffuse toward the surface and therefore forms small nanoparticles that are homogeneously dispersed on the material. These kind of new materials are gradually obtaining more interest also by the engineering community because they can provide a strategy for tailoring materials for fuel cell electrodes, catalytic oxidation or reduction and thermochemically drive hydrogen production from water. [25,26] Authors in literature report that A-site-deficiency is actually implied in enhancing exsolution patterns as it creates oxygen vacancies during reduction, which destabilizes the perovskite structure and results in spontaneous exsolution of B-site cation. Kwon et al. claim that spontaneous exsolution phenomenon occurs in layered perovskites when considerable amounts of oxygen vacancies and B-site metal vacancies could be introduced instantaneously (co-segregation) by reduction, and then the metal oxide can be converted to the corresponding metal or metal oxide. This mechanism of exsolution in layered perovskites is expressed as point defect (Schottky-type defect) reaction in which the B-site dopant in the transition metal site with net charge zero reacts with oxygen in oxygen site with net charge zero giving a transition metal oxide, an oxygen ion vacancy with net charge +2 and a cation vacancy with net charge -2. [24]

To further reduce the amount of active metal used, keeping nonetheless a satisfactory catalytic activity, a third set of samples was synthetized with an innovative approach. The fundamental idea is, also in this case, to investigate Ni activity when the metal is deposited on different supports and with different interactions with the support itself. The chosen support was again ceria, given its high stability and robust structure. [27,28] Supported Ni was achieved as the deposition in one case (depLN07@CeO_2) and the direct grafted synthesis in the other on ceria (synLN07@CeO_2). Further details on the synthesis are provided in the section “Materials and methods”.

The samples were characterized by different points of view to obtain information regarding their morphology (SEM - Scanning Electron Microscopy), crystal structures (XRD - X-Ray Diffraction), reducibility (H_2-TPR-Hydrogen Temperature Programmed Reduction), surface area (BET - Brunauer-Emmett-Teller N_2 physisorption isotherms), surface and bulk composition (EDX - Energy Dispersive X-Ray spectroscopy, XPS - X-Ray Photoelectron Spectroscopy) and functional behavior (catalytic tests, performed as described below).

4.2 Materials and methods

Ni/CeO_2 composite catalysts, containing different nickel nominal molar ratios, were prepared by both wet impregnation (WI) and templated impregnation (TI). In the first case CeO_2 is dispersed in water and a solution of $Ni(NO_3)_2$ is obtained. After 2 hours of mixing and heating at 95°C the dispersion is dried and calcined at 600°C for 6 hours. In the second case instead a templating agent is employed. As explained in the introduction the chosen templating agent is citrate, thanks to its excellent pH-regulated complexing capability and its larger size compared to other templating agents. For these reasons, citric acid is added to the water dispersion of ceria and nickel nitrate in a 1.9[Ni^{2+}] molar ratio, as reported previously and adapted to the case of Ni dispersion. [29] Then the slurry is heated up to 80°C in a water bath to promote solvent evaporation and obtain a wet-gel. The gel is treated at 400°C for 2 h in air to decompose the organic framework. At the end of the heat treatment the powder is calcined at 600°C. The resulting powder is therefore ground before being tested in the catalytic setup. The composition of the samples (in particular the different loadings and preparation techniques) are reported in detail in Table 20.

.

Sample	Composition
TI – 1.7 wt.	Ni@CeO2 1.7% wt TI
WI – 1.7 wt.	Ni@CeO2 1.7% wt WI
TI – 13.4 wt.	Ni@CeO2 13.4% wt TI
LN0.7	$La_{0.7}NiO_3$ *in situ* reduction
LN0.5	$La_{0.5}NiO_3$ *in situ* reduction
depLN0.7@CeO_2	$La_{0.7}NiO_3$ 10%wt. deposition on CeO_2 with citric acid
synLN0.7@CeO_2	$La_{0.7}NiO_3$ 10%wt. deposition by synthesis in situ CeO_2 with citric acid

Table 20 Composition of the samples.

The perovskite samples which underwent exsolution to expose on surface Ni particles were instead synthetized using the citrate route: it employs the complexing power of citrate ion to set the right distance between metal ions in order to obtain the perovskite oxide structure. The precursor used were salts and oxides of the metal in the structure: namely La_2O_3 (Sigma-Aldrich 99.9%), $Ni(NO_3)_2{\cdot}6H_2O$ (Sigma-Aldrich 99.0% purity), citric acid monohydrate (Sigma-Aldrich, ≥99.0%). The precursors were dissolved in water (adding of HNO_3 in the case of lanthanum (III) oxide as it is scarcely soluble). Once dissolved they were mixed and citric acid was added to the solution with a molar ratio of 1.9:1 with respect to the total amount of cations. Then the solution was heated up to 80°C to promote slow solvent evaporation and to obtain a wet gel. The gel was treated at 400°C for 2 h in air to decompose the resulting organic framework made up by citrate complexation network. At the end of the thermal treatment the powder was finely ground and calcined at 750°C. The calcination temperature was selected as low as possible to obtain a reasonable crystal purity of the sample, as reported elsewhere for similar materials. [29]

The perovskite/ceria composites were obtained starting from the synthesis of LN0.7 (see Table 20). The sample named "*dep*" was prepared depositing already prepared substoichiometric $La_{0.7}NiO_3$ perovskite on ceria by means of citric acid mediated templated impregnation, with a 10% weight ratio. The synthesis of the sample named "*syn*", conversely, was carried out as a conventional citrate-route perovskite synthesis in presence of CeO_2, added at the final stages of the preparation, with the aim of grafting the so-obtained perovskite onto the ceria surface, creating a supported perovskite on the oxide. Again, the ratio used was 10% wt. In both cases the solution was dried until a wet-gel was obtained and combustion removed the citrate network obtained, leaving only the desired nanocomposite. A final calcination treatment completed the synthetic procedure (750°C for 6 hours, with a ramp of 6°C/min) enhancing the crystal purity of the samples.

Literature reports similar examples of this technique in which perovskites are deposited onto oxides that act as support for catalytic application.[30–35] This approach allows to reduce the amount of active catalyst used, still providing enough active surface sites and favorable support to promote the proceeding of the reaction of interest.

The composition of the samples is reported in Table 20.

Field emission-scanning electron microscopy and energy dispersive X-ray spectroscopy measures are carried out on a Zeiss SUPRA 40VP. Both morphological and compositional analyses are carried out setting the acceleration voltages at 20 kV. XRD analyses are performed with a Bruker D8 Advance diffractometer with Bragg–Brentano geometry using a Cu Ka radiation (40 kV, 40 mA, k = 0.154 nm).

Temperature Programmed Reduction (TPR) is performed with an Autochem II 2920 Micromeritics, equipped with a TCD detector. TPR measurements are carried out in a quartz reactor by using 50 mg of sample and heating from RT to 900 °C at 10 °C/min under a constant flow of H_2 5% in Ar. TPR samples were previously outgassed with He (50 $ml \cdot min^{-1}$) at RT. The surface area of all samples is determined by Asap 2020 Plus from Micromeritics. The measurements are carried out at liquid

nitrogen temperature (77K). The specific surface area is calculated using the Brunauer-Emmet-Teller (BET) equation. Prior to N_2-sorption, all samples are degassed at 200 °C for 16 hours.

XPS measurements were carried out with a Perkin Elmer 5600 ci Multi Technique System. The spectrometer is calibrated by assuming the Binding Energy (BE) of the Au 4f7/2 line to be 84.0 eV with respect to the Fermi level. Both extended spectra (survey, 187.85 eV pass energy, 0.5 eV/step, 0.05 s/step) and detailed high-resolution spectra (23.5 eV pass energy, 0.1 eV/step, 0.1s/step) are collected with a standard Al K α source working at 200 W. The standard deviation in BE values of the XPS line is 0.10 eV. The atomic percentage, after a Shirley-type background subtraction,[36] is evaluated by using the PHI sensitivity factors.[37] The peak positions are corrected for the charging effects by considering the C1s peak at 284.8 eV and evaluating the BE differences.[38]

4.3 Results and discussion

The X-ray diffractograms of Ni/CeO_2 catalysts and of $La_{1-x}NiO_3$ perovskites are shown in Figure 53. In the case of impregnated samples, the signal assigned to the presence of Ni or NiO is not visible, due to its low amount in the sample. The only phase which is recognizable is ceria [96-900-9009], in both cases. In other words there is no significant evidence for the formation of a solid solution resulting from the mixture of Ni and CeO_2.

The perovskites undergoing exsolution show diffractographic patterns which are compatible with the presence of the desired phase, $LaNiO_3$ [34-1181].[39] The substoichiometry is not detected by XRD patterns, however stoichiometry was carefully controlled through synthesis and no other phases, that

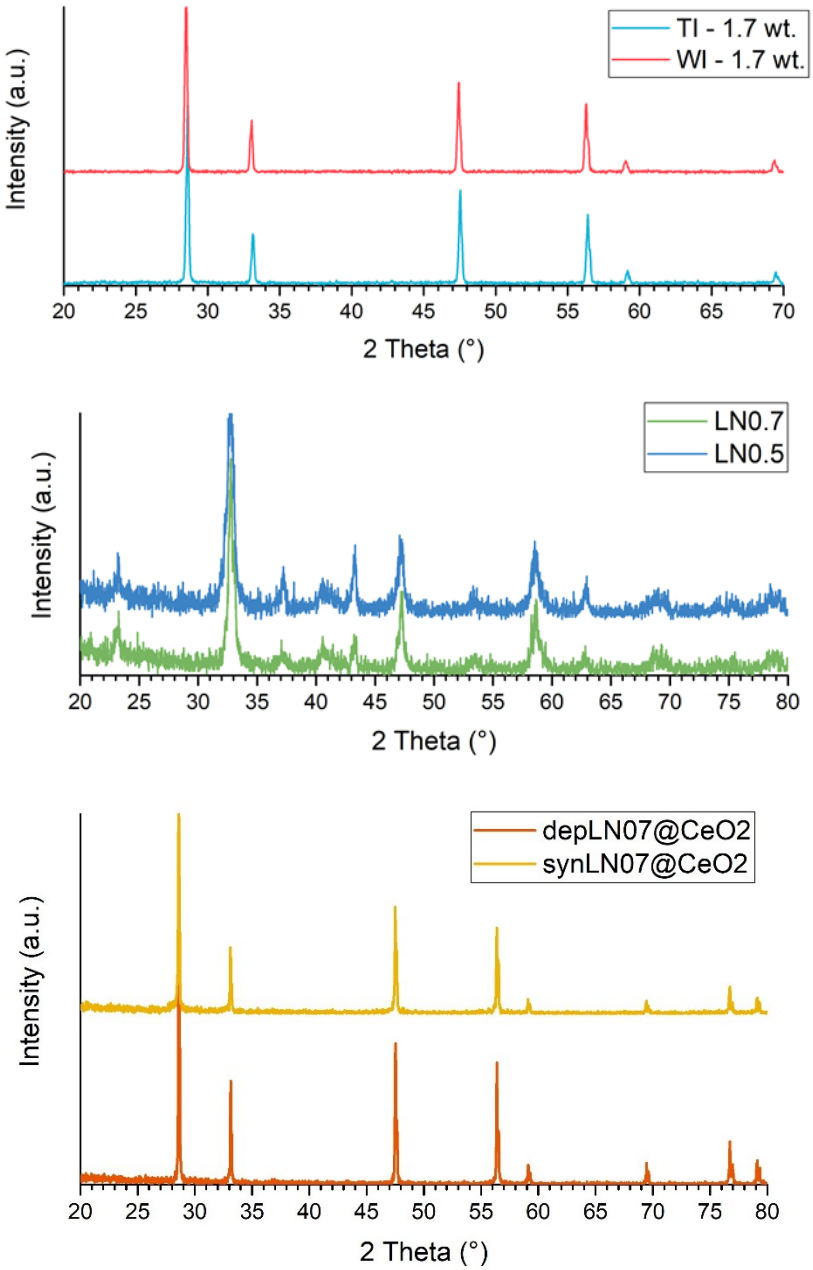

Figure 53 XRD of the samples.

could prove an inaccurate synthesis, (La_2O_3, NiO) are present. Please note that the XRD patterns are collected prior to exsolution, for this reason metallic Ni phase is not present. Exsolution was performed *in situ* just before the catalytic reaction.

The samples depLN07 and synLN07, due to the predominant composition based on ceria, have a similar diffractographic pattern as the samples TI1.7 and WI1.7. No trace of the perovskite phase is visible, since X Ray Diffraction is mainly a bulk technique.

H_2-TPR profiles show two distinct peaks in the region 100-900°C in which the reduction under hydrogen flow was performed.

The H_2-TPR analysis was performed on the two samples with the lowest loading obtained by WI and TI to compare the effect of the preparation on the metal reducibility of the samples and consequently to shed light on the different dimensions of the Ni particles deposited on the surface (see Figure 54). The results allowed to demonstrate that the Ni particles in the samples obtained by TI are smaller and more easily reducible as the first peak of reduction, which is ascribed to Ni (II) being reduced to Ni (0), is placed at 323°C instead of 366°C, the temperature at which Ni is reduced in the WI obtained sample. Also the signal attributed to the reduction of Ce (IV) to Ce (III) is shifted towards lower temperature in the case of the TI sample. By literature data the reduction of NiO supported on CeO_2

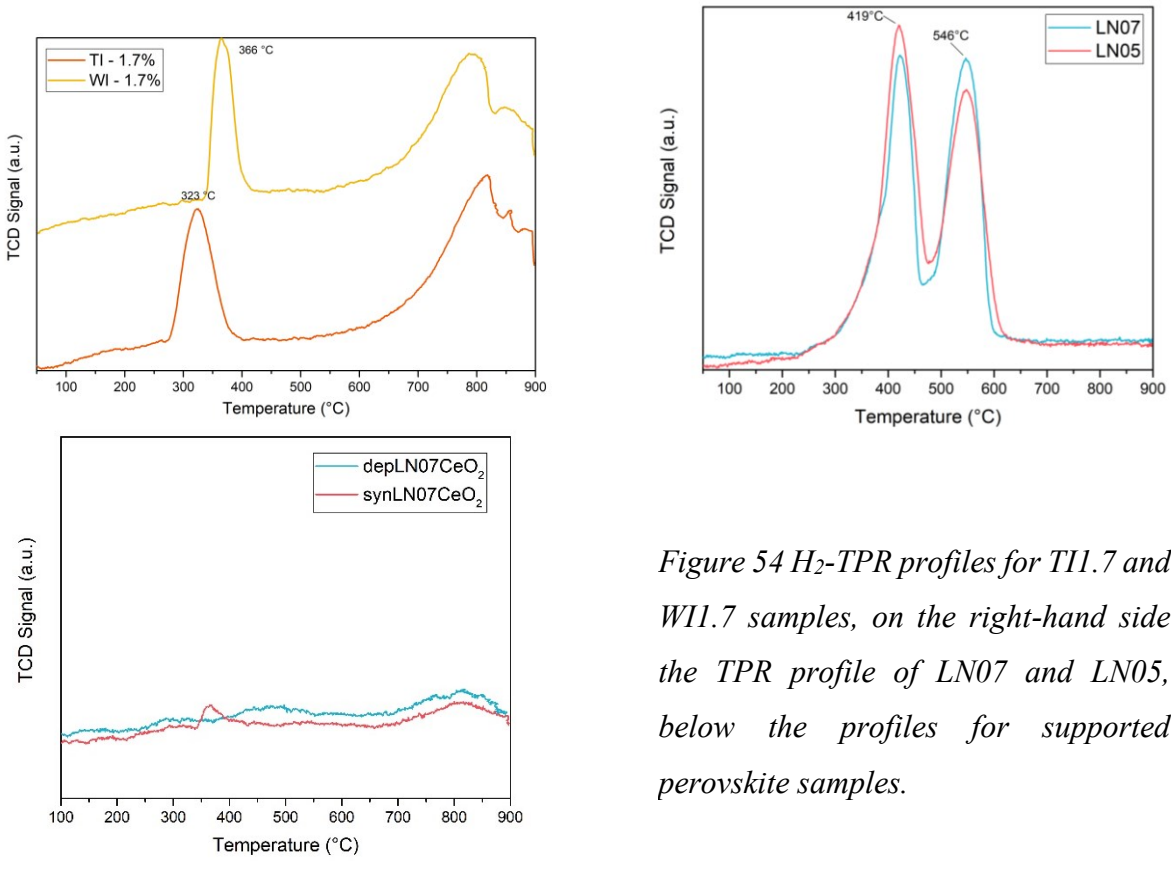

Figure 54 H_2-TPR profiles for TI1.7 and WI1.7 samples, on the right-hand side the TPR profile of LN07 and LN05, below the profiles for supported perovskite samples.

generally occurs in the temperature range 400-700°C, depending on nickel particle size and on the strength of the nickel-support interactions. [13,40]

In this case the temperatures for NiO reduction are lower, implying that the bond between Ni and the support is not as strong as elsewhere. However this represents an advantage because it implies an easier reducibility of the sample and therefore the pretreatment conditions to get an active catalyst are not necessarily too harsh. Indeed the material needs to be reductively pretreated before being tested as the preparation mainly leads to the deposition of NiO if such procedure is carried out in air. Hydrogen TPR instrumentation was also used to determine the minimum time and temperature necessary to complete the reduction of NiO on the surface to metallic Ni, considered the active species of the catalytic process. In this case the tests were repeated several times to determine the minimum time and temperature necessary to ensure the complete reduction, verified by running a successive H_2-TPR test, which showed no signal in the case of complete reduction of the sample. The same conditions were then applied as pretreatment for the catalytic testing.

The width of the peak of the TI sample referred to Ni (II) to Ni (0) reduction is slightly larger than that of WI sample, and this might suggest a more pronounced heterogeneity in the species of Ni present on the surface of the support, which means different kinds of Ni species and chemical environments are present on ceria.

Supported perovskites show only a weak CeO_2 reduction (again at Figure 54) at high temperature (800°C, to be compared with the reduction profile of Ni@CeO_2 samples), and only a very small peak between 300 and 400°C for synLN07 sample, most likely caused by Ni (II) reduction, which is present in very small amount (the peak is extremely weak).

The specific surface area is calculated using the Brunauer-Emmet-Teller (BET) equation, after heated degassing. The morphological features of the samples are reported in Table 21. The BET analysis was employed to determine the surface area of the samples, to investigate the role that a greater porosity might have on the catalytic results. Unfortunately for CeO_2 impregnated samples, the

analysis did not give any useful hint to distinguish the samples as regards surface area because the values obtained are quite similar for each sample: each of them has a surface area around 15 m^2/g and so it was not recognized as a crucial parameter in the functional activity demonstrated by the catalytic assessment tests. The same phenomenon took place also in the case of the perovskite samples, in which the surface area values are quite similar and relatively low, likely due to the combustion synthesis approach employed. Notably combustion synthesis of perovskites results in a lower surface area than bulk impregnated ceria.

BET measurements for supported perovskites showed poor surface areas, as expected from the synthesis employed, as low as 3.1 m^2/g.

Sample	BET Surface Area (m^2/g)
TI – 1.7 wt.	15.2
WI – 1.7 wt.	16.1
TI – 13.4 wt.	15.7
LN0.7	5.0
LN0.5	4.8

Table 21 Specific surface areas of the samples

To better understand the role of morphological properties of the materials in the catalytic behavior, an electron microscopy technique, FE-SEM, was used. The pictures are reported in Figure 55.

As concerns the nanocomposite samples (Ni/CeO_2) the morphology reveals the difference in the dispersion obtained by the two different preparation techniques: in the case of WI sample indeed the metal particles appear bigger and less uniformly dispersed on the metal oxide surface, whereas in the case of TI sample, they look smaller and less confined on the surface of the support. In both cases the support size belongs to the micron scale, with aggregates that tend to be more compact in the case of WI synthesis. However the metal nanoparticles in the WI sample look much different from those of

the WI sample: TI particles appear like a fine dust on the aggregates of the metal oxide whereas WI sample shows larger flake-like bodies on the surface.

LN-based samples show a dissimilar morphology: the structures of both are lamellar and look quite porous, despite the low specific surface area. It appears as if globular cavities were formed by the synthetized compound with little aggregates on the surface.

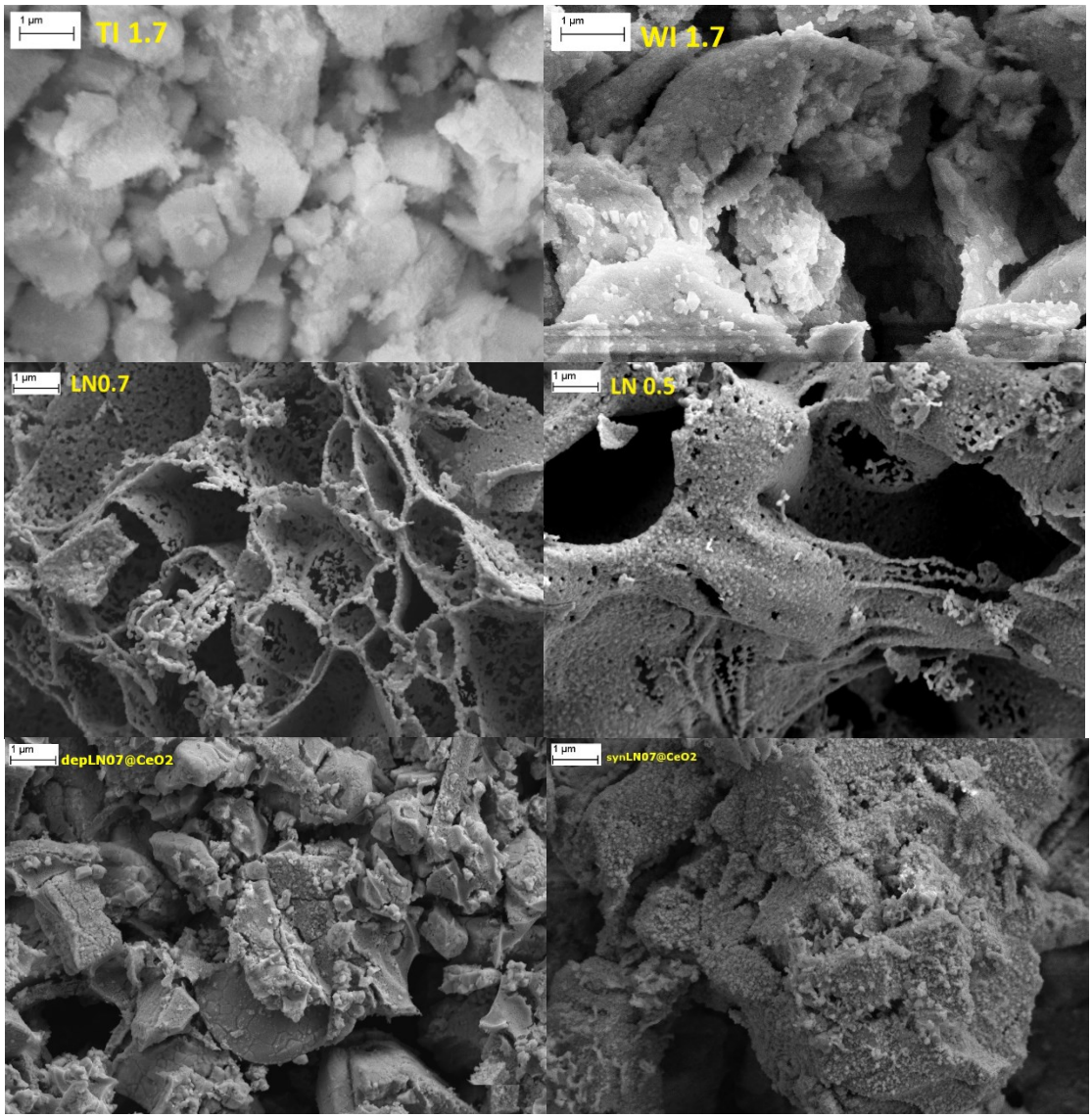

Figure 55 SEM images for the samples TI1.7, WI1.7, LN0.7, LN0.5, depLN07@CeO_2 and synLN07@CeO_2.

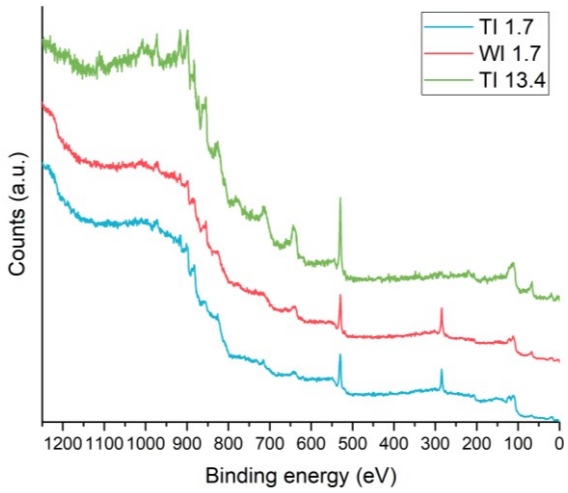

Figure 56 XP spectra for the Ni deposited ceria samples.

If we look at the ceria supported perovskites, an evident difference in the appearance of the samples can be spotted. When the substoichiometric nickel lantanate is simply deposited on the surface, larger aggregates on the ceria support are visible as compact bodies on the macrostructure of ceria. In the other case, when the perovskite was grafted onto the support, a tiny dust, most likely the perovskite itself, is covering the oxide macrostructure, giving the general impression of a more homogeneous dispersion, with smaller particle size and broader distribution on the ceria. The particles are within the range of 100 nm as dimensional range. This is particularly appreciable by means of higher magnification images, that show small globular particles with such a diameter covering the support.

The XP detailed spectra obtained for the Ni deposited samples are shown in Figure 58, whereas the peak positions are summarized in Table 22.

As regards the samples Ni/CeO_2 the XP spectroscopy analysis gave quite similar results with some interesting differences: Ni 2p spectra are identical for each sample, as it can be seen in Figure 56 and Figure 58. The characteristic peak for Ni 2p 3/2 is centered at 853.4 eV, which is a typical value for NiO [41]. Ni $2p_{1/2}$ signal is not reported in the graphs since it overlaps with Ce 3d signals in the region 875-910 eV (binding energy scale). O1s spectra appear different in the samples and they show the presence of surface hydroxilic species for the samples with lower loading. Indeed the sample with the

highest loading (TI 13.4% wt.) is characterized only by oxide species in the O1s XP spectrum, as it can be deducted from the XPS peak placed at 529.2 eV, typical for metal oxides, whereas 1.7%wt. loaded samples (WI 1.7 and TI 1.7) show the typical shoulder at 532.3 eV that accounts for the presence of surface hydroxide. [42] As noticed by Glisenti et al. Ce3d XP spectrum can give useful information about the oxidation state at which Ce is present in the structure. In the case of presence of Ce (III) besides Ce (IV), the characteristic Ce (IV) signals are accompanied by the signals denominated V' and U', typical for Ce (III). Indeed the signal placed at 886 eV in the binding energy scale is well noticeable in the samples with low loading, whereas in the case of higher loading the presence of Ce (III) decreases and the signal disappears. [42]

For perovskite-only samples, XPS surveys (Figure 59) pointed out only the presence of the expected elements, although C1s is not visible. Unfortunately for technical reasons high resolution spectra are not available for these samples, due to an instrument malfunctioning. Moreover the interpretation of the spectra is more challenging because of the overlapping of the most intense regions of the elements present in the compounds: La3d is recorded between approximately 825 and 870 eV, Ni2p between 850 and 880 eV and finally (for the CeO_2 supported samples) Ce3d between 875 and 930 eV. The consequence of this impossibility to separately identify the contribution of each element leads to a certain inaccuracy in the surface composition elemental analysis. For this reason, later, only EDX is discussed, since significant error could be introduced by this experimental setback. Anyway it was possible to observe the O1s region, showing peaks centered at 529.2 and 529.4 eV for the perovskite pure samples, typical for perovskite oxygen. [29,41,43–53] A very similar Binding Energy value was retrieved for *dep* and *syn* LN07@CeO_2, namely 529.4 and 530.6 eV respectively, still in agreement with the main contribution given by CeO_2 and the minoritarian perovskite phase.[54]

X-ray photoelectron spectroscopy gives also useful information about the surface composition in the first atomic layers of the material analyzed. Indeed XPS, EDX and nominal atomic compositions have

been compared in order to better understand the segregation phenomena; the sampling depth is in the tens of nanometer range for XPS and around 1 μm in EDX.

Peak	WI 1.7%	TI 1.7%	TI 13.4%
Ni $2p_{3/2}$	853.4 eV – typical for NiO	853.4 eV – typical for NiO	853.4 eV – typical for NiO
O1s	532.3 eV - Surface hydroxilic species	532.3 eV - Surface hydroxilic species [42]	529.2 eV - Metal oxides
Ce3d	886 eV – Ce (IV)	886 eV – Ce (IV)	882 eV - Ce (III)

Table 22 Schematic report of XPS results for the first set of samples (WI and TI).
For both cases the compositions considered was only cation-only, to allow a comparison to nominal metal composition. For the graphs please see Figure 57 and Figure 60.

Concerning Ni-deposited samples, nominal composition agrees with the composition detected by EDX spectroscopy. In this framework XPS (*i.e.* surface) compositions are different from bulk composition: with a higher prevalence of Ni on the surface, compatible with the deposition procedure carried out.

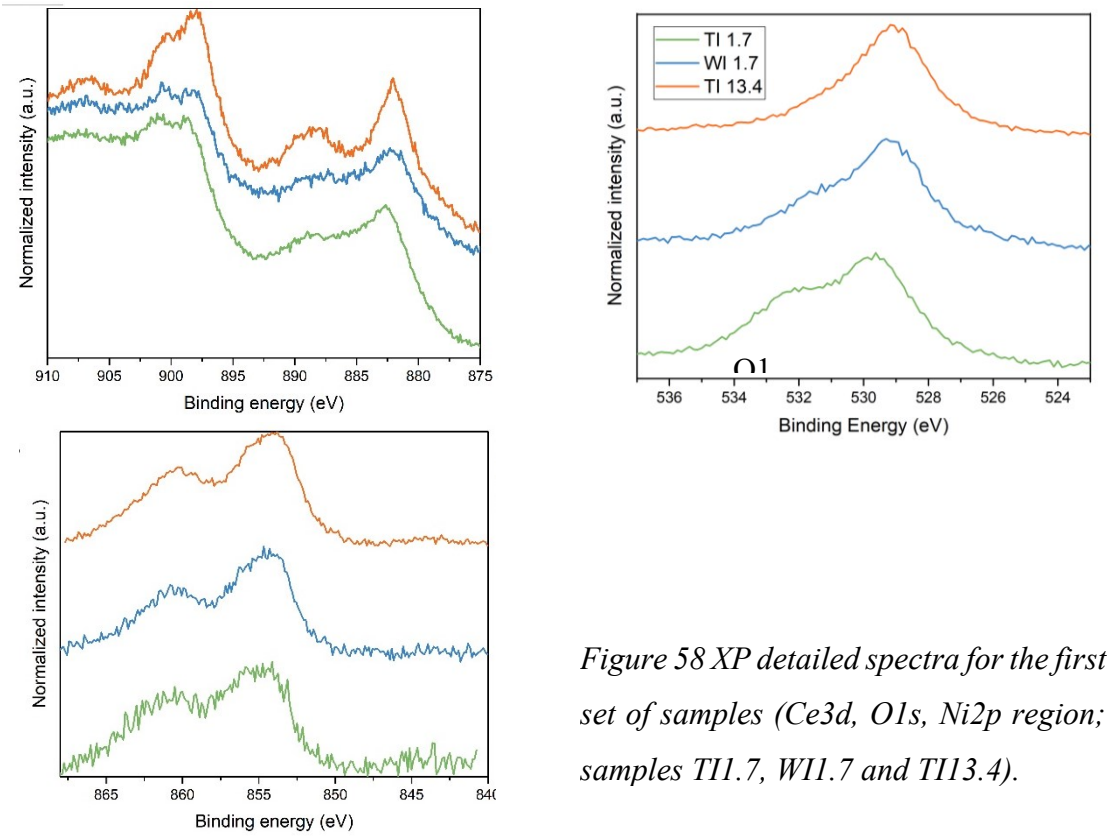

Figure 58 XP detailed spectra for the first set of samples (Ce3d, O1s, Ni2p region; samples TI1.7, WI1.7 and TI13.4).

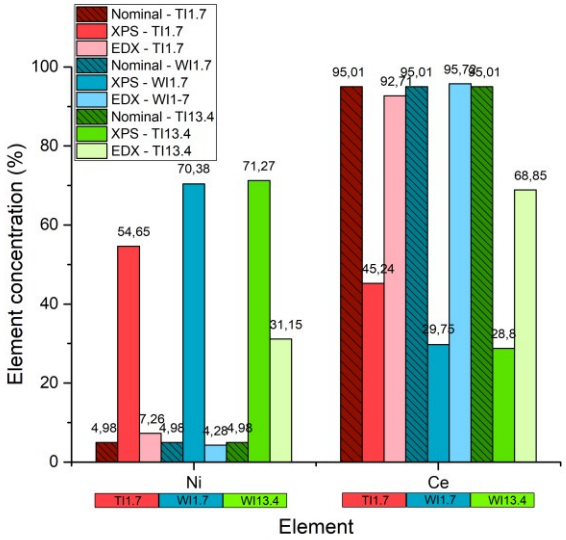

Figure 57 Cation-only composition for Ni deposition samples (XPS vs EDX).

As regards perovskite samples, EDX and nominal composition are basically within the experimental error. Although inaccurate for the reasons explained before, XPS compositions show Ni segregation, similarly to Ni-deposited samples.

A very similar situation is retrieved with supported perovskites sample, where EDX confirms the desired elemental composition and XPS suggests Ni and La segregation on the surface.

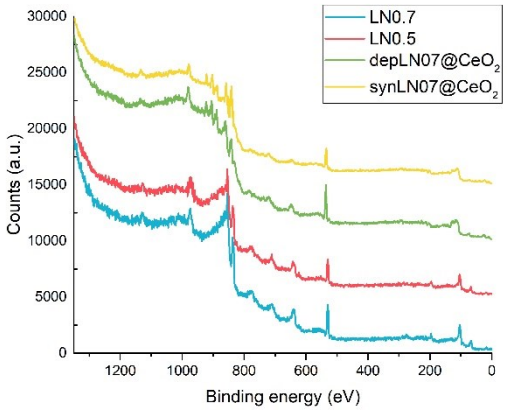

Figure 59 XP spectra for the perovskite-based samples.

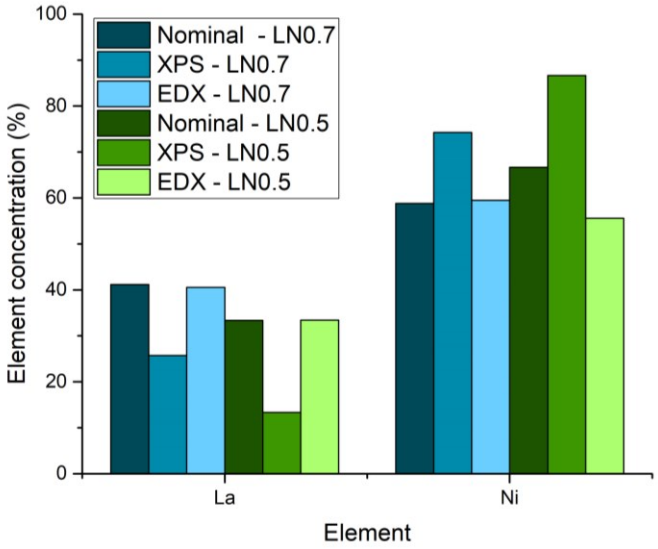

Figure 60 Cation-only composition for perovskite samples (XPS vs EDX).

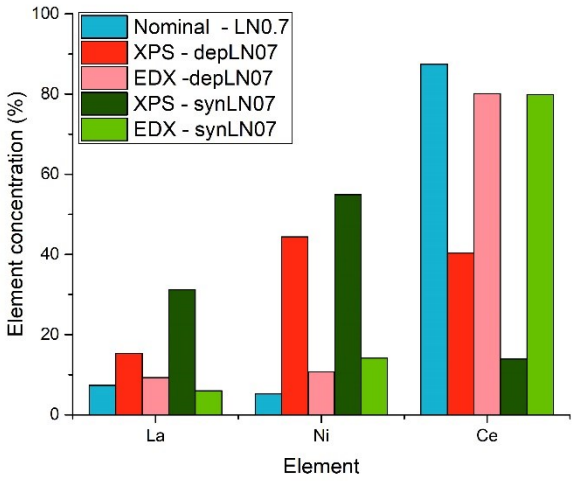

Figure 61 Cation-only composition for supported perovskites (XPS vs EDX). In the text the reasons for a cautious consideration of XPS results are addressed.

4.3.1 Functional activities

Initially, functional activity assessment was carried out by the use of GC (Gas Chromatography) technique at atmospheric pressure. The inlet composition was varied according to the following CO_2:H_2 ratios: 1:4 (stoichiometric ratio, eventually selected as the standard testing protocol), 1:8, 1:12 and 1:20, keeping the catalyst fraction constantly at 100% (*i.e.* without a dilution in inert bed filler, such as SiC). A quartz reactor (6 mm ID) with a packed bed of powders is employed, the temperature is monitored by a thermocouple right upstream of the bed. The inert carrier used was He and the reaction mixture was made up by H_2 and CO_2. The temperature of the bed was varied between RT and 500°C. The vapor in the outlet gas was condensed to avoid its presence in the GC columns (which could alter the detection results) and, as previously mentioned, the mixture was continuously analyzed by GC (Agilent 7820) with Porapak Q and MS5A packed columns in series, so that each measurement was taken approx. each 7 minutes, a TCD detector was used.

However, after the first measurements an undesired leak of atmospheric oxygen (and nitrogen) entering the gas line was detected, causing a partial quenching of the reductive reaction. To overcome such technical difficulty, the testing facility chosen was changed in favor of a chemisorption tester, Micromeritics Autochem II 2920, commonly used for chemisorption analysis such as among others Temperature Programmed Reduction (H_2-TPR, CO-TPR), Temperature Programmed Desorption (O_2-TPD, etc), single point BET surface area determination. Given the reliability of such instrument in TPRs, it was hypothesized that no atmospheric oxygen was able to permeate the reaction chamber, the inlet and outlet gas flows. Much effort has therefore been devoted to the customization of the instrument to obtain a suitable reactor for the methanation reaction. A Quadrupole Mass Spectrometer (QMS) was connected to the outlet of the reactor just before the original TCD of the instrument, which was no longer convenient to analyze the mixture of outflowing gases, and the already existing Mass Flow Controllers (MFCs) of the instrument were connected to the reactant gases tanks. Doing so, the reactants gases were pre-mixed by the MFCs directly by the instrument and introduced in its U-shaped reactor, in which the sample was inserted in a fixed amount (50 mg) and held in place by quartz wool. The instrument performs the desired temperature ramp and thermal pre-treatments when needed. The only significant difference in the experimental procedure, as compared to the GC conventional testing, is the need for the analyte gas calibration before each testing. Another disadvantage of this solution is the impossibility to quantify precisely H_2 concentration in the mass spectrometer facility, due to its low m/z ratio. However such limitation can be overcome by the inspection of the other reactant gas, CO_2.

In each cases the samples underwent reductive pretreatment *in situ* with a 25% H_2 flow at 500°C (previously monitored by H_2-TPR) and a stable ramp temperature of 1°C/min up from 100°C to 500°C, an appropriate temperature range for the reactivity in CO_2 methanation. Different tests have been carried out changing reactant gas proportions, pretreatment conditions and the sample tested. In Figure 64 the samples presented are compared in the same conditions (see legend for further details).

Blank tests (support-only, not reported) show complete inactivity. The first result is that only TI samples show activity, the impregnation method is thus crucial in catalytic activity. A common trait of these samples is their activation at relatively low temperatures (300°C). Different tests were carried out on the most active sample to assess its reactivity in different environments (Figure 63), namely at different relative concentration of the reactant gas mixture. The results of such testing are summarized in Figure 64 that correlates the reactants ratio ($[H_2]$:$[CO_2]$=4 is the stoichiometric ratio) and the lowest CO_2 concentration value remaining in the outlet flow and the maximum methane yield obtained during the reaction. Noteworthy the trend between hydrogen excess and performances (in terms of conversion and yield) is not monotonous, showing an unusual behavior of the material subjected to the mixture: considering ratio 1:20 an outlier (given the large excess of hydrogen), the performances are at best with a ratio 1:8, but get worse with ratio 1:12. This suggests that reducing conditions might alter the interaction among Ni nanoparticles and the support, switching Ce(IV) to Ce(III). Another surprising finding is that increasing the pretreatment temperature up to 600°C, the performances overall worsen, so one can expect an irreversible phase change occurring between 500°C and 600°C in the crystalline phase (metallic Ni or the support CeO_2), impairing the hydrogen spillover from Ni to grain borders and interfaces of the support. Moreover CO, a common byproduct in carbon dioxide methanation is not detected. For these reasons the collected data support the hypothesis by which the mechanism involved in the reaction implies the coordination of C to the Ni atom, and not of the O atom, typical prelude of CO formation.[55–57] The results are shown in Figure 65 and the samples here presented perform better than previous work in literature, especially since they show higher selectivity towards methane, not producing significant amount of CO.[13]

Similar testing was carried out on the exsoluted perovskites (the second and third sets). *In situ* exsolution was performed according to the H_2-TPR results, and therefore 2 hours at 500°C with H_2 5% (after which no reduction peak was detected by TCD-detected TPR).

In this case, given the experience with the supported-Ni catalysts, the ratio was kept constant and stoichiometric (1.2% CO_2 + 4.8% H_2, Ar as carrier), a choice that allowed also to better compare the results with the literature.

In the next section the catalytic results for substoichiometric "pure" perovskites and ceria supported perovskites are reported and discussed and the graphs reporting the catalytic activities are shown in Figure 66.

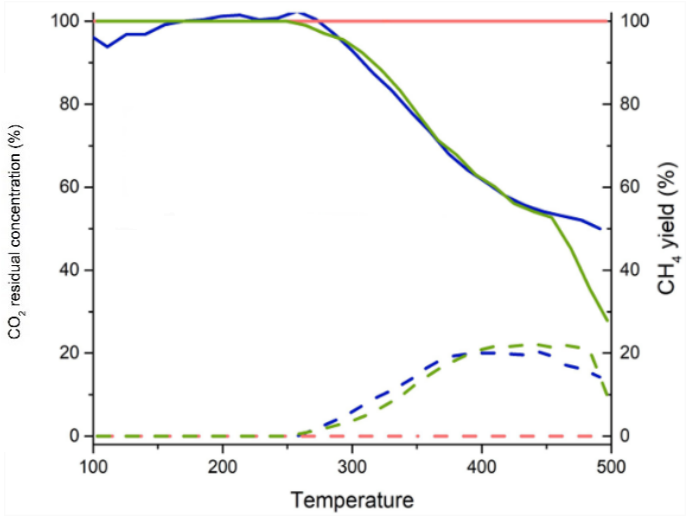

Figure 62 Catalytic testing of samples in Table 1: TI 1.7% in blue, WI 1.7% in pink and Ti 13.4% in green. The conversion is reported in solid line, whereas the yield is in dashed line.

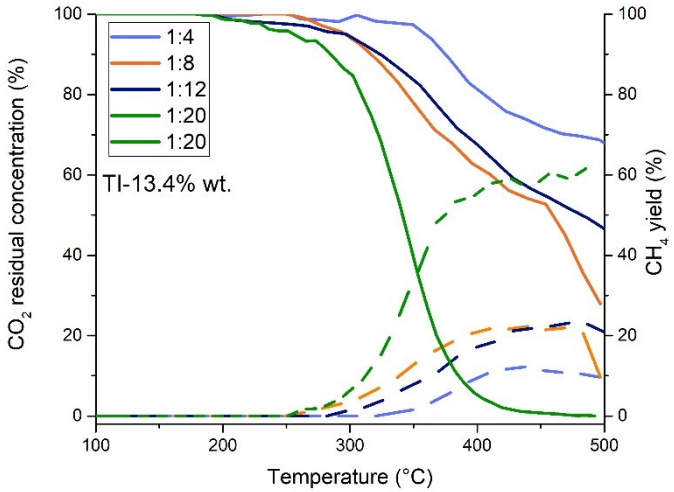

Figure 63 Catalytic testing of TI 13.4% sample. The sample was tested at different reactant ratios to evaluate the effect of the over-stoichiometry of reagents.

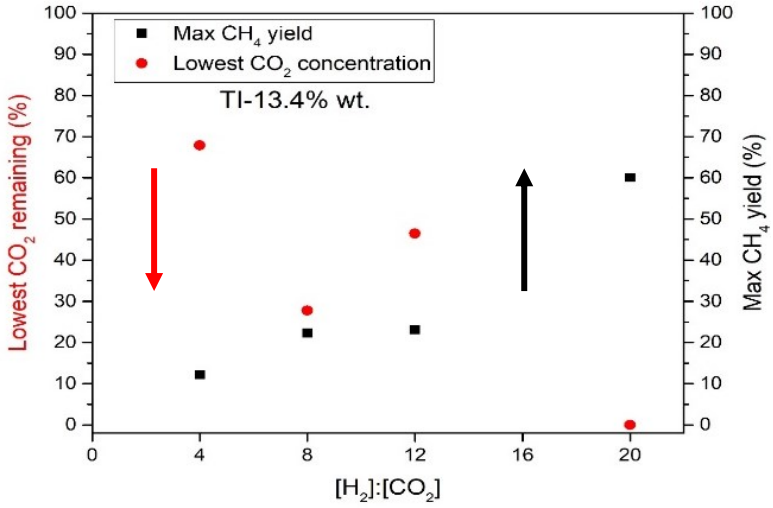

Figure 64 Summary of the results for the test presented in Figure 63.

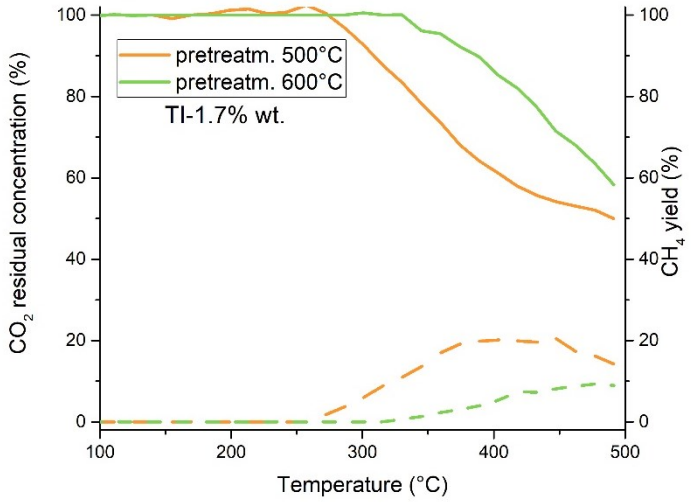

Figure 65 TI 1.7% wt. tested with different pretreatment temperatures (H_2 25% in both cases).

First and foremost, byproducts concentration is not shown since no significant CO or methanol production was detected in any analysis, giving encouraging results about the selectivity of the process.

The behavior for "pure" perovskite samples is quite interesting: carbon dioxide concentration starts to decrease simultaneously with the CH_4 appearance in the reaction mixture. Both samples are active

from 250°C, with a maximum production of methane at 370°C. The trend of methane formation shows a decrease after this peak: as already mentioned, parasite reactions start to take place at higher temperature. However, since no CO was detected, we argue that coking was mostly taking place after the maximum methane production, letting carbon dioxide concentration decrease but not forming CH_4 at the same time.[58] Another evidence for coke deposition onto the catalysts is given by the concentration gap between residual carbon dioxide and produced methane, whose yield never reaches 100% of the expected value. Coking is a well known problem for Ni based catalysts working with carbon based molecules, and many examples in literature correlate this tendency with the particle dimensions: the smaller the less prone to coking.[59–62] Consequently, as we observe a higher carbon dioxide abatement in the case of LN05, but not a higher methane yield, we can conclude that coking is taking place predominantly in the LN05 sample. This sample had the same crystal structure as its homologous LN07 but the stoichiometry is less favoured in this case, probably causing some NiO outside the perovskite structure, although not detected by XRD because of the low amount and, we suppose, low crystalline degree. Some evidence of this behaviour can be supported by H_2-TPR profile: the peak at the lowest temperature (most likely NiO already on the surface) is slightly more intense for LN05, suggesting the presence of reducible Ni on the surface already on the as-prepared sample. It is thus reasonable to hold true that Ni exsolution proceeds through a sort of Ostwald ripening of the particle on the surface, merging with the already present NiO.

Finally the tests carried out on the same LN07 perovskite, but on a support and with a low loading (10% wt.) gave surprising results. With such a loading a very scarce CO_2 conversion was expected, and this was indeed the case for *depLN07*: carbon dioxide concentration was not significantly changing during the ascending temperature ramp (therefore not shown in Figure 66) and methane formation was extremely low, at the lower detection threshold for the instrument. Nevertheless it was possible to quantify it and to obtain a trend: again the temperature of maximum formation was approximately 300°C as in the case of unsupported LN07 but the yield was remarkably low (0.2%).

The surprise came with *synLN07*: despite the same nominal composition and the same low Ni loading, in this case the results were drastically different. Carbon dioxide was converted up to a residual concentration of approximately 70% (double than pure LN07) but with a much lower Ni amount. Also methane yield was interestingly not as low as *depLN07*, allowing us to draw some unexpected and promising conclusions. The synthetic approach employed in this case was able to produce a novel catalyst, in which ceria and the perovskite oxide structure are both formed but also innovatively interacting with each other. We hereby suppose that the synergy between ceria's marked oxygen storage capacity and the perovskite's known oxygen mobility within the structure can contribute to a more efficient exsolution strategy, that allows to achieve a homogeneous Ni particle distribution on the surface resulting from an effective reducing treatment. These results may pave the way to fabrication of supported Ni-catalyst with a fraction of the conventional Ni content that is usually considered noteworthy in catalytic applications, but still with remarkable retained catalytic activity.

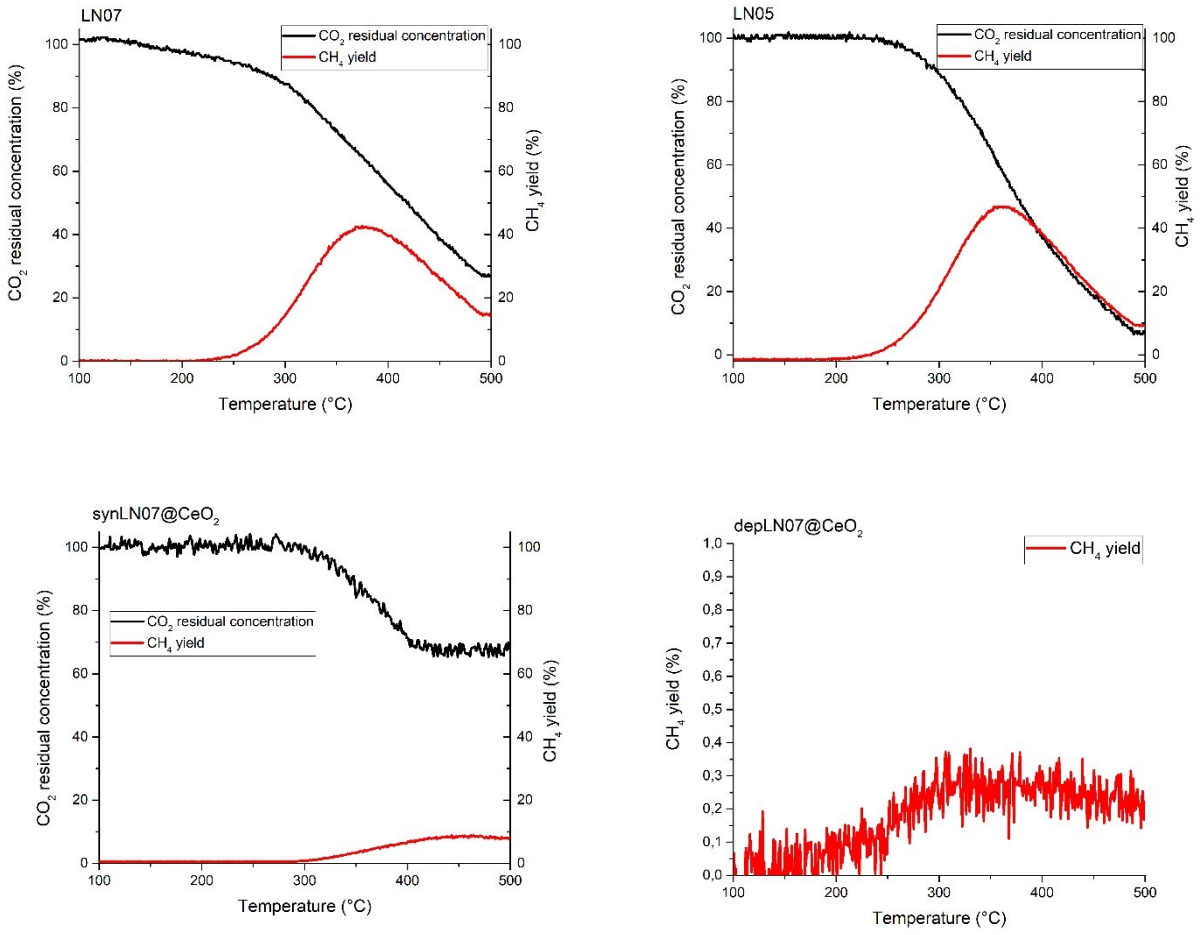

Figure 66 LN07, LN05 and ceria supported LN07 samples tested with stoichiometric CO_2 and H_2 ratio, with a total flow of 100 sccm. Tested in ascending temperature ramp after reducing pretreatment.

4.4 Conclusions

One of the scopes of the presented project was to investigate the role of the interaction between the active catalyst, nickel in this case, and the support, be it ceria, a perovskite or both. Moreover the sustainability of the preparation was carefully evaluated, with a concrete attempt to reduce the amount of catalyst needed to reach satisfactory conversion rate and by avoiding precious metals, a resource which will progressively be in short supply in the next years.[63] The results of this investigation are promising: low amount of active catalyst does not automatically mean inactive materials, but instead a careful tuning of the interaction between support and supported metal can enhance the features of the catalyst with surprising experimental outcome. A similar approach will be discussed and presented in Chapter 6, where single-atom catalysis is attempted in a very peculiar setup, carbon membrane reactors.

Not only material design but also setup design was addressed in this project, much effort was devoted in finding the proper analytical technique and experimental setup to assess the catalytic activity of the materials obtained. Both Gas Chromatography and Mass Spectrometry were employed and considered to define the best protocol to test all the samples presented, also with the final aim of achieving comparable results with the literature. Similarly also the choice of the pretreatment led to several preliminary tests to determine the best experimental conditions that could balance effectiveness of the catalysts and its industrial "readiness" in concrete applications, which we always considered as our final target.

Combining all these aspects together, satisfactory carbon dioxide abatement was reached (up to 10% of residual carbon dioxide concentration), although the role of coking still is an open issue in this field and would need further quantification. At the same time methane was successfully produced and detected with promising yields as well.

All things considered, a straightforward preparation and mild experimental conditions (all measurements were carried out at atmospheric pressure and at temperatures below 500°C) were able

to deliver unexpected catalytic results that will be further examined in depth in the next Chapters, dealing with carbon dioxide as well.

References

(1) Hepburn, C.; Adlen, E.; Beddington, J.; Carter, E. A.; Fuss, S.; Mac Dowell, N.; Minx, J. C.; Smith, P.; Williams, C. K. The Technological and Economic Prospects for CO2 Utilization and Removal. *Nature* **2019**, *575* (7781), 87–97. https://doi.org/10.1038/s41586-019-1681-6.

(2) Quéré, C.; Andrew, R.; Friedlingstein, P.; Sitch, S.; Hauck, J.; Pongratz, J.; Pickers, P.; Ivar Korsbakken, J.; Peters, G.; Canadell, J.; Arneth, A.; Arora, V.; Barbero, L.; Bastos, A.; Bopp, L.; Ciais, P.; Chini, L.; Ciais, P.; Doney, S.; Gkritzalis, T.; Goll, D.; Harris, I.; Haverd, V.; Hoffman, F.; Hoppema, M.; Houghton, R.; Hurtt, G.; Ilyina, T.; Jain, A.; Johannessen, T.; Jones, C.; Kato, E.; Keeling, R.; Klein Goldewijk, K.; Landschützer, P.; Lefèvre, N.; Lienert, S.; Liu, Z.; Lombardozzi, D.; Metzl, N.; Munro, D.; Nabel, J.; Nakaoka, S. I.; Neill, C.; Olsen, A.; Ono, T.; Patra, P.; Peregon, A.; Peters, W.; Peylin, P.; Pfeil, B.; Pierrot, D.; Poulter, B.; Rehder, G.; Resplandy, L.; Robertson, E.; Rocher, M.; Rödenbeck, C.; Schuster, U.; Skjelvan, I.; Séférian, R.; Skjelvan, I.; Steinhoff, T.; Sutton, A.; Tans, P.; Tian, H.; Tilbrook, B.; Tubiello, F.; Van Der Laan-Luijkx, I.; Van Der Werf, G.; Viovy, N.; Walker, A.; Wiltshire, A.; Wright, R.; Zaehle, S.; Zheng, B. Global Carbon Budget 2018. *Earth Syst. Sci. Data* **2018**, *10* (4), 2141–2194. https://doi.org/10.5194/essd-10-2141-2018.

(3) Thema, M.; Bauer, F.; Sterner, M. Power-to-Gas: Electrolysis and Methanation Status Review. *Renewable and Sustainable Energy Reviews*. Elsevier Ltd September 1, 2019, pp 775–787. https://doi.org/10.1016/j.rser.2019.06.030.

(4) Wang, W.; Gong, J. Methanation of Carbon Dioxide: An Overview. *Front. Chem. Eng. China* **2011**, *5* (1), 2–10. https://doi.org/10.1007/s11705-010-0528-3.

(5) Vogt, C.; Monai, M.; Kramer, G. J.; Weckhuysen, B. M. The Renaissance of the Sabatier Reaction and Its Applications on Earth and in Space. *Nat. Catal.* **2019**, *2* (3), 188–197. https://doi.org/10.1038/s41929-019-0244-4.

(6) Frontera, P.; Macario, A.; Ferraro, M.; Antonucci, P. L. Supported Catalysts for CO2 Methanation: A Review. *Catalysts*. MDPI AG February 13, 2017. https://doi.org/10.3390/catal7020059.

(7) Rönsch, S.; Schneider, J.; Matthischke, S.; Schlüter, M.; Götz, M.; Lefebvre, J.; Prabhakaran, P.; Bajohr, S. Review on Methanation - From Fundamentals to Current Projects. *Fuel* **2016**, *166*, 276–296. https://doi.org/10.1016/j.fuel.2015.10.111.

(8) Aziz, M. A. A.; Jalil, A. A.; Triwahyono, S.; Ahmad, A. CO2 Methanation over Heterogeneous Catalysts: Recent Progress and Future Prospects. *Green Chem.* **2015**, *17* (5), 2647–2663. https://doi.org/10.1039/c5gc00119f.

(9) Younas, M.; Loong Kong, L.; Bashir, M. J. K.; Nadeem, H.; Shehzad, A.; Sethupathi, S. Recent Advancements, Fundamental Challenges, and Opportunities in Catalytic Methanation of CO 2. *Energy & Fuels* **2016**, *30* (11), 8815–8831. https://doi.org/10.1021/acs.energyfuels.6b01723.

(10) EUROPEAN COMMISSION. COMMITTEE AND THE COMMITTEE OF THE REGIONS on the 2017 List of Critical Raw Materials for the EU; 2017; Vol. Brussels,.

(11) Cárdenas-Arenas, A.; Quindimil, A.; Davó-Quiñonero, A.; Bailón-García, E.; Lozano-Castelló, D.; De-La-Torre, U.; Pereda-Ayo, B.; González-Marcos, J. A.; González-Velasco, J. R.; Bueno-López, A. Isotopic and in Situ DRIFTS Study of the CO2 Methanation Mechanism Using Ni/CeO2 and Ni/Al2O3 Catalysts. *Appl. Catal. B Environ.* **2020**, *265*, 118538. https://doi.org/10.1016/j.apcatb.2019.118538.

(12) Madier, Y.; Descorme, C.; Le Govic, A. M.; Duprez, D. Oxygen Mobility in CeO2 and CexZr(1-x)O2 Compounds: Study by CO Transient Oxidation And18O/16O Isotopic Exchange. *J. Phys. Chem. B* **1999**, *103* (50), 10999–11006. https://doi.org/10.1021/jp991270a.

(13) Marconi, E.; Tuti, S.; Luisetto, I. Structure-Sensitivity of CO 2 Methanation over Nanostructured Ni Supported on CeO 2 Nanorods. *Catalysts* **2019**, *9* (4), 375. https://doi.org/10.3390/catal9040375.

(14) Mebrahtu, C.; Abate, S.; Perathoner, S.; Chen, S.; Centi, G. CO2 Methanation over Ni Catalysts Based on Ternary and Quaternary Mixed Oxide: A Comparison and Analysis of the Structure-Activity Relationships. *Catal. Today* **2018**, *304*, 181–189. https://doi.org/10.1016/j.cattod.2017.08.060.

(15) Li, G.; Hu, L.; Hill, J. M. Comparison of Reducibility and Stability of Alumina-Supported Ni Catalysts Prepared by Impregnation and Co-Precipitation. *Appl. Catal. A Gen.* **2006**, *301* (1), 16–24. https://doi.org/10.1016/j.apcata.2005.11.013.

(16) Italiano, C.; Llorca, J.; Pino, L.; Ferraro, M.; Antonucci, V.; Vita, A. CO and CO2 Methanation over Ni Catalysts Supported on CeO2, Al2O3 and Y2O3 Oxides. *Appl. Catal. B Environ.* **2020**, *264*, 118494. https://doi.org/10.1016/j.apcatb.2019.118494.

(17) Le, T. A.; Kim, M. S.; Lee, S. H.; Kim, T. W.; Park, E. D. CO and CO2 Methanation over Supported Ni Catalysts. *Catal. Today* **2017**, *293–294*, 89–96. https://doi.org/10.1016/j.cattod.2016.12.036.

(18) Ricca, A.; Truda, L.; Palma, V. Study of the Role of Chemical Support and Structured Carrier on the CO2 Methanation Reaction. *Chem. Eng. J.* **2019**, *377*, 120461. https://doi.org/10.1016/j.cej.2018.11.159.

(19) Zhou, G.; Liu, H.; Cui, K.; Xie, H.; Jiao, Z.; Zhang, G.; Xiong, K.; Zheng, X. Methanation of Carbon Dioxide over Ni/CeO 2 Catalysts: Effects of Support CeO 2 Structure. *Int. J. Hydrogen Energy* **2017**, *42* (25), 16108–16117. https://doi.org/10.1016/j.ijhydene.2017.05.154.

(20) Yu, Y.; Chan, Y. M.; Bian, Z.; Song, F.; Wang, J.; Zhong, Q.; Kawi, S. Enhanced Performance and Selectivity of CO2 Methanation over G-C3N4 Assisted Synthesis of Ni CeO2 Catalyst: Kinetics and DRIFTS Studies. *Int. J. Hydrogen Energy* **2018**, *43* (32), 15191–15204. https://doi.org/10.1016/j.ijhydene.2018.06.090.

(21) Iglesias, I.; Quindimil, A.; Mariño, F.; De-La-Torre, U.; González-Velasco, J. R. Zr Promotion Effect in CO2 Methanation over Ceria Supported Nickel Catalysts. *Int. J. Hydrogen Energy* **2019**, *44* (3), 1710–1719. https://doi.org/10.1016/j.ijhydene.2018.11.059.

(22) Ocampo, F.; Louis, B.; Roger, A. C. Methanation of Carbon Dioxide over Nickel-Based Ce0.72Zr0.28O2 Mixed Oxide Catalysts Prepared by Sol–Gel Method. *Appl. Catal. A Gen.* **2009**, *369* (1–2), 90–96. https://doi.org/10.1016/J.APCATA.2009.09.005.

(23) Pan, Q.; Peng, J.; Sun, T.; Wang, S.; Wang, S. Insight into the Reaction Route of CO2 Methanation: Promotion Effect of Medium Basic Sites. *Catal. Commun.* **2014**, *45*, 74–78. https://doi.org/10.1016/J.CATCOM.2013.10.034.

(24) Kwon, O.; Sengodan, S.; Kim, K.; Kim, G.; Jeong, H. Y.; Shin, J.; Ju, Y. W.; Han, J. W.; Kim, G. Exsolution Trends and Co-Segregation Aspects of Self-Grown Catalyst Nanoparticles in Perovskites. *Nat. Commun.* **2017**, *8*. https://doi.org/10.1038/ncomms15967.

(25) Sun, Y. F.; Li, J. H.; Zhang, Y. Q.; Hua, B.; Luo, J. L. Bifunctional Catalyst of Core-Shell Nanoparticles Socketed on Oxygen-Deficient Layered Perovskite for Soot Combustion: In Situ Observation of Synergistic Dual Active Sites. *ACS Catal.* **2016**, *6* (4), 2710–2714. https://doi.org/10.1021/acscatal.6b00081.

(26) Motohashi, T.; Kimura, M.; Masubuchi, Y.; Kikkawa, S.; George, J.; Dronskowski, R. Significant Lanthanoid Substitution Effect on the Redox Reactivity of the Oxygen-Storage Material BaYMn2O5+δ. *Chem. Mater.* **2016**, *28* (12), 4409–4414. https://doi.org/10.1021/acs.chemmater.6b01501.

(27) Jiang, M.; Wang, B.; Yao, Y.; Li, Z.; Ma, X.; Qin, S.; Sun, Q. A Comparative Study of CeO2-Al2O3 Support Prepared with Different Methods and Its Application on MoO3/CeO2-Al2O3 Catalyst for Sulfur-Resistant Methanation. *Appl. Surf. Sci.* **2013**, *285*, 267–277. https://doi.org/10.1016/j.apsusc.2013.08.049.

(28) Montini, T.; Melchionna, M.; Monai, M.; Fornasiero, P. Fundamentals and Catalytic Applications of CeO 2 -Based Materials. *Chem. Rev.* **2016**, *116* (10), 5987–6041. https://doi.org/10.1021/acs.chemrev.5b00603.

(29) Garbujo, A.; Pacella, M.; Natile, M. M.; Guiotto, M.; Fabro, J.; Canu, P.; Glisenti, A. On A-Doping Strategy for Tuning the TWC Catalytic Performance of Perovskite Based Catalysts. *Appl. Catal. A Gen.* **2017**, *544* (July), 94–107. https://doi.org/10.1016/j.apcata.2017.07.009.

(30) Giroir-Fendler, A.; Alves-Fortunato, M.; Richard, M.; Wang, C.; Díaz, J. A.; Gil, S.; Zhang, C.; Can, F.; Bion, N.; Guo, Y. Synthesis of Oxide Supported LaMnO3 Perovskites to Enhance Yields in Toluene Combustion. *Appl. Catal. B Environ.* **2016**, *180*, 29–37. https://doi.org/10.1016/j.apcatb.2015.06.005.

(31) Alifanti, M.; Florea, M.; Somacescu, S.; Parvulescu, V. I. Supported Perovskites for Total Oxidation of Toluene. *Appl. Catal. B Environ.* **2005**, *60* (1–2), 33–39. https://doi.org/10.1016/j.apcatb.2005.02.018.

(32) Peter, S. D.; Garbowski, E.; Perrichon, V.; Primet, M. NO Reduction by CO over Aluminate-supported Perovskites. *Catal. Lett. 2000 701* **2000**, *70* (1), 27–33. https://doi.org/10.1023/A:1019027619209.

(33) Lim, S.; Choi, J. W.; Jin Suh, D.; Lee, U.; Song, K. H.; Ha, J. M. Low-Temperature Oxidative Coupling of Methane Using Alkaline Earth Metal Oxide-Supported Perovskites. *Catal. Today* **2020**, *352*, 127–133. https://doi.org/10.1016/J.CATTOD.2019.11.014.

(34) Voorhoeve, R. J. H.; Remeika, J. P.; Trimble, L. E.; Cooper, A. S.; Disalvo, F. J.; Gallagher, P. K. Perovskite-like La1-XKxMnO3 and Related Compounds: Solid State Chemistry and the Catalysis of the Reduction of NO by CO and H2. *J. Solid State Chem.* **1975**, *14* (4), 395–406. https://doi.org/10.1016/0022-4596(75)90061-4.

(35) Gallagher, P. K.; Johnson, D. W.; Schrey, F. Studies of Some Supported Perovskite Oxidation Catalysts. *Mater. Res. Bull.* **1974**, *9* (10), 1345–1352. https://doi.org/10.1016/0025-5408(74)90057-9.

(36) Shirley, D. A. High-Resolution x-Ray Photoemission Spectrum of the Valence Bands of Gold. *Phys. Rev. B* **1972**, *5* (12), 4709–4714. https://doi.org/10.1103/PhysRevB.5.4709.

(37) Briggs, D. Handbook of X-Ray Photoelectron Spectroscopy C. D. Wanger, W. M. Riggs, L. E. Davis, J. F. Moulder and G. E.Muilenberg Perkin-Elmer Corp., Physical Electronics Division, Eden Prairie, Minnesota, USA, 1979. 190 Pp. $195; Chastain, J., Ed.; Eden Prairie, 1981; Vol. 3. https://doi.org/10.1002/sia.740030412.

(38) Umbach, E. *Practical Surface Analysis*; Wiley: New York, 1992; Vol. 11. https://doi.org/10.1016/0165-9936(92)87016-d.

(39) Yang, E.; Moon, D. J. Synthesis of LaNiO 3 Perovskite Using an EDTA-Cellulose Method and Comparison with the Conventional Pechini Method: Application to Steam CO 2 Reforming of Methane. *RSC Adv.* **2016**, *6* (114), 112885–112898. https://doi.org/10.1039/C6RA22945J.

(40) Luisetto, I.; Tuti, S.; Di Bartolomeo, E. Co and Ni Supported on CeO2 as Selective Bimetallic Catalyst for Dry Reforming of Methane. *Int. J. Hydrogen Energy* **2012**, *37* (21), 15992–15999. https://doi.org/10.1016/j.ijhydene.2012.08.006.

(41) Naumkin, V. A.; Kraut-Vass, A.; Gaarenstroom, S. W.; J., P. C. NIST X-Ray Photoelectron Spectroscopy Database. *Meas. Serv. Div. Natl. Inst. Stand. Technol.* **2012**, *20899* (20), 20899. https://doi.org/10.18434/T4T88K.

(42) Rebellato, J.; Natile, M. M.; Glisenti, A. Influence of the Synthesis Procedure on the Properties and Reactivity of Nanostructured Ceria Powders. *Appl. Catal. A Gen.* **2008**, *339* (2), 108–120. https://doi.org/10.1016/j.apcata.2007.12.031.

(43) Natile, M. M.; Poletto, F.; Galenda, A.; Glisenti, A.; Montini, T.; De Rogatis, L.; Fornasiero, P. La0.6Sr0.4Co1-YFeyO 3-δ Perovskites: Influence of the Co/Fe Atomic Ratio on Properties and

Catalytic Activity toward Alcohol Steam-Reforming. *Chem. Mater.* **2008**, *20* (6), 2314–2327. https://doi.org/10.1021/cm703329k.

(44) Galenda, A.; Natile, M. M.; Krishnan, V.; Bertagnolli, H.; Glisenti, A. LaSrCoFeO and Fe 2 O 3 /LaSrCoFeO Powders: Synthesis and Characterization. *Chem. Mater.* **2007**, *19* (11), 2796–2808. https://doi.org/10.1021/cm062742i.

(45) Natile, M. M.; Ponzoni, A.; Concina, I.; Glisenti, A. Chemical Tuning versus Microstructure Features in Solid-State Gas Sensors: LaFe1-XGaxO3, a Case Study. *Chem. Mater.* **2014**, *26* (4), 1505–1513. https://doi.org/10.1021/cm4018858.

(46) Glisenti, A.; Pacella, M.; Guiotto, M.; Natile, M. M.; Canu, P. Largely Cu-Doped LaCo1-XCuxO3 Perovskites for TWC: Toward New PGM-Free Catalysts. *Appl. Catal. B Environ.* **2016**, *180*, 94–105. https://doi.org/10.1016/j.apcatb.2015.06.017.

(47) Tabata, K.; Matsumoto, I.; Kohiki, S. Surface Characterization and Catalytic Properties of La1-x-SrxCoO3. *J. Mater. Sci.* **1987**, *22* (5), 1882–1886. https://doi.org/10.1007/BF01132422.

(48) Tejuca, L. G.; Fierro, J. É. L. G. XPS and TPD Probe Techniques for the Study of LaNiO3 Perovskite Oxide. *Thermochim. Acta* **1989**, *147* (2), 361–375. https://doi.org/10.1016/0040-6031(89)85191-3.

(49) Kang, Z.; Li, L.; Wei, Q. An XPS Study of Perovskite Oxides RECrO3. *Chem. Res. Chinese Univ.* **1996**, *12* (3), 280–284.

(50) Galenda, A.; Natile, M. M.; Nodari, L.; Glisenti, A. La0.8Sr0.2Ga0.8Fe0.2O3-δ: Influence of the Preparation Procedure on Reactivity toward Methanol and Ethanol. *Appl. Catal. B Environ.* **2010**, *97* (3–4), 307–322. https://doi.org/10.1016/j.apcatb.2010.04.004.

(51) Haber, J.; Stoch, J.; Ungier, L. X-Ray Photoelectron Spectra of Oxygen in Oxides of Co, Ni, Fe and Zn. *J. Electron Spectros. Relat. Phenomena* **1976**, *9* (5), 459–467. https://doi.org/10.1016/0368-2048(76)80064-3.

(52) Mullica, D. F.; Perkins, H. O.; Lok, C. K. C.; Young, V. The X-Ray Photoemission Spectra of La(OH)3. *J. Electron Spectros. Relat. Phenomena* **1993**, *61* (3–4), 337–355. https://doi.org/10.1016/0368-2048(93)80024-G.

(53) Sunding, M. F.; Hadidi, K.; Diplas, S.; Løvvik, O. M.; Norby, T. E.; Gunnæs, A. E. XPS Characterisation of in Situ Treated Lanthanum Oxide and Hydroxide Using Tailored Charge Referencing and Peak Fitting Procedures. *J. Electron Spectros. Relat. Phenomena* **2011**, *184* (7), 399–409. https://doi.org/10.1016/j.elspec.2011.04.002.

(54) Marta M. Natile, *; Giovanni Boccaletti, and; Glisenti, A. Properties and Reactivity of Nanostructured CeO2 Powders: Comparison among Two Synthesis Procedures. *Chem. Mater.* **2005**, *17* (25), 6272–6286. https://doi.org/10.1021/CM051352D.

(55) Aitbekova, A.; Wu, L.; Wrasman, C. J.; Boubnov, A.; Hoffman, A. S.; Goodman, E. D.; Bare, S. R.; Cargnello, M. Low-Temperature Restructuring of CeO 2 -Supported Ru Nanoparticles Determines Selectivity in CO 2 Catalytic Reduction. *J. Am. Chem. Soc.* **2018**, *140* (42), 13736–13745. https://doi.org/10.1021/jacs.8b07615.

(56) Lee, J.; Ryou, Y.; Chan, X.; Kim, T. J.; Kim, D. H. How Pt Interacts with CeO 2 under the Reducing and Oxidizing Environments at Elevated Temperature: The Origin of Improved Thermal Stability of Pt/CeO 2 Compared to CeO 2. *J. Phys. Chem. C* **2016**, *120* (45), 25870–25879. https://doi.org/10.1021/acs.jpcc.6b08656.

(57) Kobune, M.; Sato, S.; Takahashi, R. Surface-Structure Sensitivity of CeO2 for Several Catalytic Reactions. *J. Mol. Catal. A Chem.* **2008**, *279* (1), 10–19. https://doi.org/10.1016/j.molcata.2007.09.027.

(58) Wang, S.; Lu, G. Q. (Max). Catalytic Activities and Coking Characteristics of Oxides-Supported Ni Catalysts for CH 4 Reforming with Carbon Dioxide. *Energy & Fuels* **1998**, *12* (2), 248–256. https://doi.org/10.1021/ef970092m.

(59) Peña, J. A.; Herguido, J.; Guimon, C.; Monzón, A.; Santamaría, J. Hydrogenation of Acetylene over Ni/NiAl2O4Catalyst: Characterization, Coking, and Reaction Studies. *J. Catal.* **1996**, *159* (2), 313–322. https://doi.org/10.1006/JCAT.1996.0093.

(60) Dias, Y. R.; Perez-Lopez, O. W. Carbon Dioxide Methanation over Ni-Cu/SiO2 Catalysts. *Energy Convers. Manag.* **2020**, *203*, 112214. https://doi.org/10.1016/J.ENCONMAN.2019.112214.

(61) Valinejad Moghaddam, S.; Rezaei, M.; Meshkani, F.; Daroughegi, R. Carbon Dioxide Methanation over Ni-M/Al2O3 (M: Fe, CO, Zr, La and Cu) Catalysts Synthesized Using the One-Pot Sol-Gel Synthesis Method. *Int. J. Hydrogen Energy* **2018**, *43* (34), 16522–16533. https://doi.org/10.1016/J.IJHYDENE.2018.07.013.

(62) Razzaq, R.; Zhu, H.; Jiang, L.; Muhammad, U.; Li, C.; Zhang, S. Catalytic Methanation of CO and CO2 in Coke Oven Gas over Ni–Co/ZrO2–CeO2. *Ind. Eng. Chem. Res.* **2013**, *52* (6), 2247–2256. https://doi.org/10.1021/IE301399Z.

(63) Baskaran, G. Firms' Approach to Mitigating Risks in the Platinum Group Metals Sector. *Miner. Econ.* **2021**, *34* (3), 385–398. https://doi.org/10.1007/S13563-021-00249-4/FIGURES/8.

5. Exsoluted mesoporous Ti-based perovskites for carbon dioxide methanation

In this Chapter a joint project with Prof. Simone Mascotto's group at the University of Hamburg (Germany) will be presented. His research group "Functional Nanoceramics" has developed a sound experience about the synthesis of functional ceramics with tunable porosity, and thus also synthesis of perovskite oxides endowed with mesoporosity for catalytic applications. Therefore, selected perovskite compositions were evaluated towards carbon dioxide methanation combining their competences in synthesis with our catalytic assessment of the samples and XPS analysis of the synthetized materials. The following Chapter was partially written by Prof. S. Mascotto and a former coworker, A. I. Tsiotsias (synthesis of the materials and main characterization techniques), to whom my grateful acknowledgements go.

5.1 Introduction

The relevance of the carbon dioxide methanation reaction has already been addressed previously in this work. Ni-based catalysts have proven to be active in this reaction thanks to their high methanation activity, low cost and natural abundance,[1,2] although with some limitations due to the tendency of sintering and coking.[3] To cope with this notable drawback, it is advantageous to design and develop novel catalysts with high porosity, a proper dispersion of Ni nanoparticle on the surface and tunable metal-support interactions.[4] Mesoporous supports, as the ones employed for this project, are used as they might inhibit sintering of the metal nanoparticles and enhance useful metal-support interactions, and promote as well the dissociation and adsorption of CO_2.[5,6] Authors claim that tuning the redox properties of the support and the active metal center can promote electron transfer between across the interphase, increasing the electron density on the metal. These acquired electrons can enhance the coupling between nickel and carbon, thereby favoring the breaking of the C=O bond and ultimately

the formation of methane.[7] Moreover the physicochemical features of the support influence the crystal size, the surface properties, the reducibility and the catalytic properties of Ni particles.[8–10] Similarly to what is reported in Chapter 4, perovskite oxides can be successfully exploited as supports thanks to their peculiar physical and chemical properties, *e.g.* high thermal stability, good reactivity of lattice oxygen, low cost and easy preparation. They have been already widely used in a number of high temperature reactions, such as carbon dioxide methanation, indeed in literature examples of exsoluted Ni particles from a perovskite matrix can be retrieved, similarly lanthanum titanate with Sr and Ni doping are already described for the formation of Ni nanoparticles on the surface by means of reductive treatments. [4,11–13] B-site located Ni in perovskites can form metal nanoparticles in a reducing environment [14], and this results in numerous and uniformly distributed catalytically active sites on the surface of the perovskites, with also good thermal and redox stability. [14,15] Moreover, as reported elsewhere, [16] mesoporous supports are of great interest since they can provide confinement in the well-developed mesopores of support materials, inhibiting the Ni nanoparticles from sintering. For these reasons, both of morphological and chemical nature, mesoporous perovskites look like a suitable and promising solution for Ni nanoparticles exsolution for catalytic applications.[17,18]

5.2 Experimental part

5.2.1 Material synthesis

The synthesis route used for the preparation of the template-free perovskite oxides is based on a modified Pechini method, optimized by Kayaalp et al. [19,20] (Figure 67). Titanium (IV) isopropoxide ($Ti(OCH(CH_3)_2)_4$) was first introduced to 11.9 ml of glycerol and stirred for 30 min at room temperature. Afterwards, 40.7 mmol of citric acid were added and the solution was heated up to 60 ^oC in an oil bath. After further stirring for 30 min in order for the citric acid to be dissolved, stoichiometric amounts of $Sr(NO_3)_2$, $La(NO_3)_3{\cdot}6H_2O$ and $Ni(NO_3)_2{\cdot}6H_2O$ were added into the reaction mixture at 15 min intervals. $Sr(NO_3)_2$ was initially dissolved in an amount of deionized H_2O equal to its solubility limit and stirred for 30 min before being added into the reaction mixture. The

molar ratio of glycerol to citric acid and to the total amount of metal cations was set to 30:4:1. After 2 h of further stirring, the temperature was increased up to 130 ºC and the mixture was stirred for another 2 h, to promote the polycondensation between the chelating agents. The resulting gel is then calcined in air at 400 ºC for 2 h and 600 ºC for 2h (2°Cmin^{-1} heating rate). The obtained $La_{0.2}Sr_{0.8}Ti_{0.94}Ni_{0.06}O_3$ (LSTN) powder was then treated once with an acetic acid (HOAc) solution to remove carbonate impurities with the powder being washed extensively afterwards with deionized water to ensure pH neutrality. Two more samples, named LSTN_800 and LSTN_1000, were prepared, with the only difference being the final calcination temperature, which was set at 800ºC and 1000ºC respectively.

The cooperative assembly synthesis of the templated perovskite oxides (*Figure 68*) is performed with a similar procedure, with the addition of appropriate amounts of prehydrolyzed TEOS (TetraEthyl OrthoSilicate) solution before the polymerization step. The resulting gel is then calcined in air at 400 ºC for 2 h and 600ºC for 2h (2C min^{-1} heating rate) to form an interpenetrating SiO_2/perovskite nanocomposite. The obtained powders were treated once with an acetic acid (HOAc) solution to remove carbonate impurities and twice with NaOH (2 M) at room temperature to etch out the silica template. A final acetic acid treatment was repeated for all samples in the end. After each step, the powders were washed extensively with deionized water to ensure pH neutrality. The prepared sample

was named LSTN_Si2 when the molar ratio between TEOS and total metal cations was 20% and LSTN_Si4 when the molar ratio was 40%.

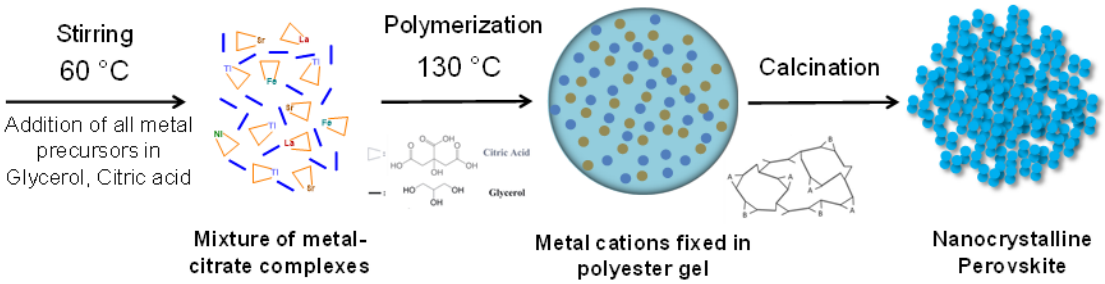

Figure 67 Formation mechanism of mesoporous perovskite oxides via a modified Pechini synthesis route. Glycerol and citric acid molecules in the initial mixture polymerize to form a polyester gel with fixed and highly distributed metal cations. This gel yields a porous nanocrystalline perovskite after calcination.

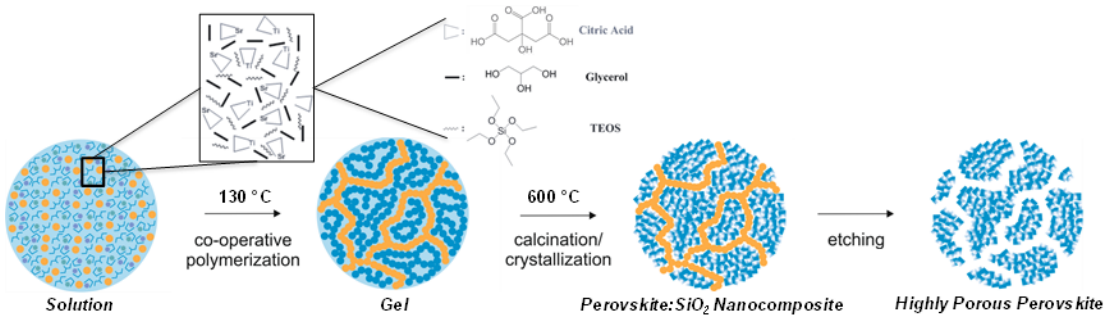

Figure 68 Formation mechanism of mesoporous perovskite oxides via the cooperative assembly synthesis route. The yellow and blue symbols represent the silica and the complex-polymer/ perovskite respectively.

5.2.2 Material characterization

X-ray diffraction analysis was carried out with an X'Pert Pro diffractometer (PANalytical Corp.) with 1.5406 Å Ni-filtered Cu-K_α radiation, operating at 45 kV and 40 mA. The mean crystallite sizes were

calculated from the full width at half maximum (FWHM) of the most intense reflection using the Scherrer equation [21].

Infrared (IR) spectra were obtained on KBr pellets in the region 400–4000 cm^{-1} in transmission mode with a Bruker Vertex 70 FTIR spectrophotometer.

The nitrogen physisorption isotherms were obtained at 77 K using a Quadrasorb SI-MP by Quantachrome. Outgassing was performed with a Masterprep Degasser (Quantachrome Corp.) at 120°C for 12 h. Specific surface areas were determined with the Brunauer-Emmett-Teller (BET) method [22] at p/p^o = 0.07-0.3. Pore size distribution was determined with the NLDFT method [22] applying the model for silica cylindrical pores on the adsorption branch by using the Quantachrome ASiQWin software.

Transmission electron microscopy measurements were carried out on a JEOL JEM 2200 FS operating at 200 kV equipped with two CEOS Cs correctors (CETCOR, CESCOR), a JEOL JED-2300 Si(Li) EDX (Energy Dispersive X-ray spectroscopy) detector, a Gatan 4K UltraScan 1000 camera and a HAADF (High Angle Annular Dark Field) detector. The sample was ground into a fine powder, which was suspended in ethanol by sonication and dropped on a carbon coated 400 mesh TEM grid. The excess solvent was removed with a filter paper and by drying the grid under air. Energy dispersive X-ray spectra and mapping were acquired using 256x256 pixels (pixel size of 0.7 nm) and a dwell time of 0.5 ms $pixel^{-1}$ (corrected for dead time) with 30 cycles. Additionally, EDX measurements were repeated at least on three positions for each sample.

Thermal characterization was carried out using a NETZSCH STA 449F3 coupled with an Äeolos QMS403C mass detector, employing a 10°C min^{-1} ramping rate until the final temperature of 600°C with a dwell time of 1 h. The gas stream employed at first was O_2/Ar (volume ratio 20/80). The total flow rate was set at 1.2 l h^{-1} and 80 mg of the solid material were used. The system was left to cool down and an Ar gas stream was subsequently flowed, using the same ramping rate, final temperature and total flow.

Reduction treatments of the prepared perovskite oxide powders (TPR-MS) were carried out using a U-shaped quartz tube filled with 0,35 g sample and coupled with a Cirrus2 MKS mass spectrometer. 5% H_2/N_2 (volume ratio 5/95) was chosen as the reducing gas and the flow rate was set at 20 ml min^{-1}. A ramping rate of 10°C min^{-1} was employed to reach the final temperature, which was set at 100ºC lower than the sample calcination temperature (500ºC for LSTN, LSTN_Si2 and LSTN_Si4 samples, 700ºC for the LSTN_800 sample and 900ºC for the LSTN_1000 sample). The dwell time at the final temperature was set at 1 h. The suffix "_Red" was added after the name of the corresponding calcined sample to indicate the sample in its reduced form, after the corresponding reduction treatment.

XPS (X-ray Photoelectron Spectroscopy) measurements were performed on the samples both prior and after catalytic testing. The aim is to evaluate whether the oxidation states of the cations present in the structure have changed and to complete the carbon balance calculation: indeed, a well-known issue in CO_2 methanation performed on Ni-based catalysts is coking, so the detection of an increased amount of elemental carbon on the surface is diagnostic of the formation of this by-product. XPS measurements were carried out with a Perkin Elmer ϕ 5600 ci Multi Technique System. The spectrometer was calibrated by assuming the Binding Energy (BE) of the Au $4f_{7/2}$ line to be 84.0 eV with respect to the Fermi level. Both extended spectra (survey – 117.0 eV pass energy) and detailed spectra (for La 3d, Sr 3d, Ti 2p, Ni 2p, C 1s, O 1s, Si 2p) were collected with a standard Al Kα source working at 200 W. The atomic percentage, after a Shirley-type background subtraction, was evaluated using the PHI sensitivity factors.[23,24] The peak positions were corrected for the charging effects by considering the C 1s peak at 284.8 eV and evaluating the BE differences. [25]

5.2.3 Catalytic testing

The catalytic activity towards carbon dioxide methanation on LSTN-type catalysts was measured in a U-shaped Micromeritics reactor, blocked at the bottom by quartz wool at atmospheric pressure. Autochem II 2920 Micromeritics integrated mass flow controllers were used to control the flow rate of the reagents. Before each measurement the sample was kept under inert gas flow (He) for 30

minutes. Each measurement was performed under an increasing temperature ramp from room temperature to 500°C (3°C/min). The reactant gas mixture used was supplied in stoichiometric ratio (1.2% CO_2 + 4.8% H_2, Ar as carrier). The reactor products were samples with a gas-sampling valve, and the composition was monitored with a Quadrupole Mass Spectrometer (European Spectrometry Systems – ESS) connected to the output of the Micromeritics reactor. Prior to every measurement the calibration of the reagent gases was performed comparing the signal of the spectrometer to the known concentration of the supplied gas. Each sample was tested without any pretreatment as Ni nanoparticles were already exsoluted from the composite starting material by a prior reductive treatment. CO_2 concentration is calculated from the mass spectrometer signal, with the following formula:

Concentration of $CO_2 = 100*\left(\frac{x_{CO2}}{x^0_{CO2}}\right)$

Where x_{CO2} is the concentration at different temperature and x_{CO2}^0 is the concentration at the beginning of the test. Methane yield is obtained as a percentage of an expected theoretical 100% yield (complete conversion of carbon dioxide into methane).

Sample	La	Sr	Ti	Ni
LSTN_1000	0.23	0.55	0.94	0.03
LSTN_800	0.22	0.59	0.94	0.04
LSTN	0.21	0.60	0.94	0.04
LSTN_Si2	0.20	0.57	0.94	0.04
LSTN_Si4	0.13	0.43	0.94	0.04

Table 23 Average atomic composition regarding the elements determined by STEM/EDX (at % values normalized by the titanium amount in $La_{0.2}Sr_{0.8}Ti_{0.94}Ni_{0.06}O_3$ molecular formula) in the samples with $La_{0.2}Sr_{0.8}Ti_{0.94}Ni_{0.06}O_3$ nominal stoichiometry calcined at different temperatures and with increasing template loads.

5.3 Results and discussion

From the X-ray diffractograms of the samples after etching (Figure 69), we can observe pure phase perovskite structure for the template-free LSTN and LSTN_800 samples calcined at 600 ºC and 800 ºC respectively, as well as for the templated sample prepared with the use of 20% (mol) of siliceous template (LSTN_Si2), with their reflections roughly matching the ones for pure $SrTiO_3$ perovskite. An amorphous bump in the region of 25 – 32 2θ and reflections attributed to NiO phase for the sample synthesized using 40% (mol) of siliceous template (LSTN_Si4) can be observed. Furthermore, secondary reflections assigned to crystalline rutile phase (TiO_2) can be observed for the template-free LSTN_1000 sample calcined at 1000 ºC.

An important factor that determines the materials textural properties and possibly the homogeneity of metal dispersion is the calcination temperature. Higher calcination temperature typically yields more crystalline materials with larger crystallite sizes, but lower specific surface areas.[26] However, the presence of rutile reflections on the LSTN_1000 sample means that higher calcination temperature

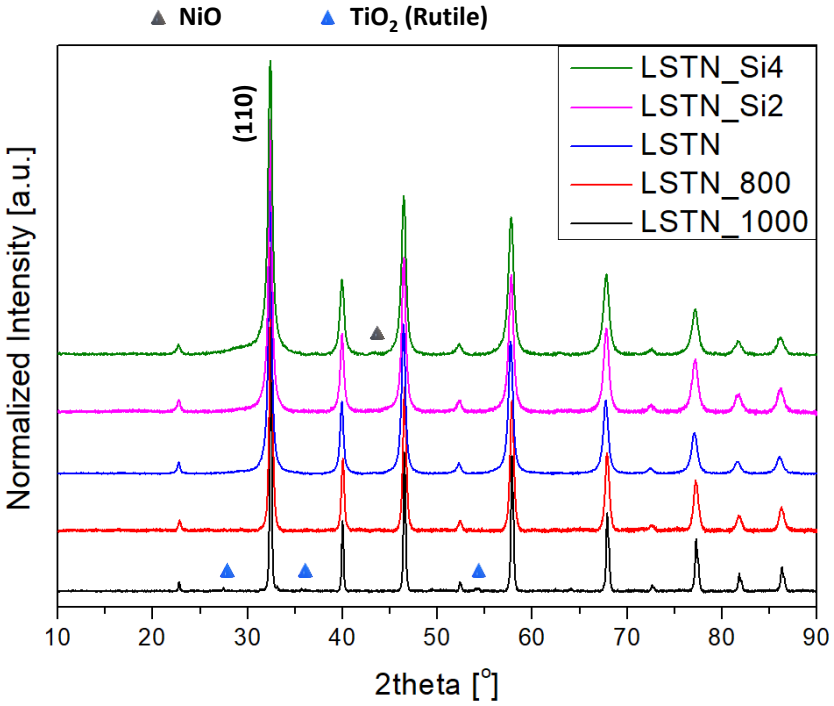

Figure 69 X-ray diffractograms of the samples with $La_{0.2}Sr_{0.8}Ti_{0.94}Ni_{0.06}O_3$ nominal stoichiometry calcined at different temperatures and with increasing template loads.

does not always lead to samples of higher purity with a homogenous metal dispersion throughout the perovskite lattice. It is also evident that the perovskite crystallite size is drastically increased as the calcination temperature increases since the perovskite reflections become much sharper. The average calculated perovskite crystallite size calculated by applying the Scherrer equation on the (110) perovskite reflection rises with increasing calcination temperature from around 28 nm when the perovskite is calcined at 600ºC to 78 nm when the perovskite is calcined at 1000ºC.

A significant broadening of the perovskite reflections also takes place upon using higher template loads. The average calculated perovskite crystallite drops with increasing template load from around 28 nm when no TEOS is added to 19 nm when 40% TEOS (molar ratio) is added. This drop in the average perovskite crystallite size could be explained by the hindering of the mass transport of the perovskite phase during calcination, due to the addition of the siliceous precursor [27]. This hindrance of the mass transport during calcination can also account for segregation of NiO in the LSTN_Si4 sample.

N_2 physisorption (Figure 70) clearly shows a progressive increase of porosity upon lowering the calcination temperature and upon using higher template loads. Type IV(a) isotherms with a broad

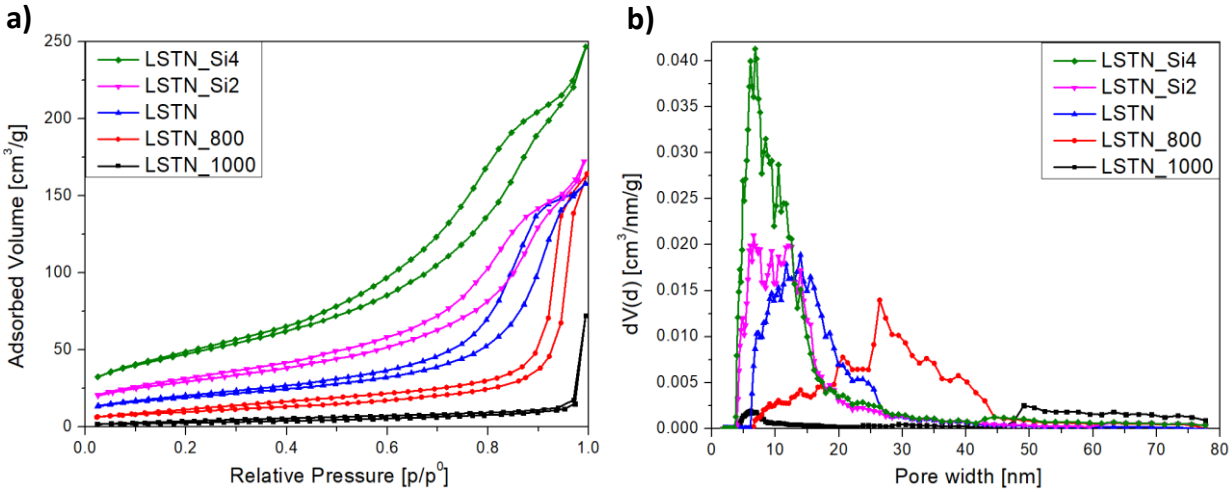

Figure 70 (a) Physisorption isotherms and (b) pore size distributions of the samples with $La_{0.2}Sr_{0.8}Ti_{0.94}Ni_{0.06}O_3$ nominal stoichiometry calcined at different temperatures and with increasing template loads.

hysteresis loop, typical of mesoporous materials, are obtained via N_2 physisorption in all of the aforementioned samples, except for the LSTN_1000 one, as shown in Figure 70. Regarding the LSTN_1000 sample calcined at 1000 ºC, the physisorption isotherm is Type III, typical of a macroporous or nonporous solid with a weak adsorbent-adsorbate interaction [22]. Its BET surface area has collapsed, being around 10 m^2/g, while it probably consists of macropores (> 50 mm) with a low amount of small mesopores. The LSTN_800 sample is more porous and consists mostly of mesopores, whereas the LSTN sample calcined at 600 ºC is significantly more porous, with a higher contribution of smaller mesopores and with a surface area of around 68 m^2/g, a very high one when compared with similar template-free perovskites in the literature obtained by using other preparation methods [28,29]. Afterwards, a great increase of the BET surface area and a sharpening of the pore size distribution with a simultaneous shift towards smaller pores can be achieved by increasing the template load. The BET surface area of the samples can jump up to 170 m^2/g when 40% molar ratio of TEOS precursor is added during the synthesis. The results obtained from the N_2 physisorption, as well as the mean crystallite sizes calculated from the X-ray diffractograms, are summarized in Table *24*.

Sample	Crystallite size [nm]	BET surface area [m^2/g]	Total pore volume [cm^3/g]	Average pore diameter [nm]
LSTN_1000 (_Red)	78 (80)	10 (10)	0.07 (0.06)	49 (63)
LSTN_800 (_Red)	30 (31)	38 (39)	0.23 (0.23)	26 (21)
LSTN (_Red)	28 (28)	68 (68)	0.24 (0.25)	14 (14)
LSTN_Si2 (_Red)	24 (23)	105 (91)	0.25 (0.25)	9 (10)
LSTN_Si4 (_Red)	18 (18)	170 (142)	0.34 (0.33)	8 (9)

Table 24 Results obtained from the N2 physisorption for the samples with $La_{0.2}Sr_{0.8}Ti_{0.94}Ni_{0.06}O_3$ nominal stoichiometry calcined at different temperatures and with increasing template loads before and after reduction, as well as their mean crystallite sizes calculated with the help of the Scherrer equation ((110) perovskite reflection from XRD). Values after the sample reduction are displayed in parentheses.

Employing transmission electron microscopy (TEM), we observe all the samples, except for the LSTN_1000, consist of aggregates of small crystallites and that they exhibit a significant porosity with a disordered distribution of interconnected pores. The example for the template-free LSTN sample is shown in

Figure *71* (a and b). Regarding the templated samples, no major differences can be spotted from TEM images apart from a slightly lower crystallite size. TEM images regarding the LSTN_800 and LSTN_1000 samples calcined at 800ºC and 1000ºC respectively can be found in

Figure *71* (c and d). LSTN_800 sample consists of aggregates of small crystallites similarly to LSTN calcined at 600ºC. The main difference between the two samples is that individual crystallites are of larger size in the sample calcined at 800ºC. However, when the calcination temperature is raised to 1000ºC, the size of the individual crystallites appears as high as 50-100 nm. Large voids between the crystallites up to 50 nm in diameter are also apparent in this case.

From the example of STEM-EDX mapping of the template-free LSTN sample calcined at 600ºC ( ) we can observe that there is a homogenous distribution for all the elements (O, La, Sr, Ti) except for

Ni. By taking into account EDX mapping for Ni from various areas, it appears that there is an inhomogeneous distribution of this element throughout the sample. There are some areas where Ni looks incorporated into the perovskite structure and some others where there is a clear Ni segregation in the form of small particles, probably in the form of NiO. NiO segregation is also apparent and slightly more pronounced in the EDX mapping of the templated LSTN_Si2 and LSTN_Si4 samples. This observation is also in line with the appearance of NiO reflections in the X-ray diffractograms of the LSTN_Si4 templated sample. The use of a higher calcination temperature at 800ºC (LSTN_800) could disperse the nickel into the perovskite structure by a greater extent, meaning that less areas of the sample exhibited this effect of NiO segregation. This can be attributed to the enhanced diffusion of Ni^{2+} cations throughout the support lattice at higher temperature.[15] However, the distribution of Ni for the sample calcined at 1000ºC was worse than the one calcined at 800ºC, probably as a result of NiO expulsion from the perovskite lattice. [30]

Regarding the templated samples, there is also a significant amount of residual silicon remaining even after the NaOH and HOAc etching steps, as similarly observed in the work of Kayaalp *et al.* [27] for templated $SrTiO_3$ by employing ^{29}Si NMR spectroscopy. The exact amount of residual silicon is however hard to be determined using EDX spectroscopy, since its characteristic X-ray emission peak overlaps with that for Sr (1.739 keV for Si and 1.806 keV for Sr).

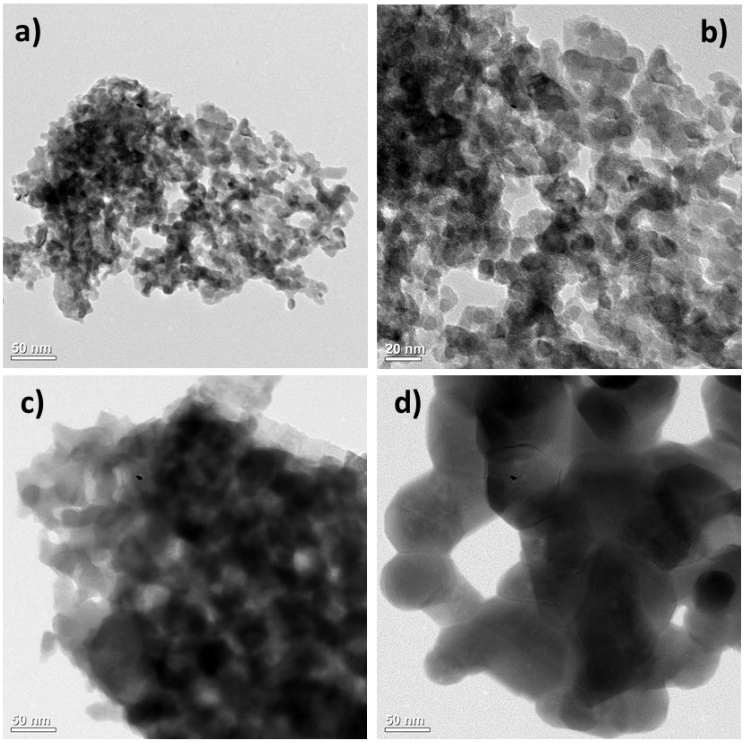

Figure 71 TEM micrographs of the template-free samples with nominal composition $La_{0.2}Sr_{0.8}Ti_{0.94}Ni_{0.06}O_3$ calcined at a), b) 600°C (LSTN) with different magnification, c) 800°C (LSTN_800), and d) 1000°C (LSTN_1000).

Employing EDX spectroscopy, the element composition of the samples can also be estimated (Table *23*). In order to compare the amounts of lattice cations, their values obtained from EDX were normalized with the total amount of titanium (taken as 94% of the B-site cations), since that element is in excess. We can observe a significant Sr-deficiency for all samples because Sr tends to form large amounts of $SrCO_3$ impurities at low calcination temperatures, which get removed afterwards by the etching treatments. The more pronounced Sr leaching in the LSTN_Si4 templated sample, where the largest template load was used, could be explained by the preferential binding of template siliceous species near lattice Sr-sites and their joint removal upon NaOH etching [20,31]. Increase of the template load leads to an increase of cation leaching and to an increased deviation from the nominal

$La_{0.2}Sr_{0.8}Ti_{0.94}Ni_{0.06}O_3$ stoichiometry. As a result of this extensive Sr leaching, all the prepared materials are *de facto* A-site deficient, at least close to their surface.

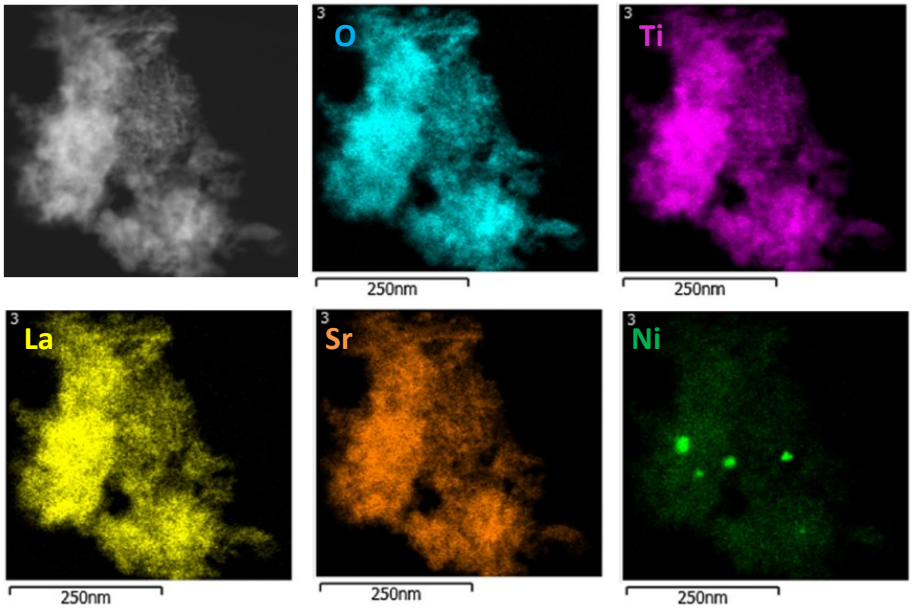

Figure 72 STEM micrograph of the template-free LSTN sample calcined at 600°C sample and STEM/EDX mapping for the elements in the sample.

The Mass Spectrometer signal evolution for H_2 and H_2O upon the LSTN sample reduction at up to 500°C using 5% H_2/N_2 and dwell time of one hour can be found in

Table 24 Results obtained from the N2 physisorption for the samples with La0.2Sr0.8Ti0.94Ni0.06O3 nominal stoichiometry calcined at different temperatures and with increasing template loads before and after reduction, as well as their mean crystallite sizes calculated with the help of the Scherrer equation ((110) perovskite reflection from XRD). Values after the sample reduction are displayed in parentheses.

There two main H_2 consumption peaks are visible during the reduction of the template-free LSTN sample calcined at 600°C (example presented in Figure 73), a smaller one at 330ºC followed by a larger one at 480ºC close to the final temperature. Regarding the water evolution, there is a peak after 100ºC due to the moisture desorbed from the sample, as well as two following peaks that correspond to H_2 consumption and are attributed to the reduction of oxygen species released from the sample. The first reduction peak at around 330ºC could be attributed to the reduction of nanosized segregated NiO supported on the perovskite, that interacts weakly with its support [32]. The temperature of the NiO to Ni reduction can generally vary, depending on the size of the NiO particles and their interaction with the support. [33,34] The second reduction peak at 480ºC, close to the point of reaching the 500°C final temperature, could be attributed to the exsolution of Ni that was previously incorporated into the perovskite lattice. [14]

Common diagrams of the hydrogen partial pressure with temperature are plotted for all samples, as shown in Figure 73, to compare the temperature where reduction occurs, as well as the amount of consumed hydrogen. As a rule, the final reduction temperature attained was 100ºC lower than the calcination temperature, *i.e.* 500ºC for LSTN, LSTN_Si2 and LSTN_Si4, 700ºC for LSTN_800 and

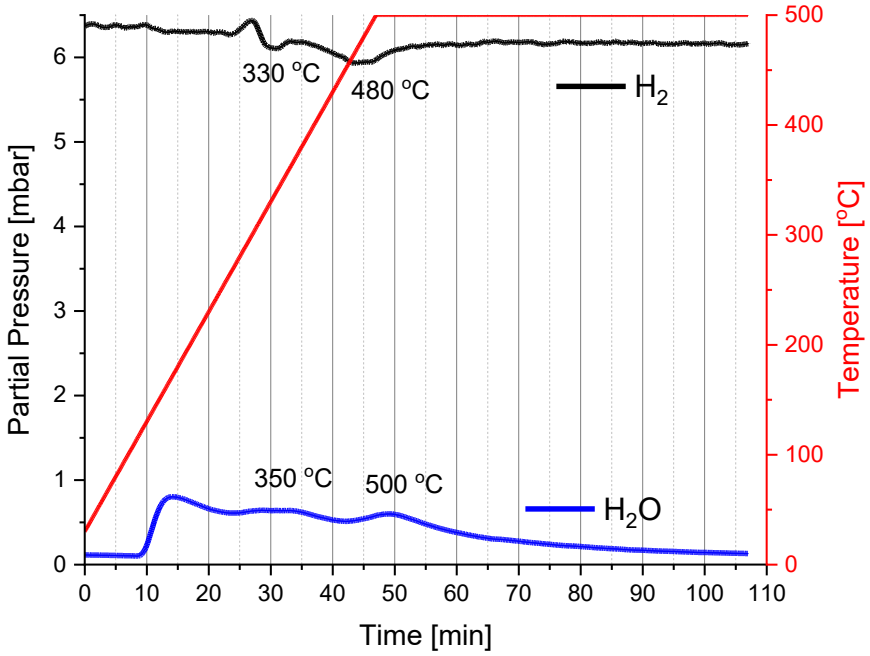

Figure 73 Mass spectrometric analysis of the outflowing gases during the reduction treatment for the LSTN sample. The partial pressure evolution for m/z = 2 (H_2) and m/z=18 (H_2O) is plotted together with the temperature ramp.

900°C for LSTN_1000. We always observe a larger hydrogen consumption peak close to the final attained temperature that could correspond to nickel exsolution from the perovskite lattice, as well as some amount of NiO reduction that interacts strongly with the support.[14,32] The lower temperature peak in the samples can be attributed to the reduction of NiO interacting weakly with the support. This peak appears around 330-350°C for the template-free samples and it shifts to lower temperatures for the templated samples, probably because the interaction of segregated NiO with the perovskite support gets weaker upon templating and/or extensive NaOH and HOAc etching treatments.[35] The amount of consumed hydrogen is higher with increasing loading, judged by the intensity of the H_2 consumption peaks (see Figure 74). This could be explained by the higher surface area and smaller crystallite sizes upon templating, leading to shorter diffusion pathways for nickel cations and to an increased reducibility of the perovskite oxide lattice.[14]

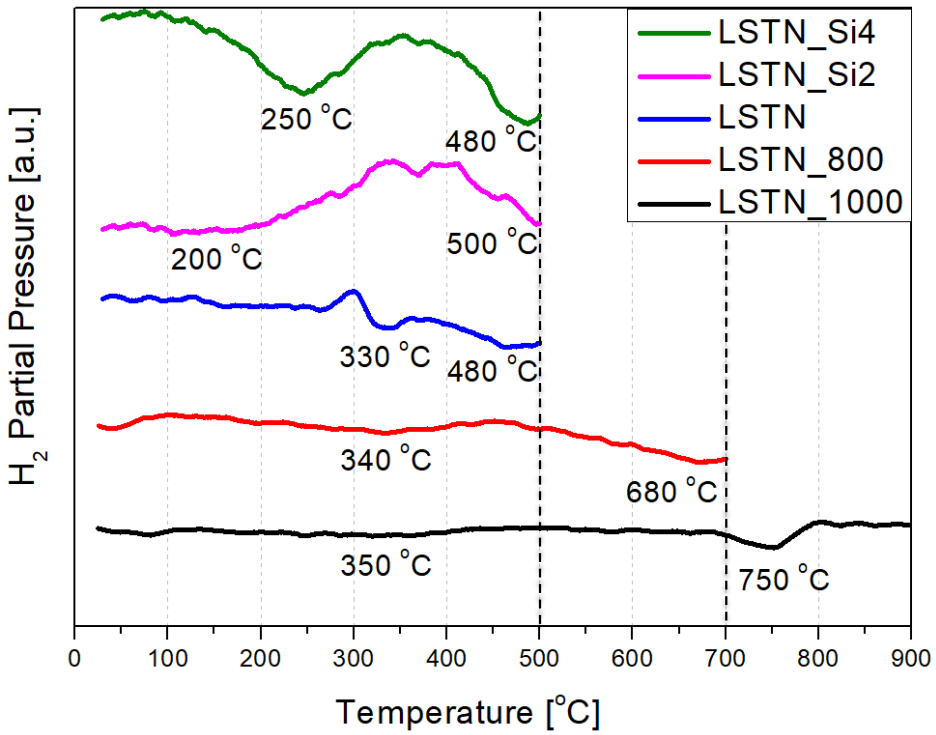

Figure 74 Partial pressures of the outflowing gas with m/z = 2 (H2) during the reduction treatment for the samples with $La_{0.2}Sr_{0.8}Ti_{0.94}Ni_{0.06}O_3$ nominal stoichiometry calcined at different temperatures and with increasing template loads. The lines for some samples are shifted upwards for comparison.

Regarding the samples calcined at temperature higher than 600ºC (LSTN_800 and LSTN_1000), their reduction profiles also present a low temperature peak assigned to the reduction of NiO interacting weakly with the support. However, this H_2 consumption peak is less intense, probably as a result of less NiO segregation. The high-temperature peak assigned to Ni exsolution shifts to higher temperature due to the stronger interaction of the Ni^{2+}/Ni^{3+} cations with the rest of the perovskite lattice, in which they are incorporated.[36] Thus, the H_2 consumption peak assigned to Ni exsolution shifts to 680ºC for the sample calcined at 800ºC (LSTN_800) and to 750ºC for the sample calcined at 1000ºC (LSTN_1000), since a higher reduction temperature is needed to exsolve the incorporated Ni species in these samples calcined at higher temperatures.

Characterizations after reduction

The reduced samples were then further characterized via XRD, N_2 physisorption and TEM, as well as STEM-EDX mapping. From the X-ray diffractograms (Figure 75) one cannot observe any difference between the oxidized and reduced forms for the template-free sample calcined at 600ºC (LSTN_Red for reduced sample), the 20% TEOS templated sample (LSTN_Si2_Red for reduced sample), and the sample calcined at 800°C (LSTN_800_Red for reduced sample). This could be due to the small size and high dispersion of the exsolved Ni nanoparticles, that could average a crystallite size lower than the XRD detection limit. However, for the templated sample with 40% TEOS (LSTN_Si4_Red for reduced sample), the initial NiO reflections that were visible in the oxidized form (LSTN_Si4 in Figure 69) disappear and a new metallic Ni reflection appears after the reduction treatment. This probably happens due to the reduction of previously segregated NiO to metallic Ni, as well as to further Ni exsolution from the perovskite lattice that increases the size of the original nanoparticles. Furthermore, a metallic Ni reflection also appears for the sample calcined at 1000ºC (LSTN_1000_Red), along with the rutile (TiO_2) reflections that were also apparent in its oxidized form (LSTN_1000 in Figure 69). The occurrence of the metallic Ni reflection for this sample could be attributed to the larger size of exsolved Ni nanoparticles, since the reduction temperature used in this case (900ºC), was higher than that of the other samples.

From N_2 physisorption, one can observe that the textural characteristics of the template-free samples (LSTN, LSTN_800 and LSTN_1000) remain practically unchanged after the reduction treatment, except for a slight shift towards smaller pore diameters, due to a pore rearrangement, in LSTN_800_Red. Regarding the templated samples (LSTN_Si2_Red and LSTN_Si4_Red), a small decrease in the BET surface area (around 15% loss) occurs. This effect is more pronounced when a higher template load is used (40% TEOS) since the initial porosity is also higher. Overall, the changes are rather small as a result of the reduction treatment at a much lower temperature (500ºC for the templated samples) when compared to the literature [14,29]. An example regarding the textural

characteristics for the non-templated LSTN sample, calcined at 600°C, before and after reduction is shown in Figure 76.

Table *24* provides a complete summary of the results obtained from the N_2 physisorption, as well as the mean crystallite sizes calculated from the X-ray diffractograms, before and after reduction treatments for all the aforementioned samples.

From STEM-EDX mapping after reduction of the samples, a homogenous distribution of the elements O, La, Sr and Ti and an almost complete Ni segregation is observed. *Figure 77* shows the EDX mapping for the Ni element in specific areas of all 5 samples. Since the samples were treated with a reducing atmosphere, we assume that segregated Ni is in the metallic Ni^0 state. All Ni nanoparticles have a spherical shape, while their size varies a lot. Some quite small nanoparticles around 5 nm in diameter are present, while some bigger ones can reach up to 30 nm in diameter.

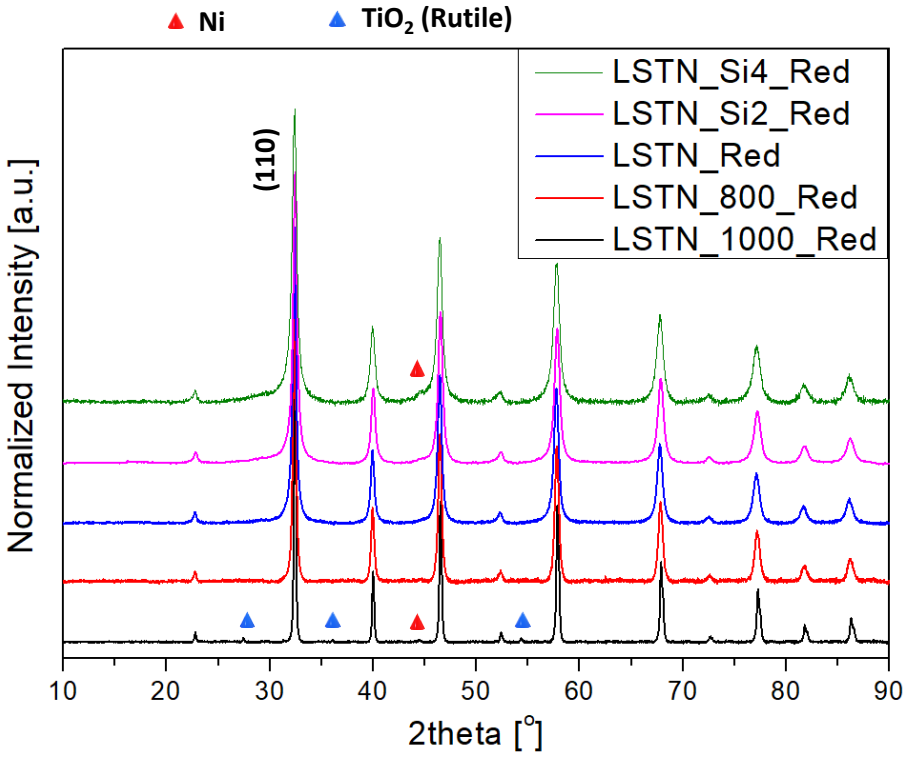

Figure 75 X-ray diffractograms of the samples with $La_{0.2}Sr_{0.8}Ti_{0.94}Ni_{0.06}O_3$ nominal stoichiometry calcined at different temperatures and with increasing template loads, after reduction treatment using 5% H_2/N_2 at a temperature that is 100°C lower than the calcination temperature.

The average size of the Ni nanoparticles is roughly similar in all samples, while the variation of the size of the nanoparticles within the samples themselves is quite large. The Ni nanoparticles in the template-free sample calcined at 600ºC (LSTN_Red) appear to have an average diameter of roughly 20 nm, whereas in the templated samples (LSTN_Si2_Red and LSTN_Si4_Red), the average nanoparticle diameter is roughly 15 nm. In the samples calcined at temperature higher than 600ºC and reduced at a temperature higher than 500ºC (LSTN_800_Red and LSTN_1000_Red), the average Ni nanoparticle size is also smaller than the LSTN_Red sample, being around 15 nm in both cases. The final composite materials after the reduction procedure exhibit a Ni/perovskite structure with Ni nanoparticles supported on a $La_xSr_{1-x}TiO_{3+\delta}$ perovskite oxide support (Ni/LST). TEM images with different magnification depicting an exsolved Ni nanoparticle along with the Ni/perovskite interface in the LSTN_1000_Red sample are presented in *Figure 78*.

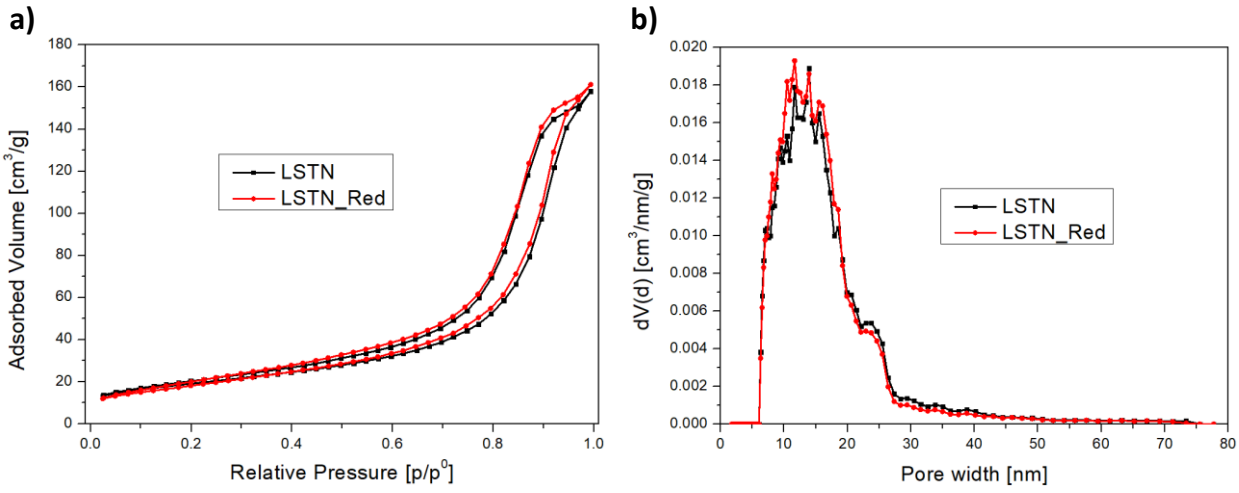

Figure 76 a) Physisorption isotherms and b) pore size distributions of the template-free LSTN sample before and after the reduction treatment (calcination at 600°C and reduction at 500°C)

A possible formation mechanism of the Ni nanoparticles supported on the reduced materials, is that part of them originate from the reduction of previously segregated NiO to Ni and part of them originate through exsolution from the parent perovskite. This different formation mechanism could explain the large nanoparticle size variation within the samples. An assumption would be that bigger nanoparticles originate from the reduction of previously segregated NiO particles into Ni metallic ones, whereas smaller nanoparticles originate purely by Ni exsolution from the perovskite lattice [14].

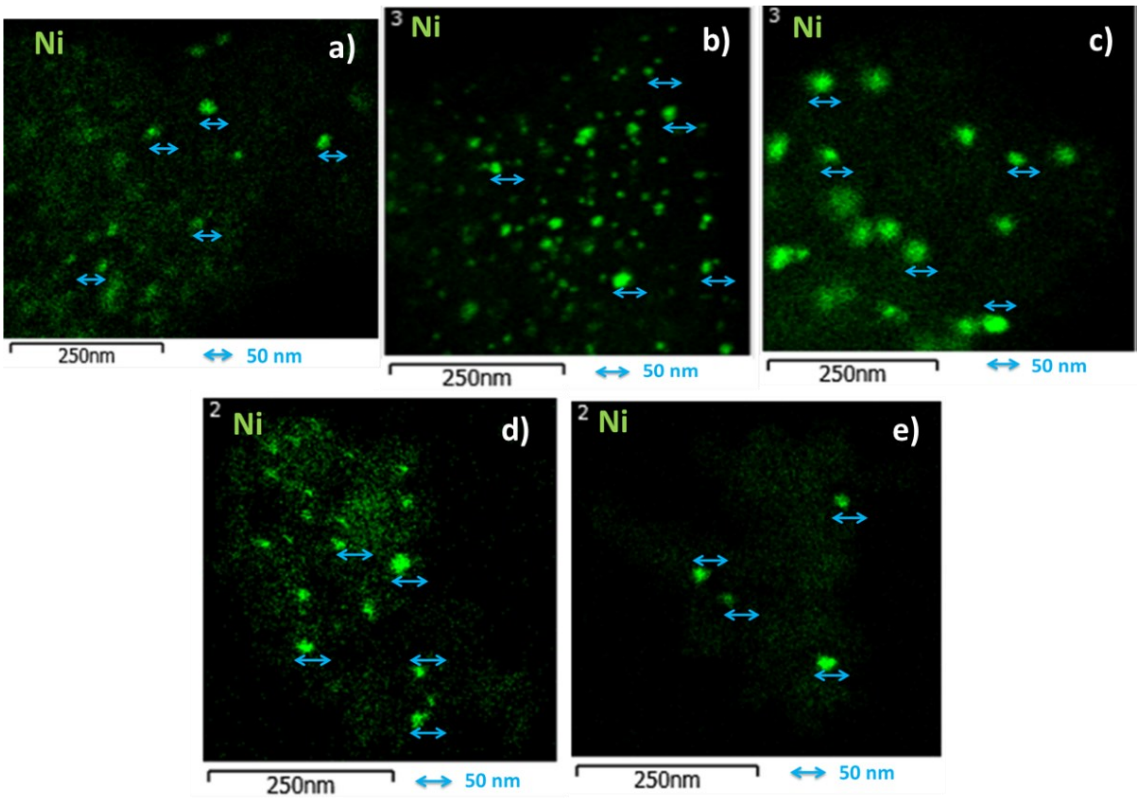

Figure 77 STEM/EDX mapping for the Ni element Ni of a) the reduced 40% TEOS templated sample (LSTN_Si4_Red), b) the reduced 20% TEOS templated sample (LSTN_Si2_Red), c) the reduced template-free sample calcined at 600°C (LSTN), d) the reduced sample calcined at 800°C (LSTN_800_Red), and e) the reduced sample calcined at 1000°C (LSTN_1000_Red).

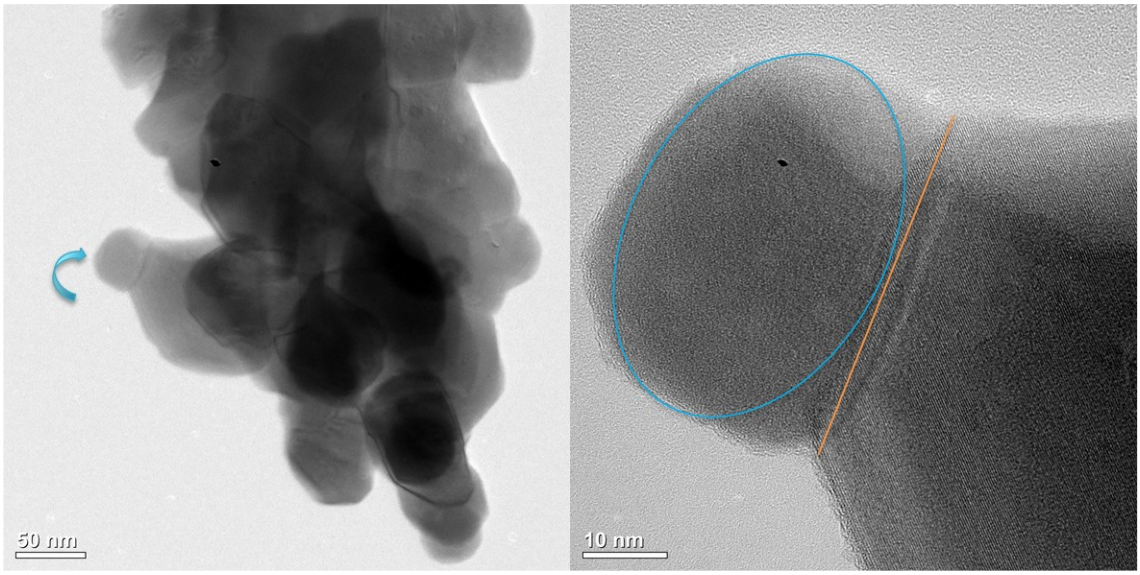

Figure 78 TEM micrographs with different magnification of the LSTN_1000_Red sample calcined at 1000°C and reduced at 900°C depicting an exsolved Ni nanoparticle and its interface with the perovskite support.

Nevertheless, the final composite materials consist of a large number of highly dispersed Ni nanoparticles, similar to other systems created by Ni exsolution from perovskite bulk materials [14,37,38]. A significant advantage of some of the prepared samples (the ones calcined at 600°C) is their very high BET surface area, which is desirable for applications in heterogeneous catalysis, such as the dry reforming of methane and CO_2 methanation [1,37,38].

XPS measurements were useful both to gain insights on the chemical environment of the species present in the samples and the global surface composition of the obtained perovskites.

Ni and La quantification via XPS analysis is quite challenging because the two most intense regions respectively overlap in a significant way: La3d is usually recorded between 820 and 880 eV, whereas Ni2p is studied between 840 and 880 eV. Since La is more abundant than Ni, Ni signal becomes negligible compared to La. Accordingly Ni2p signal is not reported due to the broad overlap with La3d signal, which does not allow to obtain significant spectra. Other signals, e.g. Ni3p, could be in

principle used as an alternative, however the signal drops due to the low sensitivity factor of such photoelectrons, and the low concentration at which Ni is present in the samples.

A preliminary evaluation of the effect of exsolution was performed on the sample LSTN_1000: high resolution XP spectra and quantitative analysis (to the extent allowed by the technical limitations explained above) were performed on the as-prepared sample and on the same sample after exsolution treatment. Due to the great overlapping between La3d and Ni2p regions, an attempt to use Ni3p region was made, with satisfactory results: a comparison with nominal composition and other evidences in literature confirm the reliability of the data.[39–42]

The compositional data are reported in , both for cation-only results (visible also in Figure 80) and including C1s and O1s regions. Titanium and nickel compositions are similar in the samples, the only difference concerns lanthanum and strontium surface segregation: La segregates distinctly in the surface after the exsolution, whereas before the reductive treatment Sr was more present on the outermost layers of the sample. Ni content increases after exsolution, in agreement with the expectations. Looking at the oxygen content, the unreduced sample shows a higher value, compatible with the reductive treatment.

In the following graphs (Figure 81), the XP regions are showed with an indication of the position of the main peak(s). La3d and Ti2p peak position is compatible with the perovskite analyzed. O1s shows the typical signal associated to perovskite lattice (529 eV), and the broadened bell shape is in agreement with the presence of active oxygen species on the surface. C1s signal shows little content of carbonates on the surface (broadening of the 284.8 eV centered signal). Sr3d signal is typical for $La_{1-x}Sr_xTi_{1-y}Ni_yO_3$, with a double-spiked peak with low resolution. The asymmetry at higher Binding Energies is typical for the presence of residues of oxides or hydroxides. Ni3p signal has been analyzed disregarding Ni2p region, more intense but highly overlapped with La3d region. Ni and NiO 3p signals are centered at 66.40 eV and 67.30 eV respectively. Here we see that the most intense peak is located at lower Binding Energy (approx. 62 eV), which is a signal attributed to Ti3s (Ti_2O_3 data are

only available, 61.0 eV, no reference for $SrTiO_3$). A fitting on the peak is performed on the samples to find the position of Ni3p contribution (Figure 82): metallic Ni position is reported in XPS databases at 66.40 eV, in the case of the sample after the exsolution the value obtained resembles more the one of metallic Ni (66.16 eV vs 65.64 eV of the sample prior to exsolution, more similar to NiO, from databases positioned at 67.30 eV, Ni^{2+}). All the considerations and interpretations given above are taken accordingly to ref. [43,44]. In conclusion, exsolution was successfully accomplished according to XP spectroscopic results.

Some further XPS analysis was performed: both fresh and spent samples were analyzed and the compositional results are reported in Table 26 and Figure 80, by reason of the different nominal compositions, the samples LSTN, LSTN_Si2 and LSTN_Si4 are reported (the composition was evaluated after reductive treatment in all cases). Although recorded, Si2p region will not be reported and discussed since the signal was too weak for as-prepared samples, and too contaminated by SiO_2 (quartz wool) used for catalytic testing for the spent samples.

In the case of Si-containing samples, we cannot see noticeable difference between as-prepared and spent catalysts. Moreover, the results confirm the expected composition (as well as oxidation numbers), the observations expressed for the previous set are still valid also for this second Si-containing set (peak position, peak shape and so on). The conclusion one can draw with this XPS data is that the samples are very stable in the conditions employed for catalytic testing (*i.e.* reducing environment and high temperatures, up to 500°C).

However, differently from the previous set of samples, Sr 3d signal is not as broad as non Si-containing samples after the testing, which might mean that Sr is more exclusively present as $SrTiO_3$-like phases (perovskite phases).[25,43,45] Moreover the amount of carbon detected on the outmost layer by XPS is diagnostic for carbon deposition that took place during the catalytic testing, most probably due to coking. Some evidence of this behavior is given also by the catalytic results, as shown below. Indeed as it can be seen in Figure 80 carbon elemental composition is much higher after the catalysis

in all samples.

	LSTN_1000R*	LSTN_1000*	NOMINAL*	LSTN_1000R	LSTN_1000
La3d	15.9	10.9	10.0	2.6	2.6
Sr3d	27.5	32.3	40.0	4.5	7.8
Ti2p	47.1	48.6	47.0	7.8	11.8
Ni3p	9.4	8.2	3.0	1.6	2.0
O1s				39.1	47.3
C1s				44.4	28.5

*Table 25 XPS obtained compositions for LSTN_1000 prior and after (denoted by R at the end) exsolution. Cation-only composition is denoted by *.*

Element-XPS region	**LSTN (fresh)**	**LSTN (spent)**	**LSTN_Si2 (fresh)**	**LSTN_Si2 (spent)**	**LSTN_Si4 (fresh)**	**LSTN_Si4 (spent)**
La3d	4.1	3.0	5.0	2.2	2.0	2.3
Sr3d	9.4	7.4	6.0	5.4	3.7	5.2
Ti2p	16.6	12.0	17.8	9.6	15.6	14.1
Ni2p	0.6	10.4	0	8.3	0	8.3
C1s	12.8	20.0	11.2	46.5	22.9	52.0
O1s	56.5	47.2	60.0	28.1	55.7	18.0

Table 26 XPS compositional analysis (atomic percentage) of selected samples, before and after catalytic testing.

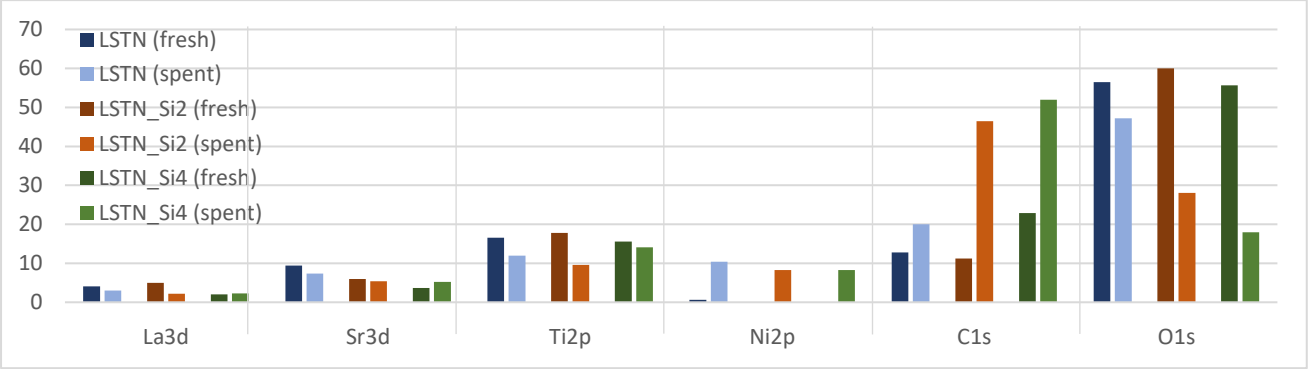

Figure 80 XPS compositional analysis (atomic percentage) of selected samples, before and after catalytic testing.

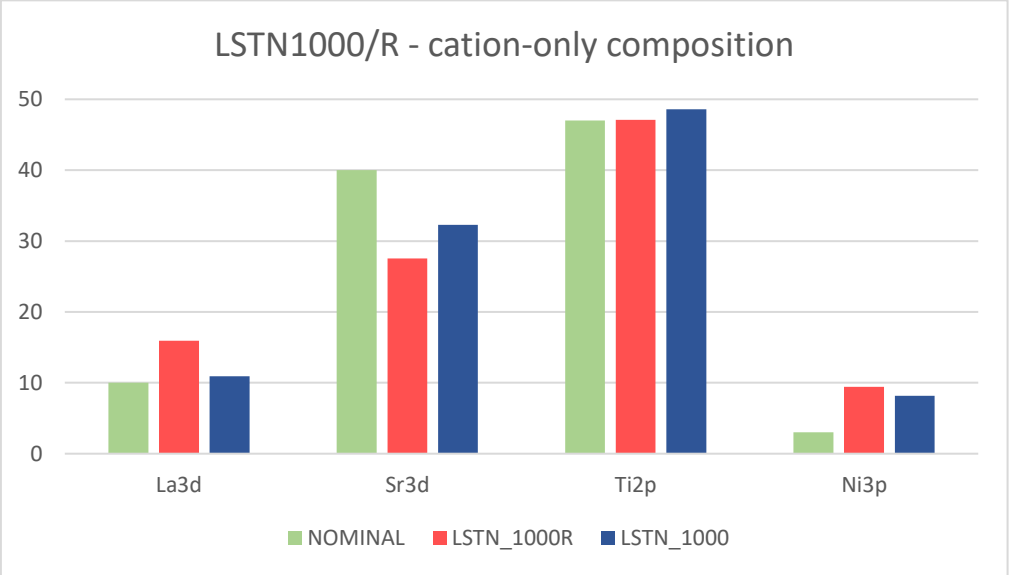

Figure 80 Histograms representing cation-only compositions for LSTN1000R and LSTN1000.

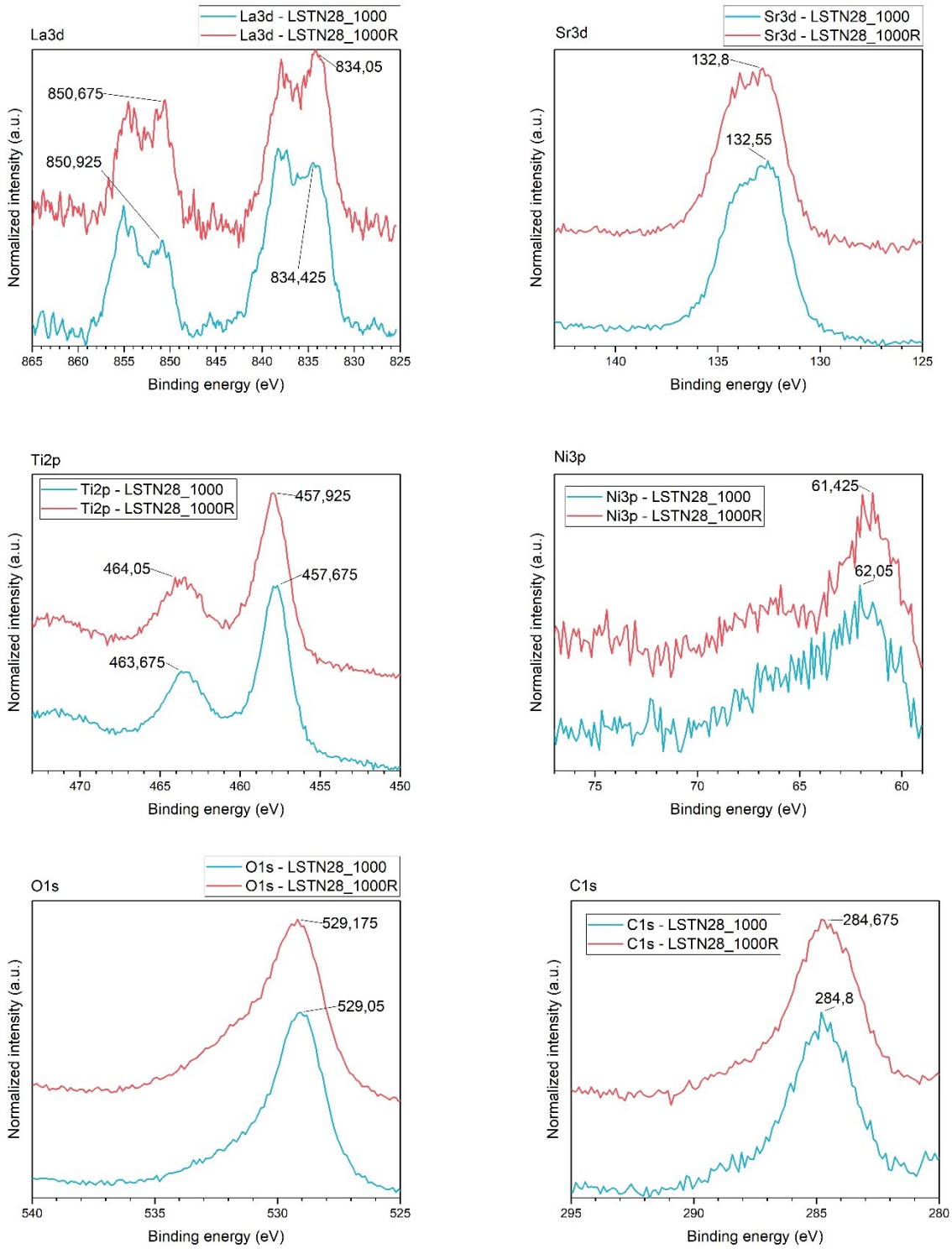

Figure 81 XP high resolution spectra for the sample LSTN1000 before and after the exsolution process.

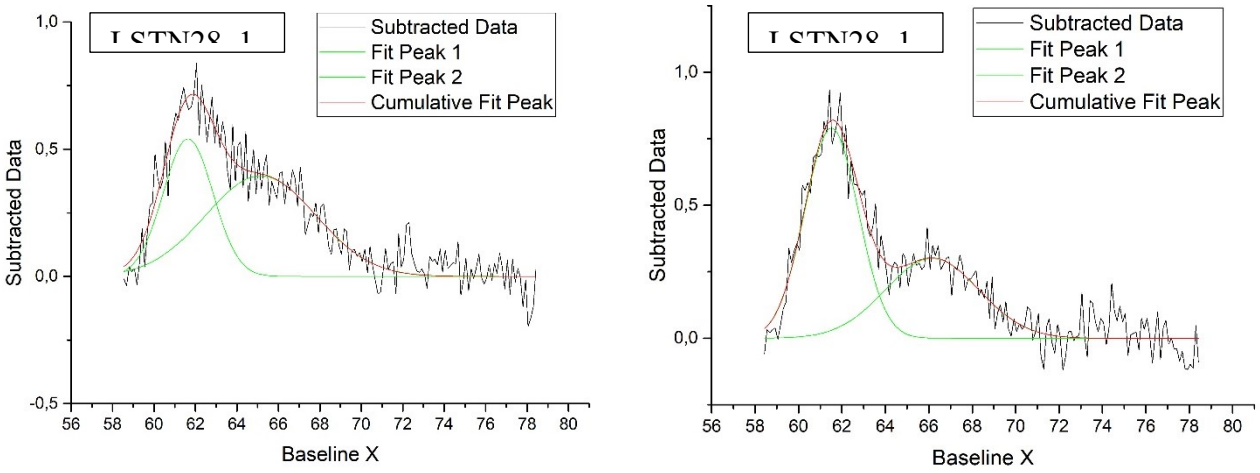

Figure 82 Deconvolutive fitting results for Ni3p region, sample LSTN1000.

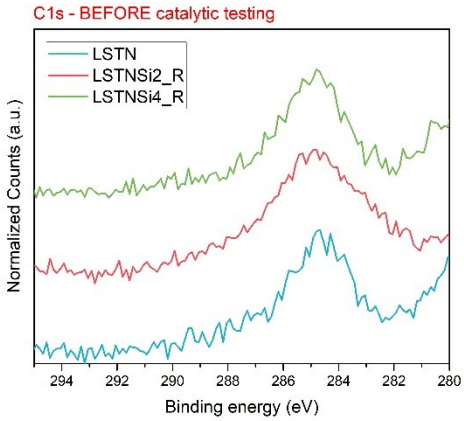

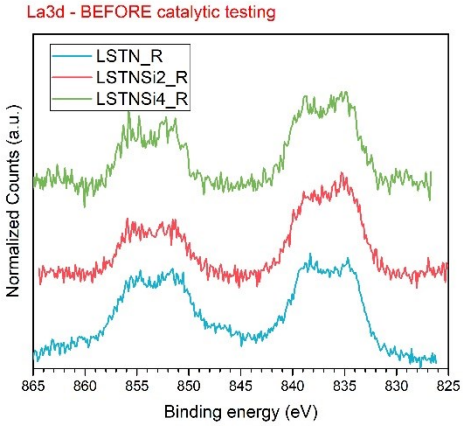

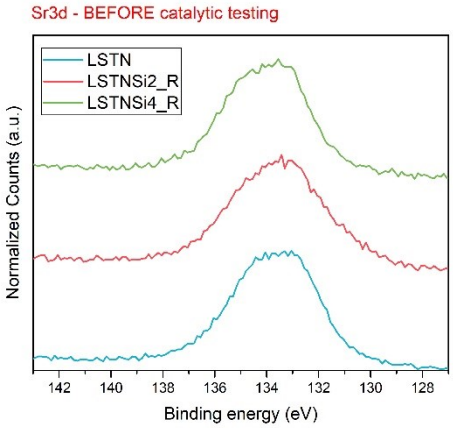

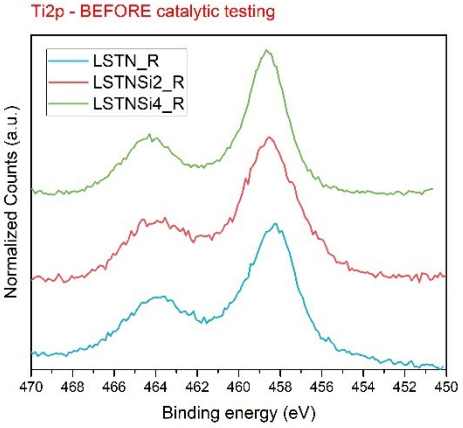

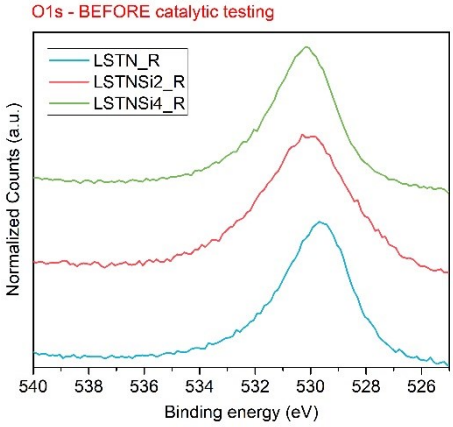

Figure 83 XP high resolution spectra of selected compositions, recorded with the as-prepared samples.

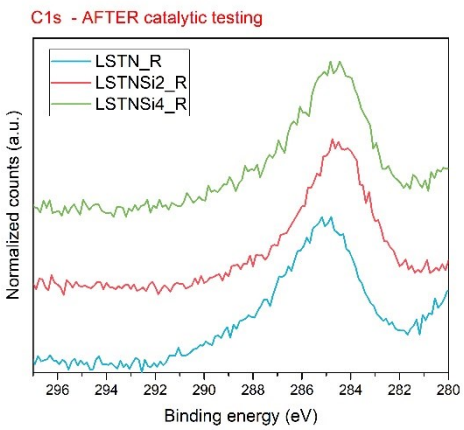

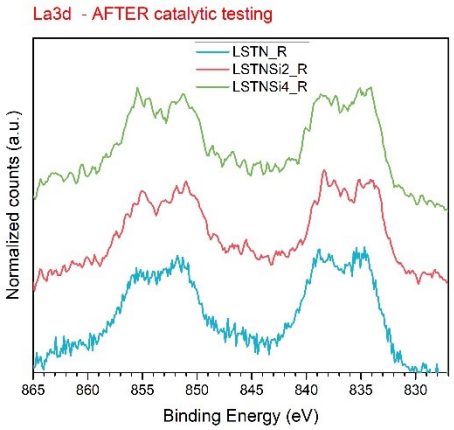

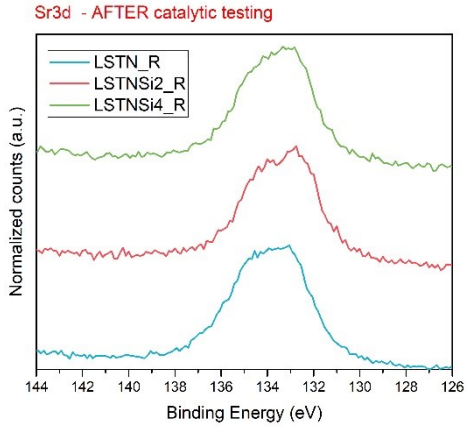

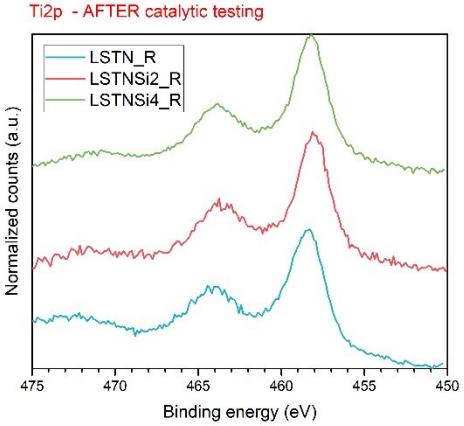

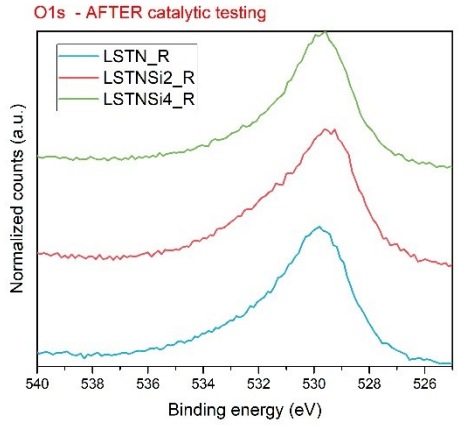

Figure 84 XP high resolution spectra of selected compositions, recorded with the as-prepared samples.

Catalytic assessment

Theoretically CO_2 conversion should be accompanied by a four-fold decrease in H_2 concentration, as requested by the stoichiometry of the reaction. However, this was not observed. This discrepancy in the conversions is determined by the difficult evaluation of H_2 concentration using Quadrupole MS, due to the low molecular mass of the analyte (typically analytes with m/z<10 do not give reliable signals). Another explanation could be due to partially non-selective reaction paths, that made possible also the formation of other unwanted by-products: mainly CO, CH_3OCH_3 and CH_3OH.[2] However these products were observed in negligible amounts, as it can be seen from the following graphs.

In the graphs reported below, the conversions of carbon dioxide for each sample are shown. Methane and other byproduct signals are reported on a separated graph. Due to CH_4 fragmentation, the most diagnostic signal is the one at m/z=15, which is attributed to CH_3^+.

The samples treated at 800°C and 1000°C were tested before and after reductive exsolution, in order to confirm the convenience of the method to produce active metallic Ni nanoparticles on the surface, as Ni(II) species are not active in carbon dioxide methanation catalysis.[46]

In this particular case hydrogen is also displayed, in order to highlight the low reliability of its quantification through Quadrupole Mass Spectrometry. In the following cases this will not be pursued anymore. The results, before and after exsolution, show that the reductive treatment affects the results. Looking at sample LSTN_800, before the exsolution no change in carbon dioxide concentration is detected in the temperature range between 100 and 500°C. Byproducts are not detected as well, so we can conclude that the sample is inert in this atmosphere. Comparing its performances with the same composition, but reductively treated (LSTN_800R), hydrogen consumption is observed, but CO_2 concentration does not change throughout the test. We did not detect byproducts, thus hydrogen did not react with carbon dioxide, but instead it reduced the sample, probably activated towards reducing atmosphere thanks to the previous exsolution. We argue that the already-formed Ni

nanoparticles on the surface could lower the activation energy of further Ni reduction, even with a lower hydrogen concentration with respect to the one employed for exsolution treatments.

For the sample treated at 1000°C, the same considerations apply: no carbon dioxide conversion is detected (nor as reagent decrease or product formation) and hydrogen is being consumed only in the case of the exsoluted sample, again we argue this might be an exsolution-activated surface reduction.[14,15,47]

Similar testing has been performed on the sample LSTN and the Si-template ones, LSTN_Si2 and LSTN_4. The results (CO_2 conversion and methane formation mass spectrometer signal, i.e. ion current) are shown in Figure 85. Carbon dioxide is effectively consumed in any case but LSTN_Si4, is able to convert only a small percentage of inlet carbon dioxide (around 10%). However, we did not achieve satisfactory performances for what concerns methane production. Please refer to the right-hand side of Figure 85. Methane ion current (and precisely the ion current of fragment CH_3^+) is displayed instead of the methane concentration, due to the extremely low signal detected, much below a reliable quantification range obtained by calibration. A rough estimate of its maximum concentration for sample LSTN (achieved at approximately 400°C) gives a yield that is less than 3%. Although the values obtained are extremely low, we can still draw some interesting conclusions from this data: firstly, the trend for methane production is in agreement with thermodynamical data (refer to Chapter 4 for further information). Moreover, methane production onset temperature corresponds to the temperature at which carbon dioxide is being converted, showing a clear trend of carbon dioxide activation on the surface of the material starting from 300°C. Of course, though, carbon dioxide conversion is not matching the methane conversion obtained. To this purpose the concentrations of carbon monoxide, methanol and dimethyl ether (common byproducts for this reaction mixture) have been monitored and unfortunately they were not detected. This means that coking is a serious issue for this kind of materials, accounting for a non-negligible percentage of the total carbon balance. Even with some limitations due to the impossibility to gain an accurate quantification of the produced

methane, it is still possible to conclude that Si-etched samples show a higher degree of surface coking. As this is typical of non-homogenously dispersed catalyst (Ni in this case) nanoparticles, we can argue that this might be a result of imperfect etching, that poisoned the surface favoring metal clustering or sintering on top of it as a result. Some examples in literature may confirm this hypothesis, as it took places also in similar systems. [48–51]

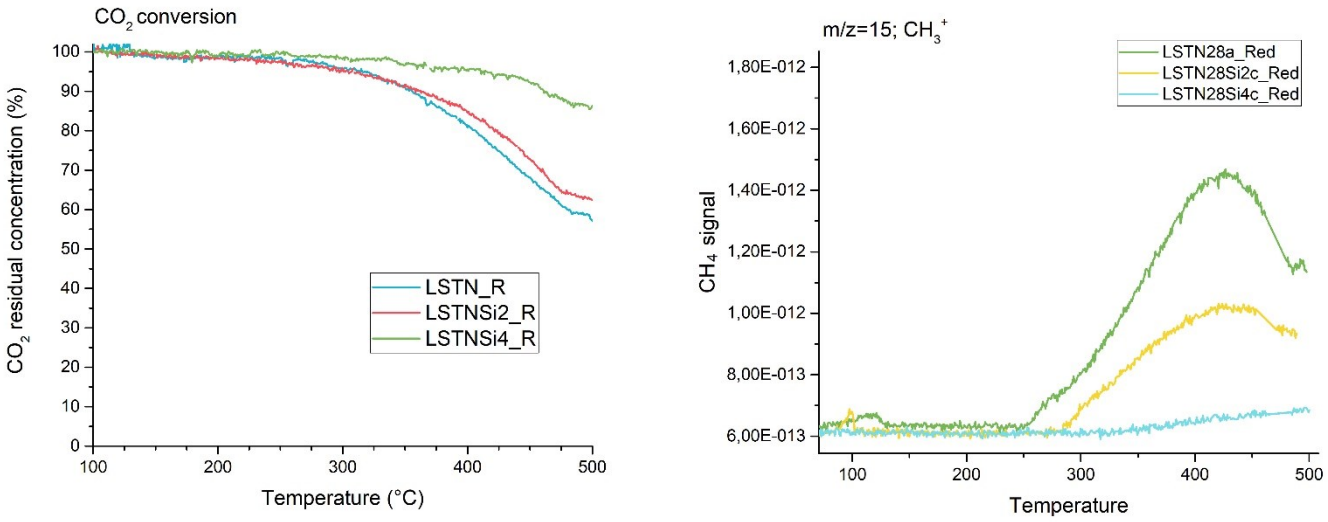

Figure 85 Catalytic activities towards carbon dioxide methanation of LSTN sample and Si-etched ones.

5.4 Conclusions

Mesoporosity and composition design were exploited in this project to obtain catalytically active mixed oxides (with a perovskite structure), making use also of the exsolution technique to generate active metal nanoparticles serving as active sites for carbon dioxide methanation. The synthesis in this case is the conventional Pechini route, optimized to achieve higher surface areas on the final material. TEOS (a Si-derivative) was also used to template the material to a higher porosity and was etched out with a base medium. An extensive characterization was performed as well, to gather information about structure, composition, vibrational spectroscopy behavior, physisorption features (and therefore porosity), micromorphology through TEM measurements and reductive functionality.

Catalytic tests complete the picture that we can get from these sets of samples towards carbon dioxide methanation.

First of all, the synthetic procedures here employed have proved to be effective, with satisfactory crystalline patterns obtained by X-Ray Diffraction. Mesoporosity is a key feature of the samples, especially when TEOS precursor (*i.e.* a powerful templating agent) is added, as it can be retrieved from the nitrogen physisorption isotherms. SEM-EDX pictures show homogenous samples but with some notable NiO segregation outside the particles in Si-templated samples and also in samples that were calcined at lower temperatures. Hydrogen Temperature Programmed Reduction was employed to determine the reductive functionality of the samples, with a particular focus on NiO reduction peaks, that are known to be sensitive to particle size and interaction with the support. From this investigation, it was demonstrated that at 500°C with 5% hydrogen concentration (the same used in TPR) Ni is completely reduced to its metallic oxidation state. For this reason, these will be the chosen conditions for nickel particle exsolution from the perovskite structures.

After reduction XRD, nitrogen physisorption, TEM and SEM-EDX are repeated: the observed alterations are in agreement with segregated NiO reduction, especially because morphology techniques show metallic Ni clusters on the surface, with a diameter from 5 to 30 nm.

X-Ray Photoelectron Spectroscopy assessment was not straightforward: La3d and Ni2p signals, respectively the most intense signal for each element, are overlapping and therefore they do not allow a proper elemental analysis. To this purpose Ni3p was chosen instead, despite its photoelectronic cross section is much lower. In the samples tested before and after exsolution La and Sr showed surface segregation to different extents. Agreeing with expectations, Ni segregates more after exsolution, confirming an ion migration taking place in sufficiently reductive atmospheres. XPS elemental analysis performed on the samples recovered from the testing setup clearly show coking as excess of deposited carbon on the surface; indeed, catalytic testing demonstrated that these sets of samples greatly suffer from surface poisoning that is caused by coking. This was particularly clear

since carbon dioxide concentration does decrease along the temperature ramp, but methane formation does not occur quantitively, nor are the other possible byproducts (*i.e.* lesser degree of carbon dioxide reduction: carbon monoxide, methanol, dimethlyether) detected.

In conclusion, we can consider this project as a proof-of-concept of exsoluted mesoporous perovskites for catalytic applications, even if the yields obtained were not particularly high: exsolution was successfully achieved and the so-obtained metal nanoparticles were particularly stable. Indeed, the samples were exsoluted many days prior characterization and catalytic testing, showing great stability over time. This is an encouraging result, since in Chapter 4 we performed *in situ* exsolution to avoid re-oxidation of Ni nanoparticles, which in this case did not occur. At the same time, we have to take into account that the employed active species concentration was particularly low and alkaline etching might have altered the surface in an irreversible way, leading thus to more compact Ni clusters on the surface, less active towards heterogeneous catalysis in general.

To sum up, this project opened the way to further studies on exsoluted mesoporous perovskites, that might be designed more efficiently, for example in composition and porosity, to obtain finer dispersion of metallic Ni, the real catalytic actor performing on the stage of Sabatier's reaction.

References

(1) Tsiotsias, A. I.; Charisiou, N. D.; Yentekakis, I. V. Bimetallic Ni-Based Catalysts for CO 2 Methanation : A Review To. **2021**.

(2) Frontera, P.; Macario, A.; Ferraro, M.; Antonucci, P. L. Supported Catalysts for CO2 Methanation: A Review. *Catalysts*. MDPI AG February 13, 2017. https://doi.org/10.3390/catal7020059.

(3) Lv, C.; Xu, L.; Chen, M.; Cui, Y.; Wen, X.; Li, Y.; Wu, C. E.; Yang, B.; Miao, Z.; Hu, X.; Shou, Q. Recent Progresses in Constructing the Highly Efficient Ni Based Catalysts With Advanced Low-Temperature Activity Toward CO2 Methanation. *Front. Chem.* **2020**, *8*, 269. https://doi.org/10.3389/fchem.2020.00269.

(4) Gac, W.; Zawadzki, W.; Słowik, G.; Sienkiewicz, A.; Kierys, A. Nickel Catalysts Supported on Silica Microspheres for CO2 Methanation. *Microporous Mesoporous Mater.* **2018**, *272*, 79–91. https://doi.org/10.1016/j.micromeso.2018.06.022.

(5) Ye, R.-P.; Gong, W.; Sun, Z.; Sheng, Q.; Shi, X.; Wang, T.; Yao, Y.; Razink, J. J.; Lin, L.; Zhou, Z.; Adidharma, H.; Tang, J.; Fan, M.; Yao, Y.-G. Enhanced Stability of Ni/SiO2 Catalyst for CO2 Methanation: Derived from Nickel Phyllosilicate with Strong Metal-Support Interactions. *Energy* **2019**, *188*, 116059. https://doi.org/10.1016/j.energy.2019.116059.

(6) Bacariza, M. C.; Graça, I.; Bebiano, S. S.; Lopes, J. M.; Henriques, C. Micro- and Mesoporous Supports for CO2 Methanation Catalysts: A Comparison between SBA-15, MCM-41 and USY Zeolite. *Chem. Eng. Sci.* **2018**, *175*, 72–83. https://doi.org/10.1016/j.ces.2017.09.027.

(7) Liu, H.; Xu, S.; Zhou, G.; Xiong, K.; Jiao, Z.; Wang, S. CO2 Hydrogenation to Methane over Co/KIT-6 Catalysts: Effect of Co Content. *Fuel* **2018**, *217*, 570–576. https://doi.org/10.1016/j.fuel.2017.12.112.

(8) Pizzolitto, C.; Pupulin, E.; Menegazzo, F.; Ghedini, E.; Di Michele, A.; Mattarelli, M.; Cruciani, G.; Signoretto, M. Nickel Based Catalysts for Methane Dry Reforming: Effect of Supports

on Catalytic Activity and Stability. *Int. J. Hydrogen Energy* **2019**, *44* (52), 28065–28076. https://doi.org/10.1016/j.ijhydene.2019.09.050.

(9) Bian, Z.; Kawi, S. Highly Carbon-Resistant Ni–Co/SiO 2 Catalysts Derived from Phyllosilicates for Dry Reforming of Methane. *J. CO2 Util.* **2017**, *18*, 345–352. https://doi.org/10.1016/j.jcou.2016.12.014.

(10) Rönsch, S.; Schneider, J.; Matthischke, S.; Schlüter, M.; Götz, M.; Lefebvre, J.; Prabhakaran, P.; Bajohr, S. Review on Methanation – From Fundamentals to Current Projects. *Fuel* **2016**, *166*, 276–296. https://doi.org/10.1016/j.fuel.2015.10.111.

(11) Lee, J. J.; Kim, K.; Kim, K. J.; Kim, H. J.; Lee, Y. M.; Shin, T. H.; Han, J. W.; Lee, K. T. In-Situ Exsolution of Ni Nanoparticles to Achieve an Active and Stable Solid Oxide Fuel Cell Anode Catalyst on A-Site Deficient La0.4Sr0.4Ti0.94Ni0.06O3-δ. *J. Ind. Eng. Chem.* **2021**, *103*, 264–274. https://doi.org/10.1016/j.jiec.2021.07.037.

(12) Aldana, P. A. U.; Ocampo, F.; Kobl, K.; Louis, B.; Thibault-Starzyk, F.; Daturi, M.; Bazin, P.; Thomas, S.; Roger, A. C. Catalytic CO2 Valorization into CH4 on Ni-Based Ceria-Zirconia. Reaction Mechanism by Operando IR Spectroscopy. *Catal. Today* **2013**, *215*, 201–207. https://doi.org/10.1016/j.cattod.2013.02.019.

(13) Centi, G.; Perathoner, S. Opportunities and Prospects in the Chemical Recycling of Carbon Dioxide to Fuels. *Catal. Today* **2009**, *148* (3–4), 191–205. https://doi.org/10.1016/j.cattod.2009.07.075.

(14) Neagu, D.; Tsekouras, G.; Miller, D. N.; Ménard, H.; Irvine, J. T. S. S. In Situ Growth of Nanoparticles through Control of Non-Stoichiometry. *Nat. Chem.* **2013**, *5* (11), 916–923. https://doi.org/10.1038/nchem.1773.

(15) Neagu, D.; Oh, T.-S. S.; Miller, D. N.; Ménard, H.; Bukhari, S. M.; Gamble, S. R.; Gorte, R. J.; Vohs, J. M.; Irvine, J. T. S. Nano-Socketed Nickel Particles with Enhanced Coking Resistance

Grown in Situ by Redox Exsolution. *Nat. Commun.* **2015**, *6* (1), 8120. https://doi.org/10.1038/ncomms9120.

(16) Cho, E.; Lee, Y.-H.; Kim, H.; Jang, E. J.; Kwak, J. H.; Lee, K.; Ko, C. H.; Yoon, W. L. Ni Catalysts for Dry Methane Reforming Prepared by A-Site Exsolution on Mesoporous Defect Spinel Magnesium Aluminate. *Appl. Catal. A Gen.* **2020**, *602*, 117694. https://doi.org/10.1016/j.apcata.2020.117694.

(17) Xu, L.; Miao, Z.; Song, H.; Chen, W.; Chou, L. Significant Roles of Mesostructure and Basic Modifier for Ordered Mesoporous Ni/CaO–Al 2 O 3 Catalyst towards CO 2 Reforming of CH 4. *Catal. Sci. Technol.* **2014**, *4* (6), 1759–1770. https://doi.org/10.1039/C3CY01037F.

(18) Li, S.; Gong, J. Strategies for Improving the Performance and Stability of Ni-Based Catalysts for Reforming Reactions. *Chem. Soc. Rev.* **2014**, *43* (21), 7245–7256. https://doi.org/10.1039/C4CS00223G.

(19) Kayaalp, B.; Lee, S.; Klauke, K.; Seo, J.; Nodari, L.; Kornowski, A.; Jung, W. C.; Mascotto, S. Template-Free Mesoporous La0.3Sr0.7FexTi1-XO3±Δ with Superior Oxidation Catalysis Performance. *Appl. Catal. B Environ.* **2019**, *245*, 536–545. https://doi.org/10.1016/j.apcatb.2018.12.077.

(20) Kayaalp, B.; Lee, S.; Nodari, L.; Seo, J.; Kim, S.; Jung, W. C.; Mascotto, S. Pt Nanoparticles Supported on a Mesoporous (La,Sr)(Ti,Fe)O3-ΔSolid Solution for the Catalytic Oxidation of CO and CH4. *ACS Appl. Nano Mater.* **2020**, *3* (11), 11352–11362. https://doi.org/10.1021/acsanm.0c02456.

(21) Monshi, A.; Foroughi, M. R.; Monshi, M. R. Modified Scherrer Equation to Estimate More Accurately Nano-Crystallite Size Using XRD. *World J. Nano Sci. Eng.* **2012**, *2* (3), 154–160.

(22) Thommes, M.; Kaneko, K.; Neimark, A. V.; Olivier, J. P.; Rodriguez-Reinoso, F.; Rouquerol, J.; Sing, K. S. W. Physisorption of Gases, with Special Reference to the Evaluation of Surface Area and Pore Size Distribution (IUPAC Technical Report). *Pure Appl. Chem.* **2015**, *87* (9–10), 1051–1069. https://doi.org/10.1515/pac-2014-1117.

(23) Shirley, D. A. High-Resolution x-Ray Photoemission Spectrum of the Valence Bands of Gold. *Phys. Rev. B* **1972**, *5* (12), 4709–4714. https://doi.org/10.1103/PhysRevB.5.4709.

(24) Briggs, D. Handbook of X-Ray Photoelectron Spectroscopy C. D. Wanger, W. M. Riggs, L. E. Davis, J. F. Moulder and G. E.Muilenberg Perkin-Elmer Corp., Physical Electronics Division, Eden Prairie, Minnesota, USA, 1979. 190 Pp. $195; Chastain, J., Ed.; Eden Prairie, 1981; Vol. 3. https://doi.org/10.1002/sia.740030412.

(25) Umbach, E. *Practical Surface Analysis*; Wiley: New York, 1992; Vol. 11. https://doi.org/10.1016/0165-9936(92)87016-d.

(26) Zhang, T.; Liu, Q. Perovskite LaNiO3 Nanocrystals inside Mesostructured Cellular Foam Silica: High Catalytic Activity and Stability for CO2 Methanation. *Energy Technol.* **2020**, *8* (3), 1–12. https://doi.org/10.1002/ente.201901164.

(27) Kayaalp, B. E.; Lee, Y. J.; Kornowski, A.; Gross, S.; D'Arienzo, M.; Mascotto, S. Cooperative Assembly Synthesis of Mesoporous SrTiO3with Enhanced Photocatalytic Properties. *RSC Adv.* **2016**, *6* (93), 90401–90409. https://doi.org/10.1039/c6ra13800d.

(28) Huang, X.; Zhao, G.; Wang, G.; Irvine, J. T. S. Synthesis and Applications of Nanoporous Perovskite Metal Oxides. *Chem. Sci.* **2018**, *9* (15), 3623–3637. https://doi.org/10.1039/c7sc03920d.

(29) Nair, M. M.; Kaliaguine, S.; Kleitz, F. Nanocast LaNiO3 Perovskites as Precursors for the Preparation of Coke-Resistant Dry Reforming Catalysts. *ACS Catal.* **2014**, *4* (11), 3837–3846. https://doi.org/10.1021/cs500918c.

(30) Beale, A. M.; Paul, M.; Sankar, G.; Oldman, R. J.; Catlow, C. R. A.; French, S.; Fowles, M. Combined Experimental and Computational Modelling Studies of the Solubility of Nickel in Strontium Titanate. *J. Mater. Chem.* **2009**, *19* (25), 4391–4400. https://doi.org/10.1039/b902591j.

(31) Kayaalp, B. Design Strategies towards SrTiO 3 Based Perovskite Nanostructures for Environmental Catalysis, 2019.

(32) Charisiou, N. D.; Siakavelas, G.; Papageridis, K. N.; Baklavaridis, A.; Tzounis, L.; Polychronopoulou, K.; Goula, M. A. Hydrogen Production via the Glycerol Steam Reforming Reaction over Nickel Supported on Alumina and Lanthana-Alumina Catalysts. *Int. J. Hydrogen Energy* **2017**, *42* (18), 13039–13060. https://doi.org/10.1016/j.ijhydene.2017.04.048.

(33) Li, J.; Li, P.; Li, J.; Tian, Z.; Yu, F. Highly-Dispersed Ni-Nio Nanoparticles Anchored on an Sio2 Support for an Enhanced Co Methanation Performance. *Catalysts* **2019**, *9* (6). https://doi.org/10.3390/catal9060506.

(34) Azancot, L.; Bobadilla, L. F.; Santos, J. L.; Córdoba, J. M.; Centeno, M. A.; Odriozola, J. A. Influence of the Preparation Method in the Metal-Support Interaction and Reducibility of Ni-Mg-Al Based Catalysts for Methane Steam Reforming. *Int. J. Hydrogen Energy* **2019**, *44* (36), 19827–19840. https://doi.org/10.1016/j.ijhydene.2019.05.167.

(35) Charisiou, N. D.; Papageridis, K. N.; Tzounis, L.; Sebastian, V.; Hinder, S. J.; Baker, M. A.; AlKetbi, M.; Polychronopoulou, K.; Goula, M. A. Ni Supported on CaO-MgO-Al2O3 as a Highly Selective and Stable Catalyst for H2 Production via the Glycerol Steam Reforming Reaction. *Int. J. Hydrogen Energy* **2019**, *44* (1), 256–273. https://doi.org/10.1016/j.ijhydene.2018.02.165.

(36) Neagu, D.; Kyriakou, V.; Roiban, I. L.; Aouine, M.; Tang, C.; Caravaca, A.; Kousi, K.; Schreur-Piet, I.; Metcalfe, I. S.; Vernoux, P.; Van De Sanden, M. C. M.; Tsampas, M. N. In Situ Observation of Nanoparticle Exsolution from Perovskite Oxides: From Atomic Scale Mechanistic Insight to Nanostructure Tailoring. *ACS Nano* **2019**. https://doi.org/10.1021/acsnano.9b05652.

(37) Steiger, P.; Kröcher, O.; Ferri, D. Increased Nickel Exsolution from LaFe0.8Ni0.2O3 Perovskite-Derived CO2 Methanation Catalysts through Strontium Doping. *Appl. Catal. A Gen.* **2020**, *590*. https://doi.org/10.1016/j.apcata.2019.117328.

(38) Wei, T.; Jia, L.; Zheng, H.; Chi, B.; Pu, J.; Li, J. LaMnO3-Based Perovskite with in-Situ Exsolved Ni Nanoparticles: A Highly Active, Performance Stable and Coking Resistant Catalyst for

CO2 Dry Reforming of CH4. *Appl. Catal. A Gen.* **2018**, *564*, 199–207. https://doi.org/10.1016/j.apcata.2018.07.031.

(39) Gao, Y.; Lu, Z.; You, T. L.; Wang, J.; Xie, L.; He, J.; Ciucci, F. Energetics of Nanoparticle Exsolution from Perovskite Oxides. *J. Phys. Chem. Lett.* **2018**, *9* (13), 3772–3778. https://doi.org/10.1021/acs.jpclett.8b01380.

(40) Gao, Y.; Chen, D.; Saccoccio, M.; Lu, Z.; Ciucci, F. From Material Design to Mechanism Study: Nanoscale Ni Exsolution on a Highly Active A-Site Deficient Anode Material for Solid Oxide Fuel Cells. *Nano Energy* **2016**, *27*, 499–508. https://doi.org/10.1016/J.NANOEN.2016.07.013.

(41) Kwon, O.; Sengodan, S.; Kim, K.; Kim, G.; Jeong, H. Y.; Shin, J.; Ju, Y. W.; Han, J. W.; Kim, G. Exsolution Trends and Co-Segregation Aspects of Self-Grown Catalyst Nanoparticles in Perovskites. *Nat. Commun. 2017 81* **2017**, *8* (1), 1–7. https://doi.org/10.1038/ncomms15967.

(42) Nenning, A.; Fleig, J. Electrochemical XPS Investigation of Metal Exsolution on SOFC Electrodes: Controlling the Electrode Oxygen Partial Pressure in Ultra-High-Vacuum. *Surf. Sci.* **2019**, *680*, 43–51. https://doi.org/10.1016/J.SUSC.2018.10.006.

(43) Naumkin, V. A.; Kraut-Vass, A.; Gaarenstroom, S. W.; J., P. C. NIST X-Ray Photoelectron Spectroscopy Database. *Meas. Serv. Div. Natl. Inst. Stand. Technol.* **2012**, *20899* (20), 20899. https://doi.org/10.18434/T4T88K.

(44) J., C. Handbook of X-Ray Photoelectron Spectroscopy; Eden Prairie, 1992.

(45) Vasquez, R. P. SrTiO3 by XPS. *Surf. Sci. Spectra* **1992**, *1* (1), 129–135. https://doi.org/10.1116/1.1247683.

(46) Wang, W.; Gong, J. Methanation of Carbon Dioxide: An Overview. *Front. Chem. Eng. China* **2011**, *5* (1), 2–10. https://doi.org/10.1007/s11705-010-0528-3.

(47) Tsekouras, G.; Neagu, D.; Irvine, J. T. S. Step-Change in High Temperature Steam Electrolysis Performance of Perovskite Oxide Cathodes with Exsolution of B-Site Dopants. *Energy Environ. Sci.* **2013**, *6* (1), 256–266. https://doi.org/10.1039/C2EE22547F.

(48) Tsai, L.; Fang, H.; Lin, J.; Chen, C.; Tsai, F. Recovery and Stabilization of Heavy Metal Sludge (Cu and Ni) from Etching and Electroplating Plants by Electrolysis and Sintering. *Sci. China Ser. B Chem.* **2009**, *52* (5), 644–651. https://doi.org/10.1007/s11426-009-0047-6.

(49) Anklekar, R. M.; Bauer, K.; Agrawal, D. K.; Roy, R. Improved Mechanical Properties and Microstructural Development of Microwave Sintered Copper and Nickel Steel PM Parts. *Powder Metall.* **2005**, *48* (1), 39–46. https://doi.org/10.1179/003258905X37657.

(50) Owate, I. O.; Freer, R. Thermochemical Etching Method for Ceramics. *J. Am. Ceram. Soc.* **1992**, *75* (5), 1266–1268. https://doi.org/10.1111/j.1151-2916.1992.tb05567.x.

(51) Kafkaslıoğlu, B.; Tür, Y. K. Pressureless Sintering of Al 2 O 3 /Ni Nanocomposites Produced by Heterogeneous Precipitation Method with Varying Nickel Contents. *Int. J. Refract. Met. Hard Mater.* **2016**, *57*, 139–144. https://doi.org/10.1016/j.ijrmhm.2016.03.009.

6. Carbon membranes for carbon dioxide methanation

6.1 Introduction

As an integration to my project, seen as an implementation in the investigation of Ni deposition on different supports, the fabrication of a Ni-deposited carbon membrane reactor was pursued to perform carbon dioxide methanation, to enrich our knowledge besides testing catalytically active powders. Membranes have many advantages as compared to a conventional powder-based lab-scale testing, enabling convenient separation of gases and being more suitable for industrial up-scaling. Indeed, it is possible to tailor membrane properties according to, among others, their chemical composition, surface properties, pore size, hydrophilicity/hydrophobicity and shape.

To the best of our knowledge, no prior encapsulation of the catalyst in the carbon matrix of a pyrolytic carbon membranes was pursued, since no documentation is available in literature about this asset.

This part of the PhD project was carried out at the Eindhoven University of Technology, in the Netherlands, under the supervision of Prof. Fausto Gallucci. His research at the Inorganic Membranes and Membrane Reactors (SIR) research group is related to the development of membranes and novel multiphase reactors, in particular membrane reactors and dynamically operated reactors. The main focus is on the interaction of heterogeneous catalysis, transport phenomena, and fluid mechanics in these novel multifunctional reactors. The membrane reactor research is carried out through integration of (in house developed) advanced experimental techniques and experimental Proof of Concept of novel reactor concepts. The project has been conducted with the consultation of Tecnalia, a Spanish research center that deals with carbon membrane production. The novelty provided by our intuition was to add catalytically active species directly into the carbon matrix in the fabrication step, in order to obtain a complete device able to combine both separation and catalytic boost to the reaction. For this reason, we chose carbon membranes that are commonly employed in processes such as water separation in dehydrogenation reactions; the advantages of this choice are several: they are well-

established as concerns preparation and modification, they are not expensively produced and, above all, separating water they represent a convenient way to shift the equilibrium of Sabatier's reaction to the side of the products.

Membrane processes for gas separation applications have seen a remarkable development and increase in their properties and are now commercially used for hydrogen recovery, carbon dioxide removal from natural gas and on-site nitrogen production from air.[1–3] Two fundamental parameters that evaluate the performances of a membrane are permeability and selectivity: most of the times a trade-off between the two shall be reached, usually through the optimization of the material, keeping into consideration also other important features such as thermal and chemical stability in the working conditions, sometimes quite challenging. Traditionally polymeric membranes were employed, but the use of innovative materials such as silica, zeolites and carbon push the upper bound limits of the permeability vs selectivity trade-off, reported in 1991 and 2008 by Robeson.[4–6] In his famous articles Robeson initially draws a correlation between separation factors and permeability for polymeric membranes, and then expands his considerations to a more general point of view, including several gas pairs separation processes for which the so-called "upper bound" relationship was shown to be valid. He considered the following gas pairs: O_2/N_2, CO_2/CH_4, H_2/N_2, He/N_2, H_2/CH_4, He/CH_4, He/H_2, H_2/CO_2 and He/CO_2. The upper bound relationship proposed by Robeson is $P_i = k\alpha_{ij}^n$, where P_i is the permeability of the more permeable gas, α is the separation factor (ratio of P_i/P_j) and n is the slope of the log-log limit. The so-called log-log plot is the logarithmic plot of α_{ij} vs P_i. The slope n can be related to the difference between the gas molecular diameter, where the gas molecular diameter chosen is the Lennard-Jones kinetic diameter.[5] Another parameter that is often found in literature about membrane reactor is the so-called *permselectivity*, a concept that is valid only for dense membrane. Its IUPAC definition is "preferential permeation of certain ionic species through ion-exchange membranes".[7] Considering a two-component mixture (comprising A and B as components),

the permselectivity is given by the ration of the respective selectivity coefficient, that are in turn provided by the product of the diffusivity coefficient of a certain component, and the solubility coefficient. In porous membrane a new physical quantity is introduced to express the same concept, or, in other words, a measure of the flow resistance; it is obtained as the permeate volume divided by the measuring time, the effective membrane area and the difference of pressure across the two sides of the membrane.

Carbon Molecular Sieve Membrane (CMSMs) have emerged as promising candidates for gas separation both in terms of separation properties and selectivity.[8]

Carbon membranes are typically polymer hollow fibers permeable to different gases, such as CO_2, H_2O and NH_3, and to a minor extent to CH_4 and H_2. [9] Polymeric-only membranes (*i.e.* non carbonized) though suffer from plasticization and swelling, reducing their lifetime, moreover they reach an upper bound limit, with a compromise between CO_2 flux and CO_2/CH_4 separation (perm-selectivity). [2,6] For these reasons composite carbon molecular sieves (CMSMs) have been developed, surpassing the upper bound of polymeric membranes and not being affected by plasticization. Molecular sieve carbon can easily be obtained by pyrolysis of many thermosetting polymers such as, among others, polyacrylonitrile (PAN), poly(vinylidenecloride) (PVDC), perfluoroalkoxy alkane (PFA), cellulose, cellulose triacetate, saran copolymer, phenol formaldehyde resins and various coals such as coconut shell. [10] Pyrolysis of thermosetting polymers have been found to yield an exact mimic of the morphology of the parent material. [11] Such pyrolysis, also referred to as carbonization, is conventionally performed under an inert atmosphere or vacuum. Not only carbon membranes outdo polymeric only membranes for better selectivity, but also they can function at high temperatures and in harsh environments.[12] As described in the following section, CMSMs are endowed with a peculiar and unique microporous structure, that consequently allows them to discriminate gas molecules by size and shape.[1] The pore size distribution greatly affects the gas separation performances, and therefore an optimized method to obtained controlled pore size is needed. Not only the pore size, but

also carbonization temperature history, gas atmosphere and pre- or post-treatments can alter the microporous structure of the final membrane. Finally, great care must be put in the choice of the precursors, on which adsorption and mechanical properties of the membrane will depend. Phenolic resins are suitable and convenient precursor since they are inexpensive and possess high carbon yield, being able to resist high temperatures without losing their shape. [13–15] Among their properties we can find a high glass transition temperature, decomposing before achieving their melting point and therefore assuring a resultant defect-free carbon structure.

6.2 Transport of gas through carbon membranes

Depending on the pore structure many different mass transfer processes of gases are possible through a membrane. The main mechanisms are four: Poiseuille flow, Knudsen diffusion, partial condensation/capillary diffusion/selective absorption and molecular sieving. [11] We will deal with the latter since most carbon membranes show the molecular sieving mechanism as shown in Figure 86:[16] the carbon membrane contains constrictions in the carbon matrix, which approach the molecular dimensions of the absorbing species. This system exhibits high selectivity and permeability for the smaller component of the gas mixture. Carbon matrix itself does not allow any other form of permeation unless through the pore system, constituted of (relatively) wide openings with narrow constrictions. The openings contribute to the major part of the pore volume and they are thus responsible for the adsorption capacity, while the constrictions are responsible for the stereoselectivity of pore penetration by host molecules and for the kinetics of penetration.[17] Hence,

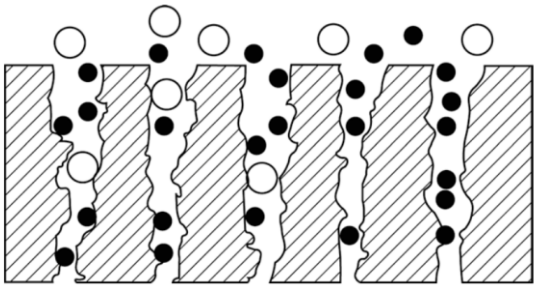

Figure 86 Typical molecular sieving mechanism

controlling the pore size is of paramount importance to modify the diffusivity of gases in a carbon molecular sieve. When the gas molecules approach the constrictions of the carbon matrix, the interaction energy between the molecule and the carbon is comprised of both dispersive and repulsive interactions. When the opening becomes sufficiently small relative to the size of the diffusing molecule, the repulsive forces dominate and the molecule requires activation energy to pass through the constrictions. [11] In this region of activated diffusion, molecules with only slight differences in size can be effectively separated through molecular sieving. [18] For these reasons the permeation and uptake through porous solids (such as carbon membranes) are closely related to the internal surface area, to the dimensions of the pores and to the surface properties of the solid, rather than its bulk properties of the solid as in the case of polymers.[19]

Molecular sieving process is favored when the membrane pores have roughly the same size as the molecules separated themselves, with a typical size that can be below 2 nm. An empirical relationship that is usually observed is that the pore diameter should be less than three times the molecular diameter of the gas molecules to be separated, with preferentially strong interactions between the diffusing molecule and pore wall. In this case, and unlikely selective adsorption, the transport rate in micropores increases with temperature. The most typical examples of this behavior are zeolite and carbon membranes.

Another transport mechanism of carbon membranes is selective adsorption-surface diffusion mechanism, although this is more common with polymeric carbon membranes. In this case adsorption-selective carbon membranes (from now on ASCMs) are able to separate non-adsorbable or weakly adsorbable gases (typically O_2, N_2, CH_4) from adsorbable gases, such as NH_3, SO_2, H_2S and chlorofluorocarbons (CFCs). Differently from molecular sieving carbon membranes, ASCMs present a carbon film with micropores slightly larger than CMSMs, probably in the range of 5-7 Å, whereas CMSMs have a typical pore diameter of 3-5 Å.[20] Therefore, we may consider carbon membranes as a refractory porous solid where the permeants are non-soluble and merely penetrate

through the pore system.[21] The natural consequence of this behavior is that pore size must be controlled finely, since it is the only factor that regulates the efficient passage of permeants through the carbon membranes.

The other mass transport mechanisms are typical of other systems, because they rely on different pore size, larger than those usually retrieved in carbon membranes. In Figure 88 (taken from ref.[22]) a pictorial representation of the others mechanisms is shown: the pore size effect is evident and so is also the effect of adsorption phenomena on the surface of the membrane material. Viscous flow, also known as the Poiseuille flow (or Hagen-Pouisselle flow), occurs when the pores are wide compared to the mean free path and transport is made possible by bulk fluid through the large pores. The gas permeability is in this case $P = \frac{\varepsilon \eta r^2}{8 \mu R T} p$, where ε is the porosity, μ viscosity (Pa s), η shape factor (reciprocal tortuosity of the medium), r pore radius, p average pressure. The porosity is the ratio of the membrane volume occupied by pored and the total membrane volume.

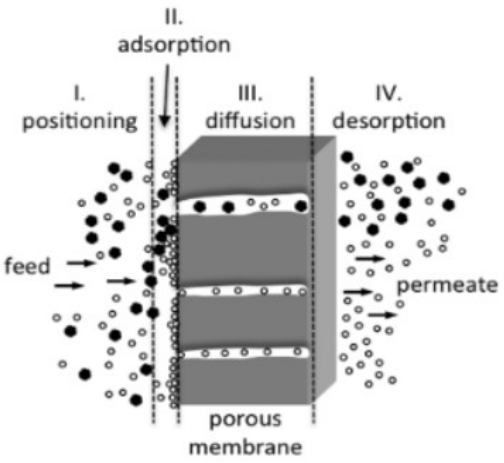

Figure 87 A sketch of molecular transport through membrane by surface diffusion. (I) Positioning of adsorbing molecule against membrane surface; (II) adsorption of the molecule on the membrane surface; (III) diffusion of the adsorbed molecule through membrane pores; (IV) desorption of the molecule on the permeate side of the membrane. The picture is taken from Gitis et al. (2016).

Knudsen diffusion takes place when the pore size is larger than the molecule size but smaller than the mean free path of the gas molecules in the system. Collisions between gas molecules and pore wall (rather than between gas molecules themselves) occur and the collisions are elastic with negligible interaction between molecules and pore wall, therefore substantially no diffusion takes place. In this particular case the permeability P is defined as $P = \frac{2\varepsilon\eta r v}{3RT}$, where ε is the porosity, μ viscosity (Pa s), η shape factor (defined as reciprocal tortuosity of the medium), *r* pore radius. Since *v*, the molecular velocity, is $\sqrt{\frac{8RT}{\pi M}}$, where M is the molecular weight of the gas molecule, the selectivity factor α, defined as the ratio of the permeability of the two components of the mixture, will be the square root of the ratio of molecular weight ($\sqrt{\frac{M_B}{M_A}}$). This allows a simple verification of the Knudsen selectivity, as by comparing the ratio of permeability of two different gases and the square root of the ratio of their molecular weight, an indirect evaluation of the pore size is made possible. Surface diffusion is the preferential mechanism whenever one component is preferentially adsorbed, in particular when, at low temperature, gas molecules cannot escape from the surface potential field due to the strong interaction between inner surface and gas molecules. A pictorial reference is reported in ref.[22]. Four main phases are evidenced in the picture: first the molecules are positioned against the pore wall by the feed stream, then the preferential adsorption occurs and diffusion along the porous membrane can start. Finally, desorption completes the process. In this case the permeability for surface diffusion phenomena (P_{SD}) is defined as follows $P_{SD} = P_0 exp\left(\frac{-\Delta H_a - \Delta E_{SD}}{RT}\right)$, that including enthalphy and activation energy for the process, defines the energy barrier for diffusing molecules to permeate through the membrane. Capillary condensation is another possibility in the range of likely events for membrane gas separation: the multilayer adsorption from the vapour into a porous medium proceeds to the point at which pore spaces become filled with condensed liquid from the vapour. Liquid may block the pores and different scenarios are possible: the first path is that the pressure in the

condensating pore is higher than that in other pores. It occurs selectively in some pores due to the pore size distribution. The pore is not clogged, and it might selectively increase the transport of large vapour molecules. The second alternative is that a continuous increase in the applied pressure results in the formation of a liquid drop. The drop clogs the pore and occurs in smaller pores at lower pressure than in larger ones. The condensate phase travels from the feed to the permeate by hydrostatic pressure difference or by capillary suction pressure in unfilled pores.

6.3 Preparation

The membrane is prepared starting from a novolac phenolic resin precursor material. The preparation method consists of three consecutive steps: 1) dip coating of the porous support, 2) drying and 3) carbonization in inert atmosphere. It is very important that the carbonization does not take place in oxygen (or air) because otherwise the carbon constituting the membrane would be oxidized to CO_2. As said, the novelty of this approach is the idea of incorporating a nickel precursor in the membrane dip coating solution to get a membrane endowed with a better dispersion, as compared to conventional techniques, such as impregnation, which is currently the most used in industry, due to its simplicity

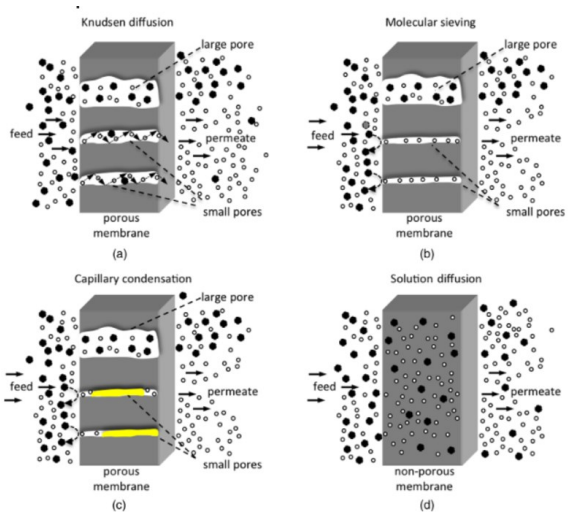

Figure 88 Transport mechanisms in gas separation through ceramic membrane: Knudsen diffusion (a), molecular sieving (b), capillary condensation (c) and solution diffusion (d). The picture is taken from Gitis et al. (2016).

and minimal generation of waste streams. Moreover, carbonization is a process that limits aggregation and coalescence, which is a major issue to be tackled when dealing with non-noble transition metal catalysts (like Ni, Cu, Fe etc), especially at high metal loading.

In this case the metal precursor chosen is Ni (II) acetylacetonate (acac), in which the organic moiety will be converted to carbonaceous deposits on the metal particles and this can control Ni particle size by reducing the metal mobility during the membrane preparation (in particular during the carbonization step). The reason behind this precursor choice lies in high solubility of the nickel complex in the chosen solvent (NMP). Furthermore, when preparing molecular sieves carbon membranes, this addictive can act as a way to introduce a metal center to the structure increasing at the same time the polarity of the overall membrane. This is explained by the charge unbalance provided by the Ni center onto the surface, controlling therefore the selectivity towards gases with different polarities. Moreover some evidences of the use of $Ni(acac)_2$ as a precursor on carbonaceous supports (other than carbon membranes) were found in literature.[23] Das et al. reported in 2019 a successful impregnation of SiO_2 with the employ of this precursor. In our case the support is not Si-based, but instead it is an amorphous carbon support obtained by pyrolysis of a polymer solution.

The conventional technique to prepare a carbon molecular sieve membrane usually requires the carbonization of some polymeric material. Such material presents an amorphous structure and disordered blocks formed by graphite-like layers constitute it. Void spaces between blocks are very narrow (less than 10 Å) and they provide the micro-porosity of CMS.[15] In our case we employed phenolic resin as polymeric precursor. Such resins are very popular and inexpensive polymers. The phenolic resin is obtained by the polycondensation reaction of phenol and formaldehyde, initially to form oligomers. The molar ratio between the two species is carefully controlled and set to a value of 0.8. Therefore, polycondensation reaction is limited by formaldehyde. The reaction is carried out in acidic conditions. There are two forms of phenolic resins: resol and novolac. Resol resins are the product of basic catalysis in excess of formaldehyde (formaldehyde/phenol ratio, F/P>1). Such resins

are not stable because the polymerization reaction continues with the time due to the presence of reactive methylol groups in the resin and their properties will depend on the basic catalysts used during their preparation. It results in a low-molecular-weight prepolymer with CH_2OH groups attached to the phenol rings. On heating, resol condenses further, with loss of water and formaldehyde, to yield thermosetting polymers. However resol polymer, being more prone to propagation polymerization (and not step-wise polymerization, unlike Novalac process) gives a structurally different material, with less surface hydroxylic groups, and therefore less hydrophilicity.[24]

Being the pH acidic and the molar ratio between phenol and formaldehyde less than 1 (between 0.75 and 0.85), we obtain Novolac resin. Curing to network polymer is accomplished by the addition of more formaldehyde or, in some cases, of compounds that decompose to formaldehyde on heating. Novolac resins are not endowed with reactive methylol groups and therefore, without hardening groups, cannot condense further on heating; to complete the condensation reaction, it is necessary to add formaldehyde and/or amine to achieve the cross-linking.[25]

The solvent used to obtain the dip-coating solution is NMP (N-Methyl-2-Pyrrolidone), which guarantees high boiling point (202°C) and a density like that of water.

Ceramic (Al_2O_3) porous supports are glued to non-porous Al_2O_3 tubes and sealed with a glass sealant at 900°C for 10 minutes (1°C/min heating and cooling ramp). The porous supports are asymmetric in the pore size radial distribution, with a diameter of 10 mm or 14 mm. It was also checked that no membrane showed gas leakage submerging them in ethanol under a He flow (1 atm) from inside to the outside of the membrane.

Novolac resin was prepared mixing 97.5 g of phenol, 1.5 of oxalic acid, 69 g of formaldehyde with a 10-hour reflux. The average molecular weight of the polymer was 3372.5 g/mol, with a dispersity (formerly called polydispersity index) of 2 (a value in agreement with the step-wise polymerization process).

To prepare the first dip-coating solution Novolac resin was diluted in N-methyl-2-pyrrolidone (NMP), to get the following concentrations: Novolac 3 g (26% wt.), formaldehyde 2.4 g (2.1% wt.), NMP 83.2 g (72.0% wt.). Two membranes were prepared with this only-organic solution, whereas the following ones were obtained after $Ni(acac)_2$ was added in a 1% and 1.5% wt. amount, to get differently metal loadings.

The Al_2O_3 supports are dip-coated and the obtained resin-based membranes are dried at 30°C at 30% relative humidity overnight to avoid a quick release of the solvent during the carbonization stage that could damage the carbon matrix, causing cracks or defects. The procedure is similar to that described elsewhere.[15]

The following step is carbonization in inert atmosphere. The carbonization end temperature is typically chosen to be above the decomposition point of the polymer and below the graphitization temperature, in this way it is usually comprised between 550°C and 1100°C, depending on the polymer used. In the case of Novolac resin 500°C to 600°C is the range commonly preferred. Many examples in literature show that tuning carbonization temperature is a powerful tool to control permeation and hydrophobicity/hydrophilicity features of the membranes.[1]

A higher temperature induces an increased hydrophobicity due to hydroxylic groups leaving the surface, moreover it tends to reduce pore size due to aggregation of the carbon matrix on top.

In our case the membranes were carbonized at 500°C or 600°C, see Table 28.

A second approach has been developed, in collaboration with Tecnalia (grateful acknowledgements go to Dr Pacheco-Tanaka and Dr Llosa-Tanco): since CH_4 has a much larger kinetic radius that the reagent molecules involved, the membrane pore size needs to be finely controlled and enlarged as compared to conventional carbon membrane matrix (whose pore size is around 0.5 nm). For this reason, adding PEG to the polymeric solution will grant larger pores and the same ease of carbonization of the carbon matrix. However, combining bigger pore size for the catalytically active

layer and smaller pore size for the outer layer seems even more promising. In this way indeed the outer layer will act as a filter if the reaction takes place in a mixture of gases, and not just the reagents in stoichiometric amount. Therefore, the outer layer will be obtained with a precursor solution very similar to those already described, with the only difference being the adding of ethylene diamine, a basic additive which is able to capture CO_2, due to its acidic features. At the same time hydrogen passes through the membrane due to its small size. At this point the reagents encounter a matrix with larger porosity and they find themselves space-confined, therefore more prone to reacting with each other. Ni nanoparticles decorate the surface of the pores and act as catalysts of the methanation reaction. The so-obtained methane has no other way out than passing through this inner membrane layer and through the ceramic support (which is endowed with larger pore size itself). This enriches the permeate phase with methane, acting as a filter for the desired product. Water is passing through as well due to the hydrophobicity of the membrane.

Accordingly, a new dipping solution was prepared. Novolac resin was obtained mixing 97.5 g pf phenol, 1.5 g of oxalic acid, 69 g of formaldehyde with a 7-hour reflux. The average molecular weight of the polymer was 3886 g/mol.

Once Novolac was obtained, two different dip coating solutions were prepared, with concentrations shown in Table 27. The one containing both Ni complexes and PEG will be deposited first, forming the inner layer of the membrane, whereas the one without such additives will be deposited after the drying and carbonization of the first layer. In this way the alkaline functionalization of the outer layer will be able to interact with CO_2 from the gas mixture, enhancing the selectivity with which carbon dioxide penetrates the outer layer of the membrane.

Unfortunately, most of the membranes experienced cracking at the connection with the non-porous support, where glass sealant was applied. This was not commonly observed when similar membranes were employed for different applications, so we argue that this might be the result of the remarkable exothermicity of the reaction (ΔH= -165.0 kJ/mol)[26] that causes localized hotspots. The thermal

expansion for the sealant is not matching the non-porous alumina one and this determines the breakage. Due to this technical inconvenience, the membranes enriched with PEG and ethylene diamine were obtained but not tested since they broke very quickly during their first test.

	Solution 15 Amount (g)	Solution 15 Relative amount (%)	Solution 17 Amount (g)	Solution 17 Relative amount (%)
Novolac	30	25.5	30	25.8
Formaldehyde	2.4	2.1	2.4	2.1
Ethylene diamine	0	0	0.6	0.5
NMP	83.2	70.5	83.2	71.6
PEG	0.69 (added to 69.5 g solution)	1	0	0
$Ni(acac)_2$	0.69 (added to 69.5 g solution)	1	0	0

Table 27 Composition of the solutions employed for dip coating the second set of membranes.

6.3.1 Preparation: Carbonization and pyrolysis

A brief description of the process of carbonization will be here addressed. Conventionally, carbon membranes for separation applications are prepared by carbonization, *i.e.* in this case pyrolysis, of polymeric precursor membrane at high temperature under vacuum or inert atmosphere.

Starting from the selection of the most suitable precursors, one should take into consideration several factors, such as a high aromatic carbon content, high glass transition temperature, chemical stability and the capacity of providing superior separation properties. The pyrolysis conditions impose strong effects on the gas permeation properties of carbon membranes: from these parameters the resulting pore population in the carbon matrix will be strongly affected. This is why phenolic resins are such a common choice for this systems: the pyrolysis of these materials provide carbon films with molecular

sieve properties[27] and they have high carbon yield after carbonization. Polymeric membranes can be prepared by means of different techniques: spin and dip coating are the most common ones. A solution with NMP as solvent and Novolac resin polymer is prepared with different dilutions, and it can be deposited on the outer face of a ceramic (alumina or zirconia) tube and subsequent spinning at a temperature around 30°C, to avoid cracking due to fast drying of the solvent.

Nr.	**Layers**	**Dip Coating solution**	**Carbonization temperature (°C)**	**Size and material**
232	1	Novolac	600	10 mm
233	**1**	**Novolac**	**500**	**10 mm**
234	2	Novolac+1%Ni	500	14 mm
235	2	Novolac+1%Ni	600	14 mm
236	2	Novolac+1%Ni	600	14 mm
237	**1**	**Novolac+1%Ni**	**500**	**14 mm**
238	1	Novolac+1%Ni	600	10 mm
239	2	Novolac+1.5%Ni	500	14 mm
240	**2**	**Novolac+1.5%Ni**	**600**	**10 mm**
242	2	Solution 15+solution 17	600	14 mm
243	2	Solution 15+solution 17	500	14 mm

Table 28 Membrane prepared with preparation conditions. Only the one in bold were characterized and tested for technical reasons.

It is believed that greater stability membranes are obtained after stabilization under air atmosphere mainly due to the contribution of oxygen in the dehydrogenation reaction. Indeed, oxygen mainly acts as a dehydrogenation agent in the conversion of C-C bonds to C=C bonds and generates oxygen-bearing groups in the polymer backbone, such as -OH and C=O. These kinds of groups promote

intermolecular crosslinking of the polymer chains and provide greater stability to sustain high temperature in the subsequent carbonization process. If the stabilization process is not completed throughout the entire membrane cross section, a significant weight loss can occur at higher temperatures. The stabilization process offers the potential to prevent the melting and fusion of the polymeric membranes and avoid excessive volatilization of carbon element in the subsequent pyrolysis process.[28] Additionally, as the stabilization temperature increases, the degree of decomposition and cross-linking in the membrane increases, which results in different micropore structures of carbon membranes. The degree of cross linking in the precursor membrane obtained is usually determined by dissolution tests.[29]

The pyrolysis process proceeds by various steps. At the first stage most chemical reaction and volatile emission occur. The typical volatile byproducts are NH_3, HCN, CH_4, H_2, N_2, CO and CO_2. Generally, this takes place simultaneously with a high weight loss and hydrogen evolution can be detected, forming a graphite-like structure. In the advanced phases of pyrolysis, part of the heteroatoms present in the polymer structure is eliminated while leaving behind a cross-linked and stiff carbon matrix. As a result of the rearrangement of the structure of the polymeric precursor, an amorphous microporous structure of carbon membrane is created by the evolution of gases.[30] Many examples in literature report that the microstructure of the carbon membranes (pore size, pore volume and pore distribution) could be tailored by controlling the conditions of pyrolysis process (e.g. temperature, heating, thermal soak time, pyrolysis atmosphere).[9,31–37] The pyrolysis is normally carried out at a temperature between 500 and 1000°C, which is between the decomposition and graphitization temperatures of the precursors. In the case of phenolic resin precursor, it was observed that the pores appear at approximately 500°C and they enlarge up to 700°C to 800°C. Pore shrinkage occurs conversely at higher temperatures due to decomposition and chemical condensation of the precursor and evolution of volatile compounds.[29] Moreover low heating rate are preferable to obtain small pores and enhance carbon crystallinity. High rates usually bring cracks, pinhole formation, distortions of the structure

and blisters. In the case of phenolic resin precursors, it was observed that high heating rates for pyrolysis shift the pore size distribution towards smaller pores and it is beneficial for improvement of the molecular sieve separation features.[38] The atmosphere can easily be changed and produces many effect on the resulting membrane: it can either be vacuum, an inert atmosphere (helium, nitrogen, argon, or any other inert gas) or oxidative (such as diluted carbon dioxide). A tuned atmosphere can control the chemical damage resulting from pyrolysis. Examples in literature evidence that the inert gas environment accelerates the carbonization reaction through increased gas-phase heat and mass transfer to form a more open porous matrix. It was observed that the membrane pyrolyzed under nitrogen flow has better separation properties than a similar one in vacuum: pyrolysis under inert gas flow favored the volatile compound release during carbonization and avoided the carbon deposition in the pores already formed.[39–44] Trick et al.[45] reported the possible mechanisms of the pyrolysis of phenolic resin in a carbon/phenolic composite, recognizing it as a critical step in the manufacture of carbon membrane and trying to understand the kinetics of the pyrolytic process. They followed the gas evolution from the membrane being pyrolyzed through Fourier Transform Infrared Spectroscopy (FTIR) the gas product evolution analysis. The structure of cured phenolic matrix is primarily methylene bridged phenolic units and the duty of pyrolysis is to eliminate all non-carbon species and produce a char of coalesced carbon rings. Three main possible mechanisms have been identified. Ouchi et al.[45] propose a mechanism consisting of three steps. During the first one additional cross-links are formed resulting from the condensations between functional groups of the cured phenolic resin. One condensation reaction involves two phenol groups and results in an ether crosslinks, the second one occurs between a phenol group and a methylene group, ending up in a C-H crosslink. In a second reaction stage, crosslinks are broken, releasing methane, hydrogen and carbon monoxide. Finally, hydrogen atoms are stripped from the ring structure and hydrogen gas is evolved. Jackson et al.[46] argue that the pyrolysis of cured phenolic resins occurs as an oxidative degradation. Although pyrolysis, by definition, takes place in an inert environment, this hypothesis

states that the decomposition products provide a source of oxygen. The proposed reaction results in the formation of a carbonyl crosslinks, in open contrast with the ether link formation suggested by Ouchi. Hydrogen atoms do not become available for combination to H_2. Parker et al.[45] propose a mechanism involving the formation of a thermally crosslinked intermediate structure with elimination of pendant aromatic rings and retention of all aromatic carbons that are multiple-bonded in the initial polymer structure. The mechanism predicts the evolution of phenol and cresol from the scission of the pendant aromatic rings. No water evolution is predicted by the mentioned mechanism, until the very last stage of pyrolysis.

As underlined, Ouchi's and Jackson's mechanisms are relatively complete but contradictory towards each other, and they predict that water is formed at early stages of the pyrolytic process. Parker, conversely, predict water evolution only on a later stage of the process. As a result of water evolution Ouchi predicts that a diphenyl ether crosslink develops and Jackson postulates that a carbonyl crosslinks forms instead. Another remarkable difference in Ouchi's and Jackson's views is the hydrogen evolution, which is completely excluded by Jackson. Finally, only Parker states that evolution of phenol and cresol actually takes place. The method adopted by Trick and coworkers was to follow the progression of the pyrolysis reaction through FTIR to identify the intermediate structures present during the pyrolysis. They identified two wavelengths corresponding to aromatic C-H bond and aliphatic C-h bonds, respectively at 3027 and 2922 cm^{-1}. The concentration of both types of bonds increases along the progression of the pyrolysis and then decreases. The phenolic polymer structure does not immediately begin to break apart but rather forms additional bonds in the initial stage. A third band was monitored, corresponding to tetra-substituted benzene rings at 1735cm^{-1}. The position of this peak shifts to lower wavenumbers as pyrolysis progresses, due to additional ring substitution (and not to carbonyl band, that in these systems is expected to appear at lower wavenumbers). An aromatic summation peak is visible at 1607 cm^{-1} and it is caused by the stretching of C-C bonds in benzene rings. The concentration associated with this peak increases before decreasing later in the

reaction and a faster increase is seen in the intermediate phase of pyrolysis. Other bands at lower wavelengths are also indicative of changes in the nature of the aliphatic bridges between aromatic moieties, stretching bands of the C-O bonds of a diphenyl ether and phenol structures (1264 and 1200 cm^{-1}) illustrate that the ratio of the concentration of the diphenyl ether link to the concentration of the phenol structure increases. A change in the relative heights of peaks below 1000 cm^{-1} indicates that ring substitution changes as the pyrolytic process proceeds. To summarize the results of the FTIR analysis, in the early stages additional intermolecular crosslinks are formed, as the study observes more aliphatic bridges and diphenyl ether links, as well as carbonyl links and increasing benzene ring substitution. Before being eliminated aliphatic crosslinks are also altered. At higher temperatures these bonds break (crosslink associated peaks decrease in intensity). Moreover, crosslink elimination is evidenced by the increased aromatic/aliphatic C-H bond ratio.

According to Trick and coworkers, this suggests that a diphenyl ether intermediate structure exists, and its concentration increases steadily during pyrolysis.

Finally, gas evolution analysis gave some further insights on the mechanisms taking place during the pyrolysis. Phenol and cresol evolved in the first region of the reaction that was carried out up to 900°C (below 500°C), together with water. Between 400 and 800°C the main evolved species are hydrogen, methane, carbon monoxide, water (though less than in the previous macroregion) and small amounts of carbon dioxide and ethane. Finally, between 560 and 900°C, hydrogen, carbon monoxide and water are evolved.

From this data collection, the authors were able to identify three regions with a dominant type of reaction occurring. In region 1 phenol and cresol are evolved. The scission of a terminal benzene ring results in the evolution of phenol and cresol dependent on the position of scission. Water is evolved from a condensation reaction involving methylene and hydroxyl functional groups, leaving a C-H crosslink. In the second region, the second water producing reaction occurs involving two hydroxyl functional groups to form an ether crosslink. FTIR provides evidence of the formation of the ether

link from the reaction of phenol groups. The first H_2 evolution peak occurs in this region and it results from stripping of previously formed C-H crosslinks and methylene crosslinks present in the original cured resin. Eventually in the third region hydrogen has been identified as the dominant product and results from the splitting of hydrogen atoms directly bound to benzene. FTIR spectra show a shift of benzene peak and a change in relative intensity, indicating a change in the ring structure. The final structure is therefore char with coalesced rings.

The microporosity of carbon membrane for molecular sieve like separation applications is provided by the microstructure of the pyrolized polymers, presenting an amorphous structure and disordered block constituted by char-like layers obtained as described before. Void spaces between blocks are very narrow (below 10 Å) and they are responsible for the resulting microporosity.[12,15,27]

6.4 Permeability testing

Permeability and selectivity are two key parameters to assess the performances of carbon membranes, and in general, membrane reactors. As abovementioned, permeability, P, is often defined as P=SD, where S is solubility and D is the diffusivity of a gas. This follows the so called solution (sorption)-diffusion model. [11] The diffusion coefficient is generally affected by the size of the penetrant gas: larger gases tend to have lower diffusion coefficient due to mass transfer mechanism. The solubility is described as the ratio of the concentration of gas in a membrane, C, to the pressure of the gas, P, adjacent to the membrane. [47] Permeability is the ability of a membrane to allow the permeating gas to diffuse through the material of the membrane as a consequence of the pressure difference over the membrane and can be measured in terms of the permeate flow rate, the membrane thickness and area the pressure difference across the membrane. It can be calculated as the ratio of permeability of two gases in binary separation.[47] Permeability is calculated including the thickness and it is therefore made independent from it, otherwise it is called permeance and its measure units are $(mol \cdot m^{-2} \cdot s^{-1} \cdot Pa^{-1})$.

In total three sets of measurements have been performed. The first was a single gas permeability test using only CO_2 and H_2, separately. The second one was the actual catalytic testing in which CO_2 and H_2 are mixed in stoichiometric ratio and the third one was a further investigation on the catalytic activity of a sample

From a technical point of view, the tests have been performed as follows: for permeability tests the membrane was introduced in a 10 L steel reactor filled with the corresponding gas (CO_2 or H_2) and the pressure was set to 1, 2, 4 or 6 bar. At each pressure the permeate flow was measured by a film flow meter with repeated measures. The permeance was determined as volumetric flow normalized to (geometric) measured membrane area and pressure. The calculation of the selectivity was performed considering that it is the ratio between the detected flow of hydrogen and of carbon dioxide.

After the single gas test, the membranes were put in contact with the reagent mixture (4:1 ratio between H_2 and CO_2). The temperature ranged from 100 to 500°C with a ramp of 3°C/min. A micro-GC was employed to analyze the composition of the outlet gases (permeate after the methanization reaction). After these tests (identical for each membrane tested), a membrane was selected to be tested also in relation to the analysis of the composition of the retentate gas mixture. The measurement of the flow of permeate allowed, as a difference, to obtain the retentate flow and by GC its exact relative composition. By knowing both the retentate and permeate composition it was possible to calculate the mass balance. This was particularly useful to evaluate specifically carbon balance, since we cannot calculate oxygen balance due to the massive production of water during the reaction (such water was not quantified). The resulting data were insightful to gain an estimate on the coking trend of the samples, a typical phenomenon of Ni catalysts.

Finally, the membranes were tested as powders in order to verify the contribution of the membrane structure in relation to the catalytic activity: the same conditions (temperature, pressure and reagent composition) were applied, and the products were evaluated by the use of a GC (with TCD detector).

The reactor used in this case was a titanium tube, able to resist the employed pressure (6 bar, as in the membrane test) and the temperature (up to 500°C).

6.5 FTIR characterization of dip-coating solutions

Fourier Transform Infrared (FTIR) spectra were recorded to characterize the polymeric precursor solutions for dip-coating, giving insights on both the change of composition obtained adding $Ni(acac)_2$ and carbonization temperature, see Figure 89. The solutions analyzed were the one without any Ni loading and the one with 1% wt $Ni(acac)_2$ loading carbonized separately at 500°C and 600°C. The visible peaks are in agreement with the ones reported in literature for Novolac resin FTIR spectra.[37] O-H stretching is usually reported at 3400 cm^{-1} and it is much more evident for the only-Novolac solution carbonized at 500°C. The two solutions containing Ni show a smaller peak at the same wavelength and the carbonization temperature effect is particularly visible since the sample carbonized at 600°C shows to have lost much of its -OH groups due to the higher carbonization temperature. Indeed in this sample such peak is almost negligible. A similar effect is present also for

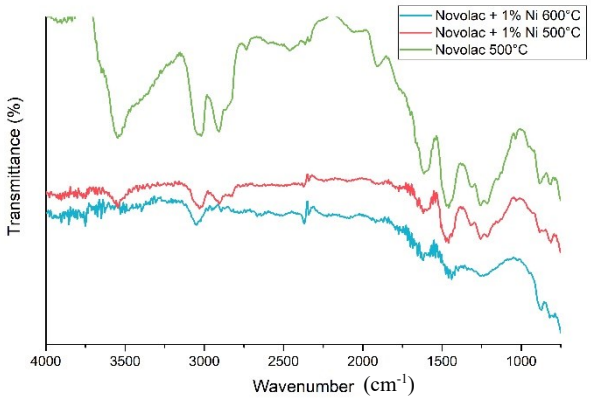

Figure 89 FTIR spectra of the precursor solutions with 0% and 1% Ni loading.

the peak around 3000 cm^{-1} (3040 cm^{-1} and 2900 cm^{-1}), attributed to C-H stretching. The peak placed at 2900 cm^{-1} is caused by aromatic rings and it is less evident for the sample carbonized at higher temperatures, showing the detrimental effect of temperature over 500°C to aromatic moieties in

Novalac resins. The same evidence is conveyed by the peaks at 1610 cm^{-1} and 1460 cm^{-1}, attributed to C=C stretching in aromatics. The low intensity of this peak in the sample carbonized at higher temperatures, once again demonstrates the breaking of the aromatic backbone in the polymer at high temperatures (600°C). Under 900 nm literature reports other bending modes (C-H and C=C), visible in the spectra of each sample. We cannot detect the effect of the presence of Ni in the wavelength of the peak, although a heavier atom in the oscillator should generate a shift towards lower wavenumber values. The explanation for this absence could be due to the low percentage of Ni added (1% wt.) or to the absence of C-Ni bonds. The prominent effect on the intensity of the peaks is the one due to carbonization temperature, that was proved to influence the composition and the structure of the resulting precursor solution.

6.1 XPS characterization of dip coating solutions

X-Ray Photoelectron Spectroscopy (XPS) was performed at the Eindhoven University of Technology on three precursor solutions, respectively 0% Ni loading (carbonization temperature 500°C), 1% and 1.5% Ni loading (carbonization temperature 500°C and 600°C). The quantitative results have also been collected and reported in Table 29.

Solution	Carbonization temperature (°C)	C 1s	O 1s	N 1s	Ni 2p
0% $Ni(acac)_2$	500	91.03	8.46	0.51	0
1% $Ni(acac)_2$	500	89.07	10.37	0	0.56
	600	90.03	8.49	0.54	0.95
1.5 % $Ni(acac)_2$	500	73.05	26.95	0	0
	600	85.91	12.86	1.09	0.13
	700	91.16	8.40	0	0.44
1% $Ni(acac)_2$ 1% PEG	500	85.05	11.62	2.49	0.84
	600	83.34	14.83	1.79	0.03
	700	94.43	4.71	0	0.86

Table 29 XPS elemental analysis on precursor dip-coating solutions.

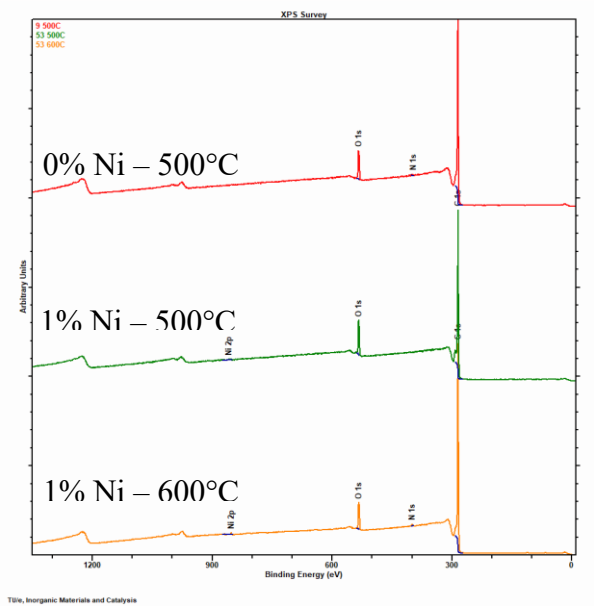

Figure 90 XP spectra of the precursor solutions.

Since the surface oxygen content decreases with higher carbonization temperature (in the Ni-loaded sample) we can confirm that the hydrophobicity increases with the carbonization temperature, since

by condensation reaction hydroxide groups leave the surface forming water as leaving product. Moreover, the surface oxygen is also affected by the Ni doping, that seems to be able to retain more oxygen on the surface with low carbonization temperatures and at the same time tends to lower the amount of surface oxygen from the surface. For these reasons we can argue that Ni doping in the structure can alter the hydrophobicity of the surface as well.

At the same time also nitrogen content was measured, and some samples showed a residual nitrogen concentration, most likely from an incomplete solvent evaporation, as reported also elsewhere,[48] since no other source of nitrogen could be identified. Unexpectedly this was observed for the Ni containing samples carbonized at higher temperatures, and for the Ni-free sample carbonized at 500°C.

High resolution spectra analysis was performed for the regions relative to O1s and C1s and for the membranes with 1.5% wt $Ni(acac)_2$ and PEG enriched dip coating solution. The effect of carbonization temperature was also taken into consideration, comparing the same membrane carbonized respectively at 500, 600 and 700°C.

C1s region shows a progressive tendency towards surface carbonates formation when the carbonization temperature increases, except for the case of PEG enriched solution (shown in dark red). This exception is also retrieved in the O1s region, in which a progressive shift of the peak towards higher binding energy is not shown, unlike the other samples. This shift is indeed indicative of organic C=O bond, and therefore surface carbonates. We therefore argue that PEG in the structure might have undergone a chemical decomposition occurring at an intermediate temperature between 600 and 700°C, since the spectra recorded for the sample carbonized at 600°C is in agreement with the observed trend.[49] At the same time C1s spectra are also showing some carbide contribution to the carbon chemical environment, since a slight increase of the signal is also seen below 284.8 eV, the typical binding energy for aliphatic C-C. The only case in which this is possible is the presence of carbide, which means the presence of bond of carbon to a cation, and we argue that in this case a Ni-C is actually present in the structure. Others found similar results for systems featuring carbon and

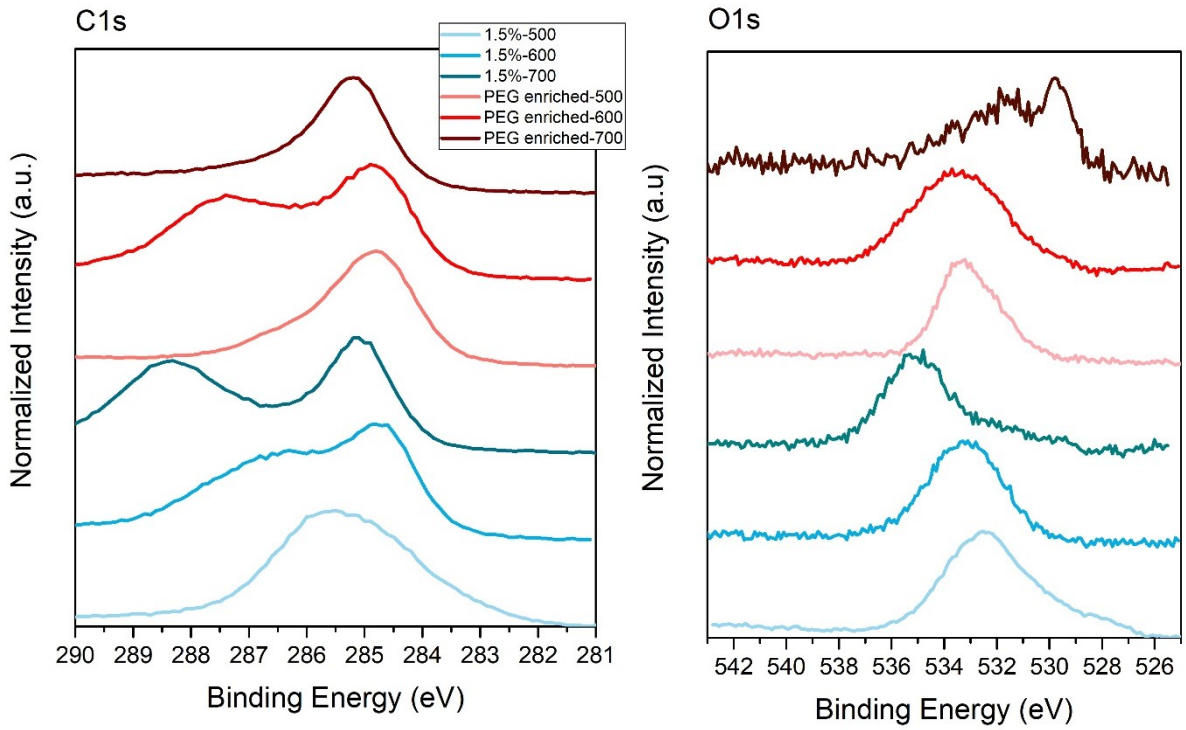

Figure 91 XP high resolution spectra for the dip-coating precursor with 1.5%wt Ni(acac)2 loading and PEG enriched solutions.

confined nickel.[50,51] This might suggest the establishment of a system that might resemble single-atom catalysis, with individual Ni atoms bound to carbon in the matrix. Unfortunately, although that could have provided a confirmation of this hypothesis, for technical reasons we were not able to record the high resolution Ni2p region, given the low concentration and therefore high signal-to-noise ratio.

6.6 XPS and H_2-TPR characterization of prepared membranes

A similar analysis has been performed at the University of Padova for selected membranes by means of X-Ray Photoelectron spectroscopy. As a further investigation on the properties of the obtained membrane, the sputtering technique was also employed, to achieve a depth profiling characterization of the carbon layer supported on alumina: by the impact of the surface with accelerated argon ion, the identification of chemical variations across different depth in the material is possible.

The membranes were mechanically cut after permeability and catalytic testing and the entire structure (included alumina support) underwent XPS analysis, to get the most resembling system to the tested one.

A first assessment dealt with sputtering time: as the samples are constituted by polymers, that could be affected by sputtering-induced thermal decomposition, a preliminary time testing was necessary. According to previous experience and literature we estimate the sputtering depth rate around 3 nm/min.[52] In Figure 93 the C1s region spectra are shown, they refer to the single layer Ni-free membrane carbonized at 500°C. As it can be seen after ten minutes of sputtering treatment the broadening of the peak is evident, although no significant alteration in the maximum intensity binding energy is recorded. This is diagnostic of an increase of the number of chemical environments experienced by carbon atoms in the sample, *i.e.* the present carbon species are increasing in number. For this reason, we cannot consider the polymer "intact" and resembling its original nature before sputtering and there is a significant risk of an artificial alteration of the surface nature in the sample. Consequently we kept the sputtering time fixed at five minutes, when, as shown by the blue line in

Figure 93, the broadness of the peak is almost the same as in the as-prepared sample. A different picture comes from O1s region, where an intense sputtering (10 minutes) shows a slightly larger peak but, most importantly, a different peak position, at lower biding energy. This is typical for metal oxides, and since no Ni is present in this membrane, the logical conclusion is that it must be the contribution coming from the alumina porous support. The graph is shown in Figure 92.

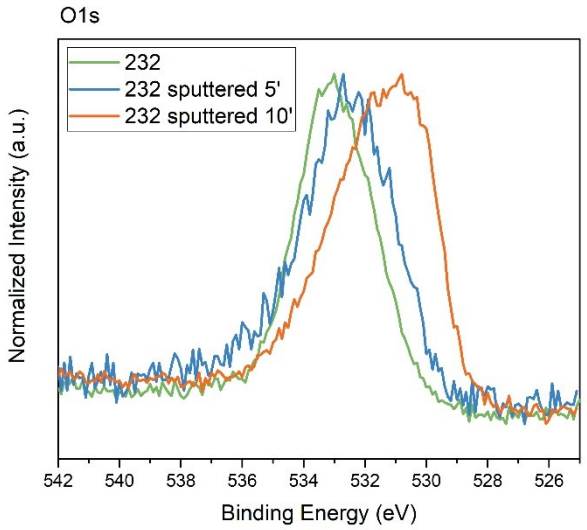

Figure 92 XP high resolution O1s spectra for the single layer Ni-free membrane carbonized at 500°C.

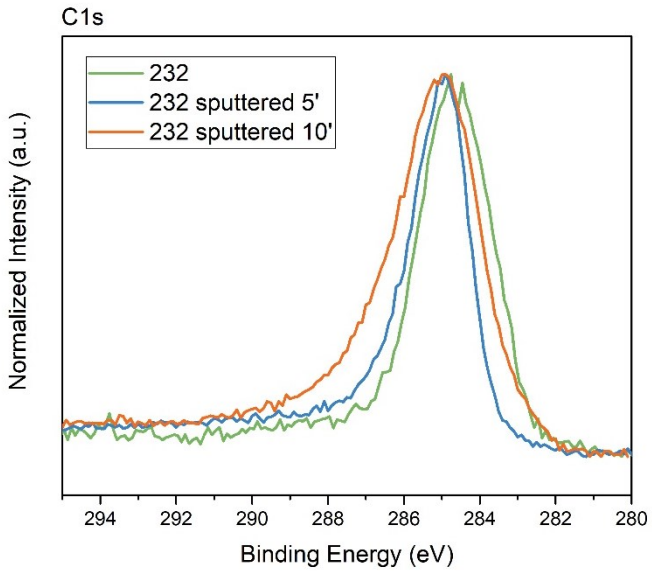

Figure 93 XP high resolution C1s spectra for the single layer Ni-free membrane carbonized at 500°C.

To avoid too intense mechanical stress on the surface, as said, the sputtering time was fixed at five minutes. However, to be able to gain enough information about the depth profiling of the surface, angle resolved XPS depth profiling was attempted, that is to say different angles between the sample surface and the detector were employed. The conventional angle is fixed at 45° for standard XPS measurements. In this case the detector was placed also at 20° and 70° from the sample surface. A grazing angle acquisition (*i.e.* 20°) provides more surface sensitivity in the compositional analysis (approximately 5 nm from the surface), whereas high angles (*i.e.* 70°) enhance an "in depth" analysis, with the XPS technique limitations given by the limited mean free path of the electrons, providing a sampling depth up to 10 nm.[53] The standard technique with a 45° oriented detector is usually to give compositional analysis of the first layers of the surface, below 10 nm in total depth.[54]

Significant results came from the C1s spectrum at different angles, whereas in the case of N1s and O1s there was no substantial difference in the shape and position of the peaks but only their relative intensity (which reflects in different elemental composition as shown in Table 30 and Figure 94). From these data, a prevalence of oxygen on the surface, at expense of carbon percentage on the outermost layers is highlighted; at the same time the nitrogen content has a non-monotonous behavior being detected only at intermediate detection angles. The only source of nitrogen was provided by the incomplete evaporation of the solvents, and these data might suggest that it tends to be confined to intermediate depths in the outer layers of the material. A similar behavior was observed for carbides, present only at intermediate depth, as seen in Figure 95.

Ni-loaded membranes (with 1% wt loading) were tested to compare the possible effect of carbonization temperature on the surface composition and chemical identity. Once again, the membranes underwent sputtering in XPS measurements. Their compositional analysis is reported in Table 31. With the exception (discussed above) of the last sputtering measurement for the Ni-free membrane, oxygen content decreases along the thickness of the membrane, and we attribute this behavior to the tendency of hydroxylic group to stay on the surface, as for the oxidative of air

exposure. Accordingly carbon content increases and nickel instead seems to be more abundant on the outermost section of the material. Due to the high porosity of the material we should keep in mind

Unsputtered			
	20°	45°	70°
C1s	78.85	67.65	91.55
O1s	14.8	17.51	8.45
N1s	5.71	14.94	--
Approximately 15 nm sputtering			
	20°	45°	70°
C1s	88.61	80.40	86.34
O1s	11.39	18.35	13.66
N1s	--	1.26	--

Table 30 Elemental percentage composition in Ni-free membrane (232) deposited as single layer and carbonized at 500°C. The results are obtained by angle resolved XPS combined with Ar ion sputtering.

that we are not looking at a homogeneous flat surface and Ni, if it tends to stay on the outer layer of the carbon matrix, could be displaced at different heights, that the sputtering technique itself does not allow to differentiate with extreme accuracy. The value we obtain is therefore an average and shows in general that carbonization at higher temperatures enables higher metal mobility in the matrix and therefore higher surface content. At the same time one could argue that nickel and oxygen are present together at typical XPS sampling depth due to the formation of NiO particles on the surface. To verify this possibility temperature programmed reduction in hydrogen (H_2-TPR) tests on powdered membranes were carried out and not reported, since each repeated test pointed out that no reductive activity could be performed on the samples, and therefore we conclude no NiO is present in the sample. Still, XPS high resolution spectra in the Ni2p region was not possible on these samples. The high-resolution spectra for the samples recorded in the C1s region, before and after sputtering to an approximate depth of 15 nm, are reported in Figure 96. The peaks are centered at typical values for

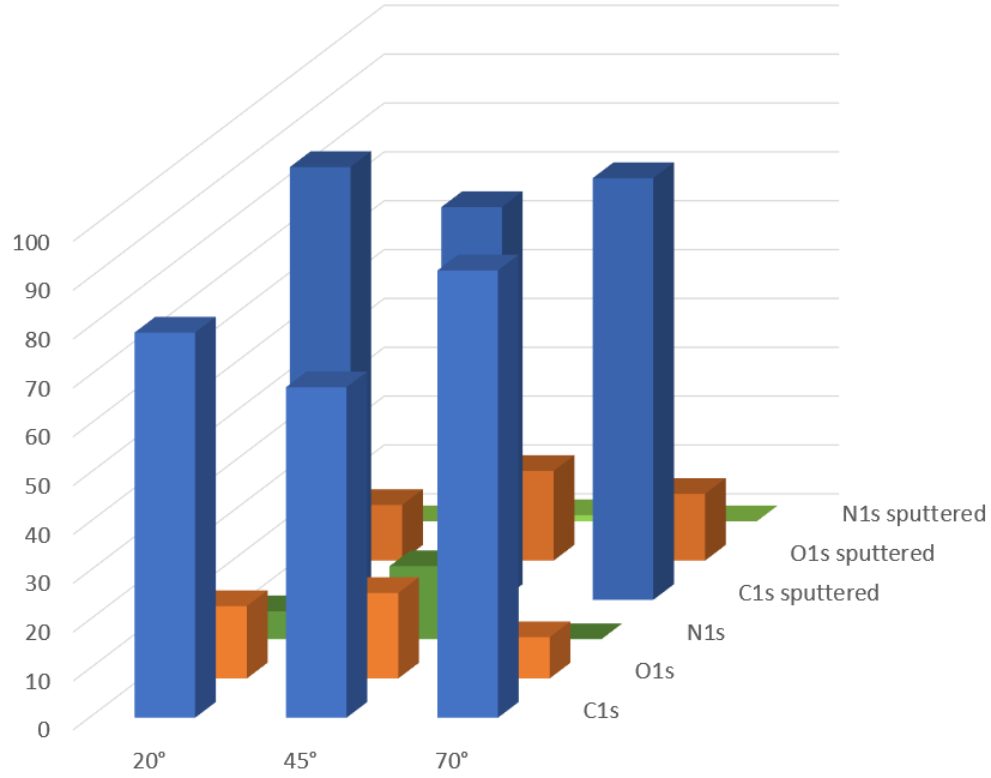

Figure 94 Histogram representation of the results presented in Table 30.

C-C single bonds, with a narrow shape, except for the case of the 1% $Ni(acac)_2$ loaded sample carbonized at 500°C, in which the broadening of the main carbon peak suggests the presence of oxidized carbon on the surface (mainly carbonate species, O-C=O bond).[55] This contribution is reduced by the sputtering procedure, pointing out its main occurrence on the outermost layers of the structure. This circumstance is confirmed as well by high-resolution spectra of O1s region, visible in Figure 97, where a shift of the binding energies for the oxygen main peak suggests again the formation of carbonates on the surface of the sample, which does not show the same composition after sputtering treatment.

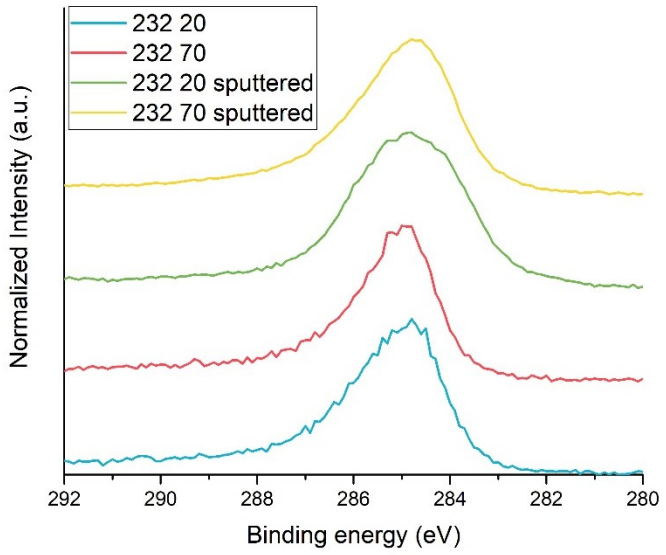

Figure 95 XP high resolution C1s spectra for the single layer Ni-free membrane carbonized at 500°C, recorded with angle resolved sputtering-aided XPS.

Carbonization temperature (°C) - layers	Dip coating solution	Membrane code	C 1s	O 1s	N 1s	Ni 2p
500 Single layer	0% Ni	232	67.65	17.51	14.94	0
			80.40	18.35	1.26	0
			79.92*	20.08*	0*	0*
500 Double layer	1% Ni	234	72.69	12.15	12.62	2.53
			91.09	7.87	0	1.03
600 Double layer	1% Ni	236	73.91	10.59	12.71	2.79
			92.79	5.82	0	1.39

Table 31 Elemental percentage composition in Ni-free membrane (232) and 1% Ni-loaded membranes (234 and 236) carbonized at 500°C or 600°C (see Table). The first row for each membrane indicates as prepared samples, the second one the layer after sputtering for five minutes (approximately 15 nm depth) and the third (*) one, only for the Ni-free membrane is detected after ten minutes of sputtering (30 nm).

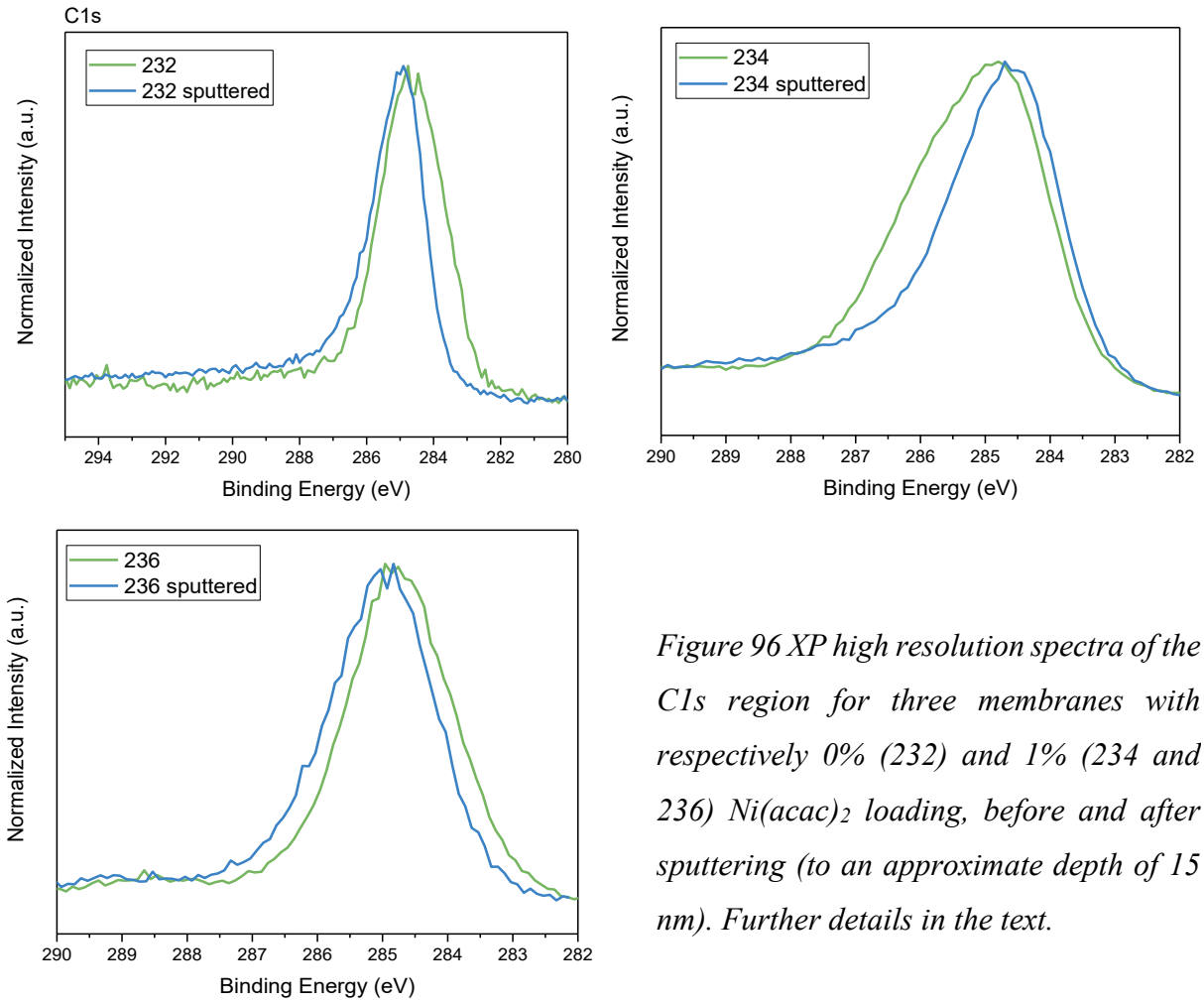

Figure 96 XP high resolution spectra of the C1s region for three membranes with respectively 0% (232) and 1% (234 and 236) $Ni(acac)_2$ loading, before and after sputtering (to an approximate depth of 15 nm). Further details in the text.

6.6 Morphological investigation: Permporometry and SEM images

Porometry of the membranes is of course a parameter of fundamental importance in evaluating their behavior in gas separation. As aforementioned gas transport mechanisms, unlike polymer membranes, rely mostly on the pore size distribution on carbon membranes,[27] and high selectivities are reached when the pore size resembles the one of the molecules to be separated. Moreover, such data are useful to determine the effectiveness of a certain preparation procedure: in the case of dip coating, several treatments often reduce the porosity, decreasing gas permeation rate but enhancing permselectivity (a compound parameter in which both permeability and selectivity are considered).

The porometry of double coated membranes was evaluated through the permporosimetry technique: it is based on the controlled expulsion of a suitable liquid from pores of different sizes by increasing

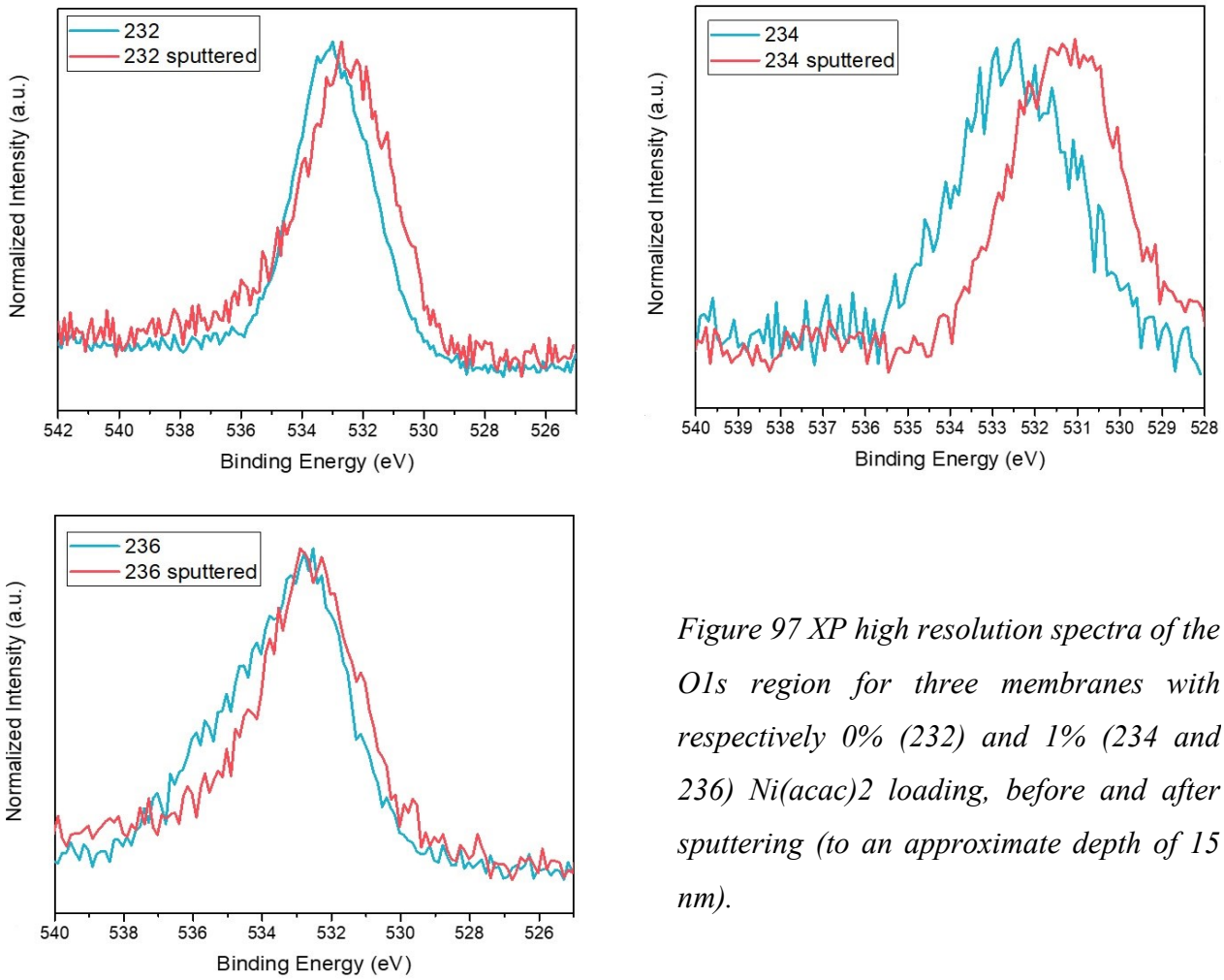

Figure 97 XP high resolution spectra of the O1s region for three membranes with respectively 0% (232) and 1% (234 and 236) Ni(acac)2 loading, before and after sputtering (to an approximate depth of 15 nm).

the gas pressure difference across the tested porous solid, vapour saturated beforehand. The gas flow rate through liquid-free pore corresponds to the number of pores with different sizes. The main difference as compared to conventional BET physosorption mediated surface area determination is that this technique only evaluates open pores and not cavities, the only pores responsible for the passage of gas through the membrane.[56] The resulting pore size distribution is shown in Figure 98. The distribution of pore sizes is encouraging: adding Ni does not decrease the most frequent pore size but, quite the opposite, it sharpens the distribution towards smaller pore sizes. A typical pore size of 0.4 nm (4.0 Å) is obtained and this is in line with expectations for carbon membranes for molecular sieving separation of the following gases (in brackets their kinetic diameter in Å): carbon dioxide (3.3 Å), methane (3.8 Å) and hydrogen (2.9 Å).[57,58]

Figure 99 reports SEM images obtained from Ni-free and Ni-loaded membranes: no evident change is notable after repeating twice the dip coating procedure. The average thickness of the membrane is 4.2 µm.

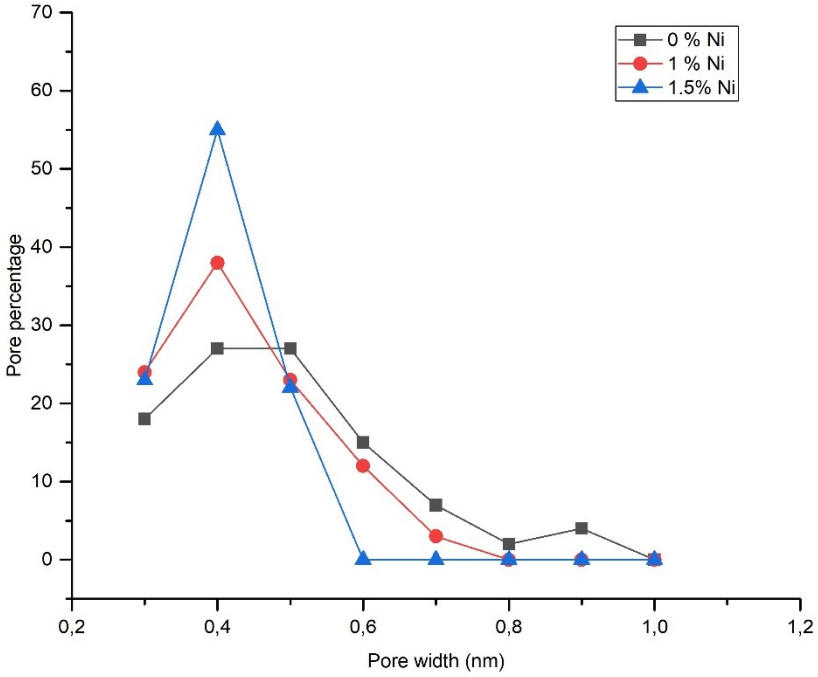

Figure 98 Permporometry results on double coated membranes with increasing $Ni(acac)_2$ content.

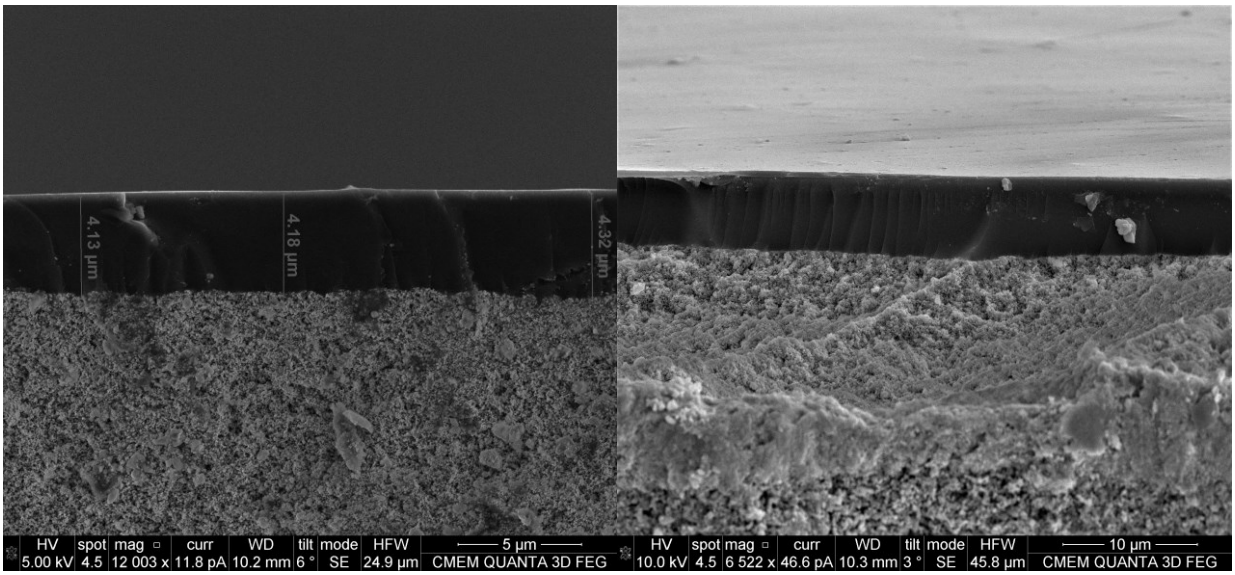

Figure 99 SEM images of double coated Ni-free and Ni-loaded membranes: the thickness obtained is very similar in the two cases.

6.7 Gas separation performances

Selectivity and permeance will be herein considered: this is done in accordance to Robeson's collection and famous paper "The Upper Bound Revisited"[6], in which all the examples previously known in gas separation applications are reported, divided as per gas pair investigated. At the end of this section it will be possible to identify the position of the presented membranes on Robeson's graph for the hydrogen/carbon dioxide pair.

The permeance, whose measure units are $[mol \cdot m^{-2} \cdot s^{-1} \cdot Pa^{-1}]$ is reported for three membranes, with different Ni loading (from no loading to 1.5% $Ni(acac)_2$ loading). This will be then converted into permeability, in Barrers, according to the formula reported in reference[59,60] and used as a benchmark in the Robeson's graph: $permeability\ (B) = \frac{permeance\ (mol \cdot m^{-2} \cdot s^{-1} \cdot Pa^{-1})}{thickness\ (m)} \cdot 3.35 \times 10^{-16}$.[61]

Figure 100 illustrates the behavior of selected membranes (233, 237 and 240, respectively 0% Ni, 1% and 1.5% $Ni(acac)_2$ loading) towards carbon dioxide and hydrogen permeation. We can notice in the first case that carbon dioxide is permeating decreasingly with the increase of temperature, a typical trend observed for adsorption diffusion mass transport mechanism (in which of course an increase of the temperature leads to desorption and therefore it does not benefit to the adsorption step of the mechanism). Hydrogen shows instead a more complex behavior: a first decrease with the temperature is followed by a rapid increase. This suggests a competition between two models: surface adsorption at the beginning and at a later stage molecular sieve mechanism, highly dependent from the pore size of the membrane. In the second case (membrane code 237, 1% $Ni(acac)_2$ loading) the carbon dioxide permeance value is significantly lower than in the carbon-only membrane and therefore we can conclude that it is a consequence of a smaller pore size and/or a larger thickness of the resulting membrane. Finally, the highest Ni loading (membrane code 240) results in a remarkably higher carbon dioxide permeance (and increasing with temperature) but worse selectivity towards the

CO_2/H_2 gas pair. According to the mass transport model applied in this case, the effective pore size could be significantly larger in this case, as it is also reported by other studies with similar systems.[62] Selectivities for hydrogen/carbon dioxide gas pair are also reported, and they were obtained by simply computing the ratio of the flow rate of hydrogen over the one of carbon dioxide at the same pressure and temperature conditions. In the graphs (Figure 101) the ratio of the flows is shown as a function of the pressure difference between the two sides of the membrane in single gas conditions. Different markers illustrate different temperature. Since the catalytic tests are carried out at a pressure difference of 6 bar, the last point in the graph is what we are mostly interested in.

Selectivity can be easily compared to the Knudsen limit (derived by the Knudsen selectivity), deriving from molecular weights of the two separated gases, as illustrated in the section regarding mass transport mechanisms occurring in porous membranes. Knudsen's limit is in this case equal to 4.7. The data reported in Figure 101 are indicative of a partial Knudsen behavior, since most of the selectivities reported lie below this limit, especially at high pressure differences.

Gathering all these data and applying the abovementioned formula to convert permeance into permeability (we considered the average value of 4.2 μm as obtained from SEM images), the selectivity is the following: 1.7<selectivity<4 and the permeability (in Barrer) is the following: 238<permeability<5373. In Figure 102, a green shade highlights the region in which the performances of our membranes are located. It is possible to notice that this bidimensional interval is tangent to the Robeson's upper bound, showing the high quality of these performances as compared to previous membranes reported in literature.[5,6]

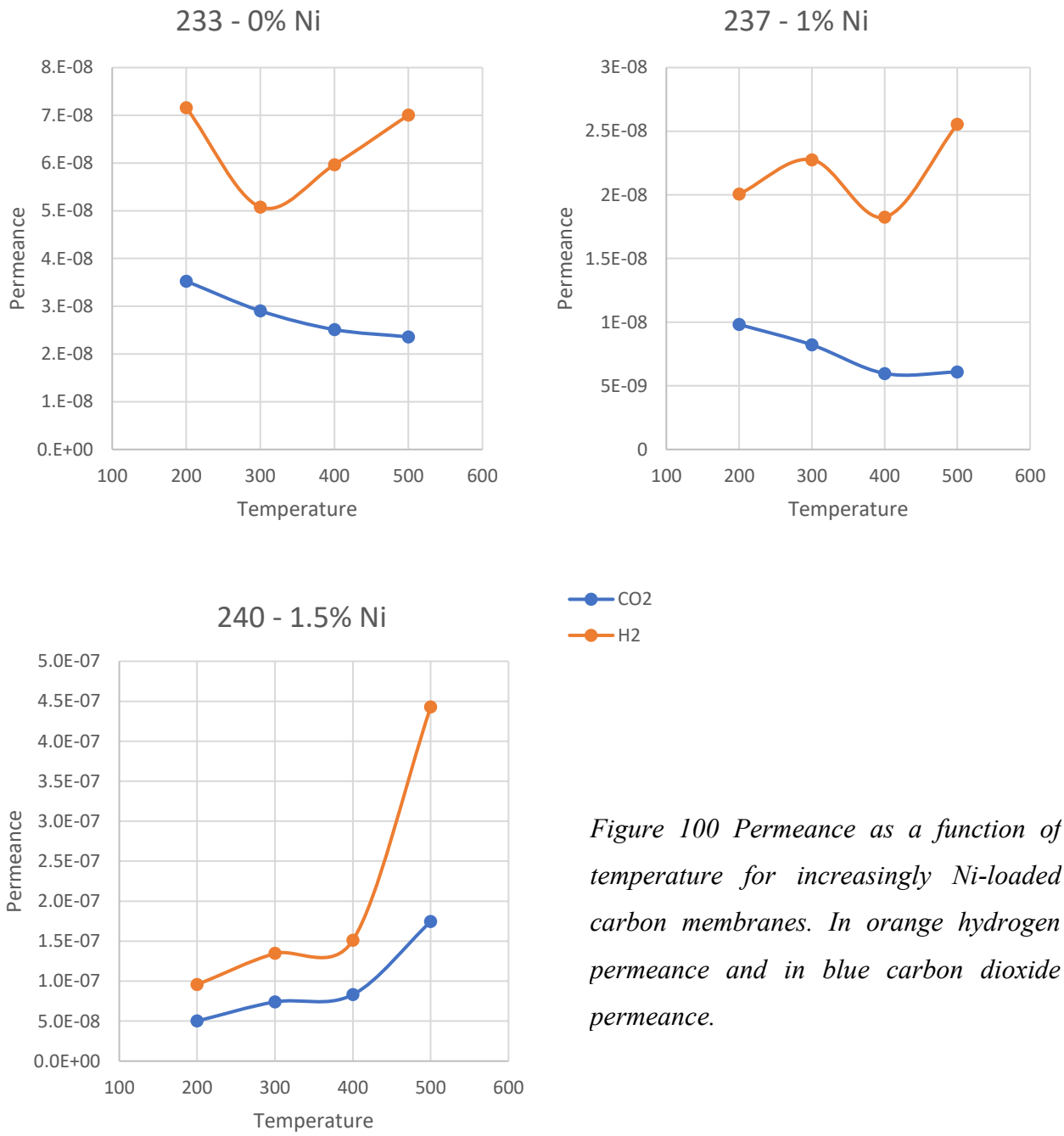

Figure 100 Permeance as a function of temperature for increasingly Ni-loaded carbon membranes. In orange hydrogen permeance and in blue carbon dioxide permeance.

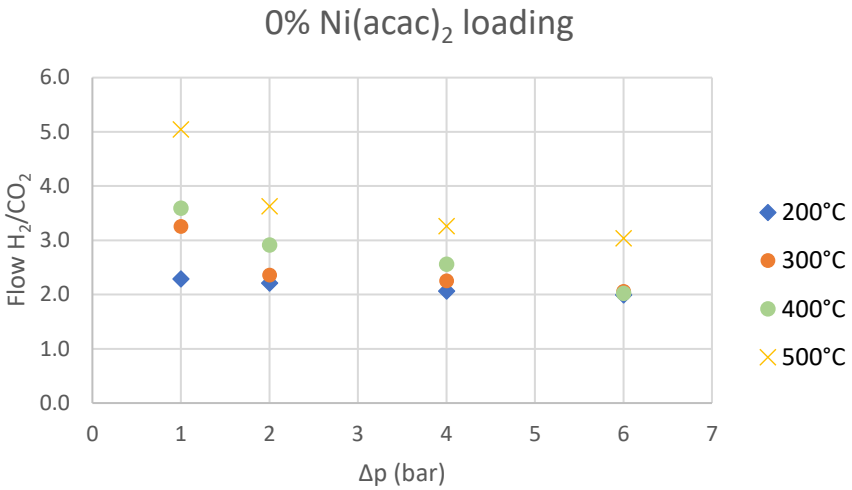

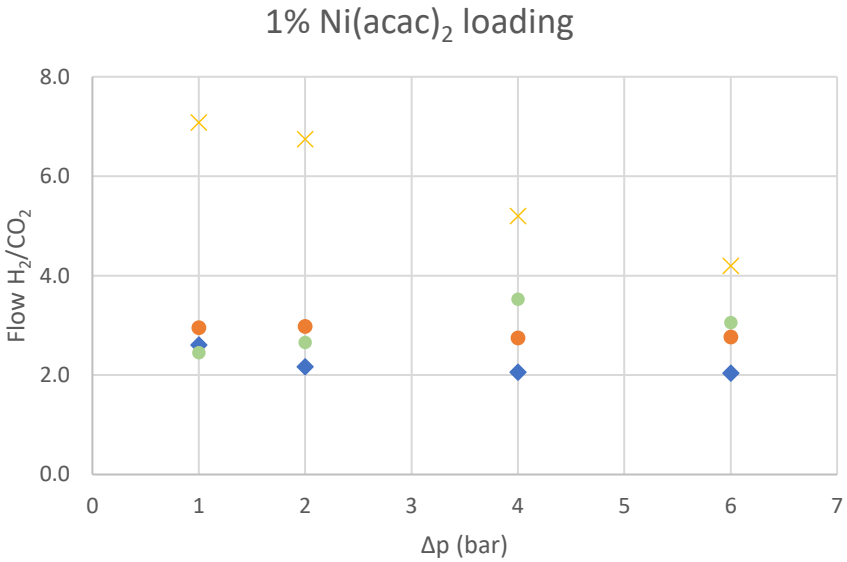

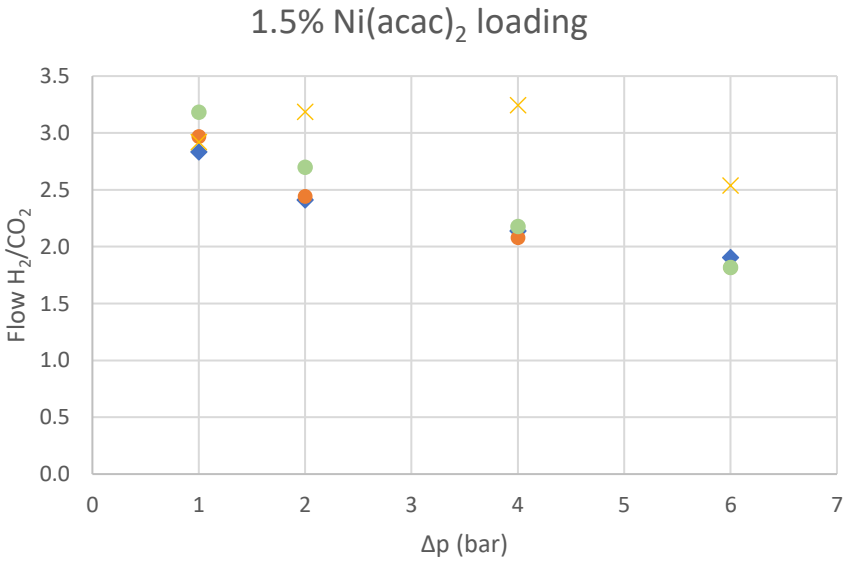

Figure 101 Selectivities (H_2/CO_2) for selected carbon membranes, as a function of temperature and pressure difference across the membrane sides.

6.8 Catalytic tests

The following membranes were tested under stoichiometric ratio of the reagents (40% H_2, 10% CO_2 and 50% N_2) and Δp=6 bar. The other reaction conditions have already been listed. In this section only the permeate composition will be discussed, since the retentate composition was not analyzed. The results for the only-carbon monolayer membrane (membrane code 233) are illustrated in Figure 103. Interestingly no CO side production was detected by the GC, nor other accidental byproducts such as methanol or dimethyl ether (DME). Even if the pore size of this membrane does not allow an excellent selectivity to hydrogen, we can still observe satisfactory results, which we attribute to the separation capability of the membrane, and its hydrophobicity that will shift the equilibrium to the right-hand side of the reaction equation: $CO_2 + 4H_2 \rightarrow CH_4 + H_2O$. Moreover the decrease of hydrogen concentration between 300 and 500°C (approximately a 6% increase) corresponds to a 1.5% increase in methane concentration, the 4:1 proportion expected for carbon dioxide methanation. Different proportions (3:1 and 1:1) are retrieved in unwanted reactions with the same reagents: respectively $CO_2 + 3H_2 \rightarrow CH_3OH + H_2O$ and $CO_2 + H_2 \rightarrow CO + H_2O$). Carbon dioxide concentration drops to

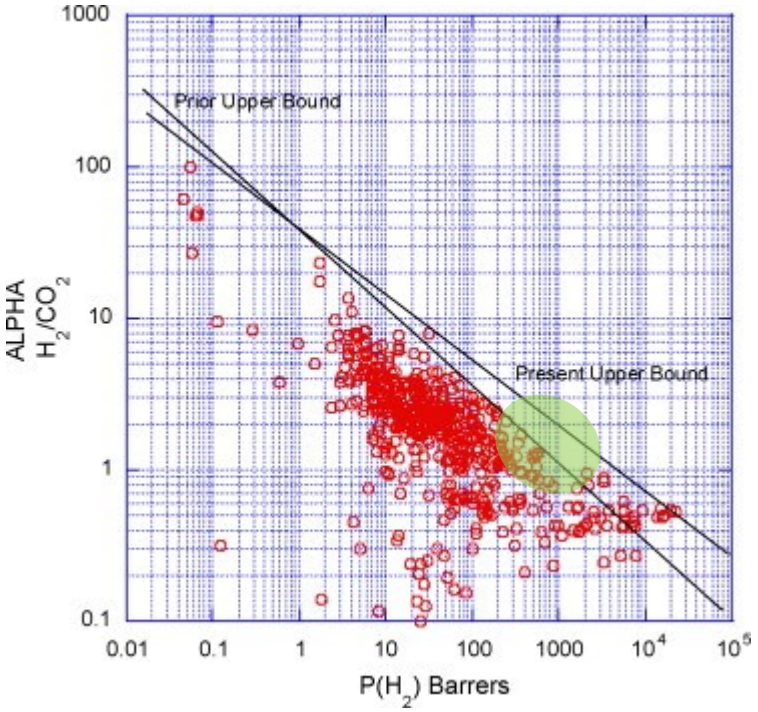

Figure 102 Empirical upper bound relationship for membrane separation of gases according to Robeson's work [Lloyd M. Robeson, The upper bound revisited, Journal of Membrane Science, 320, 1–2, 2008, 390-400, https://doi.org/10.1016/j.memsci.2008.04.030]. In green the region where the performances of the studied membranes are located.

zero at about 400°C, both for consumption and for poor permeation through the membrane (see Figure 100).

A similar picture (in Figure 104), but with significant changes is the 1% $Ni(acac)_2$ loading membrane: a similar final methane yield is obtained and hydrogen consumption is comparable to that of the previous membrane as well, but carbon dioxide undergoes a lower permeability across the membrane, meaning that the membrane is more catalytically active than the previous one, as expected by the adding of Ni catalyst. We can attribute a lower permeance to a smaller pore size and/or higher thickness of the membrane. Again at 300°C a 7% drop of hydrogen concentration is observed and a 1.3% increase of methane concentration is produced. Again neither CO or any other byproduct was detected.

Finally the most loaded membrane was tested (Figure 105, 1.5% $Ni(acac)_2$): in this case the carbon dioxide permeance is higher and increases with the temperature, but the selectivity to hydrogen is lower. This represents the first case in which CO was detected and this is the first double layer

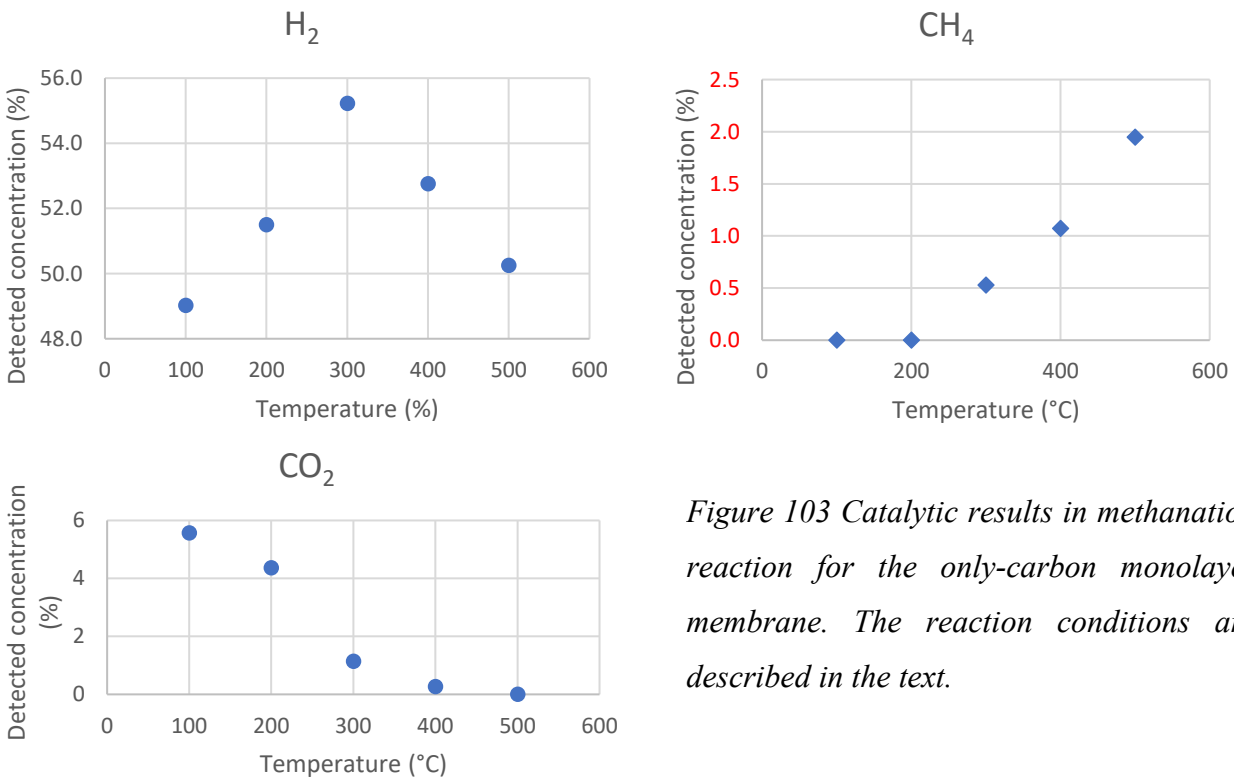

Figure 103 Catalytic results in methanation reaction for the only-carbon monolayer membrane. The reaction conditions are described in the text.

catalytically tested. Thus we argue that a higher residence time in the membrane (as a consequence of larger thickness) causes the formation of unwanted byproducts such as CO. Moreover, the carbon dioxide, despite the high permeance, at least if compared to the previous membranes, is highly converted: although a larger amount of carbon dioxide is theoretically able to permeate the membrane,

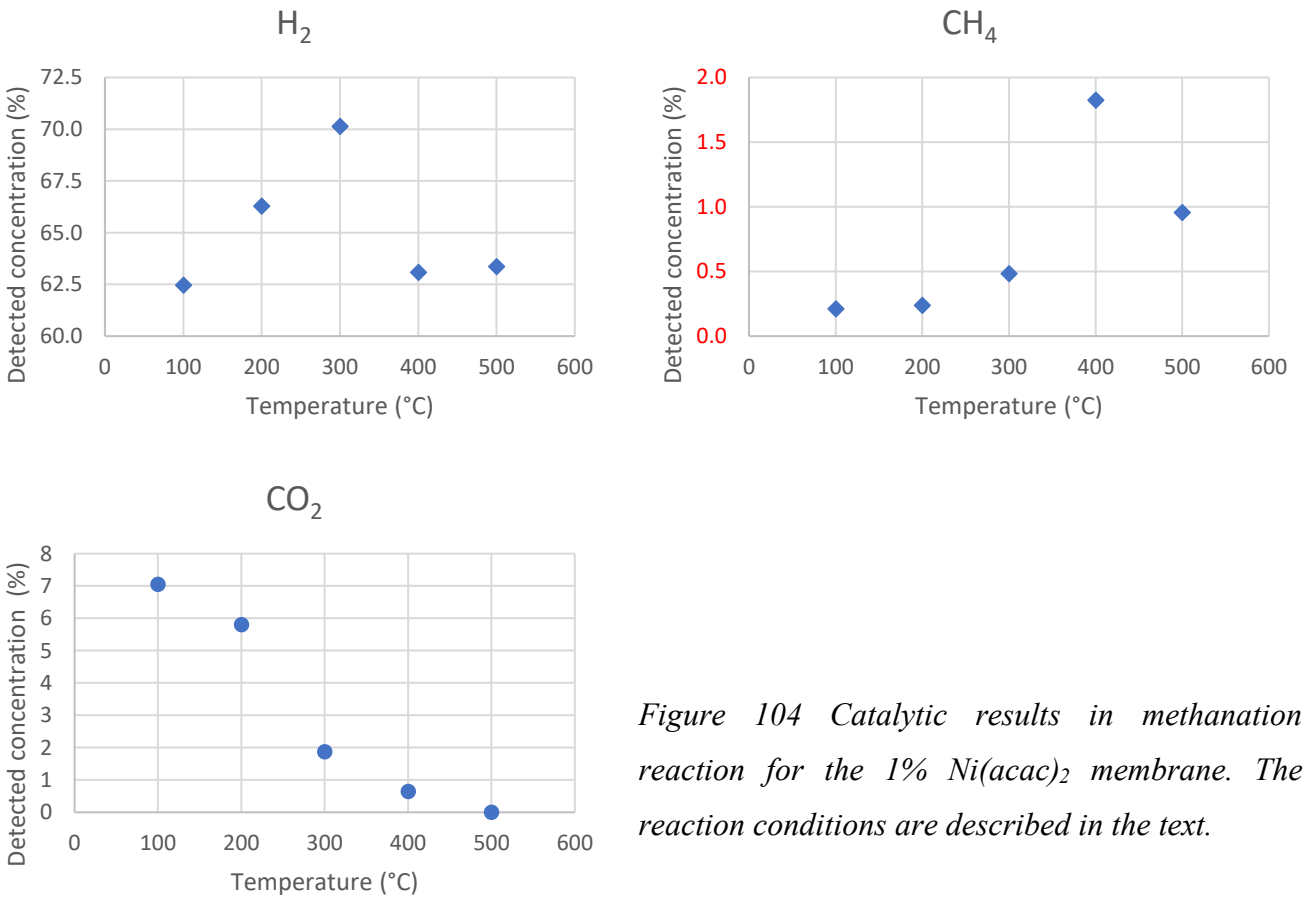

Figure 104 Catalytic results in methanation reaction for the 1% Ni(acac)₂ membrane. The reaction conditions are described in the text.

we still observe a low concentration at the end, suggesting a higher conversion activity of the membrane. Again hydrogen is decreasing with the same onset temperature in which methane and, this time, carbon monoxide are produced, *i.e.* 300°C.

6.9 Variable ratios among the reagents: 1% Ni(acac)₂ membrane to the test

To choose optimized test conditions in terms of reagent mixture, a variable reagent mixture was employed: 50% N_2 was fixed, CO_2 feeding varied from 10% and 40%, H_2 flow was regulated at the complementary percentage. The temperature was fixed at 450°C and the working pressure difference

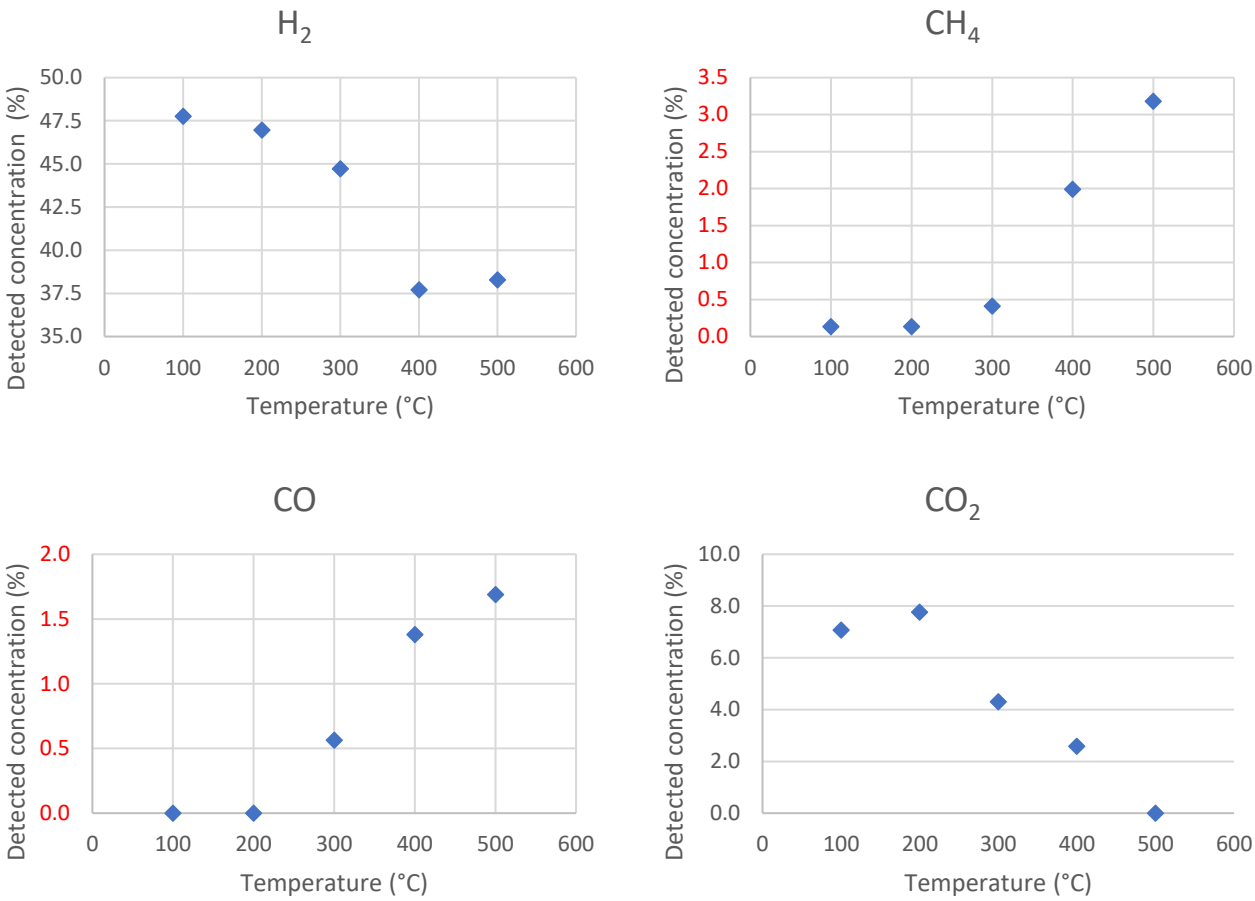

Figure 105 Catalytic results in methanation reaction for the 1.5% Ni(acac)$_2$ membrane. The reaction conditions are described in the text.

was 6 bar (Figure 106). To gain more insights about this changing testing environment, both the permeate and retentate compositions were analyzed through GC, as described beforehand. Interestingly methane and hydrogen were more abundant in the permeate region, whereas CO and CO_2 tend to stay on the retentate side of the membrane. In particular, we considered a trade-off between the minimum carbon dioxide inlet composition supply and the highest abundancy of methane in the permeate phase. This occurred at a carbon dioxide concentration of 20% (and consequently 30% hydrogen). However, the permeability of hydrogen is particularly high, and it was therefore possible to lower its concentration in the inlet feed to 20% as well. The membrane is thus acting as a

filter, balancing hydrogen concentration to the permeate side, where most of the methane is actually being produced.

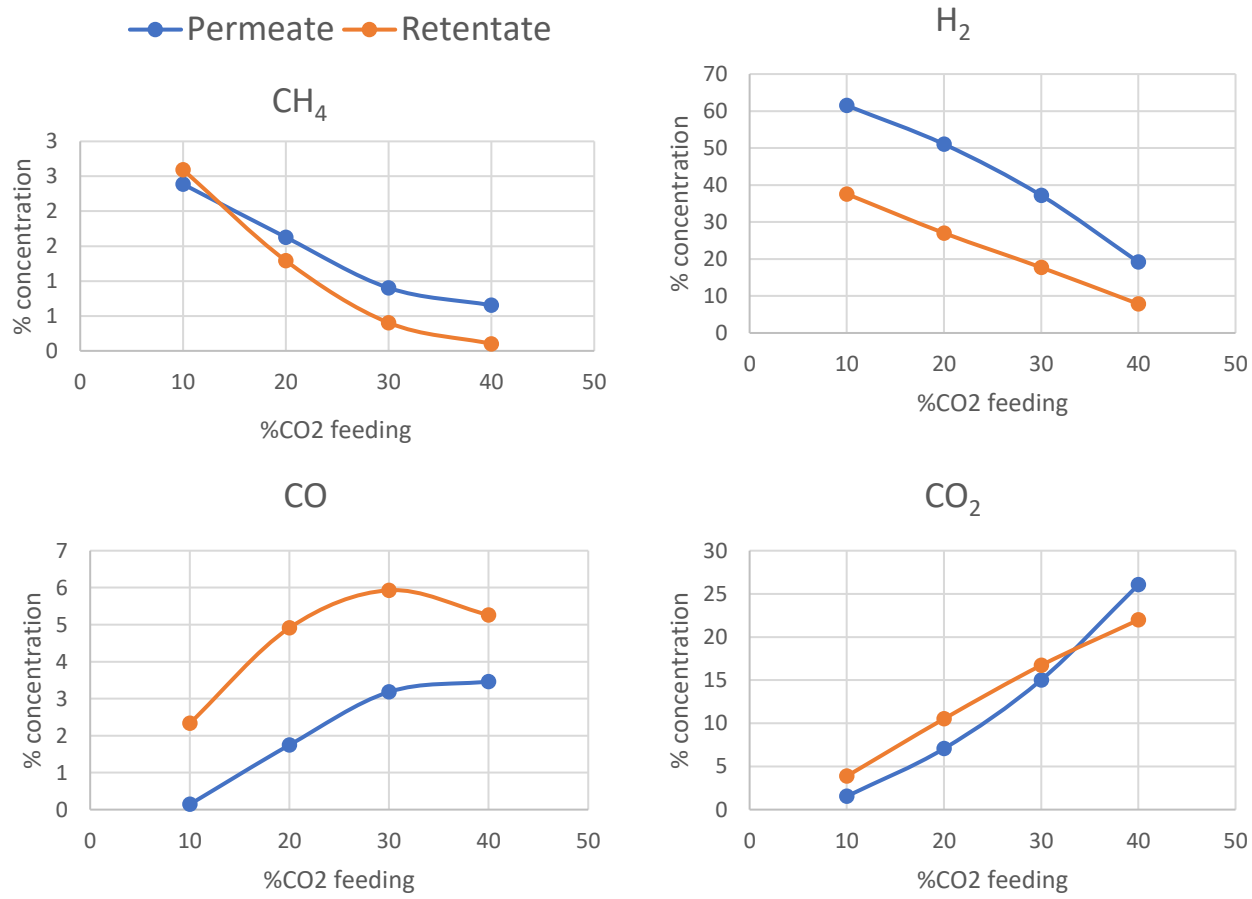

Figure 106 1% Ni(acac)₂ loaded membrane: catalytic testing with variable reagent mixture feed (450°C and 6 bar). Permeate and retentate compositions are being compared.

A successive test with a feed of 20% carbon dioxide, 20% hydrogen and 60% nitrogen at 6 bar and increasing temperature from 100 to 450°C was carried out, with the same membrane. The results are reported in Figure 107. We argue that the remarkable permeability of hydrogen across the membrane will create a more reducing environment on the permeate side of the membrane, leading to higher reduction products (methane), whereas the hydrogen depleted zone (to the retentate side) creates a more suitable environment to the production of CO, a less reduced product of carbon dioxide reduction. Moreover, CO is confirmed to be produced only in double layer membranes, pointing out

the effect of the residence time of the gas mixture inside the pores of the membranes, experiencing a marked space confinement effect on the reagents. Finally, due to the peculiar interaction of these hydrophobic membranes with water, we can suppose CO is more likely to be found on the retentate phase due to its higher solubility in an aqueous media as compared to the apolar carbon dioxide.

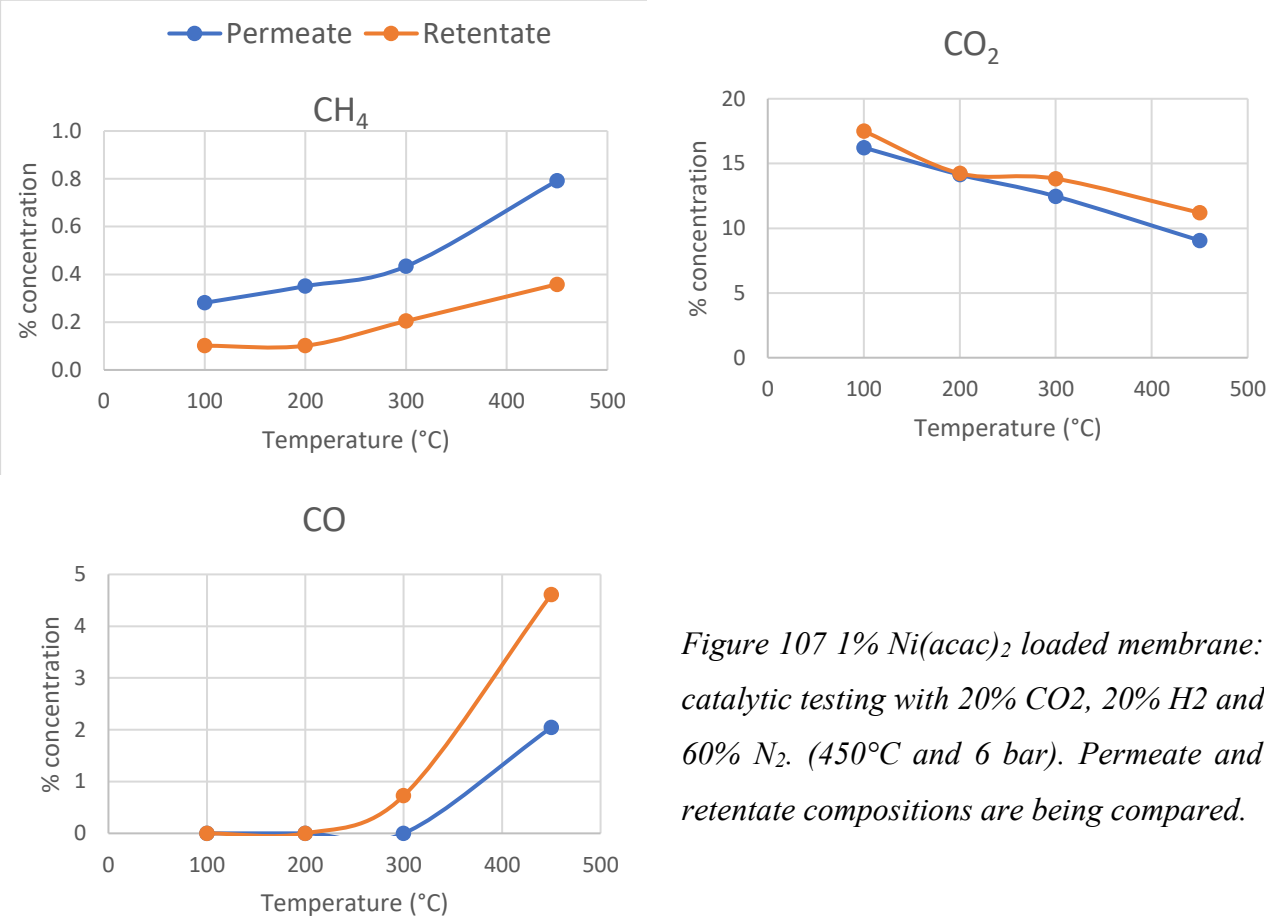

Figure 107 1% Ni(acac)$_2$ loaded membrane: catalytic testing with 20% CO2, 20% H2 and 60% N_2. (450°C and 6 bar). Permeate and retentate compositions are being compared.

This last set of tests was also useful to gain insights on the final carbon mass balance of the system, since both retentate and permeate composition, and the flow rate as well, are known. Referring to Figure 108 and Table 32 it is possible to notice a peak in "missing" carbon, here attributed to coking on the surface exactly in the region 200-300°C, the typical activation temperature range for Ni catalyst in carbon-based reactions.[63–67] Unfortunately an accurate carbon deposition quantification is almost impossible with conventional techniques (such as XPS) due to the pristine high carbon content. Any other byproduct (other than methane or carbon monoxide) was not detected by the GC analyzer, but

at the same time no evident carbon clogged the pores causing a decrease in the permeation performances of the membranes. Therefore the only logical conclusion is that carbon deposition might take place but by means of small-sized particles that do not clog completely the open porosity of the membrane.

Temperature (°C)	Carbon out (permeate+retentate) (mol/h)	Carbon in (mol/h)	% carbon in/out	% "coking"
100	9.10	10.71	84.97	15.03
200	7.67		71.59	28.41
300	7.80		72.77	27.23
450	8.29		77.33	22.67

Table 32 Evaluation of alleged coking on the membrane (1% $Ni(acac)_2$ loading) during the test presented in Figure 22.

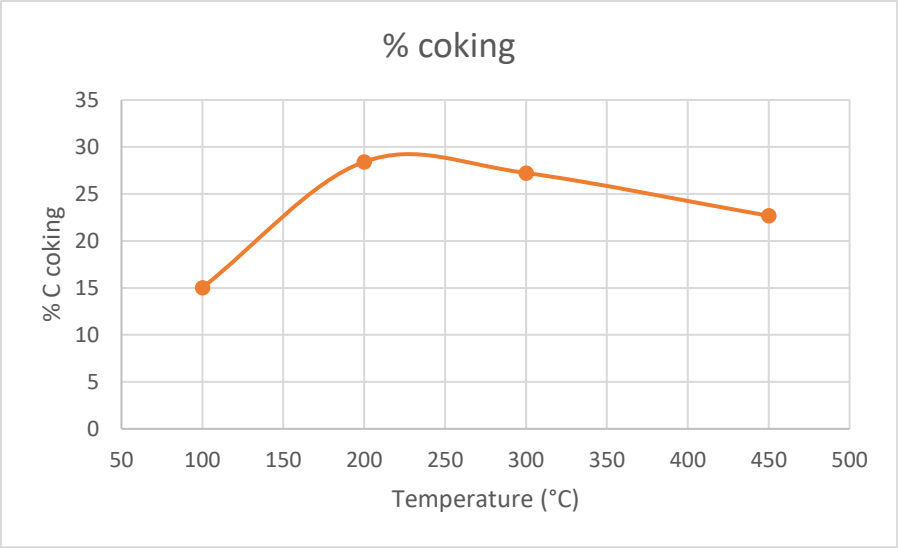

Figure 108 Graphical representation of the data reported in Table 6.

6.10 Powder tests

Finally, to shed light on the relevance of the membrane structure on which the active catalyst is supported, and to evaluate if the composition of the material is the only parameter that plays a role in this system, the first two membranes were ground and sieved, to an intermediate value of size between 100 and 250 μm. They were inserted in a titanium tube, fixed by quartz wool and zirconia beads to create a fixed bed reactor, working at the same pressures as the membranes tested, 6 bar. This reactor underwent the same heating ramp as the membrane and the feed employed was the same as described before (10% CO_2, 40% H_2 and 50% N_2). The results obtained were surprising: no activity was recorded. The same concentrations were found even without any catalyst or material in the reactor, just the empty tube.

We claim this is a clear evidence of the effect of the membrane structure, that even in the case of the carbon-only membrane was able to reach a higher final methane concentration than the powdered membranes. The methane yield obtained is the equilibrium value, that did not benefit from the presence of the prepared materials.

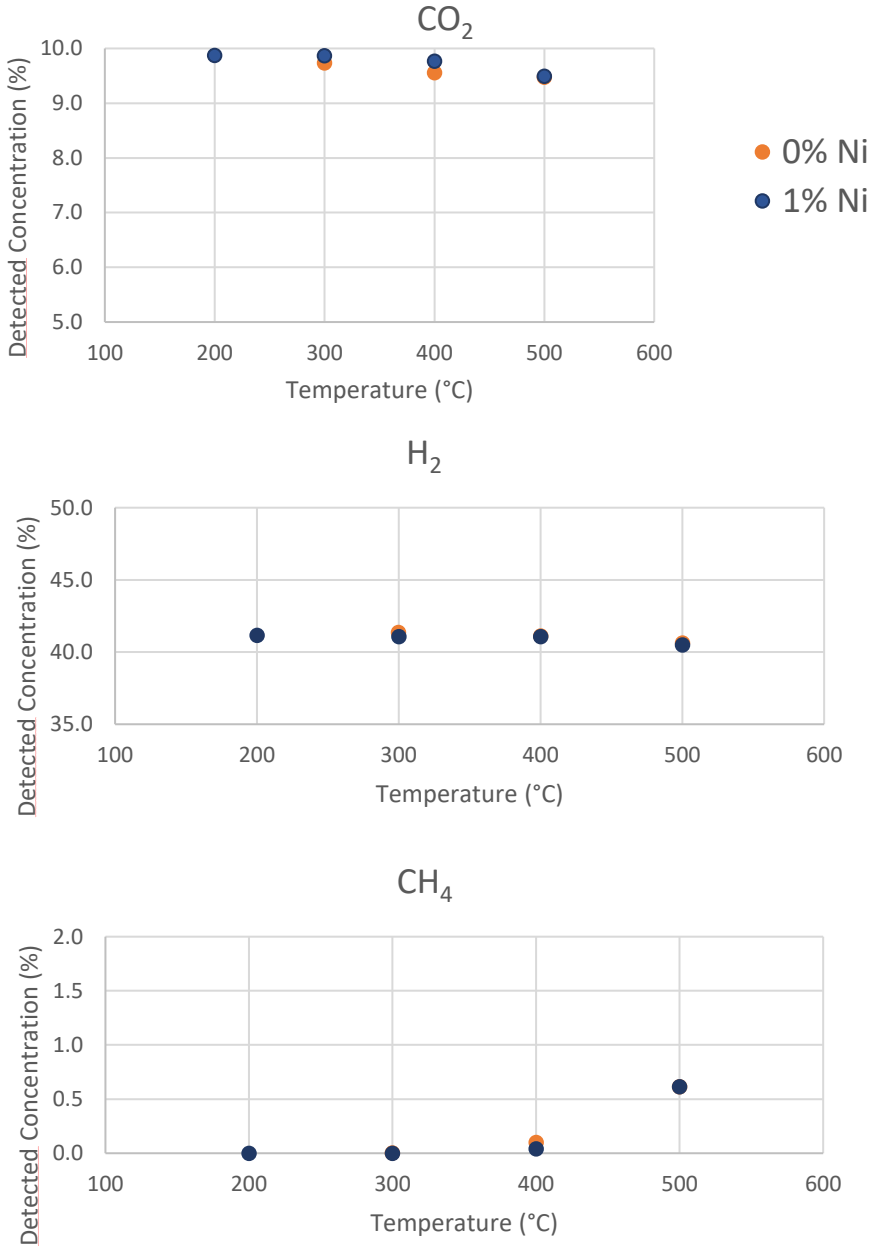

Figure 109 Powdered membranes tested as catalyst for carbon dioxide methanation in a tubular titanium reactor.

6.11 Final remarks

In conclusion an innovative procedure to create a unique device combining heterogeneous catalysis and carbon membranes for gas separation was developed, with interesting and unexpected results. To the best of our knowledge no other example of this kind is mentioned in literature and further tests are in progress to understand the exact nature of the phenomena we are observing: in particular it is still a debatable topic whether space confinement processes or single atom catalysis, or both, are taking place. The exact identification of the Ni species present in the carbon matrix is a challenging task and it is still ongoing. Moreover, new membranes have been prepared, optimizing the sealing technique to avoid breakages, increasing the Ni loading and, in some cases, changing the active metal added to the carbon matrix for different catalytic applications.

The final messages of this cutting-edge project are several and diverse: first and foremost, we learned that the membrane structure is a key factor in the catalytic conversion of carbon dioxide, since powders were completely unactive, moreover selectivity between hydrogen and carbon dioxide is preserved even after Ni integration, which was feared to worsen significantly gas separation performances of the membranes. Moreover, the membrane is able to regulate efficiently the carbon dioxide/hydrogen ratio, acting as an effective carbon dioxide filter: we have seen this effect when different feeds were attempted and the 20% CO_2 20% H_2 mixture was put to the test with surprisingly satisfactory results. Not only the peculiar composition of these membranes played a paramount role in determining their behavior in the testing environment, but we demonstrated that factors such as tortuosity, open porosity, thickness and surface areas are fundamental and may lead, in certain circumstances, to the preferential formation of an undesired product, instead of the wanted pure methane on the permeate side.

All these statements considered, we believe that incorporating nickel into such an unusual support might represent a challenging, and still fascinating, solution for an efficient carbon dioxide conversion.

References

(1) Llosa Tanco, M. A.; Pacheco Tanaka, D. A.; Rodrigues, S. C.; Texeira, M.; Mendes, A. Composite-Alumina-Carbon Molecular Sieve Membranes Prepared from Novolac Resin and Boehmite. Part I: Preparation, Characterization and Gas Permeation Studies. *Int. J. Hydrogen Energy* **2015**, *40* (16), 5653–5663. https://doi.org/10.1016/j.ijhydene.2015.02.112.

(2) Chen, X. Y.; Vinh-Thang, H.; Ramirez, A. A.; Rodrigue, D.; Kaliaguine, S. Membrane Gas Separation Technologies for Biogas Upgrading. *RSC Adv.* **2015**, *5* (31), 24399–24448. https://doi.org/10.1039/C5RA00666J.

(3) Baker, R. W.; Lokhandwala, K. Natural Gas Processing with Membranes: An Overview. *Ind. Eng. Chem. Res.* **2008**, *47* (7), 2109–2121. https://doi.org/10.1021/ie071083w.

(4) Llosa Tanco, M. A.; Pacheco Tanaka, D. A.; Mendes, A. Composite-Alumina-Carbon Molecular Sieve Membranes Prepared from Novolac Resin and Boehmite. Part II: Effect of the Carbonization Temperature on the Gas Permeation Properties. *Int. J. Hydrogen Energy* **2015**, *40* (8), 3485–3496. https://doi.org/10.1016/j.ijhydene.2014.11.025.

(5) Robeson, L. M. Correlation of Separation Factor versus Permeability for Polymeric Membranes. *J. Memb. Sci.* **1991**, *62* (2), 165–185. https://doi.org/10.1016/0376-7388(91)80060-J.

(6) Robeson, L. M. The Upper Bound Revisited. *J. Memb. Sci.* **2008**, *320* (1–2), 390–400. https://doi.org/10.1016/j.memsci.2008.04.030.

(7) *The IUPAC Compendium of Chemical Terminology*; Gold, V., Ed.; International Union of Pure and Applied Chemistry (IUPAC): Research Triangle Park, NC, 2019. https://doi.org/10.1351/goldbook.

(8) Teixeira, M.; Campo, M. C.; Pacheco Tanaka, D. A.; Llosa Tanco, M. A.; Magen, C.; Mendes, A. Composite Phenolic Resin-Based Carbon Molecular Sieve Membranes for Gas Separation. *Carbon N. Y.* **2011**, *49* (13), 4348–4358. https://doi.org/10.1016/j.carbon.2011.06.012.

(9) Medrano, J. A.; Llosa-Tanco, M. A.; Cechetto, V.; Pacheco-Tanaka, D. A.; Gallucci, F. Upgrading Biogas with Novel Composite Carbon Molecular Sieve (CCMS) Membranes: Experimental and Techno-Economic Assessment. *Chem. Eng. J.* **2020**, *394*, 124957. https://doi.org/10.1016/j.cej.2020.124957.

(10) Koresh, J.; Soffer, A. Study of Molecular Sieve Carbons. Part 1.—Pore Structure, Gradual Pore Opening and Mechanism of Molecular Sieving. *J. Chem. Soc. Faraday Trans. 1 Phys. Chem. Condens. Phases* **1980**, *76*, 2457. https://doi.org/10.1039/f19807602457.

(11) Ismail, A. F.; Rana, D.; Matsuura, T.; Foley, H. C. *Carbon-Based Membranes for Separation Processes*; Springer New York: New York, NY, 2011; Vol. 58. https://doi.org/10.1007/978-0-387-78991-0.

(12) Ismail, A. F.; David, L. I. B. A Review on the Latest Development of Carbon Membranes for Gas Separation. *J. Memb. Sci.* **2001**, *193* (1), 1–18. https://doi.org/10.1016/S0376-7388(01)00510-5.

(13) Fuertes, A. B.; Menendez, I. Separation of Hydrocarbon Gas Mixtures Using Phenolic Resin-Based Carbon Membranes. *Sep. Purif. Technol.* **2002**, *28* (1), 29–41. https://doi.org/10.1016/S1383-5866(02)00006-0.

(14) Centeno, T. . A.; Vilas, J. . L.; Fuertes, A. . B. Effects of Phenolic Resin Pyrolysis Conditions on Carbon Membrane Performance for Gas Separation. *J. Memb. Sci.* **2004**, *228* (1), 45–54. https://doi.org/10.1016/j.memsci.2003.09.010.

(15) Centeno, T. A.; Fuertes, A. B. Supported Carbon Molecular Sieve Membranes Based on a Phenolic Resin. *J. Memb. Sci.* **1999**, *160* (2), 201–211. https://doi.org/10.1016/S0376-7388(99)00083-6.

(16) Jones, C. W.; Koros, W. J. Characterization of Ultramicroporous Carbon Membranes with Humidified Feeds. *Ind. Eng. Chem. Res.* **1995**, *34* (1), 158–163. https://doi.org/10.1021/ie00040a014.

(17) Rao, M. B.; Sircar, S. Nanoporous Carbon Membranes for Separation of Gas Mixtures by Selective Surface Flow. *J. Memb. Sci.* **1993**, *85* (3), 253–264. https://doi.org/10.1016/0376-7388(93)85279-6.

(18) Rao, M. B. B.; Sircar, S. Nanoporous Carbon Membrane for Gas Separation. *Gas Sep. Purif.* **1993**, *7* (4), 279–284. https://doi.org/10.1016/0950-4214(93)80030-Z.

(19) Koresh, J. E.; Soffer, A. The Carbon Molecular Sieve Membranes. General Properties and the Permeability of CH 4 /H 2 Mixture. *Sep. Sci. Technol.* **1987**, *22* (2–3), 973–982. https://doi.org/10.1080/01496398708068993.

(20) Fuertes, A. B. Adsorption-Selective Carbon Membrane for Gas Separation. *J. Memb. Sci.* **2000**, *177* (1–2), 9–16. https://doi.org/10.1016/S0376-7388(00)00458-0.

(21) Koresh, J. E.; Soffer, A. Mechanism of Permeation through Molecular-Sieve Carbon Membrane. Part 1.—The Effect of Adsorption and the Dependence on Pressure. *J. Chem. Soc. Faraday Trans. 1 Phys. Chem. Condens. Phases* **1986**, *82* (7), 2057. https://doi.org/10.1039/f19868202057.

(22) *Ceramic Membranes: New Opportunities and Practical Applications*; Gitis, V., Rothenberg, G., Eds.; Wiley, 2016. https://doi.org/10.1002/9783527696550.

(23) Das, S.; Jangam, A.; Du, Y.; Hidajat, K.; Kawi, S. Highly Dispersed Nickel Catalysts: Via a Facile Pyrolysis Generated Protective Carbon Layer. *Chem. Commun.* **2019**, *55* (43), 6074–6077. https://doi.org/10.1039/c9cc00783k.

(24) Izumi, A.; Nakao, T.; Shibayama, M. Atomistic Molecular Dynamics Study of Cross-Linked Phenolic Resins. *Soft Matter* **2012**, *8* (19), 5283. https://doi.org/10.1039/c2sm25067e.

(25) Kosonen, H.; Ruokolainen, J.; Nyholm, P.; Ikkala, O. Self-Organized Cross-Linked Phenolic Thermosets: Thermal and Dynamic Mechanical Properties of Novolac/Block Copolymer Blends. *Polymer (Guildf).* **2001**, *42* (23), 9481–9486. https://doi.org/10.1016/S0032-3861(01)00489-X.

(26) Rönsch, S.; Schneider, J.; Matthischke, S.; Schlüter, M.; Götz, M.; Lefebvre, J.; Prabhakaran, P.; Bajohr, S. Review on Methanation – From Fundamentals to Current Projects. *Fuel* **2016**, *166*, 276–296. https://doi.org/10.1016/j.fuel.2015.10.111.

(27) Centeno, T. .; Fuertes, A. . Carbon Molecular Sieve Membranes Derived from a Phenolic Resin Supported on Porous Ceramic Tubes. *Sep. Purif. Technol.* **2001**, *25* (1–3), 379–384. https://doi.org/10.1016/S1383-5866(01)00065-X.

(28) Wang, T.; Zhang, B.; Qiu, J.; Wu, Y.; Zhang, S.; Cao, Y. Effects of Sulfone/Ketone in Poly(Phthalazinone Ether Sulfone Ketone) on the Gas Permeation of Their Derived Carbon Membranes. *J. Memb. Sci.* **2009**, *330* (1–2), 319–325. https://doi.org/10.1016/j.memsci.2009.01.006.

(29) Salleh, W. N. W.; Ismail, A. F.; Matsuura, T.; Abdullah, M. S. Precursor Selection and Process Conditions in the Preparation of Carbon Membrane for Gas Separation: A Review. *Sep. Purif. Rev.* **2011**, *40* (4), 261–311. https://doi.org/10.1080/15422119.2011.555648.

(30) Sedigh, M. G.; Jahangiri, M.; Liu, P. K. T.; Sahimi, M.; Tsotsis, T. T. Structural Characterization of Polyetherimide-Based Carbon Molecular Sieve Membranes. *AIChE J.* **2000**, *46* (11), 2245–2255. https://doi.org/10.1002/aic.690461116.

(31) Lu, G. Q.; Diniz da Costa, J. C.; Duke, M.; Giessler, S.; Socolow, R.; Williams, R. H.; Kreutz, T. Inorganic Membranes for Hydrogen Production and Purification: A Critical Review and Perspective. *J. Colloid Interface Sci.* **2007**, *314* (2), 589–603. https://doi.org/10.1016/j.jcis.2007.05.067.

(32) Steel, K. M.; Koros, W. J. Investigation of Porosity of Carbon Materials and Related Effects on Gas Separation Properties. *Carbon N. Y.* **2003**, *41* (2), 253–266. https://doi.org/10.1016/S0008-6223(02)00309-3.

(33) Lovallo, M. C.; Gouzinis, A.; Tsapatsis, M. Synthesis and Characterization of Oriented MFI Membranes Prepared by Secondary Growth. *AIChE J.* **1998**, *44* (8), 1903–1913. https://doi.org/10.1002/aic.690440820.

(34) Mateos-Pedrero, C.; Azenha, C.; Pacheco, P. T.; Sousa, J. M.; Mendes, A. The Influence of the Support Composition on the Physicochemical and Catalytic Properties of Cu Catalysts Supported on Zirconia-Alumina for Methanol Steam Reforming. *Appl. Catal. B Environ.* **2020**, *277* (September 2019), 119243. https://doi.org/10.1016/j.apcatb.2020.119243.

(35) Tanco, M. A. L.; Tanaka, D. A. P.; Rodrigues, S. C.; Mendes, A. M. Aging Studies of Composite Alumina Carbon Molecular Sieve Membranes. *Procedia Eng.* **2012**, *44*, 639–641. https://doi.org/10.1016/j.proeng.2012.08.514.

(36) Forster, L.; D'Agostino, C.; Llosa-Tanco, M. A.; Spallina, V.; Brencio, C.; Gallucci, F.; Lindley, M.; Haigh, S. J.; Pacheco-Tanaka, D. A. Tailoring Pore Structure and Surface Chemistry of Microporous Alumina-Carbon Molecular Sieve Membranes (Al-CMSMs) by Altering Carbonization Temperature for Optimal Gas Separation Performance: An Investigation Using Low-Field NMR Relaxation Measurements. *Chem. Eng. J.* **2021**, *424* (December 2020). https://doi.org/10.1016/j.cej.2021.129313.

(37) Nordio, M.; Melendez, J.; van Sint Annaland, M.; Pacheco Tanaka, D. A.; Llosa Tanco, M.; Gallucci, F. Comparison between Carbon Molecular Sieve and Pd-Ag Membranes in H2-CH4 Separation at High Pressure. *Int. J. Hydrogen Energy* **2020**, *45* (53), 28876–28892. https://doi.org/10.1016/j.ijhydene.2020.07.191.

(38) Sazali, N. The Influence of Carbonization Temperature and Heating Rate towards Carbon Membrane Performance: A Review. *J. Adv. Res. Fluid Mech. Therm. Sci.* **2019**, *62* (2), 151–158.

(39) Rodrigues, S. C.; Whitley, R.; Mendes, A. Preparation and Characterization of Carbon Molecular Sieve Membranes Based on Resorcinol-Formaldehyde Resin. *J. Memb. Sci.* **2014**, *459*, 207–216. https://doi.org/10.1016/j.memsci.2014.02.013.

(40) Tseng, H.-H.; Kumar, I. A.; Weng, T.-H.; Lu, C.-Y.; Wey, M.-Y. Preparation and Characterization of Carbon Molecular Sieve Membranes for Gas Separation—the Effect of

Incorporated Multi-Wall Carbon Nanotubes. *Desalination* **2009**, *240* (1–3), 40–45. https://doi.org/10.1016/j.desal.2008.01.048.

(41) Tin, P. S.; Xiao, Y.; Chung, T. Polyimide-Carbonized Membranes for Gas Separation: Structural, Composition, and Morphological Control of Precursors. *Sep. Purif. Rev.* **2006**, *35* (4), 285–318. https://doi.org/10.1080/15422110601003481.

(42) Barbosa-Coutinho, E.; Salim, V. M. M.; Piacsek Borges, C. Preparation of Carbon Hollow Fiber Membranes by Pyrolysis of Polyetherimide. *Carbon N. Y.* **2003**, *41* (9), 1707–1714. https://doi.org/10.1016/S0008-6223(03)00129-5.

(43) Jung, C. H.; Kim, G. W.; Han, S. H.; Lee, Y. M. Gas Separation of Pyrolyzed Polymeric Membranes: Effect of Polymer Precursor and Pyrolysis Conditions. *Macromol. Res.* **2007**, *15* (6), 565–574. https://doi.org/10.1007/BF03218832.

(44) Saufi, S. .; Ismail, A. . Fabrication of Carbon Membranes for Gas Separation—a Review. *Carbon N. Y.* **2004**, *42* (2), 241–259. https://doi.org/10.1016/j.carbon.2003.10.022.

(45) Trick, K. A.; Saliba, T. E. Mechanisms of the Pyrolysis of Phenolic Resin in a Carbon/Phenolic Composite. *Carbon N. Y.* **1995**, *33* (11), 1509–1515. https://doi.org/10.1016/0008-6223(95)00092-R.

(46) Jackson, W. M.; Conley, R. T. High Temperature Oxidative Degradation of Phenol–Formaldehyde Polycondensates. *J. Appl. Polym. Sci.* **1964**, *8* (5), 2163–2193. https://doi.org/10.1002/app.1964.070080516.

(47) Chong, K. C.; Lai, S. O.; Thiam, H. S.; Teoh, H. C.; Heng, S. L. *Recent Progress of Oxygen/Nitrogen Separation Using Membrane Technology*; 2016; Vol. 11.

(48) Yun, J.; Chen, L.; Zhang, X.; Feng, J.; Liu, L. The Effect of Introducing B and N on Pyrolysis Process of High Ortho Novolac Resin. *Polymers (Basel).* **2016**, *8* (3), 35. https://doi.org/10.3390/polym8030035.

(49) Grandi, S.; Magistris, A.; Mustarelli, P.; Quartarone, E.; Tomasi, C.; Meda, L. Synthesis and Characterization of SiO2–PEG Hybrid Materials. *J. Non. Cryst. Solids* **2006**, *352* (3), 273–280. https://doi.org/10.1016/j.jnoncrysol.2005.11.033.

(50) Hasegawa, M.; Sugawara, K.; Suto, R.; Sambonsuge, S.; Teraoka, Y.; Yoshigoe, A.; Filimonov, S.; Fukidome, H.; Suemitsu, M. In Situ SR-XPS Observation of Ni-Assisted Low-Temperature Formation of Epitaxial Graphene on 3C-SiC/Si. *Nanoscale Res. Lett.* **2015**, *10* (1), 421. https://doi.org/10.1186/s11671-015-1131-9.

(51) Czekaj, I.; Loviat, F.; Raimondi, F.; Wambach, J.; Biollaz, S.; Wokaun, A. Characterization of Surface Processes at the Ni-Based Catalyst during the Methanation of Biomass-Derived Synthesis Gas: X-Ray Photoelectron Spectroscopy (XPS). *Appl. Catal. A Gen.* **2007**, *329*, 68–78. https://doi.org/10.1016/j.apcata.2007.06.027.

(52) Itoh, K.; Yamanaka, K.; Nozue, H.; Kasama, K. Dissolution Kinetics of High Resolution Novolac Resists; Ito, H., Ed.; 1991; pp 485–496. https://doi.org/10.1117/12.46397.

(53) Hofmann, S. *Auger- and X-Ray Photoelectron Spectroscopy in Materials Science*; Springer Series in Surface Sciences; Springer Berlin Heidelberg: Berlin, Heidelberg, 2013; Vol. 49. https://doi.org/10.1007/978-3-642-27381-0.

(54) Tyler, B. J.; Castner, D. G.; Ratner, B. D. Regularization: A Stable and Accurate Method for Generating Depth Profiles from Angle-Dependent XPS Data. *Surf. Interface Anal.* **1989**, *14* (8), 443–450. https://doi.org/10.1002/sia.740140804.

(55) Naumkin, V. A.; Kraut-Vass, A.; Gaarenstroom, S. W.; J., P. C. NIST X-Ray Photoelectron Spectroscopy Database. *Meas. Serv. Div. Natl. Inst. Stand. Technol.* **2012**, *20899* (20), 20899. https://doi.org/10.18434/T4T88K.

(56) Cao, G. Z.; Meijernik, J.; Brinkman, H. W.; Burggraaf, A. J. Permporometry Study on the Size Distribution of Active Pores in Porous Ceramic Membranes. *J. Memb. Sci.* **1993**, *83* (2), 221–235. https://doi.org/10.1016/0376-7388(93)85269-3.

(57) Javaid, A.; Hughey, M. P.; Varutbangkul, V.; Ford, D. M. Solubility-Based Gas Separation with Oligomer-Modified Inorganic Membranes. *J. Memb. Sci.* **2001**, *187* (1–2), 141–150. https://doi.org/10.1016/S0376-7388(01)00341-6.

(58) Cui, X.; Bustin, R. M.; Dipple, G. Selective Transport of CO2, CH4, and N2 in Coals: Insights from Modeling of Experimental Gas Adsorption Data. *Fuel* **2004**, *83* (3), 293–303. https://doi.org/10.1016/j.fuel.2003.09.001.

(59) Lillepärg, J.; Breitenkamp, S.; Shishatskiy, S.; Pohlmann, J.; Wind, J.; Scholles, C.; Brinkmann, T. Characteristics of Gas Permeation Behaviour in Multilayer Thin Film Composite Membranes for CO2 Separation. *Membranes (Basel).* **2019**, *9* (2), 22. https://doi.org/10.3390/membranes9020022.

(60) Selyanchyn, R.; Ariyoshi, M.; Fujikawa, S. Thickness Effect on CO 2 /N 2 Separation in Double Layer Pebax-1657®/PDMS Membranes. *Membranes (Basel).* **2018**, *8* (4). https://doi.org/10.3390/membranes8040121.

(61) Stern, S. A. The "Barrer" Permeability Unit. *J. Polym. Sci. Part A-2 Polym. Phys.* **1968**, *6* (11), 1933–1934. https://doi.org/10.1002/pol.1968.160061108.

(62) Zhao, X.; Li, W.; Huang, Z.; Liu, S. Synthesis of Nickel-Incorporated Larch-Based Carbon Membranes with Controllable Porous Structure for Gas Separation. *J. Nanoparticle Res.* **2015**, *17* (11), 433. https://doi.org/10.1007/s11051-015-3229-5.

(63) Lee, W. J.; Li, C.; Prajitno, H.; Yoo, J.; Patel, J.; Yang, Y.; Lim, S. Recent Trend in Thermal Catalytic Low Temperature CO2 Methanation: A Critical Review. *Catal. Today* **2021**, *368*, 2–19. https://doi.org/10.1016/j.cattod.2020.02.017.

(64) Frontera, P.; Macario, A.; Ferraro, M.; Antonucci, P. L. Supported Catalysts for CO2 Methanation: A Review. *Catalysts*. MDPI AG February 13, 2017. https://doi.org/10.3390/catal7020059.

(65) Shen, L.; Xu, J.; Zhu, M.; Han, Y.-F. Essential Role of the Support for Nickel-Based CO 2 Methanation Catalysts. *ACS Catal.* **2020**, *10* (24), 14581–14591. https://doi.org/10.1021/acscatal.0c03471.

(66) Ashok, J.; Pati, S.; Hongmanorom, P.; Tianxi, Z.; Junmei, C.; Kawi, S. A Review of Recent Catalyst Advances in CO2 Methanation Processes. *Catal. Today* **2020**, *356*, 471–489. https://doi.org/10.1016/j.cattod.2020.07.023.

(67) Iglesias, I.; Quindimil, A.; Mariño, F.; De-La-Torre, U.; González-Velasco, J. R. Zr Promotion Effect in CO2 Methanation over Ceria Supported Nickel Catalysts. *Int. J. Hydrogen Energy* **2019**, *44* (3), 1710–1719. https://doi.org/10.1016/j.ijhydene.2018.11.059.

7. Conclusion and outlook

Many disciplines and topics have converged in this project: from environmental consciousness indeed chemistry, material science and partly chemical engineering were summoned to tackle the problem of atmospheric pollutants from various sources by means of heterogeneous catalysis systems.

From the approach followed in Chapter 2, with the aim of addressing industrial preparation issues of perovskite three-way catalysts with fixed composition, the project developed taking into accounts design optimization of the materials involved in environmentally valuable reactions in Chapter 3. In both case an extensive characterization of the materials obtained accompanied the functional assessment in order to rationalize the observed behavior.

In Chapter 2 the focus was on the effect of preparation procedure and of reproducibility of Fe-based and Mn-based perovskites with doping in the A- and B-site. $La_{0.6}Ca_{0.2}Fe_{0.8}Cu_{0.2}O_3$, LCFC, powders, obtained by different industrially relevant synthetic procedures, are compared to evaluate the methods for scale-up: Flame Spray Pyrolysis (FSP) and Co-Precipitation (COP), respectively provided by Lurederra Foundation and Johnson Matthey. The effects of varying composition (doping) and FSP process variability are considered as comparative studies on morphological, crystallographic, redox and compositional properties, and functional activity in TWC. A model reaction (CO+NO) and reactions with a more complex TWC exhaust mixture were carried out. Unexpected results on the effectiveness of doping for catalytic activity emerged, especially regarding the effectiveness of Ca-doping following different synthetic procedures. Samples prepared with the same composition proved to be significantly affected by the synthesis, with variability within the same process. As a general trend, coprecipitation results in less efficient inclusion of Ca in the perovskite lattice and therefore seems less suitable industrial approach to incorporate Ca. The insertion of Ca into the perovskite crystalline cell enhances the formation of Fe (IV) active sites for pollutant oxidation. The presence of Ca inside the lattice, also affects the perovskite lattice parameters, stabilizing copper with respect

to the segregation of Cu (II) as copper oxide. The LCFO perovskite contributes to the activation of HCs and NO only at higher temperature, when oxygen is not present anymore in the reaction mixture, this being consumed in the oxidation of non-HC species. The activity of LCFC COP is comparable to FSP analogue under stoichiometric conditions, despite differences highlighted by characterization. In an oxygen-deficient mixture, LCFC-COP yields higher NO reduction and CO oxidation activity than LCFC-FSP. The absence of Ca in the lattice was unexpectedly beneficial and the benefit can be attributed to surface La and Fe enrichment in the COP sample.

Similarly, $La_{0.9}K_{0.1}Mn_{0.9}Co_{0.1}O_3$, LKMC, powders were also synthesized by FSP and COP. A detailed comparison of the two materials reveals that the degree of K insertion inside the perovskite lattice is, again, process-dependent and the effects are observable on cell deformation, ion mobility and surface composition. La and Mn segregate to the surface in the COP catalysts while Co is accumulated at the surface in the FSP catalyst. BET specific surface area differences, moreover, cannot be claimed as the sole reason for different activity.

In the CO-assisted NO reduction, LKMC FSP is performing better than LKMC COP whereas in the complex TWC mixture the opposite is observed. The higher activity of FSP is related to the presence of oxygen active species on the perovskite surface and to a suprafacial oxidation mechanism. In the complex mixture, in contrast, the surface composition and the Mn-segregation seems to play a major role. Consistently, the results of the catalytic testing reveal that the activity is quite different among the two catalysts, with a lower ignition temperature for CO and propene oxidation by the COP sample. Regarding the NO reduction, the presence of O_2 in stoichiometric amount prevents any significant NO reduction. The catalyst is active at approximately 200°C for both samples under stoichiometric conditions. Under rich conditions, NO reduction is improved. The O_2 is inhibiting the NO reduction: when the oxygen is consumed, NO is reduced and it reaches complete conversion at 600°C for LKMC COP. Considering the O_2 inhibition during NO reduction, the compositions of bulk and surface affects the catalytic performance, in particular the concentration of active oxygen species, contributing to a

Mars-van Krevelen vacancy mechanism, and B cation distribution along the material depth. Doping of the A-site alters the mobility of metal cations throughout the structure, resulting in different, and in some cases, worse catalytic activity.

In conclusion, both LCFC and LKMC compositions, COP approach seems less effective in delivering an efficient alkali or alkali earth dopant inclusion, due to the high solubility of these ions. This leads to important consequences in the composition distribution and therefore in the catalytic activity and selectivity of these materials. The extent of structural modifications due to the synthetic approach greatly varies between different compositions.

The scope of the project reported in Chapter 3 was the development and investigation of innovative perovskite catalysts with the aim of a possible application in the abatement of carbon soot from diesel engines in the automotive sector. The materials here proposed have been tested for soot oxidation in presence of oxygen and NO, with an excess of oxygen to emulate as much as possible the conditions of a real diesel engine exhaust mixture, and for their oxygen storage capacity, to get a deeper insight on their mechanistic aspects in the abovementioned reaction. The final aim of in elucidating the functional trends of such materials is to translate this knowledge into applications such as Gasoline Particulate Filters or Four Way Catalysts.

The chosen compositions arise from redox considerations: Mn and Co are chosen due to their stability, oxygen donating performances and in the case of Co its beneficial contribution for soot and NO oxidation.

K-doping improved the catalytic activity of the A-site for both soot oxidation and NO_x conversion. K deposition was also studied to learn more about its relevance. Because it avoids extremely high temperatures and hazardous solvents, the synthetic method utilized is exceptionally environmentally friendly. Co and K dopings are not responsible for considerable surface segregation and/or perovskite structure desegregation, according to a comprehensive structural, morphological, and compositional characterization effort. The reducibility in these materials decreases when La is substituted by Sr.

XPS gives a possible explanation for this: Sr-doped samples tend to easily form carbonates and alkaline elements are prone to slight segregation on the surface, whereas Co migrates to the bulk.

Catalytic tests in presence of NO, oxygen and soot showed that the double doping (Co and K) increases notably the catalytic activity of the material in the oxidation reaction: LKMC is able to fully oxidize soot at 306°C, a considerably lower temperature than without any catalyst. Sr-doped samples are still quite active, but less than the counterpart without Sr. Another interesting result is the highest activity behavior for the K-doped sample and the K-deposited one.

Considering all these aspects as a whole, both from compositional points of view and from catalytic and Oxygen Storage Capacity tests, LKMC seems to be a good integration of the surface activity guaranteed by K with the importance of oxygen from the lattice thanks to the presence of Co.

A set of perovskites with different A-site doping, and constant B-site doping, were synthetized, extensively characterized, and compared in soot oxidation by oxygen and NO, as well as OSC via CO-TPR in the steady state. K-doping proved to induce a higher contribution of reactive surface oxygen species. Sr-instead, despite the tendency to segregate on the surface, has the positive effect of improving oxygen mobility from the inner layers of the lattice. However, this was not enough to achieve satisfactory results in soot oxidation. A heavier doping can likely cause a higher concentration of oxygen vacancies on the surface.

However, increasing Sr doping does not necessarily lead to better performances. In the more Sr-loaded case, B-site elements are more abundant on the surface than the less-doped sample, and also with respect to K-doped samples. Interestingly, the B-site Ni tends to remain inside the bulk material, despite being attracted towards the surface during reaction, as it can be imposed by the contact with soot.

In conclusion perovskite catalysts prove to be effective and comparable to noble metal catalyst in TWC applications: the versatile redox properties of metal cations and their ability to coordinate

oxygen due to the peculiar perovskite structure, allowing great oxygen ion mobility, are factors that enhance their activity in this application.

From Chapter 4 on, a different environmental challenge was tackled, pursuing the development and optimization of Ni-supported materials that could efficiently thermochemically convert carbon dioxide into methane, with no or reduced amount of byproducts such as carbon monoxide and methanol. Chapter 4 in particular dealt with the investigation of the effects of supporting Ni nanoparticle onto ceria and perovskite oxides through different surface decoration techniques such as impregnation, deposition, exsolution and grafted deposition.

The interaction between the active catalyst, nickel in this case, and the support, be it ceria, a perovskite or both, are here the first actor on the stage. Besides this sustainability in preparatory techniques is a central theme in this Chapter and an active effort to reduce the amount of catalyst needed is made.

The results of this investigation are promising: low amount of active catalyst does not automatically mean inactive materials, but instead a careful tuning of the interaction between support and supported metal can enhance the features of the catalyst with surprising experimental outcome, even at atmospheric pressure and temperatures below 400°C. Material engineering like in this case was also exploited in Chapter 6 with the unusual carbon matrix support for Ni nanocatalyst.

Promising carbon dioxide abatement was reached (up to 10% of residual carbon dioxide concentration), although the role of coking still is an open issue in this field and would need further quantification. At the same time methane was successfully produced and detected with promising yields as well.

Chapter 5 combines controlled-porosity preparation techniques with small molecule activation and conversion through a collaboration with the University of Hamburg.

Catalytically active materials were this time obtained integrating mesoporosity and composition design for thermoconversion of carbon dioxide into mehane. Active nanoparticles were extracted from the material by means of exsolution approaches.

An extensive characterization was performed as well, to gather information about structure, composition, vibrational spectroscopy behavior, physisorption features (and therefore porosity), micromorphology through TEM measurements and reductive functionality. Catalytic tests complete the picture that we can get from these sets of samples towards carbon dioxide methanation.

First of all, the synthetic procedures here employed have proved to be effective. SEM-EDX pictures show homogenous samples but with some notable NiO segregation outside the particles in Si-templated samples and in samples that were calcined at lower temperatures.

Reducibility investigations demonstrated that at 500°C with a 5% hydrogen concentration Ni is completely reduced to its metallic oxidation state, resulting in the correct exsolution conditions.

After reduction XRD, nitrogen physisorption, TEM and SEM-EDX are repeated: the observed alterations are in agreement with segregated NiO reduction, especially because morphology techniques show metallic Ni clusters on the surface, with a diameter from 5 to 30 nm.

Another significant finding was XPS assessment of post catalytic coking, which was confirmed.

In conclusion, stable materials were obtained from a mesoporosity-oriented synthesis and exsolution technique to retrieve Ni particles on the surface. Catalytic performances were unfortunately severely affected by coking deposition that most likely blocked the active sites on the surface.

Finally, in Chapter 6 an innovative carbon-based membrane reactor system is conceived, created, optimized and tested towards permeability and selectivity in single gas tests and to catalytic results with the reagent mixture. No previous example of a similar approach is known and so the project presented is extremely original and innovative.

Surprising and exciting results, in terms of methane yield, were obtained and this preliminary “proof of concept” of the combination of carbon molecular sieve membranes and Ni catalysis paved the way to new research possibilities, optimizing even further the preparation and structure of the membranes and exploring new perspectives making use of other metals in order to study new processes and not only carbon dioxide methanation.

We were able to observe the relevance of membrane structure in promoting a sort of space confinement of the gaseous reactor and the non-detrimental effect of Ni in the permselectivity of the membranes obtained with this integration. None of these results were given for granted.

Optimization of analytical setup and testing conditions was also a fruitful part of the project, giving interesting insights on the special features of the membranes, that separate efficiently and conveniently the components of the mixture, with less need of further downstream purification.

This journey across heterogeneous catalysis was therefore productive, since satisfactory results were obtained on both sides, three-way catalysis investigations and carbon dioxide methanation processing. I also think that some recurring elements are showing throughout the whole PhD project here presented; in particular, the constant balance that the material reaches between bulk and surface composition and behavior is playing a role in virtually any systems described so far. From this evidence the need of a larger picture of the material is clear and this can be achieved only by choosing wisely the analytical techniques to be applied in every case and by carefully creating logic connections between all the information we can gather. Especially in the chapters dealing specifically with perovskites this is particularly true and significant differences are observed between material outmost layers and inner bulk composition. Moreover, in this project conventional oxide catalysis had the chance to contaminate with “exotic” disciplines such as membrane reactors, that are not frequently employed for this kind of application. It was extremely satisfying having the possibility to try for the first time to merge the two scientific areas and to see a new research direction originate under our eyes.

To conclude, great efforts have been devoted to tackle both already mature material optimization, as in the case of the collaboration with industrial partners, but also to explore innovative horizons for the effective abatement of pollution to climate change mitigation.

Acknowledgements

None of these scientific achievements would have been possible without the invaluable assistance, help and trust of my supervisor, Prof. Antonella Glisenti. Throughout the three years of my PhD I have received from her innumerable and precious suggestions, ideas, proposals, questions and answers, which enriched my project, but most of all myself as a scientist and not only. I would like to thank her for giving me the confidence to pursue my ideas and my dreams, even when I was the first one to doubt them. This brought my work to a definitely higher level.

Secondly I would like to acknowledge all the scientific collaborators and partners I encountered during this journey, in particular: Prof. Fausto Gallucci, Arash Rahimalimamaghani, Serena Poto, Anouk de Leuw den Bouter, and Prof. Emiel Hensen and coworkers from the Eindhoven University of Technology, Dr. Alfredo Pacheco Tanaka and Dr. Margot Llosa-Tanco from Tecnalia (Spain), Prof. Simone Mascotto and Anastasios Tsiotsias from the University of Hamburg (Germany), Cristina Castro-Salazar from Lurederra (Spain), Andrea Eva Pascui from Johnson Matthey (UK), Prof. Paolo Canu and his coworkers from the Department of Industrial Engineering and Dr. Annalisa Sandon from the Department of Civil, Environmental and Architectural Engineering at the University of Padova. I recognize that their contributions to my project were crucial to the development of my project.

Thirdly I would like to thank my colleagues and friends at the IMPACT Research Group at the Department of Chemical Sciences at the University of Padova. I am very proud of the team we were able to create and let grow much more than I would have ever expected. Keep going!

My appreciation also goes out to my family and friends for their encouragement and support all through my project.